

Wafer-Scale Fabrication of Thin SiN Membranes and Au Films and Membranes with Arrays of Sub- μm Holes Using Nanosphere Lithography

THÈSE N° 4883 (2010)

PRÉSENTÉE LE 19 NOVEMBRE 2010

À LA FACULTÉ SCIENCES ET TECHNIQUES DE L'INGÉNIEUR

LABORATOIRE DE MICROSYSTÈMES 1

PROGRAMME DOCTORAL EN MICROSYSTÈMES ET MICROÉLECTRONIQUE

ÉCOLE POLYTECHNIQUE FÉDÉRALE DE LAUSANNE

POUR L'OBTENTION DU GRADE DE DOCTEUR ÈS SCIENCES

PAR

Mona Julia Katharina KLEIN

acceptée sur proposition du jury:

Prof. M. A. Ionescu, président du jury

Prof. J. Brugger, Dr R. Pugin, directeurs de thèse

Prof. N. de Rooij, rapporteur

Prof. O. Tabata, rapporteur

Dr H. Wolf, rapporteur



ÉCOLE POLYTECHNIQUE
FÉDÉRALE DE LAUSANNE

Suisse
2010

Abstract

In this thesis, the wafer-scale fabrication of SiN membranes, Au films and Au membranes with arrays of sub- μm holes is described. Two conceptually different processes (1) and (2) were developed, both of which are based on nanosphere lithography (NSL) with self-assembled close-packed monolayers of polystyrene (PS) beads. PS beads with a diameter D in the range of 420 nm to 530 nm were used. The hole array periodicity p was thus determined by D . Different bead deposition methods were tested; by spin-coating, a monolayer wafer coverage $> 90\%$ could be obtained. By O_2 -RIE, D could be reduced in a controlled way down to $0.3D$.

In process (1), holes were etched into the device layer using a hole etch mask made by NSL. The hole size \varnothing was determined by the reduced D . In this way, 100 nm thick SiN membranes with a maximum size of $2400 \times 2400 \mu\text{m}^2$ and a hole density on the order of 10^8 holes/ cm^2 were fabricated by etching holes into the SiN. The membrane release was done in a combined dry-/wet-etch procedure.

Similarly, hole arrays were fabricated on 2" glass wafers by sputter-etching into 200 nm thick Au films. With this process, different \varnothing , e.g. from 60 nm to 180 nm, could be obtained for initially identical mask holes by tuning the sputter-etch parameters.

In process (2), NSL was used to realize high aspect ratio Si and oxidized Si pillars that were subsequently used as a lift-off template. Free-standing, 200 nm thick, $1200 \times 1200 \mu\text{m}^2$ large Au membranes with \varnothing from 100 nm to 300 nm were successfully fabricated using Si pillars as KOH lift-off template and a Si-DRIE release procedure. Using oxidized Si pillars for lift-off in HF instead, such hole arrays in Au films could be transferred to flexible, transparent parylene films.

The fabricated devices were characterized and successfully tested for stencil and refractive index sensing applications:

Holey SiN membranes were bulge-tested and withstood pressures up to 5 bar, showing their suitability for stencil and filtration applications. Stenciling was successfully done for (a) the deposition of arrays of 230 nm in diameter Au and Ag dots onto Si substrates and (b) the etching of holes into a 500 nm thick SiN membrane.

The light transmission characteristics of wafer-scale hole arrays in Au films were reproducible for different measurement locations. Similar hole arrays were used to detect refractive index changes in water of varying glycerine concentrations. The transmission through Cr/Au membranes with sub-wavelength hole arrays was measured. Upon Cr removal, the transmission was enhanced by a factor 2.4.

Keywords Nanosphere lithography, colloidal lithography, self-assembly, hole arrays, porous membranes, Si pillars, stencil, microfiltration, plasmonics, EOT.

Zusammenfassung

In dieser Doktorarbeit wurde die Fabrikation von dünnen SiN Membranen sowie Goldfilmen und -membranen untersucht, die mit regelmässig angeordneten Löchern von $< 1 \mu\text{m}$ im Durchmesser (\emptyset) perforiert sind. Insbesondere fand die Herstellung grossflächig und auf Basis von 2" bzw. 4" Scheibensubstraten statt.

Zwei unterschiedlich Ansätze (1) und (2) wurden untersucht. Anfangs basieren beide auf Lithographie mittels autoassemblierten Monolagen sphärischer Polystyrolpartikel (PS) (en: nanosphere lithography NSL). Der PS Durchmesser D war 420 bis 530 nm. D bestimmt die Gitterkonstante der späteren Lochgitter. Es wurden unterschiedliche Methoden untersucht, um PS Monolagen aufzubringen. Durch Aufschleudern von PS Suspensionen konnten 90% der Fläche von 4" Scheiben mit Monolagen bedeckt werden. Durch Ätzen in O_2 -Plasma konnte D kontrolliert bis zu $0.3D$ reduziert werden.

In (1) wurden Löcher in die Dünnschichten hinein geätzt. Als Maskierung diente eine Lochmaske, die mittels NSL hergestellt wurde. Das Si Substrat wurde lokal durch Rückseitenätzen entfernt. So wurden 100 nm dicke SiN Membranen bis zu einer Größe von $2400 \times 2400 \mu\text{m}^2$ mit einer Porendichte $\approx 10^8/\text{cm}^2$ realisiert. Ebenfalls mittels Ätzen durch eine NSL Lochmaske wurden 200 nm dicke Goldschichten perforiert. Mit der angewendeten Ätzmethode ist es möglich, \emptyset in einem weiten Größenbereich einzustellen ohne Änderung der Lochmaske.

In (2) wurden 200 nm Au direktionell auf Si oder oxidierte Si Säulen aufgedampft. Durch das hohe Aspektverhältnis konnten diese nachfolgend durch Nassätzen in KOH bzw. HF selektiv entfernt werden. Auf dem Substrat verblieb so ein poröser Goldfilm. \emptyset wurde in diesem Fall durch den Durchmesser der Säulen bestimmt und lag im Bereich von 100 bis 300 nm. Löchrige Membranen mit einer Größe bis zu $1200 \times 1200 \mu\text{m}^2$ wurden ähnlich wie in (1) durch Rückseitenätzen des Si Substrats realisiert.

Die hergestellten porösen Filme und Membranen wurden charakterisiert sowie erfolgreich für diverse Anwendungen getestet. So zeigten Wölbungstests dass die porösen SiN Membranen als Filtrationsmembranen geeignet sind. Weiterhin wurden SiN Membranen als Schattenmaske benutzt, wodurch (a) Metall punktuell aufgedampft wurde, (b) eine 500 nm dicke SiN punktuell geätzt und damit ebenfalls perforiert.

Löchrige Au Filme und Membranen wurden bezüglich ihrer optischen Eigenschaften charakterisiert. Die Lichttransmission konnte durch Anregen von Oberflächenplasmonen um einen Faktor 2.4 erhöht werden. Schließlich konnte gezeigt werden, dass die löchrigen Au Filme als Brechungsindex-Sensor geeignet sind.

Schlüsselwörter Colloid Lithographie, Auto-assemblierung, Löcher Arrays, poröse Membranen, Si Säulen, Stencil, Mikrofiltration, Oberflächenplasmonen, EOT.

Contents

1	Introduction	3
1.1	Holey thin films and membrane applications	4
1.1.1	Applications overview	4
1.1.2	Stenciling	5
1.1.3	Filtration	7
1.1.4	Hole arrays for surface plasmon based sensing	11
1.2	State-of-the-art	17
1.2.1	Conventional fabrication methods	17
1.2.2	Self-assembly based methods	20
1.3	Research objective	24
1.4	Choice of fabrication method	26
1.5	Research outline	27
2	Bead deposition	29
2.1	Forces governing bead self-assembly	30
2.2	Convective self-assembly of beads	39
2.3	Experimental	42
2.3.1	Drop-coating convective self-assembly	44
2.3.2	Controlled convective self-assembly with CAPA tool	52
2.3.3	Spin-coating	60
2.4	Summary and conclusions	74
3	Bead size reduction	75
3.1	Etching of PS beads in oxygen plasma	76
3.2	Experimental	78
3.2.1	Anisotropic etch characteristics	78
3.2.2	Bead surface roughening	82
3.2.3	Bead dislocation	82
3.2.4	Cutting polymeric links between beads	83
3.3	Summary and conclusions	84

4	Bead pattern transfer	87
4.1	Nanosphere lithography	88
4.2	Experimental	89
4.2.1	Holey thin metal films by NSL <i>lift-off</i>	89
4.2.2	Si pillars by NSL <i>etching</i>	91
4.2.3	Micro-patterning of holes and dots/pillars	96
4.3	Summary and conclusions	104
5	Device fabrication	105
5.1	Holey SiN membranes	106
5.1.1	Process outline	106
5.1.2	Results and discussion	108
5.1.3	Preliminary conclusions	117
5.2	Hole arrays in Au films on glass substrates by sputter-etching	118
5.2.1	Process outline	118
5.2.2	Results and discussion	121
5.2.3	Preliminary conclusions	127
5.3	Holey Au films and membranes using pillars as lift-off template	128
5.3.1	Process outline	128
5.3.2	(Oxidized) Si pillars as lift-off templates	130
5.3.3	Au membranes with sub- μm holes	134
5.3.4	Au films with sub- μm holes transferred to parylene	138
5.3.5	Preliminary conclusions	141
5.4	Summary and conclusions	142
6	Characterization of SiN and Au films and membranes	143
6.1	Bulge tests of holey SiN membranes	144
6.2	Light transmission through hole arrays in Au films and membranes	146
6.2.1	Sputter-etched hole arrays in Au films on glass substrates	147
6.2.2	Sub-wavelength hole arrays in Au membranes	149
7	Stenciling and refractive index sensing	151
7.1	Deposition through holey stencils	152
7.2	Etching through holey stencils	154
7.3	Refractive index sensing	156
8	Conclusions and outlook	159
8.1	Conclusions	159
8.2	Outlook	164

Bibliography	167
---------------------	------------

A Appendix	185
-------------------	------------

Acknowledgements

Curriculum vitae

Beforehand, a brief statement on the choice of terminology.

Sub- μm = nano ? Strictly speaking, “nano” applies to patterns with *at least* one dimension $< 100\text{ nm}$ ^{1,2}. On the other hand, it is quite common in the current micro- and nanotechnology literature to refer to patterns with at least one dimension in the range of 100 nm to $1\ \mu\text{m}$ as “nano” already. This may be justified by the fact that a new set of fabrication methods, nanotechnologies, evolved with the downscaling of structures below $1\ \mu\text{m}$. Those methods are often conceptually different from the traditional tools used for MEMS (micro electro mechanical systems) fabrication¹.

Therefore, when I consider it important to differentiate the devices fabricated in this thesis from truly nanoporous films and membranes, we use the term “sub- μm ” to describe holes with a diameter in the range of 200 nm to 400 nm . The terms nanopatterning or nanofabrication are used to distinguish non-traditional from traditional fabrication methods.

Holey ? I have to admit that this term may be unfamiliar, and *porous* may be the more widely accepted term to describe materials that include a large fraction of voids. During this thesis, *holey* was coined by a collaborator. It has also been used in the literature before. I chose to take it over, as it helps to differentiate thin films and membranes decorated with laterally arranged holes (id. pores), from generally *porous* media with e.g. a sponge-like structure.

1 Introduction

Thin films and membranes with arrays of sub- μm holes are interesting for a wide range of applications. I will give a broad overview in the beginning, and then describe in more detail the advantages of such thin porous films and membranes for stenciling, filtration and surface plasmon based sensing.

Thin films and membranes with nano- to μm -size holes are not new. A brief overview of existing conventional (top-down) and self-assembly based (bottom-up) methods will be given.

In the research objective, the device specifications are defined and based on this, a fabrication approach based on nanosphere lithography is chosen.

An outline of this thesis concludes the chapter.

1.1 Holey thin films and membrane applications

1.1.1 Applications overview

Inorganic holey membranes

Thin holey inorganic membranes provide a versatile template for various material synthesis or patterning applications, for example in the form of stencil shadow masks^{3,4,5}. Micro- and nanoporous membranes are also widely used in filtration applications, such as ultrafiltration⁶, micro- and nanofiltration^{7,8,9} or reverse osmosis¹⁰, to name a few. Separation based sensing applications range from molecule or ion sensing^{11,12,13} to DNA sequencing^{14,15}. They also provide a useful tool for various life-science and medical applications, such as cell toxicology studies¹⁶, tissue engineering scaffolds¹⁷, or the use as implantable drug delivery devices¹².

The applications in this group have in common that they require a mechanically strong and chemically robust membrane material to withstand high differential pressures and harsh cleaning procedures. Silicon nitride (SiN) has a high Young's modulus and can be cleaned by organic and acidic etch treatments. It was therefore chosen as the device material for holey membranes that can be used for stenciling and filtration.

Metallic holey films and membranes

An interesting field of applications for metallic films and membranes with periodic arrays of holes is related to the interaction of light with sub-wavelength structures. Optical filters were first developed in the infrared and microwave region^{18,19}, and with the availability of nanofabrication tools, comparable devices could be fabricated operating in the visible wavelength regime²⁰. Other interesting applications are based on the excitation of surface plasmons (SPs)²¹ at sub-wavelength structures. This effect can be used for plasmonic sensing^{22,23}, enhanced spectroscopy²⁴, optical particle trapping²⁵, switching of light²⁶, or may be considered as a circuit element in nanophotonic integrated circuits²⁷.

An important material characteristic for plasmonic applications are the metal dielectric properties. In the visible wavelength regime, surface plasmons can be excited at the surface of e.g. gold (Au) or silver (Ag). Au, in addition, is chemically inert and provides a convenient surface chemistry for bio-sensing applications. This is why Au was chosen as the device material for plasmonic applications.

Below, stenciling, filtration (section 1.1.3) and SP based sensing (section 1.1.4) will be described in more detail.

1.1.2 Stenciling

Stenciling is a high resolution shadow mask fabrication method^{3,4} that can be used for the fabrication of micro- and nanoscale patterns. Material can either be deposited through the stencil membrane (stencil lithography (SL)), or the stencil can be used as an etch mask. For example, stenciling has been used for the deposition of micro- and nanodots^{4,28,29,30}, nanowires^{31,32}, ion implantation³³ or pattern transfer by dry-etching^{34,35}. Compared to photoresist based lithographic methods, stenciling has the distinctive advantage to be a “clean”, non-contact method. This allows the patterning of substrates and pre-fabricated devices that are incompatible with wet-processing, either due to a rough surface topography or delicate surface chemistry. In an unprecedented fashion, stenciling has been used for the deposition of semiconductor nanowires^{31,36}, the fabrication of CMOS integrated bio-sensors³⁷, the patterning of flexible, polymeric substrates³⁸, or the transfer of the stencil pattern onto protruding or recessed structures by dry-etching³⁹.

Stenciling principle

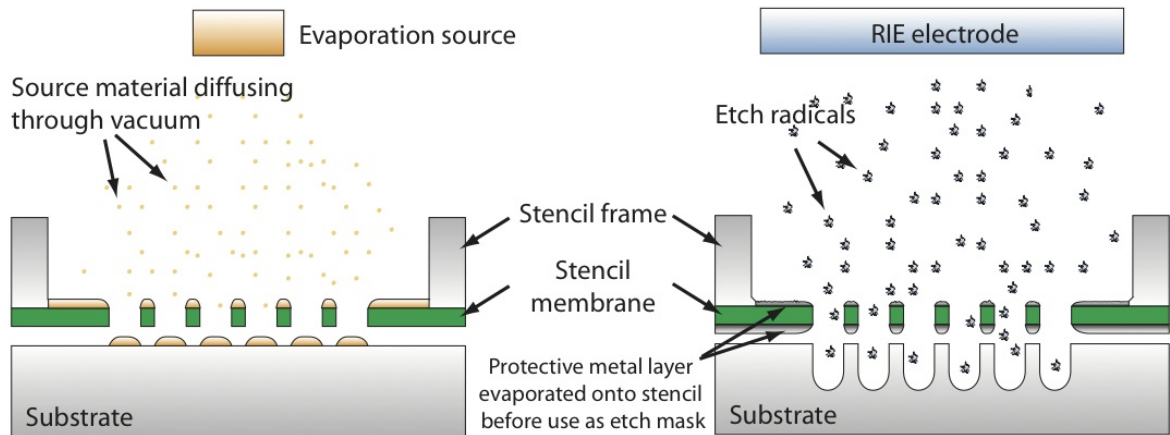


Figure 1.1: Schematic of material deposition and etching through a stencil membrane.

Figure 1.1 shows the principle of deposition and etching through a stencil. The stencil can be aligned to the substrate and mechanically fixed. Then, material is locally deposited or etched away. Directional methods, such as evaporation or anisotropic dry-etching, yield a good pattern transfer. Note that, when using the stencil as an etch mask, it is usually coated with an etch protection, for example a thin Al layer. After the patterning process, the stencil can be removed, if necessary cleaned, and then re-used.

As with any other patterning method, the result depends on process parameters and

on the experimental setup. In SL, important parameters are the stencil-material source distance, the stencil-substrate distance, and the amount of material deposited. When using the stencil as an etch mask, the question of stencil damage comes up. This will be briefly discussed in the following.

Influence of stencil-source/substrate distance

SL owes its advantages largely to the fact that it is a non-contact patterning technique. But this engenders also some limitations. A geometrical constraint is imposed due to the finite size of the source S , the source-stencil distance D and the gap in between the stencil and the substrate G . This defines the outer and inner dimensions X_o and X_i of the deposited patterns (c.f. figure 1.2). If the thickness of the stencil membrane can be

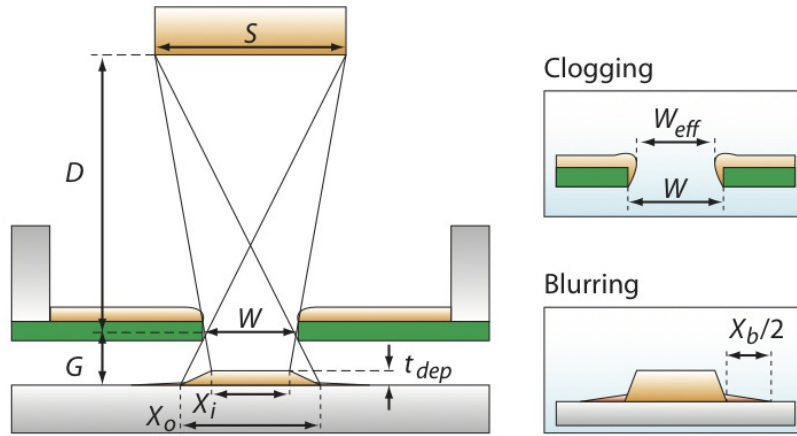


Figure 1.2: The final dimensions of patterns obtained by deposition of material through a stencil are determined by the machine configuration (S and D), the sample setting (G), aperture clogging (W_{eff}), and surface diffusion (X_b).

neglected with respect to the lateral aperture dimensions, X_o and X_i can be expressed as³:

$$X_{o,i} \approx W \pm S \frac{G}{D}. \quad (1.1)$$

This means that, for a good patterning result, S and G should be as small as possible, while D should be maximized (e.g. by using an evaporator with a source-substrate distance of ≈ 1 m). Stencil deformation induced by the evaporated material can lead to a variation of G ⁴⁰. Therefore, preferably strong membrane materials are used which are not easily deformed.

Influence of the amount of material deposited

The material deposition leads to clogging of the stencil aperture. Especially for small apertures or thick films, the reduced width $W_{eff} = W - \Delta W$ should be taken into

account when anticipating the stencil deposition result (c.f. equation 1.1). W_{eff} can be approximated by⁴⁰:

$$\Delta W \approx t_{dep} \frac{S}{2D}. \quad (1.2)$$

Here again, the importance of a large D and small S to reduce the loss in lateral pattern dimension becomes clear. Equation 1.2 is based on the assumption that no material is deposited onto the aperture sidewalls, which is valid for a high D and small S . Also, sidewall deposition can be reduced by surface modification of the stencil, e.g. by silanization³⁰.

Blurring due to surface diffusion

As schematically shown in the lower right of figure 1.2, material diffusion on the substrate surface can be another source of loss in lateral pattern dimensions²⁸. However, the influencing parameters are more difficult to assess as compared to the purely geometrical constraints. This is because blurring is greatly influenced by the substrate type, material deposited, deposition method, etc.

Stencil damage during etching through stencil and stencil cleaning ?

Quantitative reports on possible stencil damage when used as a dry-etch mask were not available at the time of this thesis manuscript. However, it can be assumed that etch induced damage due to membrane abrasion is negligible when a thin protective layer of material with a low etch rate is used (e.g. Al in case of Si dry-etching).

Stencil cleaning to remove deposited material and thus retain the aperture dimensions is especially important when depositing sub- μm -size patterns. Metals can be conveniently removed in wet-etches, thus stencils can be reused many times⁴¹. On the other hand, ultra-sonication should be avoided in all cases, which limits the removal of dust particles.

1.1.3 Filtration

Filtration is the act of passing a gas or fluid through a filter in order to remove solid particles. In its simplest form, filtration is based on a size-exclusion principle. Those who drink coffee or tea use this every day, where the permeate is a clear coffee or tea and the retentate corresponds to the ground coffee or tea leaves retained in the filter.

Micro-sieves versus mesh-type holey membranes

In order to distinguish thin filtration membranes with well-defined holes in a 2D arrangement from mesh-type holey membranes obtained by e.g. sol-gel processing or solvent-casting, the former are also called *sieves*. A sieve is characterized by a low pore height to

pore diameter ratio: $h/d \leq 1$ ⁴². Going back to the coffee example, coffee filter paper is a membrane filter while espresso machines use a perforated metallic sieve. The coffee filter versus espresso sieve example illustrates two important advantages of sieves over filters: While water will pass through the sieve almost unhindered, it slowly drips through the filter paper. This is because the filter paper is a maze of fibers with high surface area and tiny dead-end pores that soaks up water and lets it pass only slowly. The sieve, however, has a flat surface and only retains the ground coffee beans. Secondly, cleaning of the filter paper is almost impossible, while the espresso sieve is easily cleaned in running water.

In principle, this every-day example also applies for nano- and micro-sieves in comparison to fibrous, holey membranes. The improved filtration properties when using a sieve with a small pore size distribution in a thin membrane are illustrated in figure 1.3. It compares the pore size distribution of solvent cast, track-etched and micro-fabricated membrane filters and shows how this influences the flow rate through the membrane. For a micro-/nano-sieve with small pore size distribution, the flow rate is orders of magnitude higher than for solvent-cast or track-etched membranes.

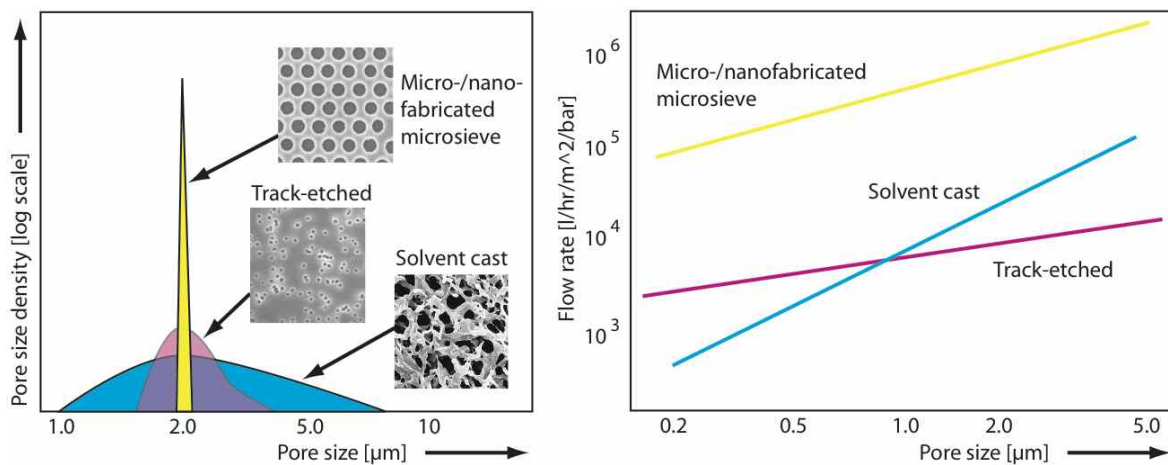


Figure 1.3: Typical pore size distribution of various membrane filters and corresponding clear water flux rate. Figure adapted from van Rijn⁴³.

The first micro-sieves were developed⁴⁴ and patented^{45,46} by Cees van Rijn in the 1990s. Today, the micro-sieves sold by his company Aquamarijn Micro Filtration BV¹ are used for diverse applications such as the filtration of beverages (beer, milk, etc.) or membrane emulsification technology.

¹www.microfiltration.nl

Microfiltration

There exist different types of filtration processes, classified according to the filtered particulate size. Figure 1.4 gives an overview of the separation process terminology. In this thesis, the targeted filtration regime is microfiltration: the physical retention of

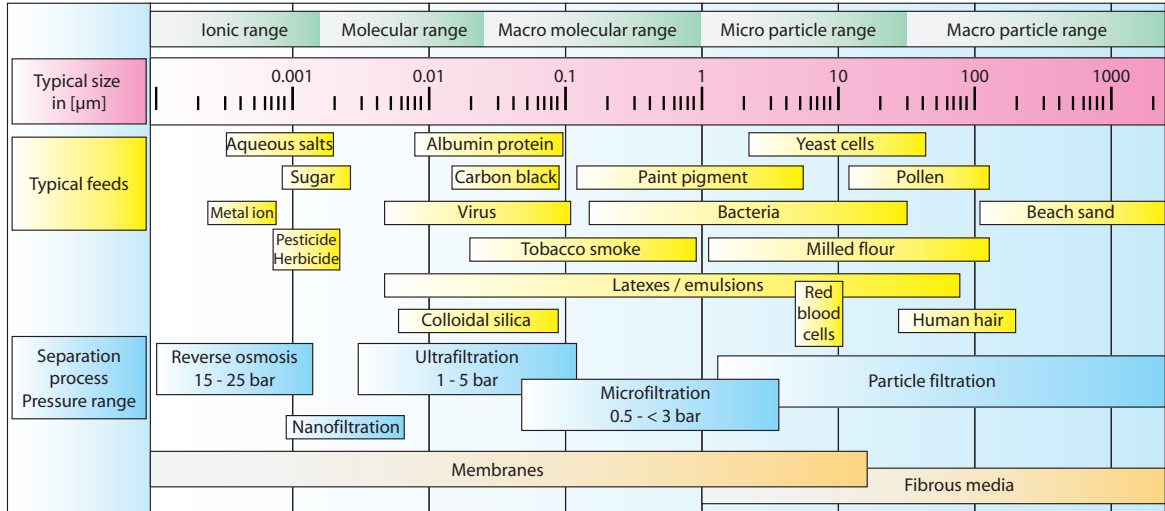


Figure 1.4: The filtration spectrum. Figure adapted from www.h2ro.com and www.millipore.com.

particles in the size range from several tens of nm to a few μm , such as bacteria, yeast cells or latex particles. In microfiltration, the typical trans-membrane pressure Δp is in the range of 0.5 to 3 bar. These low operating pressures can be used because the osmotic pressure Π can be neglected. Π is inversely proportional to the molecular weight M .²

Important factors to consider in microfiltration are the particle diffusivity D_0 and the suspension viscosity η . $D_0 \propto T/(\eta r)$, where T is the temperature and r is the particle radius⁴⁷. For a micron-size sphere in water at 20°C, D_0 is on the order of $10^{-13} \text{ m}^2/\text{s}$, which is three to four orders of magnitude lower than the diffusivity of e.g. sodium chloride. This inhibits back-diffusion of large colloids and particles away from the membrane, giving rise to membrane fouling and highlighting the importance of membrane cleaning.

Flow rate

The flow rate Q through the membrane is an important parameter in filtration applications. To obtain a high Q , the ratio of the channel length (the membrane thickness h

²For example, large colloids with M on the order of 10^4 kg/mol only build up a Π of $\approx 0.1 \text{ mbar}$. Π is described by the van't Hoff equation⁴⁷.

in this case) to the hole diameter r should be as small as possible. In the optimum case of $h/2r < 0.5$, the holes in the membrane can be treated as an orifice and the influence of h on Q can be neglected⁴⁸:

$$Q = \frac{r^3 \Delta p}{3\eta}. \quad (1.3)$$

Otherwise, for $h \approx r$,

$$Q = \frac{r^3 \Delta p}{3\eta} \left(1 + \frac{8h}{3\pi r}\right)^{-1}, \quad (1.4)$$

and thus Q scales with $1/h$. This is the reason why filtration membranes should be as thin as possible.

Mechanical membrane properties

As mentioned above, microfiltration requires that the membranes withstand differential pressures Δp of up to 3 bar. A schematic of a membrane under pressure is shown in figure 1.5 for membranes of sidelength l and for the case with and without holes. The bulge test is a convenient method to measure the membrane vertical deflection z as a function of Δp . The obtained pressure-deflection curves can be fitted to analytical models, and thus material parameters such as the intrinsic stress and Young's modulus can be extracted⁴⁹.

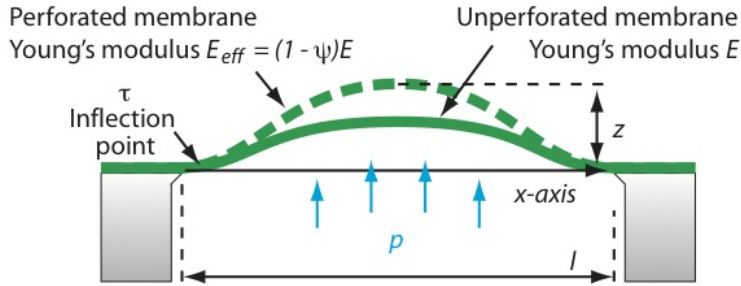


Figure 1.5: A membrane with and without holes under pressure. Under the same conditions, a holey membrane will have a higher vertical deflection z due to its weaker Young's modulus E_{eff} . The highest stress in the membrane occurs at the inflection point τ .

According to literature, the maximum tensile stress σ_{yield} before rupture occurs in low-stress SiN is on the order of 4×10 GPa. For a 100 nm thick and 1 mm wide square SiN membrane with 0.33% porosity and $E = 290$ GPa, Rijn⁴³ calculated a pressure at break p_{break} of 3.1 bar. However, in this calculation, weakening of the membranes due to the presence of holes was not taken into account. Kovacs⁵⁰ compared different analytical expressions for membrane bursting pressures and introduces an effective Young's modulus: $E_{eff} = (1 - \psi)E$, where ψ is the hole fraction. σ_{yield} has a square-root dependence

on E . Taking this into account in the above calculation, p_{break} is lowered by a factor 0.82 and thus on the order of 2.5 bar. Thus, from a theoretical point-of-view, membranes for micro-filtration applications should either be thicker, smaller in lateral dimension, or of lower porosity.

Design considerations

The membrane vertical deflection z is a function of the lateral position x . At the inflection point τ where $d^2z(x)/dx^2 = 0$, maximum stress occurs (c.f. figure 1.5). This has important consequences for the membrane design. For example, in case of a low-stress, but thick SiN membrane ($l = h = 1$ mm), τ is located ca. 25 μm away from the clamping points⁴³. For thinner membranes, or equally, materials with lower Young's modulus, τ will move closer to the clamping edges. Thus, for the membrane design, the hole array area should be placed at least 25 μm away from the support frame.

1.1.4 Hole arrays for surface plasmon based sensing

Hole arrays are a 2D form of a periodic surface structure. The interaction of light with such structured surfaces can be classified into different regions depending on the ratio of the wavelength λ to the periodicity of the structure p ⁵¹. In the intermediate regime where λ is on the order of the periodicity p , interesting light diffraction effects and coupling of light to evanescent waves occurs.

The case when a diffracted beam becomes grazing to the plane of the grating was first observed by Prof. Wood in 1902⁵² as a dip in the reflection spectrum. It was later explained by Lord Rayleigh⁵³ and is known as a Wood-Rayleigh anomalies (WR). For light under normal incidence, WR are observed when the condition $\lambda = p\sqrt{\epsilon_d}$ is fulfilled, where ϵ_d is the dielectric constant of the medium adjacent to the grating.

Much later, focussed ion beam milling made it possible to precisely fabricate hole arrays in thin metal films with a p on the order of the wavelength of visible light (VIS, $\lambda = 390 - 750$ nm). In 1989, Ebbesen published a seminal paper in which he described the unusually high transmission of light through sub-wavelength hole arrays in thin gold films (extraordinary optical transmission (EOT))⁵⁴. The high transmission is explained by the coupling of incoming light to surface plasmons (SPs, c.f. below) via light diffraction at the hole array. SPs excited at the incoming side guide light through the holes as an evanescent wave. By diffraction of this wave on the other side of the hole array, light is outcoupled again into freely propagating light. In this way, more light than actually incident on the area occupied by the holes is transmitted and gives rise to EOT.

The wavelength at which SPs are excited depends on the geometry of the hole array and on the dielectric properties of the metal and adjacent dielectric medium, ϵ_m and ϵ_d , respectively. Therefore, changes in ϵ_d will influence the wavelength at which EOT

occurs. This can be detected by measuring the spectrum of the transmitted light. For ϵ_d , one can also write $n = \sqrt{\epsilon_d}$, where n is the refractive index (RIX) of the dielectric. This is why measuring changes in the transmitted light spectrum as a function of ϵ_d is called “RIX sensing”.

Surface plasmons

Surface plasmons (SPs) are charge density fluctuations that are linked to the propagation of electromagnetic surface waves at a metal/dielectric interface²¹. This is schematically shown in figure 1.6 for a wave propagating in x . The magnetic field H is oriented perpendicular to the electric field E , thus the surface wave is transverse-magnetic in nature.

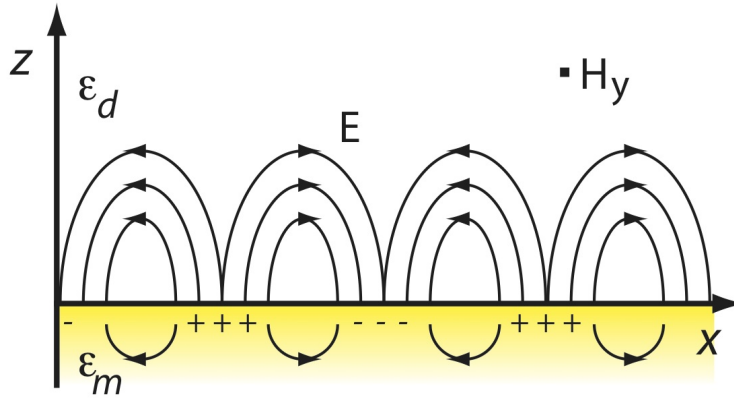


Figure 1.6: Schematic of the charge distribution in the metal free electron gas and the associated SP propagation in x -direction. Figure adapted from Barnes⁵⁵.

The wavevector of SPs, k_{SP} , follows a dispersion curve according to²¹:

$$k_{SP} = \frac{\omega}{c} \sqrt{\frac{\epsilon_m \epsilon_d}{\epsilon_m + \epsilon_d}}, \quad (1.5)$$

where ω is the angular frequency and c is the speed of light. From equation 1.5, the resonant condition for the excitation of SPs can be derived, which is that the denominator under the root needs to be less than zero: $\epsilon_m + \epsilon_d < 0$.

For real ω , real ϵ_d and a complex $\epsilon_m = \epsilon'_m + i\epsilon''_m$ with $\epsilon''_m < |\epsilon'_m|$, the wavevector of surface plasmons is also complex: $k_{SP} = k'_{SP} + ik''_{SP}$. To obtain a real k'_{SP} , $\epsilon'_m < 0$ and $|\epsilon'_m| > \epsilon_d$. At a metal-air interface, this condition is for example fulfilled for Au $\lambda < 480$ nm (also c.f. the dispersion curve for Au in the appendix A.1.). k''_{SP} is associated with internal absorption in the metal. Such losses are high for example for Cr, which is why SPs do not propagate at Cr surfaces.

Coupling of light to surface plasmons

The wavevector of freely propagating light in air, \mathbf{k}_0 , can be decomposed into a component parallel and orthogonal to the metal surface. SPs can be excited by light when the parallel component of the light wavevector $k_{//} = k_{SP}$. The maximum value of $k_{//}$ is equal to $k_0 = 2\pi/\lambda = \omega/c$. Thus, there exists a momentum mismatch $\Delta k = \sqrt{(\epsilon_m \epsilon_d)/(\epsilon_m + \epsilon_d)}$ between $k_{//}$ and k_{SP} . This is schematically shown in the SP dispersion curve in figure 1.7a. The blue region represents the range of $k_{//}$ that exist for incoming light, k_{inc} . k_{SP} always lies to the right of the light line $\omega = ck$. As a consequence of the momentum mismatch, SPs can not be excited directly by freely propagating light.

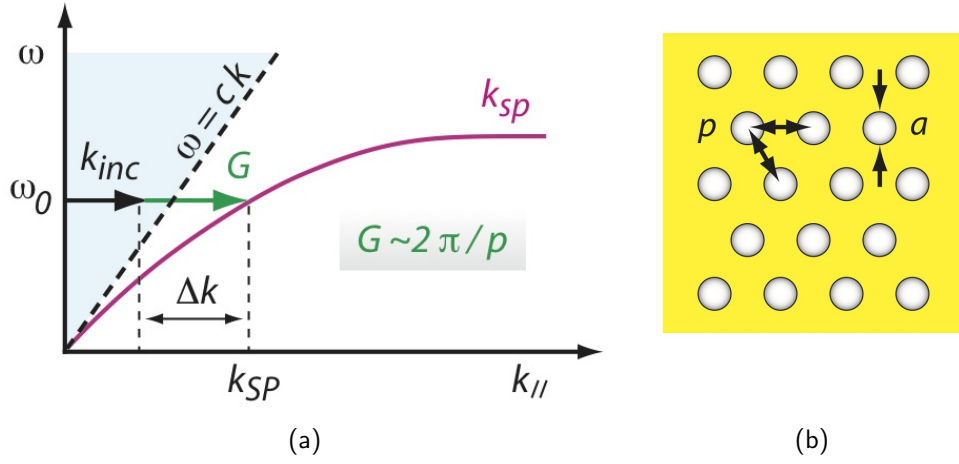


Figure 1.7: (a) k_{inc} is the wavevector of incoming light parallel to the metal surface. G provides the additional momentum Δk to couple incoming light to SPs. It can for example be provided by light scattered at the holes in a hole array with periodicity p and hole diameter a (b).

There exist two main approaches to provide for $\hbar\Delta k$. The one is based on coupling of light through a prism (Kretschmann-Raether configuration)²¹. The other one is called grating coupling where Δk is provided by light scattered at periodic corrugations with a periodicity p on the order of λ .

The periodic surface corrugation can be a 2D array of holes as shown in figure 1.7b. When the light is scattered at the holes, the situation is similar to the case where a wave propagates in a periodic potential, such as those caused by electron oscillations in a crystal lattice⁵⁶. These surface waves are therefore also called Bloch-waves. In the same way as for crystals, a reciprocal lattice vector $\mathbf{G} = \{g_x, g_y, g_z\}^T$ can be defined which fulfills the condition $\exp\{i\mathbf{G}\mathbf{R}\} = 1$, where $\mathbf{R} = \{r_x, r_y, r_z\}^T$ is the set of primitive lattice point position vectors. \mathbf{G} can be constructed from \mathbf{R} as follows: $g_x = 2\pi \frac{r_y \times r_z}{r_x(r_y \times r_z)}$. Permutation of indices gives the relations for g_x and g_y .

For a 2D hexagonal lattice, one obtains $g_x = 2\pi/p\{1, -1/\sqrt{3}, 0\}^T$ and $g_y = 2\pi/p\{0, 2/\sqrt{3}, 0\}^T$. With this, the 2D Bloch-Wave wavevector \mathbf{k}_{BW} can be constructed. Coupling to SPs will be achieved when $k_{BW} = k_{SP}$:

$$|k_{BW}| = |k_{SP}| \quad (1.6a)$$

$$\frac{\omega}{c} \sin \theta_0 \pm ig_x \pm jg_y = \frac{\omega}{c} \sqrt{\frac{\epsilon_m \epsilon_d}{\epsilon_m + \epsilon_d}} \quad (1.6b)$$

with

$$|\pm ig_x \pm jg_y| = \frac{2\pi}{p} \sqrt{4/3} \sqrt{i^2 \pm ij + j^2} \quad (1.6c)$$

Here, i and j are integers. For light under normal incidence ($\theta_0 = 0$), solving equation 1.6a yields the wavelength λ_{SP} at which freely propagating light can be coupled to SPs via a hexagonal array structure:

$$\lambda_{SP} \propto p \sqrt{\frac{\epsilon_m \epsilon_d}{\epsilon_m + \epsilon_d}} \quad (1.7)$$

Equation 1.7 shows the dependence of λ_{SP} on ϵ_d . For SP excitation in the visible wavelength regime (VIS), hole arrays with p in the range of 400 nm to 800 nm are interesting.

Light transmission through sub-wavelength holes

Bethe derived an expression which predicted the transmission efficiency η_B , the transmitted light T normalized to the hole area, through a single hole in a metal screen⁵⁷. Assuming that the screen be infinitely thin and the metal a perfect conductor, he found that $\eta_B \propto (r/\lambda)^4$. For a finite film thickness, the light is exponentially attenuated in the hole, and a cut-off wavelength $\lambda_c = 4r$ can be defined. In real metals of finite conductivity, the electric field penetrates into the metal up to a skin-depth δ . This effectively widens the hole. For example, δ of Au in the visible wavelength regime is on the order of 30 nm.

Figure 1.8 shows a schematic of T through a single hole as a function of λ . Above the cut-off wavelength, T rapidly decays. The situation is drastically different when such holes are arranged in an array, where light is resonantly coupled to SPs that guide the light in the form of evanescent waves through the holes. An example is shown in figure 1.8 for a hexagonal hole array in an opaque Ag film. The hole diameter is 130 nm, thus $\lambda_c \approx 260$ nm. Light is transmitted for $\lambda \gg \lambda_c$. EOT, defined as $\eta > 1$, is observed for the long-wavelength peak. The transmission enhancement is influenced by many parameters, such as hole size a , periodicity p , and hole depth h ^{58,59,60,61}. This is why it is important that the hole array parameters can be tuned with the hole array fabrication process.

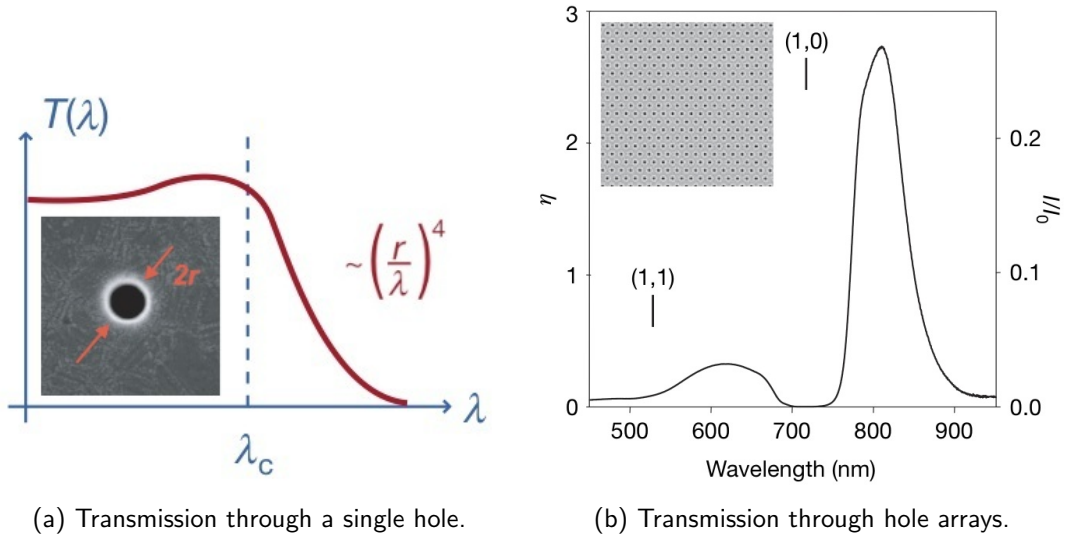


Figure 1.8: (a) Schematic of light transmission T through a single sub-wavelength hole, and (b) transmission enhancement η and normalized transmission I/I_0 measured through an array of sub-wavelength holes milled into a Ag film. Figures adapted from Genet²⁰.

Vertical lines in figure 1.8b indicate the calculated λ_{SP} for that particular hole array geometry (Ag film thickness 225 nm and $p = 520$ nm). Clearly, the transmission peaks do not coincide with the indicated λ_{SP} . An explanation for this is not very clear from the literature. One explanation is that the red-shift is due to interference of different SP modes on both sides of the metal film^{62,59}. Another one is the interference between direct transmission through the holes and the SP surface mode^{63,64}.

Refractive index sensing with hole arrays

As shown above, the excitation of SPs at periodic hole arrays gives rise to high transmission at certain wavelengths. As λ_{SP} is a function of ϵ_d , a change in RIX can be correlated to the shift of the peak transmission wavelength.

Figure 1.9 shows a schematic explanation of RIX sensing by analyzing the spectra of the light transmitted through hole arrays. Figure 1.9a shows the corresponding experimental situation: a hole array in a symmetric dielectric environment, illuminated with a white light source. One spectrum represents the transmission for an array in a medium with dielectric constant ϵ_{d1} . It is shifted relative to the spectrum when the hole array is immersed in a medium with dielectric constant ϵ_{d2} .

As mentioned before, one approach in RIX sensing is to measure the shift of the peak transmission $\Delta\lambda$ (figure 1.9)^{65,66}. Another one is to measure the change in transmitted light intensity ΔT at a constant wavelength. In this way, the white light source can be

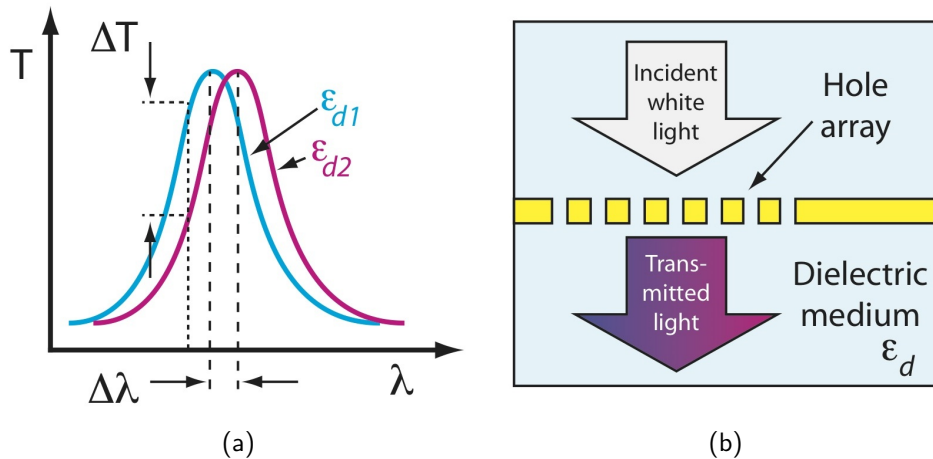


Figure 1.9: (a) The transmission spectrum is modified by changing the dielectric medium (dielectric constant $\epsilon_{d1,d2}$). This can be detected by measuring the peak wavelength shift, $\Delta\lambda$, or a change in intensity at a fixed wavelength, ΔT . (b) Schematic of the experimental situation.

replaced for example by an LED (light emitting diode) or a LASER (light amplification by stimulated emission radiation) source^{67,68}. The latter is particularly interesting for miniaturization of the measurement setup. Commonly obtained sensitivities for hole array based RIX sensors are on the order of 600 nm/RIU^{69,70}. With an optimized array design and measurement setup, Tetz et al. obtained a sensitivity of 1000 nm/RIU⁷¹.

Hole array versus prism-coupled RIX sensing

Hole array based sensors offer distinct advantages as compared to prism-coupled sensing. One is related to the experimental setup (compare the images shown in figure 1.10)^{23,70}. Integration of prism-coupled devices is challenging as it requires high angular resolution measurements or the integration of a spectrometer, which limit the setup to - if not bulky - then at least not chip-size instruments. Hole arrays on the other hand, offer a high density chip-level integration^{68,72} or can be realized as minimally invasive probes at the end of optical fibers⁷³.

Also, owing to the small hole sensitive region, the limit-of-detection can be reduced to attomolar amounts of molecules⁷⁴. Increase in measurement speed can be achieved for example by optimizing the hole geometry⁶⁹, improving the measurement setup (e.g. fixed wavelength intensity measurements with signal chopping, multiplexing with arrayed hole arrays), or increasing the hole array area (which means that more light = signal is available for spectral analysis)⁷⁵. Hole arrays in free-standing membranes with the same dielectric at both metal interfaces (symmetric systems), are promising to improve both the sensitivity and the measurement speed^{65,76}.

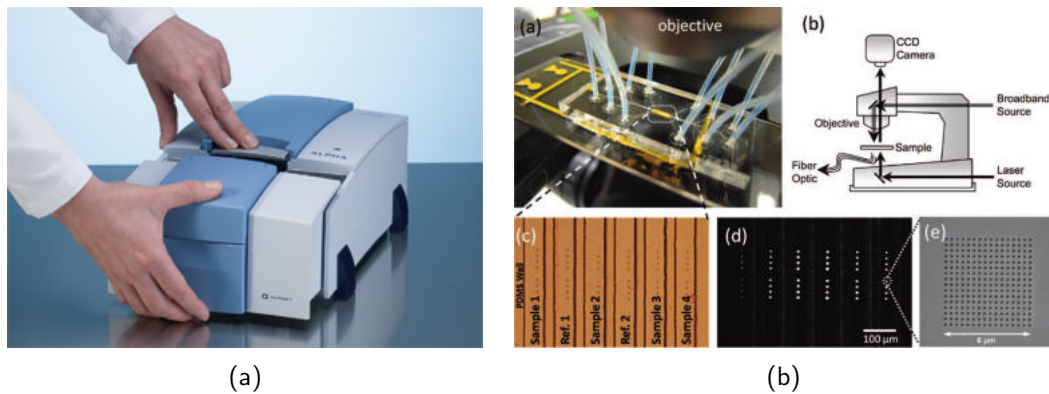


Figure 1.10: (a) Photograph of a commercial FT-IR (fourier transform infrared) spectrometer based on attenuated total internal reflection. The shown setup is sold by Bruker optics as the world’s smallest FT-IR Spectrometer. (b) A hole array based RIX sensor integrated in a fluidic multichannel microarray. The optical elements have still great potential for miniaturization, e.g. based on fiber optics. Figure taken from Im⁷².

This shows that the development of integrated hole arrays in thin metal films and membranes is a promising route to achieve miniaturized, highly sensitive and high speed RIX sensors.

1.2 State-of-the-art

In this section, a selection of state-of-the-art fabrication methods of thin Si-based and metallic films with sub- μm holes will be described. Nanotube membranes such as anodized aluminum oxide membranes⁷⁷ will not be considered. The description is divided into what will be called *conventional* or *top-down* methods, and *self-assembly* based or *bottom-up* methods. The former will also comprise recent methods that are often termed “emerging nanopatterning” methods⁷⁸. For a more detailed description of the respective methods, the reader is referred to the references given. At the end of this section, a brief comparison of the methods is made with respect to the device specification mentioned in the foregoing paragraphs.

1.2.1 Conventional fabrication methods

Of the *serial* writing techniques, focused ion beam milling (FIB) is one of the most widely employed tools to fabricate hole array geometries in both metallic⁵⁴ and insulating^{79,80} thin films and membranes⁸¹. Here, a focussed Ga^+ ion beam is used to locally ablate the substrate material. When fibbing insulating materials, a thin con-

ductive coating is applied prior to fibbing to avoid charging. A strong point of FIB is its versatility. Holes with a diameter of a few tens of nm can be fabricated. The hole shape is almost arbitrary^{82,69} and the hole arrangement can be precisely controlled, an important parameter to obtain the desired response in case of plasmonic materials^{27,83}. Furthermore, hole arrays can be placed locally as a post-process onto devices which cannot be processed otherwise^{73,84}. There do exist some drawbacks to FIB. First, the fact that it is a serial writing technique makes it inherently slow and costly. It is not suited for the fabrication of devices that should find their application in mass products, such as complementary metal oxide semiconductor (CMOS) sensors or even disposable point-of-care bio-sensors. Secondly, there are still some challenges to be solved in terms of hole shape control. Fibbed structures usually exhibit a rounded edge profile (c.f. e.g. the tilted angle SEM images in Laux⁶¹ or Przybilla⁸⁵). Contamination with Ga⁺-ions can be avoided by milling through a sacrificial layer⁸⁶, but this is not a technique that can be employed for all kinds of materials.

Another serial writing technique is electron-beam-lithography (EBL). A focussed electron beam is used to locally irradiate photosensitive material. The developed patterns can then be used as an etch mask directly⁸⁷ or as a lift-off template for evaporated metals⁸⁸. Often, EBL is used to pattern Si master molds which are then replicated into e.g. nickel shims⁸⁹ or polymeric soft stamps⁹⁰. In the same way as for FIB, EBL has the intrinsic disadvantage of being a serial writing technique. Although writing is already much faster than in case of FIB (e.g. the fabrication of a 30×30 hole array in 200 nm Au by FIB takes ≈ 2 hrs, while the same pattern can be exposed by EBL in a few minutes only), realization of wafer-scale hole array templates would still take 2-3 days, even using a fast writing technique such as dot size determination by beam defocussing and exposure time rather than “writing” dots with a strongly focussed beam. The long write time may be tolerated for one-time master fabrication. However, small amendments such as a variation of the dot size require a complete re-fabrication of the EBL written master and shims. Last but not least, both FIB and EBL have an extremely high cost-of-ownership due to the initial and maintenance costs plus the required clean-room environment.

Another method resembles the fabrication of track-etched polymeric nanopore-membranes⁹¹: thin SiN membranes are irradiated either with heavy ions, or with electrons from a transmission electron microscope (TEM)⁹². Ion irradiation has suffers from limited control over the pore position, resulting in non-uniform distribution and coalescence of pores, while TEM writing is, as most serial techniques, inherently slow and costly.

From the group of *parallel* lithography techniques, for example deep-UV (DUV)⁹³ and (laser) interference lithography (LIL)^{94,95,96} have been used to fabricate thin films and membranes with holes sub- μm in size. In case of DUV, shrinking of the dimensions is achieved by using an irradiation source generating UV light with wavelengths λ below

300 nm (e.g. using the krypton fluoride (248 nm) or argon fluoride (193 nm) line). With this, feature sizes on the order of 50 nm can be achieved. Here, the challenge is to adapt the absorption characteristics of the photosensitive material and reflection/interaction with the base substrate.

In LIL, a laser beam is split and brought to interference at the substrate surface. The interference pattern is on the order of $\lambda/2$. The appealing feature of LIL is that it is a maskless exposure technique suitable for the large area (on the order of tens of cm^2) patterning of regular structures. A one-step LIL exposures will generate a 1D grating pattern, by rotation of the substrate with respect to the laser source, 2D arrays can be obtained by double exposure⁹⁶. LIL is comparatively cost-efficient. However, exposure parameters need to be carefully adapted to the substrate type and exposed material. Generation of random structures is not possible.

Another parallel lithography method is phase-shift interference lithography (PIL)⁹⁷. Here, one takes advantage of the interference generated by phase differences to improve the resolution of standard UV lithography. Using PIL, 1D and 2D patterns with a resolution of tens of nm can be achieved. The 1D fringe pattern resembles the one obtained by LIL. In PIL, fabrication of the mask is crucial. The phase shift is usually obtained by imposing a topography onto the photomask, correlated with the opaque mask pattern. By combining PIL with a soft-lithography technique, the Odom group^{98,99} has successfully developed an advanced process (PEEL = phase-shifting photolithography, etching, electron-beam deposition, and lift-off) with multiple replication steps for the fabrication of thin metallic membranes with sub- μm holes. For plasmonic applications based on thin gold membranes, the primary challenges of this technique remain the integration of the fabricated membranes on a chip support frame that can be manipulated, as well as overcoming the need for a Cr adhesion layer for the Au to stick to the substrate before membrane release.

Finally, there exist various forms of contact-lithography techniques, such as nanoimprint lithography (NIL)¹⁰⁰ or micro-contact printing ($\mu\text{-CP}$)^{101,102}. NIL is “a parallel patterning method in which a surface pattern of a stamp is replicated into a material coated on a hard substrate by mechanical contact and 3D material displacement, to be used in fields until now reserved to electron beam lithography (EBL) and photolithography (PL). This includes all variants of reversal imprint, as long as a prepatterned film is transferred and bonded to another substrate” (a quotation taken from Schift¹⁰⁰). Going into detail into the variants of NIL is beyond the scope of this brief summary. NIL has been employed to create polymeric pillars which were then used as a lift-off template to create hole arrays in evaporated thin metal films^{103,104}. The inverse approach, etching into the material, has been employed using a NIL fabricated pillar stamp to create holes in a polymer mask layer. Using a “mix and match” strategy combining UV photolithography and conventional dry-etch processes, holey SiN membranes on a Si frame

were fabricated¹⁰⁵. One of the major challenges of NIL remains the minimization of the loss in dimension along the various replication steps. Thermal shrinkage and stamp design (pattern homogeneity, cross-sectional stamp profile, stamp rigidity etc.) need to be carefully optimized for each pattern replication step. This imposes limitations on the transferable pattern geometry (allowing only demolding of positive sidewall profile stamps) and aspect ratio (structures with an aspect ratio $\gg 1$ are difficult to demold). Nevertheless, it should be noted that recently, enormous progress has been made in this field. Relatively simple (homogeneous pattern density and low aspect ratio, e.g. for optical gratings or color filters^{106,107}) nanoscale patterns are nowadays transferred on large-scale flexible substrates using roll-to-roll processes.

μ CP has been developed since the end of the 1980s particularly in the Whitesides group^{101,108}. They demonstrated that using an elastomeric stamp, self-assembled monolayers (SAMs) of alkanethiolates could be patterned on the surfaces of coinage metals and SAMs of alkylsiloxanes on Si/SiO₂ substrates. It matured to become a low-cost technique to print sub- μ m features with a resolution of < 100 nm (c.f. ¹⁰² and references therein). Not only SAMs can be printed, but also other biological molecules or particles^{109,110}. SAMs can be used as a an etch mask for the wet-etching of thin gold films^{111,112}. Thus, it can also be employed for the fabrication of thin holey gold films and membranes.

NIL and μ CP have in common that they require a high resolution master tool. The master is usually fabricated by a high resolution serial writing technique such as EBL. Therefore, also being methods that have (proven) their potential for up-scaling and high through-put fabrication, the master fabrication is the crucial step which does require a high investment cost, high resolution lithography technique.

As last comment, it should be mentioned that the fabrication of membranes with sub- μ m holes does not necessarily require a nanopatterning (holes with a diameter < 100 nm) method. In many cases, it may also be considered to “simply” shrink the size of the holes in a post-process by conformal material deposition (e.g. Tong⁷⁹). Furthermore, this allows to adapt the surface chemistry - for example from Si-based materials to metallic surfaces.

1.2.2 Self-assembly based methods

As just described in the previous section, there exists a big toolbox of conventional methods that can be used for the fabrication of sub- μ m holes in Si-based and metallic thin films and membranes. Thus the question is justified why there is an interest in the development of bottom-up, self-assembly based methods³. Below, an outline will be given on the distinct advantages of self-assembly based methods, which are in short:

³For a more detailed explanation of self-assembly, please refer to the following chapter 2.

flexibility with respect to the choice of substrate material, low cost of ownership, speed, facile tuning of the the pattern dimensions, integration with standard micro-fabrication techniques, and one-step patterning of wafer-scale substrates.

Self-assembly refers to the process by which nanoparticles or other discrete components spontaneously organize due to direct specific interactions and/or indirectly, through their environment¹¹³. Here, the discussion will be limited to block-copolymer and nanosphere lithography.

Block-copolymer lithography

A block copolymer (BCP) consists of two (or more) polymeric chains (“blocks”) which are covalently attached to each other and which exhibit differing solvent and interfacial interactions. This is the basis for the self-assembly of such polymeric systems into nanopatterns. A comprehensive review by Hamley¹¹⁴ summarizes the principle self-assembly mechanisms as well as the various potential applications. A widely used BCP approach is based on the deposition of preformed BCP micelles. This is schematically shown in figure for spherical PS-P2VP (polystyrene - polyvinylpyridine) BCP micelles. The result is a hexagonal arrangement of polymer “bumps” with short-range order. A thin residual polymer layer remains in between the bumps, it can be removed by a brief exposure to an oxygen plasma.

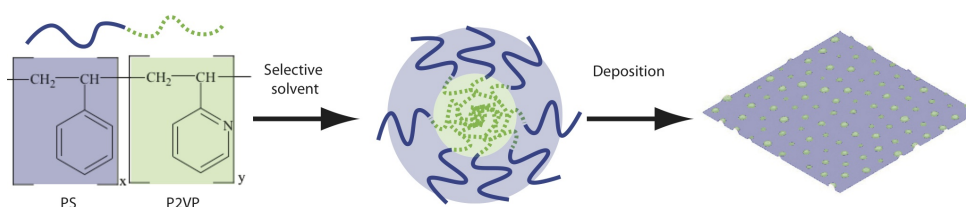


Figure 1.11: Formation of a spherical micelle from a PS-P2VP block copolymer. Deposition of the pre-formed micelles gives a “bumpy” dot pattern in a hexagonal arrangement.

There exist different routes to control the ordering of (spherical as well as elongated) micelles^{115,116}. Examples are pre-patterning of the substrate chemically or topographically¹¹⁷, adapting the BCP system used¹¹⁸, or the deposition process¹¹⁹. Typical length-scales of the polymeric pattern template are on the order of tens to a few hundreds of nm, that is on the order of the size of the BCP.

An appealing aspect of using BCPs to create nanoscale pattern templates is that the size and spacing can be conveniently controlled by tuning the macromolecular characteristics (molecular weight, block-ratio, etc.), as well as by adapting the deposition conditions^{120,121}. Pattern inversion (from “bumps” to “doughnuts”) by post-exposure

to selective solvents is also possible¹²². By spin-coating, BCP micelles can be deposited onto various kinds of wafer-scale substrates, thus making integration of the bottom-up fabricated nanostructures with conventional micron scale devices feasible.

BCP lithography - the pattern transfer of this soft, polymeric material - into Si-based or metallic materials in order to create nanoporous thin films or membranes can be achieved in different ways. A favored technique, in analogy to conventional microfabrication, is to use the polymeric pattern as an etch mask in highly selective dry-etch processes^{123,124}. If the etch selectivity to the substrate material is not high enough, a convenient method is the use of an “intermediate mask”: First, the micellar pattern is transferred into a very thin inorganic layer, which is subsequently used as the actual etch mask. Alternatively, micelles can be pre- or post-loaded with metallic nanoparticles that exhibit a higher etch selectivity¹²⁵. Finally, either the BCP bumps themselves, or after transfer of the same into a pillar template¹²⁴, can be used as lift-off template for thin (≈ 10 nm) evaporated metal layers^{126,127}.

In this way, employing the one or the other technique, porous Si^{123,128}, SiN¹²⁹ and Au^{130,131} thin films and membranes have been realized. As the pattern is on the order of macro-molecular dimensions, BCP lithography is ideally suited for true *nano*-fabrication. However, achieving pattern with characteristic length scales > 200 nm becomes challenging. While high aspect ratio structures in Si can be achieved *relatively* easily thanks to the highly selective Si process chemistry, transferring micellar patterns into high aspect-ratio insulating (such as SiO₂ or SiN) or metallic materials remains difficult.

Fortunately, there exists another self-assembly based patterning approach: nanosphere lithography (NSL), that closes the gap between nanoscale and micron-scale structures, i.e. the fabrication of *sub* – μ m patterns.

Nanosphere lithography

Nanosphere lithography (NSL, also known as colloidal (CL) or natural lithography) was first reported by Fisher¹³² and Deckman and Dunsmuir¹³³. Hulteen and van Duyne¹³⁴ described NSL as a “materials general” process for the fabrication of periodic particle arrays as it allows to obtain particle arrays of different materials - without the need to change the principal bead template. Most NSL works employ either polystyrene (PS) or silica beads with a small size distribution on the order of 2%. in the size range from 200 nm to 1 μ m. The bead size determines the feature spacing, while the actual feature size - as determined by the transfer option chosen (material deposition, beads used as etch mask, post-deposition treatment of the beads to modify their size) - can vary from tens to several hundred nm.

There exist various deposition techniques, which constitutes one basis of the versatility of NSL. A concise review on bead deposition and sub-sequent modification of the

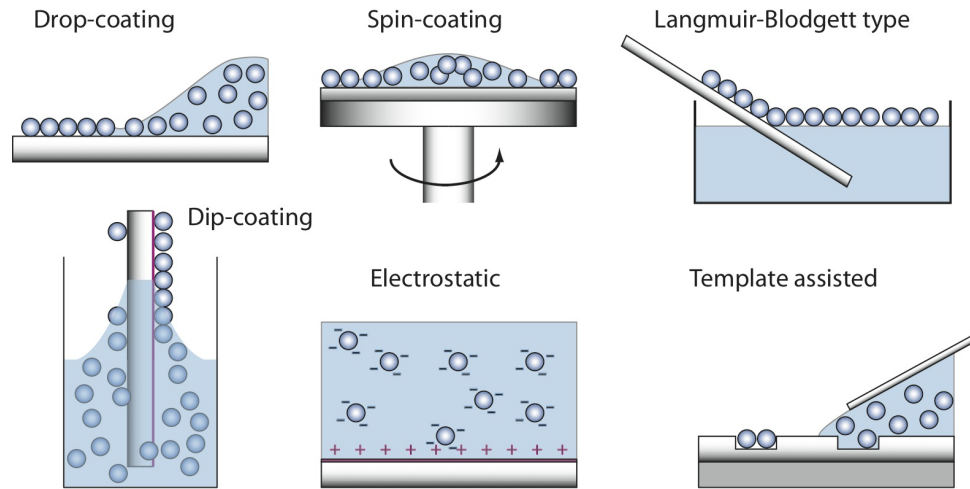


Figure 1.12: Examples of bead deposition methods.

bead template can be found in Yang¹³⁵. Figure 1.12 schematically shows some of these techniques, exploiting different experimental setups as well as different driving forces. Methods to form hexagonally close-packed arrays include drop-coating convective self-assembly (CSA)¹³⁶, dip-coating CSA¹³⁷, spin-coating¹³⁸, controlled meniscus CSA¹³⁹, and bar-coating¹⁴⁰. Here, the bead arrangement is dominated by capillary immersion forces (c.f. chapter 2). By adapting the suspension composition and deposition parameters, ordered but non-close packed arrays can also be obtained by spin-coating¹⁴¹. There exists a range of other methods to form dis-ordered, non-close packed arrays where the bead deposition is driven by electrostatic¹⁴² or molecular attraction¹⁴³. Other bead deposition methods include such as boiling¹⁴⁴, dip-pen lithography¹⁴⁵ or ink-jet printing¹⁴⁶. Finally, controlled particle placement can be achieved by template assisted bead assembly and transfer printing^{147,109,148}. Thus, there exists a large toolbox for the deposition bead in different arrangements and on various kinds of substrates with the potential for wafer-scale patterning.

An additional convenient feature of NSL using PS beads is the possibility for post-deposition modification of the bead template. This can be conveniently achieved by exposure to an oxygen plasma^{149,150,151,152} or by thermal treatment¹⁵³.

After obtaining the desired bead template, the ways to transfer the bead pattern into the substrate (bulk, thin film or membrane) material by etching or material deposition on top of the bead template are sheer unlimited^{154,135,155}. In its simplest form, NSL is similar to a lift-off process. After deposition of the spheres (or beads or colloidal particles) onto the substrate, the material to be patterned is deposited by physical vapor deposition (PVD). The resulting pattern depends on the PVD method (e.g. evaporation¹⁵⁶, sputtering¹⁵⁷, back-filling of the bead template¹⁵⁸ or atomic layer deposition¹⁵⁹)

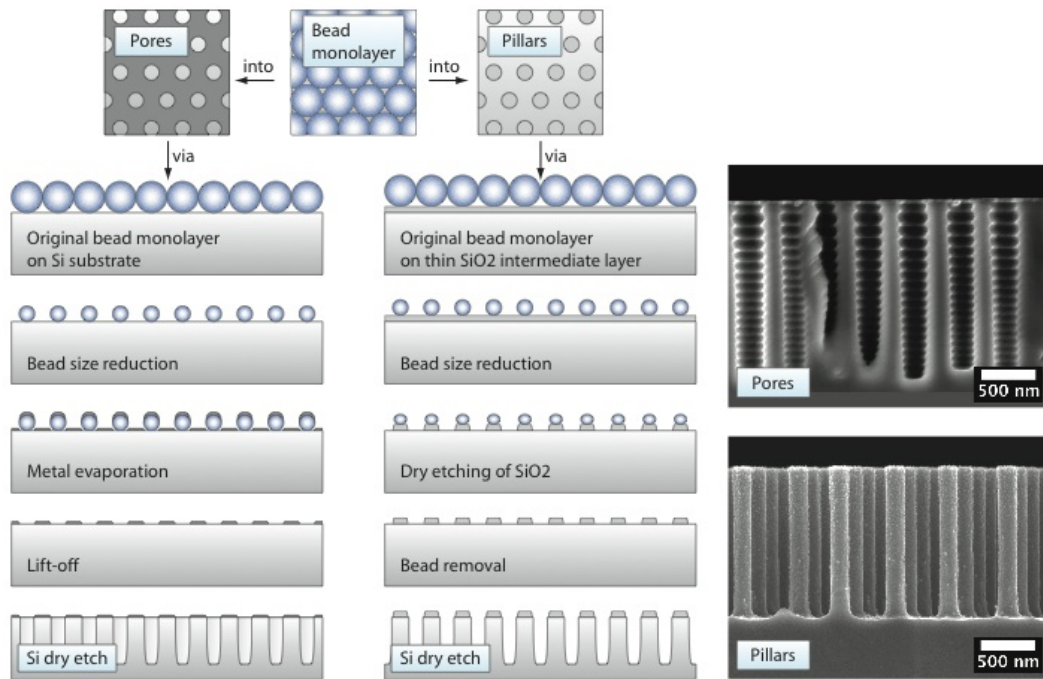


Figure 1.13: Example process scheme to transfer a monolayer of hexagonally close-packed PS beads into either pores or pillars in the Si substrate. The bead size is tuned by etching in an oxygen plasma. The SEM micrographs to the right show typical fabrication results. Pores were etched with a Bosch-type, pillars were etched with a continuous Si deep reactive ion etch process.

and the orientation of the substrate with respect to the material source¹⁵⁶. In this way, various geometric patterns such as holes, triangles, or annular holes can be obtained using the identical bead template^{160,135}. The characteristic dimensions are inherently determined by the size of the beads used. An example process scheme transferring a monolayer of hexagonally close-packed PS beads into pores or pillars in a Si substrate is shown in 1.13. At the same time, this shows the versatility of the NSL process - a tuning of the feature size and switching from pores to holes by the simple change of one process step. Thus, in varying combinations of bead pattern replication into underlying or deposited material, thin holey films have been realized for example in Si^{161,162}, SiO₂¹⁵¹, SiN^{159,163}, or noble metals^{164,165,166,75}. Instead of etching holes, pillars can serve as a structure either directly, e.g. as cell growth substrates¹⁶⁷, for the tuning of the surface wetting properties¹⁶⁸, light harvesting structures integrated in photovoltaic devices¹⁶⁹, or as lift-off templates to again create films with pores¹⁷⁰. A sophisticated way to transfer the “soft” beads directly into “soft”, photoresist pillars has been demonstrated by Wu et al. by using the PS beads as lenses¹⁷¹. Substrate with either pillars or pores can again be replicated - and thus transferred back into a “soft” material. This has been

used to fabricate gecko-like structures in parylene, or antireflective coatings by UV-NIL on glass¹⁷².

Free-standing holey SiN¹⁷³ as well as polymeric¹⁷⁴ membranes have been successfully fabricated as well. However, in case of the SiN membranes, the pore density is extremely low due to the chosen bead deposition method (electrostatic self-assembly). To our knowledge, the fabrication of metallic membranes with sub- μm hole arrays based on NSL has not been reported yet.

1.3 Research objective

The goal of this thesis is the fabrication of arrays of sub- μm holes in thin SiN and Au films and membranes. Target applications are stenciling, filtration and RIX sensing. The process should be flexible, that is it shall be possible to achieve different hole array and membrane geometries on various kinds of substrates without major process changes. Furthermore, for an easy employment, the cost-of-ownership should be low, and the overall patterning process should be fast. The table below list the specifications for holey SiN and Au films and membranes.

Criterion	SiN and Au specification
Hole diameter a	Tunable without major process changes
Patterning methods	Parallel, suited for the integration with microfabrication, micropatterning of the hole array area, fast (\ll 1 day for initial pattern template), low cost of ownership
Miscellaneous	For comparison of material properties, holey as well as non-hole films can be fabricated simultaneously
SiN specific specification	
Material	Low-stress SiN
Film thickness h	100 nm
Hole density	On the order of 10^8 holes/cm ²
Hole array order	Not needed
Membrane size	$> (400 \mu\text{m})^2$
Mechanical strength	Withstand differential pressure at break > 3 bar
Au specific specification	
Material	Au (preferentially without the use of an adhesion layer such as Cr or Ti)
Film thickness h	Tunable ≥ 100 nm
Hole spacing p	400 to 600 nm
Hole array order	Over several periodicities
Size of the array	$> (100 \mu\text{m})^2$

Table 1.1: Holey SiN and Au thin film and membranes specifications.

1.4 Choice of fabrication method

Table 1.2 gives an overview of the typical feature dimensions that can be achieved with the conventional and self-assembly based patterning methods described above. The criteria mentioned are chosen with respect to the fast and low-cost fabrication of large area short-range ordered patterns that can be potentially transferred into thin films or membranes. From table 1.2, it is clear that the choice of a certain patterning method

	Conventional methods	Self-assembly methods
Feature dimensions	From tens to hundreds of nm :-)	Limited to nanoscale for BCP lithography :- (; sub- μm for NSL :-)
Feature spacing	Few hundreds of nm :-)	At most ≈ 300 nm for BCP lithography :- (, few hundreds of nm for NSL :-)
Tunability of feature dimension and spacing	Requires careful adjustment of process parameters :- (Tuning rather straightforward by either changing deposition conditions, BCP/PS bead size, or one-step post-deposition modification :-)
Substrates	Process rather sensitive to substrate type esp. for lithographic techniques due to reflection from substrate surface :- (Substrate type dependent, but chemistry can be rather well adjusted. Various deposition methods at hand for the same resulting pattern template :-)
Potential for up-scaling	Good for parallel lithography or replica methods such as NIL or μCP :-)	Good both when used for single wafer patterning as well as for master tool fabrication :-)
Control of feature location	Controlled :-)	Limited control :- (
Integration with microfabrication	Good :-)	Good :-)
Cost-of-ownership	High for at least one instance :- (Low :-)

Table 1.2: Characteristics of conventional and self-assembly based patterning methods.

is not obvious. In this thesis, the use of a self-assembly based methods was chosen, principally due to its attractive low cost-of-ownership which is an important criterion for the use in laboratory and research conditions. This allows a fast research and development of the fabrication process as well as optimization of the device geometry (hole size, spacing, film thickness etc.), even if for future industrialization, a replica technique might be employed to multiply the patterns generated by self-assembly based methods. Another important aspect is the comparatively easy tunability of the feature dimensions. As a maskless method, dimensions can be adapted individually by adapting either the deposition conditions or post-modification of the self-assembled pattern,

without the need for renewed mask fabrication (e.g. phase shift lithography), pattern generation and dose calculations (EBL and LIL) or master tool fabrication (NIL, μ CP). Furthermore, the absence of long-range order - not straight forward to generate when designing a pattern - may be an advantage for some applications, e.g. when polarization sensitivity is undesired or uniqueness of the pattern become a distinctive feature, such as in anti-counterfeiting applications.

Choosing from either BCP lithography or NSL, NSL was chosen as it allows the fabrication of array structures with a periodicity p on the order of the wavelength of visible light (VIS), and which are thus suitable for plasmonic applications in the VIS (c.f. section 1.1.4). In addition, the PS bead size can be reduced after deposition onto the substrate and thus allows tuning of the hole size without changing the periodicity (c.f. figure 1.13).

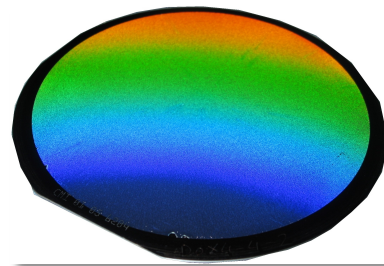
1.5 Research outline

The structure of this thesis is as follows: First, a suitable process is determined for the deposition of PS beads of different sizes. The bead monolayer should exhibit short-range order, hexagonally close packed, and homogeneously deposited onto 4" wafer substrates (chapter 2). Tuning of the hole size requires tuning of the initial bead template. This is described in chapter 3 by reducing the PS bead size by oxygen plasma treatment. For many transfer options, such as the dry-etching of SiN or Au, the etch selectivity of the polymeric pattern template is not sufficient. Also, the etching of holes requires an inversion of the bead pattern. Device integration and mechanical stability demand a micro-patterning of the hole array pattern template. The pattern inversion, transfer into an intermediate hard mask and micro-patterning is described in chapter 4. How the resulting hole and dot masks can be used for the fabrication of holey, thin SiN and Au films and membranes is described in chapter 5. Mechanical tests of holey SiN membranes and the optical characterization of hole arrays in Au films and membranes is shown in chapter 6. In chapter 7, the suitability of the fabricated devices for stenciling and refractive index sensing is demonstrated. In chapter 8, the results of this thesis are discussed, and an outlook will be given on further work that can be done based on the achievements of this thesis work.

2 Bead deposition

The topic of this chapter is the wafer-scale deposition of close-packed monolayers of polystyrene (PS) beads.

First, the forces governing bead self-assembly are described from a theoretical point-of-view. For beads confined within a liquid film, bead self-assembly is driven by capillary immersion forces.



Three bead deposition methods were investigated experimentally, namely (1) drop-coating convective self-assembly (CSA), (2) controlled CSA using the so-called “CAPA”-tool (capillary assisted particle assembly), and (3) spin-coating (SC). For each deposition method, first the experimental procedure is described, followed by a discussion of the results and a preliminary conclusion.

SC was the most efficient and reliable method. Thus, close-packed monolayers with good uniformity across the wafer surface and an average coverage $\geq 90\%$ were obtained for bead sizes in the range from 420 to 530 nm.

2.1 Forces governing bead self-assembly

Historically, with the development of the Langmuir-Blodgett technique, molecularly controlled fabrication of nanostructures by self-assembly has been used for about 70 years¹⁷⁵. In a widely referenced publication, Whitesides¹⁷⁶ defined *molecular* self-assembly as the spontaneous association of molecules under equilibrium conditions into stable, structurally well-defined aggregates joined by non-covalent bonds due to van-der-Waals or ionic interactions or hydrogen bonds. These non-covalent bonds are much weaker as compared to covalent bonds (1-5 kcal/mol as compared to several tens to hundreds kcal/mol, respectively). Stability of self-assembled systems is achieved when the constituents are joined by many of these non-covalent interactions, for example when large size molecules are held together by van-der-Waals interactions, or thanks to the existence of multiple hydrogen bonds.

Molecular self-assembly can be considered as a new strategy to chemically synthesize structures in the size range of 1-100 nm. In fact, in the upper size range, this is comparable to structures prepared by high-resolution top-down fabrication methods. In addition, several research groups have demonstrated self-assembly of larger, particulate or even chip-size building blocks of different shapes, sizes and materials into ordered superstructures^{177,178}. An important example is the self-assembly of sub- μm polystyrene or silica spheres into 2D and 3D colloidal crystals^{179,135}. Here, the autonomous organization can be achieved by different kinds of particle-particle or particle-surface interactions, such as electrostatic or capillary forces^{135,148,180}. In the following, the particle-interaction forces are described in more detail. It will be shown that, in case of particles confined within a thin liquid film on a substrate, capillary immersion forces dominate the autonomous assembly.

The DLVO theory: Electric double layer and van-der-Waals interactions

Particles, such as the PS beads used in this thesis, are usually provided as a stable colloidal suspension. Colloidal suspensions belong to the group of fluid dispersions. They contain small particles in the size range of 1 nm to 10 μm , and the interaction between the particles is dominated by Brownian motion^{181,182}. The particle and solution medium can be of the same or of different types, e.g. solid particles in air = aerosol, such as smoke; fluid in fluid = emulsion, such as milk; or solid in fluid = dispersion, such as ink, paint, or the polystyrene (PS) bead suspensions in water used in this thesis. There exist different stabilization mechanisms. One of the most widely used one is electrostatic repulsion^{183,184}.

A typical situation of negatively charged beads in a liquid with positive and negative ions is depicted in the simplified schematic 2.1¹⁸¹ based on the Gouy-Chapman model.

Let the beads be the solid substrate with negatively charged sulfate groups at their surface (c.f. Materials 2.3). Thus the bead surface has a negative potential with respect to the bulk solution. The negative surface potential is compensated by a layer of positive ions close to the bead surface (region I). This is also called the Helmholtz-layer. The second region is the so-called diffuse layer in which counter-ions, of negative charge in this case, are not rigidly attached but tend to diffuse into the bulk (region II). This diffusion is instigated by their kinetic energy, and counter-balanced by the electrostatic potential. The concentration of these ions follows a Boltzmann-type distribution (c.f. below). Region III represents the neutral bulk solution.

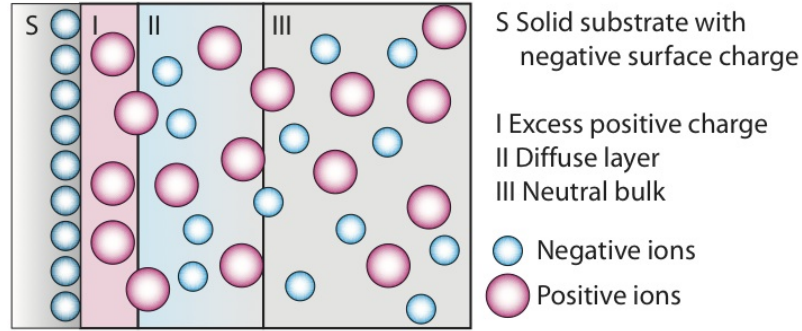


Figure 2.1: Schematic of an electric double layer.

The electric double-layer is the source of a repulsive force R , while van-der-Waals interactions cause a particle attraction A ^{184,185}. R and A are competing interactions between particles in suspensions. The resulting total interaction potential V_T is described by the Derjaguin and Landau, Verwey and Overbeek theory (DLVO theory) as a summation of R and A :

$$V_T = R + A \approx 100 \text{ J}/k_B T \quad (2.1)$$

It can be shown that the attractive van-der-Waals forces are inversely proportional to the particle separation distance L , while the double-layer repulsion follows an exponential decay with increasing L ¹⁸²:

$$A \propto \frac{1}{L}$$

$$R \propto \exp\{-\kappa L\}$$

with κ^{-1} called the Debye-length which characterizes the electrostatic potential decay from a charged surface into the bulk solution¹. The higher the solutions ionic strength, the shorter the Debye-length.

¹Below will be given more detailed definitions as well as an approximate derivation of R and A for the colloidal PS bead suspensions used in this thesis.

Figure 2.2 shows how R and A sum up to V_T as a function of the particle separation distance L . Q is a potential barrier that prevents the particles from aggregation. The energy necessary to overcome Q may be supplied by the random collisions of the particles with each other or molecules of the suspension medium - Brownian motion¹⁸⁶. The average translational energy is $\frac{3}{2}k_B T$, where k_B is the Boltzmann constant ($k_B = 1.3806 \times 10^{-23} \text{J/K}$) and T is the absolute temperature in Kelvin. (For an inter-particle collision at room-temperature, this energy is on the order of $1 k_B T$.) Consequently, as long as $Q \gg k_B T$, the colloidal suspension is stable. As the Debye-length κ^{-1} is influenced by the solvent composition, so is R via its exponential dependence on κ and L . Thus, for example by the addition of salt, a colloidal suspension will change its state from stable to un-stable (c.f. figure 2.2).

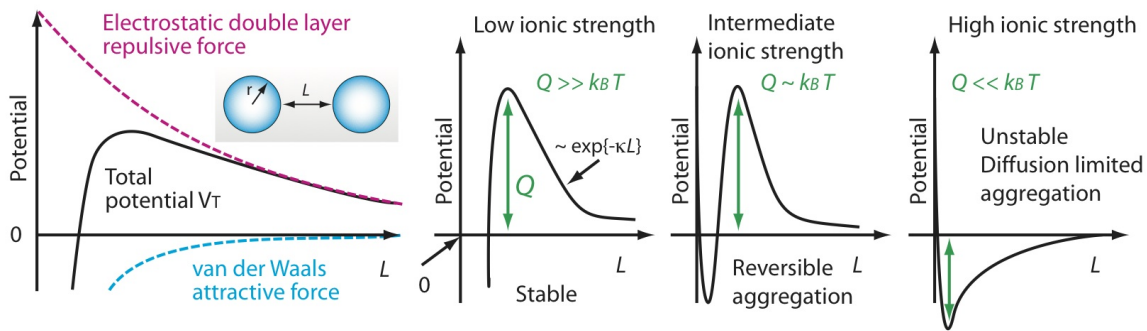


Figure 2.2: DLVO potential curves. The left-side schematic shows the attractive and repulsive contributions to the total interaction potential V_T . The smaller graphs to the right show how V_T as a function of the particle separation distance L is influenced by the solution's ionic strength. Q is the energy barrier that prevents particles from spontaneous aggregation, r is the particle diameter. Figure adapted from Schurtenberger¹⁸².

Van-der-Waals interactions

A depends on the particle size (radius r) and the separation distance between the particles L (c.f. inset in figure 2.2). The dielectric properties of the particles and the liquid contribute with a proportionality factor, the Hamaker constant, which is a complicated function of the frequency-dependent dielectric properties of all the media involved.² Thus, A can be written as^{188,186,184}:

$$A = -\frac{r H_{PS/H_2O/PS}}{12L} \quad (2.3)$$

²Note that the Hamaker constant also plays an important role in the wetting/de-wetting behavior of thin films as described for example by Seemann¹⁸⁷.

For $r = 250$ nm, $L = 2r$, a two media system of PS/H₂O/PS and $H_{PS/H_2O/PS} = 1.3 \times 10^{-20}$ J¹⁸⁴ as an approximate value for PS beads in aqueous suspension:

$$A = -0.133508 \text{ in J}/k_B T.$$

Double-layer repulsion

As mentioned above, the electrostatic double-layer repulsion R follows an exponential decay with the particle separation distance L . The constant pre-factors are the particle radius r and the dielectric properties of the liquid medium $\epsilon_0 \epsilon_r$, where $\epsilon_0 = 8.854 \times 10^{-12}$ As/Vm is the dielectric constant and ϵ_r is the relative dielectric constant. For water at 21°C, $\epsilon_r \approx 80$. The scaling factor for the exponential decay is the inverse of the Debye-length κ with the Debye-length denoted by κ^{-1} . The surface potential ψ_0 contributes with its' square. Thus:

$$R = 2\pi r \epsilon_0 \epsilon_r \psi_0^2 \exp\{-\kappa L\} \quad (2.4)$$

The Debye-length is defined as the distance from a charged particles' surface at which the surface potential has fallen to ψ_0/e or $0.368 \psi_0$. Therefore, in order to calculate κ^{-1} , the surface potential $\psi(x)$ at distance x needs to be known. It can be derived via the Poisson-Boltzmann equation which is based on the Guy-Chapman model for the electric double layer (c.f. above, Boltzmann-like distribution of ions across the diffuse layer). First, for the simple case of an electric field generated by a charged flat surface, based on Maxwell's equations one can derive:

$$\frac{d^2\psi(x)}{dx^2} = -\frac{\rho(x)}{\epsilon_0 \epsilon_r} \quad (2.5)$$

where $\rho(x)$ is the net charge density at position x . $\rho(x)$ depends on the electrolyte type and ion concentration. For dilute solutions where the potential in the bulk $\psi(B) = 0$, the local ion concentration $C_i(x)$ for ions i can be written as (Boltzmann-like distribution):

$$C_i(x) = C_i(B) \exp\left\{\frac{-Z_i q \psi(x)}{k_B T}\right\} \quad (2.6a)$$

and with this

$$\rho(x) = \sum_i Z_i q C_i(x) \quad (2.6b)$$

Here, q is the elementary charge ($q = 1.602 \times 10^{-19}$ As) and Z_i is the valence of ion i . Substituting equation 2.6b into equation 2.5 yields the *Poisson-Boltzmann* equation:

$$\frac{d^2\psi(x)}{dx^2} = -\frac{q}{\epsilon_0 \epsilon_r} \sum_i Z_i C_i(B) \exp\left\{\frac{-Z_i q \psi(x)}{k_B T}\right\} \quad (2.7)$$

For 1:1 electrolytes where $(-Z_i q \psi(0))/(k_B T) \ll 1$, which is fulfilled for $\psi_0 < 25$ mV, an approximate solution for the electrostatic potential decay is given by:

$$\psi(x) = \psi_0 \exp\{-\kappa x\} \quad (2.8)$$

κ is derived from equation 2.7 and defined as:

$$\kappa^{-1} \propto \sqrt{\frac{k_B T}{\sum_i C_i(B) Z_i^2}} \quad (2.9)$$

With these equations, one can derive approximate values for the PS suspensions used in this thesis (c.f. section 2.3). The suspensions are provided in water and thus a pH value of 7 is assumed. There is an equal amount of H_3O^+ and OH^- ions. The valency of each ion is 1. Thus the sum in the denominator in equation 2.9 per 1 cm^3 cubic volume can be written as:

$$\sum_i C_i(B) Z_i^2 = 2 \times 10^{-7} \cdot N_A / 18 \times 10^{-6} \text{ in m}^3,$$

where $N_A = 6.022 \times 10^{23}$ is the Avogadro constant and $18 \times 10^{-6} \text{ m}^3$ is the water volume containing 1 mol. Thus, inserting for $\epsilon_r = 80$ and a temperature of $T = 294 \text{ K}$, one obtains a Debye-length $\kappa^{-1} = 128 \text{ nm}$.

It remains to derive the surface potential ψ_0 . To do this accurately, the surface charge density needs to be known from which the net particle charge can be calculated by integration (equation 6.26 in¹⁸⁴). The charge density is not known however. Therefore, based on the Hückel equation, it is assumed that $\psi_{(x=\kappa^{-1})} \approx \zeta$, where ζ is the so-called Zeta-potential. (Strictly, this holds true only for $\kappa r \ll 1$). The ζ -potential depends on the ion mobility, the medium viscosity and the dielectric properties. For a rough estimate, $\psi_{(x=\kappa^{-1})} = -60 \text{ mV}$, which is in the range of the ζ -potential given by the manufacturer¹⁸⁹. Inserting this into equation 2.8 yields $\psi_0 = -163 \text{ mV}$. With these values and using equation 2.5, R can be calculated for $r = 250 \text{ nm}$ and $L = 2r$:

$$R = 147 \text{ in } J/k_B T.$$

Thus, the potential energy V_T for two PS beads in aqueous suspension separated by distance one times their diameter is clearly positive and thus repulsive. In magnitude, it by far overcomes the van-der-Waals attractive forces, thus $R \gg A$, which means that the colloidal suspension is stable.

Steric stabilization

Colloidal suspensions can also be stabilized by the adsorption of amphiphilic polymeric macro-molecules at the particle surface¹⁸⁶. The resulting stabilization mechanism is termed steric or entropic. When such particles approach each other, two effects may take

place: Interpenetration of the polymeric soft shells results in a local osmotic pressure increase, causing the inflow of solvent which will separate the particles. The second effect is a volume effect due to crowding of the inter-particle. This decreases the polymer chains' degrees of freedom, thus decreasing their entropy. This is unfavorable and causes the particles to re-solvate.

Depletion flocculation

Depletion flocculation is similar to steric stabilization, with the important difference that polymeric macro-molecules or smaller particles are only weakly adsorbed at the colloid surface¹⁸⁶. Thus, when two colloidal particles approach, the adsorbed species may be expelled from the inter-particle space. This will create a local osmotic pressure increase around the particles, sucking liquid out from the inter-particle space and thus causing particle aggregation.

Capillary flotation and immersion forces

In the above two sections, it has been shown that for PS beads in a stable colloidal suspension, the repulsive electric double layer force prevents aggregation. However, when the beads are immersed in a liquid film, capillary forces arise that cause either repulsive or attractive forces. These capillary force interactions have been extensively investigated both theoretically and experimentally by Nagayama and Kralchevsky et al.^{190,136,191,192,180,193,194,195}. The following description of bead assembly due to capillary forces is based on their works.³ Finite element simulations have been done for example by Nishikawa and Okubo et al.¹⁹⁷. They took into account typical physical parameters, especially viscous drag forces which they also measured in earlier experiments (c.f. Maenosono¹⁹⁸).

Figure 2.3 shows different situations of capillary flotation and immersion forces. Flotation forces are present for particles freely floating at the gas-liquid or liquid-liquid interface¹⁹⁹. Immersion forces occur for particles confined within a liquid film. The origin of the lateral capillary forces is an overlap of the deformed liquid menisci induced by neighboring particles (figures 2.3 (a-d)). The force interaction is attractive if both meniscus slopes ψ_1 and ψ_2 for particle 1 and particle 2, respectively, have the same sign (figures 2.3 (a) and (b)). It is repulsive for meniscus slopes of dissimilar sign. A concave slope (figure 2.3 (a)) has a negative sign, a convex slope (figure 2.3 (b)) has a positive sign.

For example, an attractive flotation capillary force occurs when the particles' gravitational potential energy can be decreased upon approaching each other. Hence, the force

³In a recent publication, the extension of their model to electro-capillary interactions is well described¹⁹⁶.

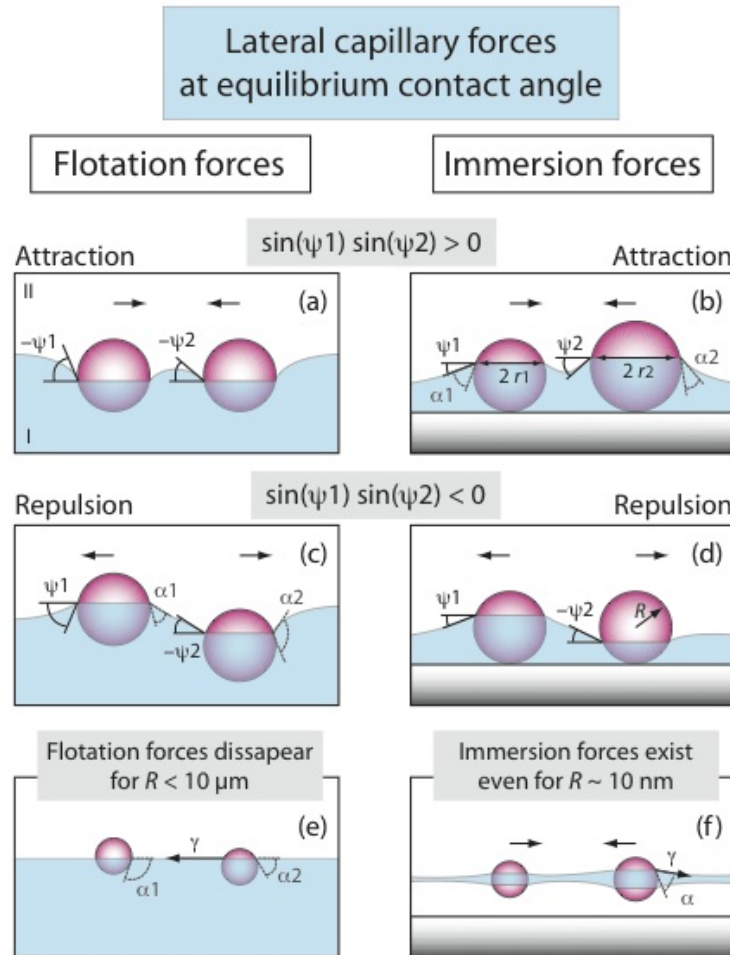


Figure 2.3: Capillary interactions between floating and immersed particles. $\psi_{1,2}$ are the meniscus slope angles; $\alpha_{1,2}$ are contact angles; γ is the liquid surface tension, R is the particle radius, and $r_{1,2}$ are the radii of the wetting film contact line at the bead surface. Beads of different sizes will possess a different “capillary charge” (c.f. below), as sketched for generalization in the immersion force attractive case. Figure according to Kralchevsky¹⁸⁰.

is related to the particle weight. $\psi \approx 0$ for particles with a radius smaller than $\approx 10 \mu\text{m}$. For such small particles, the immersion depth is solely determined by the contact angle and the thermal energy is larger than the capillary interaction.

For particles partially immersed in a liquid layer, the perturbation of the meniscus is determined by the particles wetting properties and thus the capillary immersion force depends on the position of the wetting film contact line and the magnitude of the contact angle (c.f. figure 2.4). The immersion force is significant even for particles with a radius of only a few nm^4 (figure 2.3 (f)).

It is worthwhile to note that for $\alpha = 0$, flotation forces do not exist as the particles will be submerged in the liquid, while immersion forces still do exist for $\alpha = 0$.

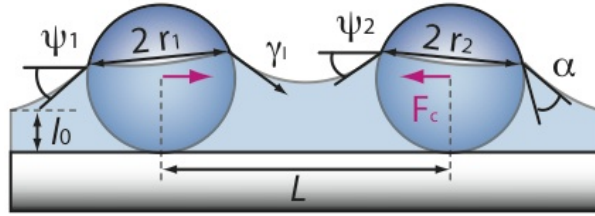


Figure 2.4: An attractive capillary immersion force F_c draws two particles separated by L closer to each other. The height of the liquid film decays at infinity to l_0 . $r_{1,2}$ are the radii of the three-phase contact line at the particle surface. R is the particle diameter. Figure adapted from¹³⁶ and²⁰⁰.

The energy of lateral capillary interaction is derived by solving the Laplace-equation of capillarity for small meniscus slopes (c.f. Denkov¹³⁶ or Kralchevsky¹⁹⁴ for a summary or Kralchevsky²⁰² and Paunov¹⁹¹ for a detailed description). The energy of the lateral capillary interaction can be written in the form

$$\Delta W \approx -2\pi\gamma Q_1 Q_2 K_0(qL), \quad (2.10)$$

where K_0 is the modified Bessel function of the second kind and zero order. Here, L is the particle center to center separation distance. For thick films, $q^2 = \Delta\rho g/\gamma$, with $\Delta\rho = \rho_{II} - \rho_I$ being the mass density difference between the lower and upper fluid (e.g. region I: air and region II: water as shown in figure 2.3 (a)), $g = 9.80665 \text{ m/s}^2$ is the acceleration due to gravity, and γ is the liquid surface tension (e.g. 73 mN/m for water). Q_i ($i = 1,2$) are so-called “fluidic charges”. In the case of immersion forces, Q_i are readily defined by the radii of the wetting film contact line r_i and the meniscus slope angles ψ_i . In case of flotation forces, Q_i are proportional to the gravity force. Chan et

⁴It has been predicted theoretically by Kralchevsky et al.²⁰⁰ and shown, for example, by Alivisatos et al.²⁰¹ that the capillary immersion force can dominate $k_B T$ for particles as small as 2 nm .

al²⁰³ derived an approximate expression under the condition that $r_i \sqrt{\Delta\rho g/\gamma} \ll 1$ and $L > 4r_i$. Thus, for the respective capillary charges, one can write:

$$Q_i \approx \frac{1}{6} q^2 r_i^2 \left(2 - 4 \frac{\rho_i - \rho_{II}}{\rho_i - \rho_{III}} + 3 \cos \alpha_i - \cos^3 \alpha_i \right) \quad \text{for flotation forces} \quad (2.11a)$$

$$Q_i = r_i \cdot \sin \psi_i \quad \text{for immersion forces.} \quad (2.11b)$$

ΔW (equation 2.10) represents a variation in the gravitational energy in case of the flotation force, or in the energy of wetting in case of the immersion force¹⁹⁴. Derivation of equation 2.10 with respect to the separation distance L yields the lateral capillary force F_c :

$$F_c = -2\pi\gamma Q_1 Q_2 q K_1(qL) \quad \text{for } r_i \ll L. \quad (2.12)$$

(K_1 : modified Bessel function) An intuitive asymptotic expression can be derived which resembles the Coulomb interaction between two electric charges^{203,194}:

$$F_c \approx -2\pi\gamma Q_1 Q_2 / L \quad \text{for } r_i \ll L \ll q^{-1}. \quad (2.13)$$

Equations 2.12 and 2.13 hold for both flotation and immersion forces. Thus they have a similar dependence on L . Their different physical origin is contained in Q_i . Thus, for particles of equal radius and $r_i \ll L \ll q^{-1}$, one finds that:

$$F_c \propto \gamma^{-1} r^6 \quad \text{for flotation forces} \quad (2.14a)$$

$$F_c \propto \gamma r_1 r_2 \quad \text{for immersion forces.} \quad (2.14b)$$

$$F_c \approx 10000 \text{ J}/k_B T \quad (2.15)$$

An increase of the liquid surface tension lowers the flotation, but increases the immersion capillary force. Also, the decrease of F_c with decreasing particle diameter is more pronounced for flotation forces, which can be understood by the fact that it is the particle weight (a volume property) which causes the deformation of the liquid surface.

Figure 2.5 shows the variational energy ΔW normalized to $k_B T$ which is associated with the flotation and immersion capillary forces as a function of particle radius R (equation 2.10) (figure adapted from Denkov¹³⁶). l_0 is the liquid film height at infinity (c.f. figure 2.4). Flotation forces were calculated using equation 4.7 in Paunov¹⁹¹, immersion forces were calculated using equation 4.11 in Kralchevsky¹⁹⁰. The particle distance is fixed at $L = 2r$ for beads of the same size which are immersed in a water film (for example polystyrene beads with $\Delta\rho = 1 \text{ g}/\text{cm}^3$ and a water surface tension $\gamma = 73 \text{ mN}/\text{m}$ and a wetting contact angle at the bead surface of $\alpha = 30^\circ$). From figure 2.5, it becomes clear that for small particles with a diameter $<$ a few tens of μm , the flotation forces become insignificant. For the particle size range shown, the

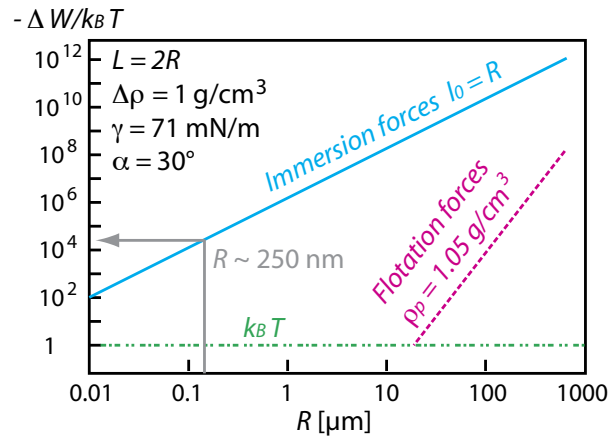


Figure 2.5: Variational energy associated with flotation and immersion forces normalized to the thermal energy as a function of the particle radius. Figure adapted from Denkov¹³⁶.

immersion forces are orders of magnitude larger than the flotation forces. As compared to the immersion force, the thermal energy plays a negligible role over the whole range. Indicated by the grey arrow is the energy that can be expected for particles with a radius $\approx 250 \text{ nm}$. The energy is on the order of $10^4 J/k_B T$ and thus a factor of 100 larger than the electric double layer repulsion.

Inter-particle and particle-substrate interactions

Provided that the colloidal suspension is stable, capillary immersion forces are the dominant forces causing assembly of particles that are partially immersed in a liquid. However, the assembly mechanism can be influenced by either modifying the inter-particle or particle-substrate interactions⁵.

For example, the influence of the magnitude of the electrostatic repulsion has been investigated for immersed (e.g. Rödner²⁰⁴) and floating particles (e.g. Sirotkin²⁰⁵). The electrostatic repulsion force was either varied by changing the electrolyte concentration²⁰⁴ or choosing particles with a different density of carboxylic surface groups²⁰⁵. The degree of order was measured by calculating the next-neighbor correlation function (e.g. Hansen²⁰⁶) or investigating the crystallinity by an analysis of Fast-Fourier-Transform images (e.g. Kittel⁵⁶). It was found that high salt concentrations, which reduced the electrostatic repulsion, transformed directly into a decreased array order when depositing particles onto a solid substrate surface. On the other hand, for freely floating particles, reduced electrostatic repulsion was to some extent advantageous for

⁵This is also true for particles floating at a liquid-gas interface, which are thus subject to flotation forces rather than immersion forces.

large domain formation. The difference in the effect of reduced electrostatic repulsion can be explained by the difference in the experimental setups and materials used, as well as by the difference in the attractive forces driving the bead assembly (capillary immersion vs. flotation forces).

Other works have investigated the influence on array order and the possibility for local deposition of particles by changing the particle-substrate interactions. The particle-substrate interactions can be tuned by several means, e.g. by modifying the surface energy (hydrophilic vs. hydrophobic substrates, e.g. Okubo²⁰⁷, Fan²⁰⁸, or Himmelhaus²⁰⁹) or inducing charges on the substrate (positive or negatively charged substrate surfaces, e.g. Yan²¹⁰). In all cases, increased particle-substrate interaction reduced the array order, which can be explained by a reduced mobility of the beads on the substrate surface. For very strong interactions, beads could be locally deposited on substrates with a patterned surface chemistry^{209,208}.

In the experiments performed in this thesis, the concept of hydrophilic/hydrophobic pre-patterning the substrate was qualitatively investigated (c.f. section 2.3.1). Also here, a decreased bead array order for an increased particle-substrate interaction was observed. The locality of the bead deposition, however, was rather stimulated by a pinning of the wetting film contact line and a change in the meniscus slope angle (c.f. section 2.2 below).

2.2 Convective self-assembly of beads

In the above section, it has been motivated that capillary immersion forces can be used for the arrangement of sub- μm particles into 2D arrays. This was confirmed by Denkov et al.¹³⁶. By investigating the influence of parameters such as particle size, particle concentration, electrolyte concentration, or the presence of surfactants, they concluded that immersion capillary forces remain dominant over other particle interactions.

The array formation process by CSA can be divided into two stages: i) the transportation of new particles to the wetting film contact line by a convective flow (figure 2.6), and ii) the integration of particles that have arrived at the wetting film contact line into the array by immersion capillary forces (c.f. figure 2.4). The position and meniscus slope angle of the wetting film contact line are crucial. Depending on the experimental setup, those parameters can be more or less well controlled (e.g. dip-coating¹³⁷ or template assisted CSA^{211,148} vs. drop-coating CSA¹³⁶ or spin-coating^{212,213}, respectively).

The following assumptions are made for the description of the convective particle flow: (i) the solvent evaporates, (ii) the contact line is pinned, and (iii) the wetting

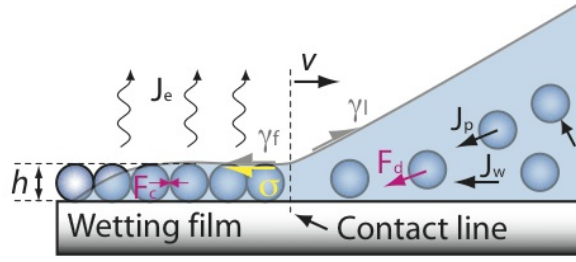


Figure 2.6: Convective flow of particles to the wetting film contact line. J_e , J_p and J_w are the water evaporation, the particle flow and the water flow from the bulk suspension to the contact line, respectively. F_d is a hydrodynamic drag force, caused by J_w . F_c is the capillary immersion force. γ_f and γ_l are the film and liquid surface tension, σ is a viscous friction force. The height of the wetting film is h , and the array growth velocity is v . Figure adapted from^{193,137}.

film slope angle is non-zero⁶. The water evaporation at the wetting film J_e causes a water flow J_w towards the contact line. J_w creates a hydrodynamic drag force F_d , which results in a continuous particle flow J_p towards the array. The surface tension of the wetting film γ_f is directed opposite the liquid surface tension γ_l . σ is a viscous drag force resulting from J_w and J_p . Together, γ_f and σ inhibit a free droplet shrinkage which leads to the formation of stripe patterns. A detailed theoretical description of this dynamic phenomenon can be found in¹⁹³. When the viscous drag force is neglected, the growth of the particle array can be described in a more simple way. Experimentally, this corresponds to a situation where the position of the contact line is controlled by moving the substrate relative to the bulk suspension^{137,148}. The array growth velocity v can then be described as a function of the water evaporation above the wetting film J_e , the volume concentration of the particles in the suspension ϕ , the wetting film height h and a proportionality constant β (equation 2.16 a,b).

$$v = \frac{\beta J_e \phi}{h(1 - \epsilon)(1 - \phi)} \quad (2.16a)$$

$$v_k = \frac{\beta J_e \phi}{2R \cdot k \cdot 0.605(1 - \phi)} \quad (2.16b)$$

β relates the water flow J_w to the particle flow J_p and has values between 0 and 1. It depends on the particle-particle and particle-substrate interactions. For non-adsorbing particles in dilute suspensions, β approaches 1. ϵ describes the porosity of the array. For example, for a hexagonally close-packed monolayer, $(1 - \epsilon) = 0.605$. If h is equal to the particle diameter $2R$, the growth velocity v_k for bead arrays with k layers can be

⁶In fact, these conditions are identical to the ones causing the well-known coffee-ring effect that gives rise to a convective particle flow similar to the one observed in CSA of beads, c.f. Deegan²¹⁴.

written as shown in equation 2.16b.

Beads can only be *integrated* into an array if an array of beads already exists. Thus, some beads need initially be immobilized on the substrate surface. For the formation of well-ordered close-packed arrays, it is advantageous if beads have a high mobility on the substrate surface (c.f. Yan²¹⁰). At the same time, it limits the probability of the formation of an initial three-phase contact line as the beads tend to be withdrawn with the receding droplet meniscus. The formation of the initial wetting film contact line depends on the deposition method, the wetting properties of the bead suspension, and the substrate surface chemistry and morphology. As an example, figure 2.7 schematically shows drop-coating CSA from wetting and de-wetting suspensions. The latter one shall also have a low contact-angle hysteresis⁷. In case of the wetting suspension, the array formation starts once the liquid film thickness has fallen below the particle diameter.

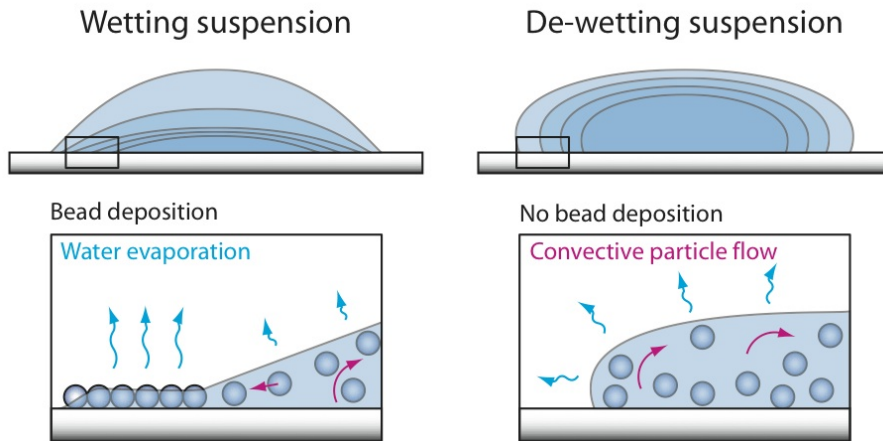


Figure 2.7: Drop-coating CSA for wetting and de-wetting suspensions.

In the de-wetting case, the beads remain contained in the droplet due to the high contact angle which prevents a thinning of the liquid film to a thickness below the particle diameter. However, by using either chemically or topographically pre-patterned substrates, pinning of the three-phase contact line and thus a controlled deposition of beads can be achieved. Fan and Stebe²⁰⁸ for example have shown the local bead deposition within micron-size hydrophilic patches within a hydrophobic surface. The bead suspension was deposited all over the substrate surface. Due to de-wetting, the suspension withdrew to the hydrophilic patches, where the three-phase contact line was pinned at the hydrophilic-hydrophobic border, initiating the bead deposition. Alternatively, substrates have been patterned topographically with grooves or protrusions. Then, by externally controlling the position of the wetting film contact line, the liq-

⁷The contact angle hysteresis is the difference in the advancing and receding contact angle¹⁸¹.

uid meniscus will be locally deformed at these surface patterns, changing the direction and increasing the magnitude of the lateral capillary force, and thus initiating the bead deposition. Experimentally, this can be realized e.g. by dip-coating²⁰¹; or by confining the bead suspension between a moving substrate and an inclined cover-glass slide as in the case of template-assisted-self-assembly (TASA) or, with a different naming, capillary-assisted-particle-assembly (CAPA)^{211,109,148}.

2.3 Experimental

Materials

Beads

Aqueous suspensions of monodisperse PS beads of different sizes were purchased from *microparticles GmbH* (Germany). Polystyrene beads are also referred to as Latex particles or PS nanospheres. The beads are synthesized by seeded-growth polymerization of styrene in aqueous solution with potassium persulfate as a polymerization initiator²¹⁵. The decomposition of the initiator molecules leads to sulfate endgroups at the bead surface. As a result, the beads are negatively charged. The ζ -potential of the obtained particle suspensions is in the range of -50 to -70 mV. Characteristic particle properties such as the size and size distribution are determined by disc centrifugation (c.f. CPS instruments²¹⁶). The coefficient of variance CV is less than 3% for the obtained particles, where $CV = \sigma/\mu$ with σ being the standard deviation and μ being the mean particle size. Modified bead suspensions, e.g. after dilution in Di-H₂O or after a solvent exchange from H₂O to ethanol, were not further characterized. However, it could be observed that the colloidal stability was reduced in ethanolic suspensions, which can be explained by a reduction of the absolute value of the ζ -potential (c.f. above). The beads used for the experiments in this thesis are listed in table 2.1.

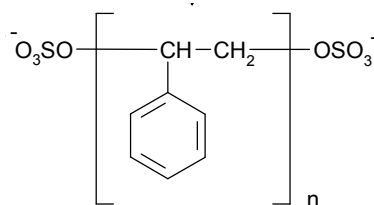


Figure 2.8: Polystyrene.

Name	Nominal bead diameter [nm]	Concentration [% w/v]	<i>microparticles</i> product name
PSB281	281 ± 2	10	PS-R-L1225
PSB284	284 ± 10	5	PS-R-B1270
PSB428	428 ± 12	10	PS-F-L2088
PSB508	508 ± 11	10	PS-R-B1035
PSB517	517 ± 18	10	PS-R-B1187
PSB535	535 ± 16	10	PS-F-B1266
PSB836	836 ± 24	10	PS-R-L1157

Table 2.1: Polystyrene bead aqueous suspensions used in this thesis.

Solvents and surfactants

The solvents used in the experiments are listed in table 2.2.

Solvent	Molecular formula	Boiling point [°C]	Manufacturer
DI-water	H ₂ O	100	(tap)
Ethanol (VLSI)	C ₂ H ₅ OH	78	BASF
Isopropanol (VLSI)	CH ₃ CHOHCH ₃	82	Rockwood
Acetone	(CH ₃) ₂ CO	56	Rockwood
Ethylene glycol	HOCH ₂ CH ₂ OH	197	N.A.
Triton-X	C ₁₄ H ₂₂ O(C ₂ H ₄ O) _n	>200	Fluka

Table 2.2: Solvents used in this thesis.

Silicon substrates

If not mentioned otherwise, the silicon substrates used in this thesis were of (100) crystal orientation and had a low dopant concentration (n: boron or p: phosphor) with a resistivity in the range of 0.1 to 100 Ω cm. Single-side and double-side polished 4" wafers (100 ± 0.5 mm in diameter) had a thickness of 525±25 μm and 380±10 μm, respectively.

2.3.1 Drop-coating convective self-assembly

In this method, a drop is dispensed onto a substrate and left for drying. Ultimately, the dispensed liquid should wet the whole substrate surface. For a given liquid, this can be achieved by a proper substrate pre-treatment. For example in the case of aqueous suspensions, the substrate can be rendered hydrophilic by treatment in an oxygen plasma or in a Piranha solution. Additionally, surfactants can be used to lower the surface tension

of the liquid and thus promote the wetting. Drying proceeds from the substrate border towards the center region. This is schematically shown in figure 2.9. The drying process may be more complicated, especially for large substrates, when other solvents such as ethanol are used due to evaporation induced instabilities at the liquid-gas interface.

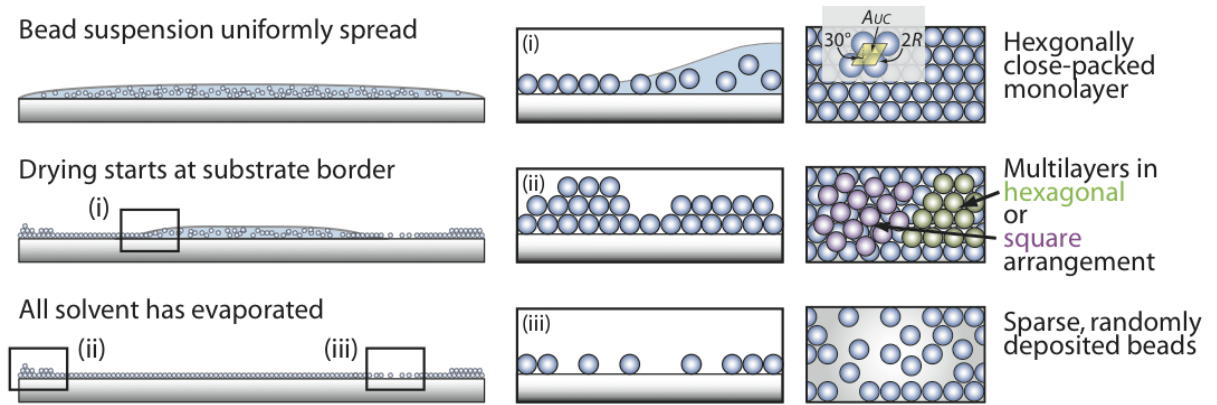


Figure 2.9: Convective self-assembly of beads using the drop-coating method.

All of the dispensed beads need to be distributed across the substrate. This is different from the other deposition techniques and an important aspect with respect to the formation of monolayers. It can be taken into account by balancing the volume necessary to obtain complete wetting of the substrate with the suspension concentration, so that the dispensed volume contains the number of beads N_{Beads} needed for a hexagonally close-packed (hcp) monolayer coating. For a given concentration, the monolayer-coating volume V_{mono} can be calculated as follows:

$$A_{uc} = (2r)^2 \cos 30^\circ \quad (2.17a)$$

$$N_{Beads} = A_{substrate}/A_{uc} \quad (2.17b)$$

$$V_{Beads} = N_{Beads} \frac{4}{3} \pi r^3 \quad (2.17c)$$

$$\text{thus: } V_{mono} \approx 100 \times V_{Beads}/c \quad (2.17d)$$

Here, A_{uc} is the unit cell area of a hexagonal lattice (c.f. figure 2.9), r is the bead radius, V_{Beads} is the volume of N_{beads} beads with a radius of r , and c is the suspension concentration in % (w/v)⁸. For example, 250 μl of a 1% w/v aqueous suspension of beads with $r = 250$ nm contains N_{Beads} for a monolayer coverage on a 4" wafer.

Drop-coating CSA in this way allows only limited control over the bead deposition parameters and hence the quality of the obtained bead layer. For a perfect hcp monolayer coating, the water evaporation rate (and thus humidity and temperature) which causes

⁸In the approximation in equation 2.17d, it is taken into account that the densities of water, ethanol and PS are similar ($\rho_{H_2O} = 1.0$ g/cm³, $\rho_{Ethanol} = 0.789$ g/cm³, $\rho_{Beads} = 1.05$ g/cm³).

the convective particle flow to the three-phase contact line, and the three-phase contact line position needed to be precisely controlled at every instant. When this is not the case, defect formation has to be taken into account. This is shown in the cross-sectional and top-view schematics in figure 2.9: They show the formations of (i) a hcp monolayer array, (ii) multilayers in a square and hexagonal arrangement, and (iii) sparsely distributed beads. (ii) preferentially occurs when the three-phase contact line is pinned to a fixed position under a high contact angle and excessive supply of beads. This situation can typically be found at the substrate edge. A sparse deposition may occur if the three-phase contact line recedes too quickly for the convective flow to provide enough beads at the array edge, or simply if the suspension has been excessively depleted.

In the following, drop-coating CSA experiments are described and qualitatively analyzed. The goal was to investigate if simple drop-coating CSA seems feasible to obtain a monolayer coverage across the whole wafer surface, or at least in specific areas, in a fast and reliable manner. Thus, no effort was made for a precise control of the liquid evaporation rate or of the position and speed of the three-phase contact line. Different suspension concentrations, volumes, and solvent compositions were used.

Experimental

Suspension compositions

Initial experiments with diluted aqueous suspensions had shown that wetting of the full wafer surface was difficult to obtain. Addition of a reasonable amount of surfactant enhanced the wetting, but resulted in the fast formation of bead agglomerates (0.1% v/v of Triton-X 100). Therefore, bead suspensions were prepared by diluting the as-delivered 10%w/v aqueous PSB517 bead suspension with a 1:1 H₂O:Ethanol mixture or pure ethanol. Optionally, 0.001% or 0.05%v/v of Triton-X 100 was added to H₂O:Ethanol solvent mixtures to further lower the liquid surface tension. All suspensions were prepared just before use.

Substrates with hydrophobic patches

Hydrophobic patches were photolithographically patterned on 4" silicon wafers. This was done with the aim of locally having a preferential deposition of beads. The wafers were silanized with HMDS (Hexadimethylsilazane) in an oven process. HMDS is a silane commonly used as an adhesion promoter for photoresists. After silanization, the wafers were spin-coated with a 2 μm thick positive tone photoresist, exposed through a photolithographic mask, and developed. One cell of the mask pattern is shown in figure 2.10a, the dimensions of the patterns per cell range from 50 μm to 1000 μm . The mask used was a bright field mask, thus patches of photoresist remained on the wafer.

With these photoresist patches as etch mask, the wafer was treated in an oxygen plasma in a barrel etcher for 1 min at 500 W. This removed any photoresist remains and silane on the exposed areas. Then, the photoresist was stripped by immersing the wafers for 5 min in a remover bath with a high content of NMP (1-Methyl-2-pyrrolidone) heated to 75°C, followed by a thorough rinsing procedure.

Procedure

The drop-coating was done under controlled ambient conditions at a temperature of 21°C and 40% relative humidity. 4" silicon wafers were used repeatedly for bead deposition experiments. Prior to each use, they were stripped of PS beads by polishing the wafers with clean-room tissue in organic solvents, followed by sonication in organic solvents and rinsing in Di-water. A final 30 min oxygen plasma in a barrel etcher at 400 W removed all possibly remaining polymer residues and rendered the substrate surface hydrophilic. Then, the wafers were placed in 5" plastic petri dishes and suspension was dispensed in the middle of the wafer. The plastic lid was closed, but not sealed. Optionally, a spacer was placed in between the lid and the dish to enhance the solvent evaporation, but avoid air turbulences at the same time. Wetting of the whole wafer surface was supported by gently tilting the wafer. Then, the wafers were kept still until all solvent had evaporated. Figure 2.10b shows a photograph of a wafer surface after the

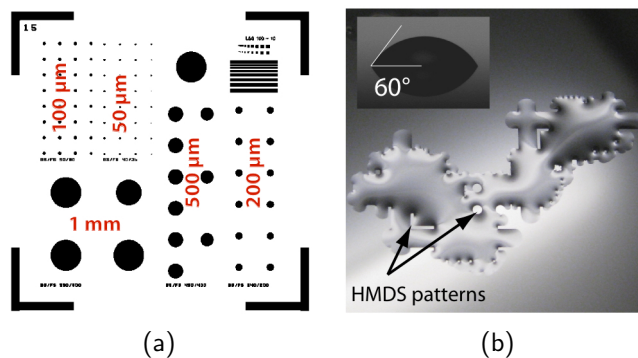


Figure 2.10: (a) One cell of the mask layout used for the photolithographic patterning of hydrophobic HMDS patches. The numbers in red indicated the dimensions of the patterns in the respective areas. The de-wetting around areas with HMDS is shown in (b).

photolithography process described above. A droplet of Di-water was dispensed onto the wafer surface. Arrows indicate the HMDS patches. The liquid is spreading well on the surface which was exposed to the oxygen plasma, but de-wets around hydrophobic patches with a size $> 200 \mu\text{m}$. Smaller hydrophobic areas are covered by the liquid. Shown in the inset of figure 2.10b is droplet of Di-water dispensed onto a HMDS patch. The contact angle was measured to be 60°. However, for a liquid to totally de-wet a

surface, the contact angle should be higher than 90° . This explains why smaller HMDS patches are still covered with water. For ease of use, HMDS patches will be referred to as “hydrophobic”.

Results and discussion

Variation of suspension concentration and dispensed volume Figure 2.11 shows photographs of wafers drop-coated with PSB517 beads. In all cases, the solvent was a 1:1 mixture of H_2O :Ethanol with 0.001%_{v/v} of Triton-X 100 surfactant. Ethanol was added in order to reduce the evaporation time; the surfactant was added in order to further decrease the liquid surface tension and thus promote the wetting of the full wafer surface. The suspension concentration was either 1%_{w/v} or 0.5%_{w/v}, and the dispensed volume was either $1 \times V_{calc}$ or $1.5 \times V_{calc}$.

Initially after dispensing the bead suspension, the three-phase contact line was pinned to the wafer border while the thickness of the liquid layer decreased. After approximately 5 min, the contact line started to recede from the wafer border towards the wafer center. This took place in two stages: an initial fast movement and a second, slower movement. (The total liquid evaporation time was 15 to 25 min.)

In all cases, a multilayer rim is formed on the wafer surface (grey dashed lines in figure 2.11 and figure 2.12a). When a 1% w/v bead suspension was used, the multilayer rim is located close to the wafer edge. It is placed closer to the wafer center in case of 0.5% w/v bead suspensions. For identical bead suspension concentrations, the multilayer rim is located closer to the wafer center for larger volumes. The region within the multilayer rim is covered with a sparse monolayer of beads (yellow dashed lines in figure 2.11 and figure 2.12b). In case of the 0.5% w/v suspensions, a sparse layer was found at the very wafer border. This sparse layer is broader when a larger amount of volume was used. Significantly large regions of hcp bead mono-layers were formed when using 0.5% w/v suspensions (star-shape patterns in figure 2.11 and figure 2.12c).

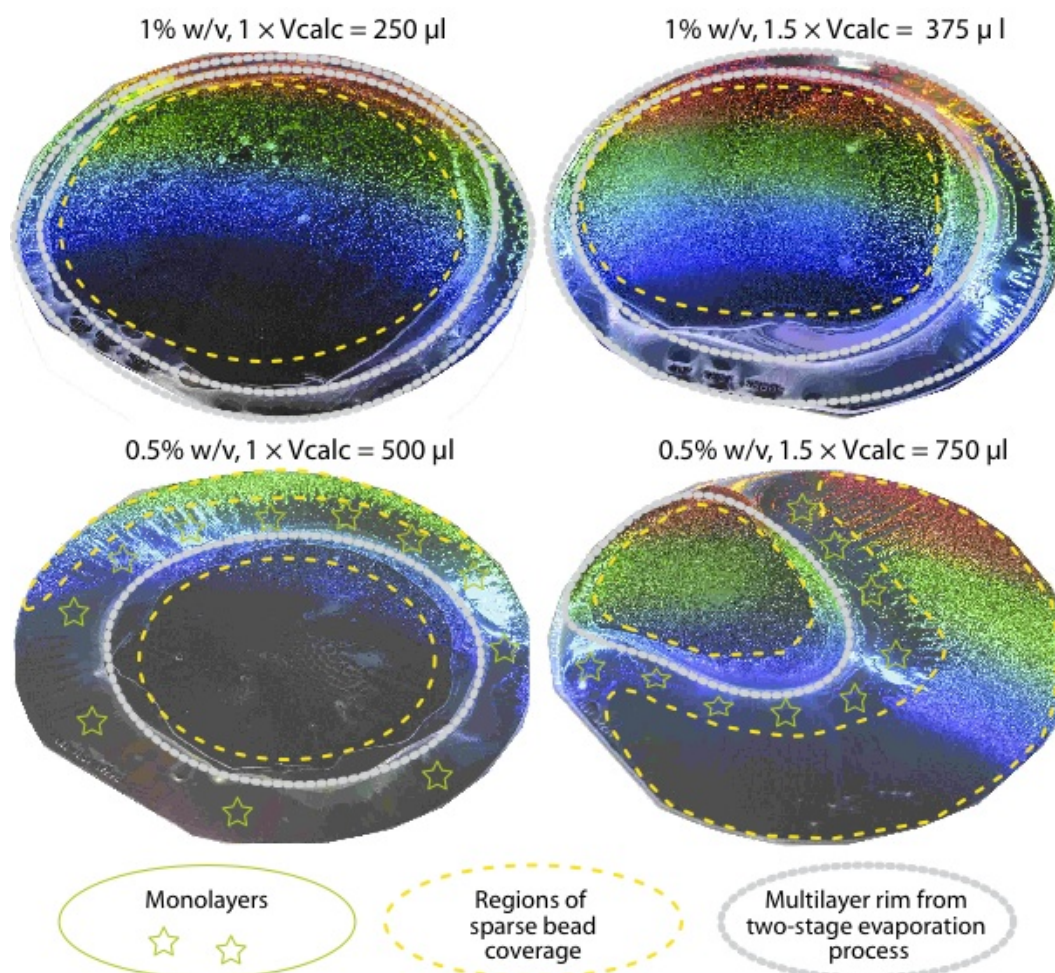


Figure 2.11: PSB517 beads deposited onto 4" silicon wafers by drop-coating CSA. The solvent was a 1:1 mixture of H₂O:Ethanol. The concentration and the volume of the bead suspension was varied from top left to bottom right as: 1%w/v $1 \times V_{calc} = 250 \mu\text{l}$, 1%w/v $1.5 \times V_{calc} = 375 \mu\text{l}$, 0.5%w/v $1 \times V_{calc} = 500 \mu\text{l}$, and 0.5%w/v $1.5 \times V_{calc} = 750 \mu\text{l}$. Mono-, multi- and sparse layers are indicated by star-shaped and dashed lines (compare figure 2.12).

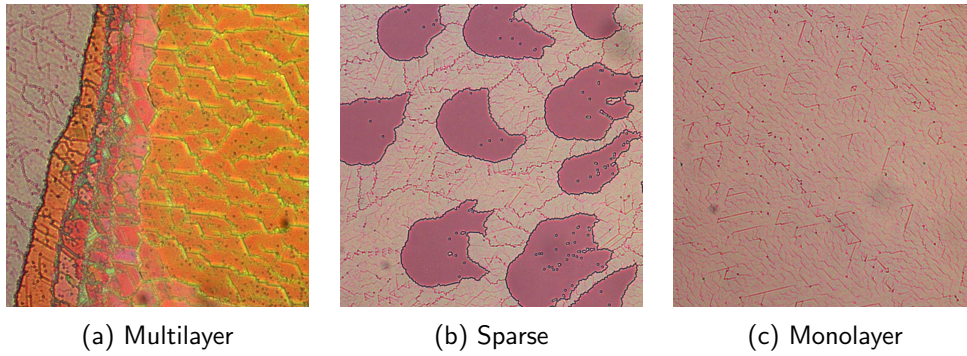


Figure 2.12: Typical optical microscope images of PSB517 multi-, sparse and monolayers of beads are shown in (a), (b) and (c), respectively. All microscope images were taken with a $40\times$ magnification objective.

The presence of the above described bead layer regions is explained as follows: A two-stage evaporation process was observed which is due to the fact that ethanol has a lower vapor pressure and thus evaporates faster as compared to water, causing the fast movement of the contact line in the first stage. At the same time, the convective flow of particles to the contact line is very high, causing multilayer deposition in case of the 1% w/v suspensions. In case of the 0.5% w/v suspensions, the liquid volume dispensed onto the wafer was doubled (equation 2.17d) in order to have the same number of beads available for deposition. This decreases the convective particle flow rate. In conjunction with the fast contact line movement, sparse bead layers are deposited first. Due to the liquid evaporation, the bead concentration increases and finally results in a monolayer deposition.

At the time when the majority of ethanol has evaporated, the contact line speed slows down. Simultaneously, a change in meniscus shape at the three-phase contact line takes place as water forms a higher contact angle on the substrates as compared to a water:ethanol mixture. A steeper meniscus slope, however, favors the deposition of multilayers (as long as it is $\leq 90^\circ$, which favors no bead deposition at all, c.f. section 2.2). Multilayer deposition is further promoted by the large amount of beads in vicinity of the contact line, transported there by the fast ethanol evaporation and thus the strong convective flow. Although the convective flow slows down upon switching to the second, water evaporation stage, a redistribution of beads within the remaining liquid layer on the substrate surface cannot be achieved instantly, nor before the beads become subject to capillary forces and are integrated in the bead array. As a result, the bead suspension is depleted, and thus the last bead layer within the center region of the wafers is sparse²¹⁴.

Drop-coating of wafers with hydrophobic patches

In the above described experiment, the wafer surface neither had chemical nor topo-

graphical surface patterns. The bead deposition was solely determined by the particle convective flow induced by the liquid evaporation rate at the three-phase contact line and its position, as well as by the bead concentration. In this experiment, it was investigated whether the position of the three-phase contact line could to some extent be controlled by patterning hydrophobic patches on the wafer surface. Also, the different surface chemistry may favorably influence the bead mobility, and thus the bead deposition, on the wafer surface (see for example Fan²⁰⁸).

The coating procedure was the same as in the above experiments. Two different 0.5% w/v bead suspensions were used. The solvent used to dilute the as-provided 10% w/v aqueous suspension was (a) a 1:1 H₂O:Ethanol mixture with 0.001‰v/v of Triton-X 100, and (b) pure ethanol. The dispensed liquid corresponded to $1.1 \times V_{calc}$, equal to 550 μ l. The petri-dishes were closed using a spacer between the petri-dish and the cover-lid.

Both bead suspensions spread well on the wafer surface. Some of the larger hydrophobic patches were not covered initially, but were recovered by a gentle tilt of the wafers. Patches larger than 200 μ m showed a tendency to de-wet again, particularly in case of the H₂O:Ethanol solvent mixture. This is due to the higher surface tension as compared to pure ethanol.

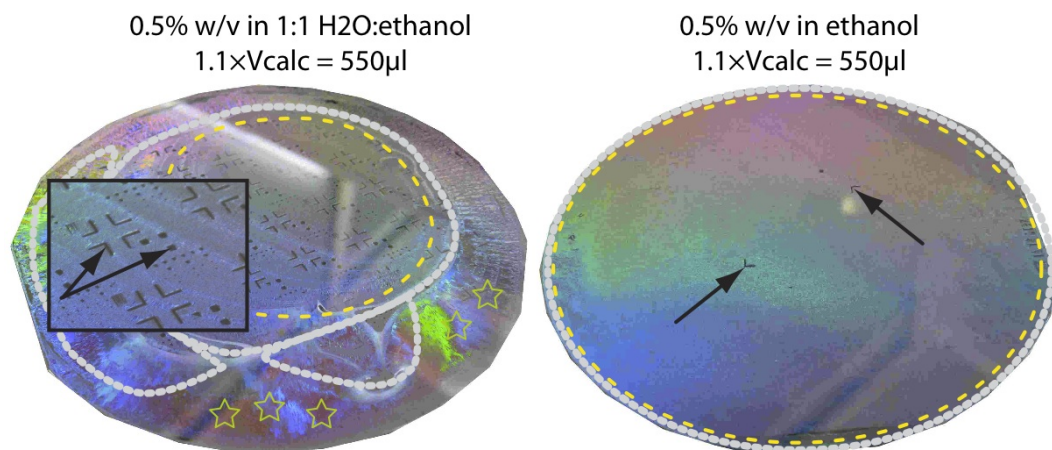


Figure 2.13: Drop-coating CSA of PSB517 beads on wafers photolithographically patterned hydrophobic patches. See figure 2.11 for the meaning of the dashed lines. Arrows indicate de-wetted areas where no beads were deposited.

Photographs of the coating results are shown in figure 2.13. The H₂O:Ethanol wafer has a bead layer coverage which is very similar to the results obtained previously for wafers without hydrophobic patches (c.f. figure 2.11). It was observed that the liquid film broke up across the largest hydrophobic patches, and thus no beads were deposited

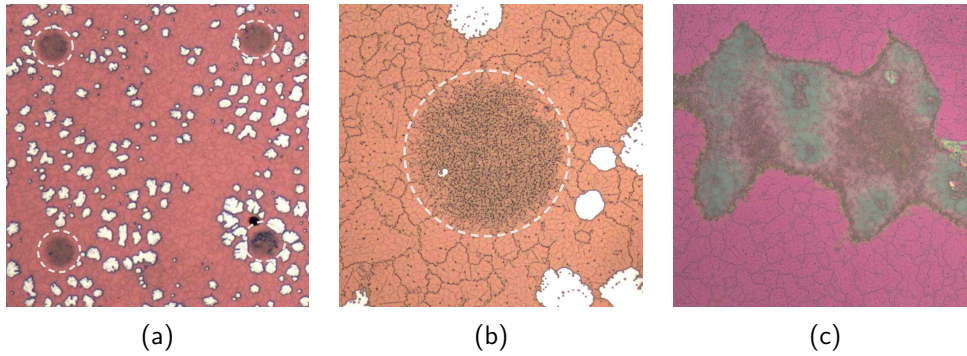


Figure 2.14: Optical microscope images of PSB517 beads deposited onto silicon wafers with photolithographically patterned HMDS areas. (b) is a zoom into the image shown in (a). (c) Bead agglomerates found on wafers coated with PSB517 suspensions in pure ethanol. (a) was taken with a $5\times$, (b) and (c) with a $40\times$ magnification objective.

within those areas (c.f. the inset in figure 2.13). Such breaking up of the wetting film was not observed when the purely ethanolic suspension was used. As a result, apart from a thin multilayer rim at the very border of the wafer, the wafer surface is homogeneously coated with a sparse monolayer of beads. The coverage is almost 100%.

On the microscopic scale, the hydrophobic patches which are actually coated with beads are very similar on both wafers. As compared to the surface coverage on the surrounding hydrophilic area, beads preferentially deposited within the hydrophobic patches. This is shown in the optical microscope images in figures 2.14a and 2.14b. Figure 2.14a is a low magnification image which shows a sparse bead monolayer with some empty areas (white spaces in the image). Indicated by dashed lines are spherical patterns which correspond to the hydrophobic patches. In comparison to the surrounding area, the hydrophobic patches are preferentially coated with beads. The hydrophobic patch appears darker due to a higher density of defects within the crystal domains (figure 2.14b).

The reason for the higher density of beads within the hydrophobic patches is the pinning of the wetting contact line when the liquid film retracts from the wafer surface. Such a pinning was observed during the drying process and is shown for pure water in figure 2.10b. Pinning of the contact line coincides with an increase of the meniscus slope due to the higher contact angle on the hydrophobic surface, both of which effects favor the bead deposition. The reduced ordering of the beads within the hydrophobic patches can be due to an increased bead-surface interaction, reducing the mobility of the beads on the substrate surface²¹⁰.

The overall homogeneous bead deposition using an ethanolic suspension is explained by the absence of a two-stage evaporation process (c.f. the experiments described above).

However, it was found that the stability of the colloidal suspension is greatly reduced in ethanol. This is contrary to what would be expected from the DLVO theory for electrostatically stabilized colloidal suspensions (section 2.1). An explanation for this observation cannot be given at the moment. An agglomerate deposited onto the wafer surface is shown in figure 2.14c. An alternative to the use of ethanol is the use of a surfactant that decreases the liquid surface tensions, thus allowing wetting of the complete wafer surface even for a small amount of aqueous suspension (which is desirable to reduce the total evaporation time), but without deterioration of the colloidal stability.

Preliminary conclusions

4" wafers plain silicon wafers and silicon wafers patterned with hydrophobic patches were coated with PSB517 beads by drop-coating convective self-assembly. The experimental setup was kept simple, for example the evaporation speed and the position of the three-phase wetting film contact line were not externally controlled. The resulting coatings were analyzed qualitatively by optical microscopy. H₂O:ethanol suspensions resulted in inhomogeneous bead coverages. Depending on the bead concentration and dispensed volume, bead multi- and sparse layers dominated the coating result in different regions on the wafer surface. The formation of bead monolayers was mainly observed towards the wafer border, which restricts the use for continued processing of the wafers with standard micromachining techniques which are optimized (under laboratory research conditions) for optimum results within the wafer center area. The bead deposition was partially controlled and directed towards specific areas by photolithographic patterning of hydrophobic patches. The best results were obtained for coatings from ethanolic suspensions. However, the colloidal suspension stability was significantly reduced, resulting in bead agglomerates deposited onto the wafer surface.

Thus, in order to obtain a controlled and uniform monolayer coating, the experimental setup has to be improved. In the following section, this is attempted by controlling the position of the wetting film contact line, as well as the evaporation rate.

2.3.2 Controlled convective self-assembly with CAPA tool

As it has been shown in the previous section, CSA of beads on large size, flat substrates using a simple setup without control over the dominant bead assembly mechanism (evaporation rate and position of the wetting film contact line) does not yield homogeneous nor reproducible results. Therefore, in the following experiments, a more sophisticated setup was used that allows the precise control of these parameters. PSB281, PSB508 and PSB517 beads were deposited onto different types of substrate (c.f. below). The

experiments were done in collaboration with Heiko Wolf and Cyrill Kümin at the IBM Rüschlikon research labs.

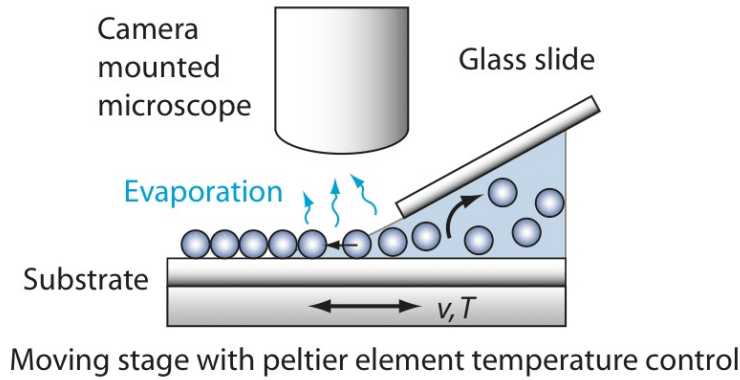


Figure 2.15: Convective self-assembly of beads controlling the water evaporation rate and the position of the three-phase contact line using the CAPA tool.

The experimental setup is schematically shown in figure 2.15. The substrate is vacuum fixed on a Peltier-element temperature controlled stage whose position and speed can be precisely controlled via a LabVIEW® interface. Typical stage speeds are a few $\mu\text{m}/\text{sec}$. A clean microscope glass slide is placed under an angle of ca. 30° in vicinity to the substrate. The gap between the lower edge of the glass slide and the substrate surface is on the order of 1 mm. Both the gap and the glass slide angle can be adjusted according to the colloidal suspension wetting properties and deposition conditions (speed, stage temperature). A small amount of colloidal suspension is carefully dispensed between the glass slide and the substrate. During the deposition process, the particles are then transported to the wetting film contact line by convective flow. The bead deposition process is monitored using a camera mounted microscope. In the following, this setup is referred to as CAPA tool (Capillary Assisted Particle Assembly), which was developed at the IBM Rüschlikon research labs for the precise particle placement on pre-patterned substrates (c.f. Kraus and Malaquin^{217,148}).

Experimental

Suspension compositions

The concentration of the bead suspensions was 0.25% w/v. The deposition of beads from aqueous, ethanolic and non-ionic surfactant modified aqueous suspensions was tested. The suspensions are listed in table 2.3.

Substrates

Suspension name	Solvent	Comment
PSB281:aq	Water	Original bead suspension diluted with Di-H ₂ O
PSB508:EtOH	Ethanol	Solvent exchange from water to ethanol by successive centrifugation and re-dispersion of beads in the new solvent
PSB517:aq	Water	Original bead suspension diluted with Di-H ₂ O
PSB517:EG	Water with 0.1% v/v EG	A small amount of EG was added to the 0.25% aqueous suspension just prior to use of the suspension

Table 2.3: Bead suspensions used in the CAPA-controlled CSA experiments. EG = ethylene glycol.

Two different types of substrates were used: 15×15 mm² manually cleaved silicon substrates coated with 100 nm of silicon oxide and 500 nm of amorphous silicon (SiO_x-aSi) and 24×24 mm² microscope coverslips coated with 300 nm of gold. These types of substrates were chosen as they were relevant for subsequent experiments (c.f. chapters 4 and 5). The gold, silicon oxide and amorphous silicon were deposited by sputter deposition and evaporation. The root-mean-square roughness R_{rms} of the gold coated substrates was determined by AFM imaging; the sputtered gold substrates had a R_{rms} of 1.39 nm, while the roughness of the evaporated gold substrates was slightly higher with a R_{rms} of 2.54 nm. The SiO_x-aSi coated substrates were cleaned by sonication in organic solvents after the cleavage. The gold coated substrates received no further treatment after deposition of the gold. Prior to the CSA experiments, the substrates were treated in an oxygen plasma at 200 W for 30 sec.

Procedure

The depositions were done under standard laboratory conditions, the ambient temperature was 18°C and the relative humidity was 54%. The glass slide was cleaned by sonication in a 1:1 H₂O:Ethanol solution for 30 min, followed by a 30 min treatment in a 200 W oxygen plasma. The distance of the lower edge of the glass slide was 1 mm in case of the SiO_x-aSi coated silicon substrates, and 1.3 mm in case of the gold coated glass coverslips. The bead deposition process was observed with a microscope-mounted camera. An example snapshot is shown in figure 2.16. For SEM imaging of the deposited bead layers, the samples were sputter-coated with a 10 nm thick gold layer.

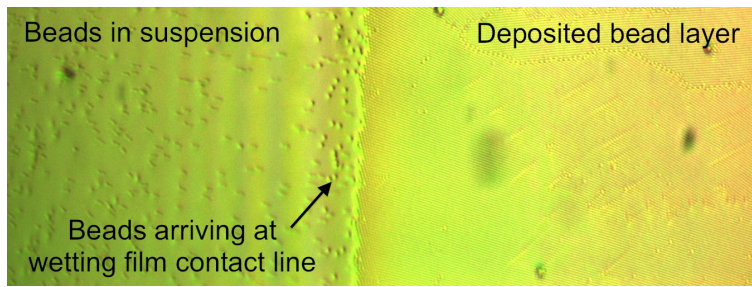


Figure 2.16: Camera snapshot during deposition of PSB517 onto SiO_x -aSi substrates.

Results and discussion

Deposition of PSB517 beads from aqueous suspension

PSB517:aq suspensions were used for CAPA-controlled CSA experiments on SiO_x -aSi and sputter-coated gold substrates. Further, the deposition of beads from PSB281:aq suspensions was tested on sputtered and evaporated gold substrates. Figure 2.17 shows

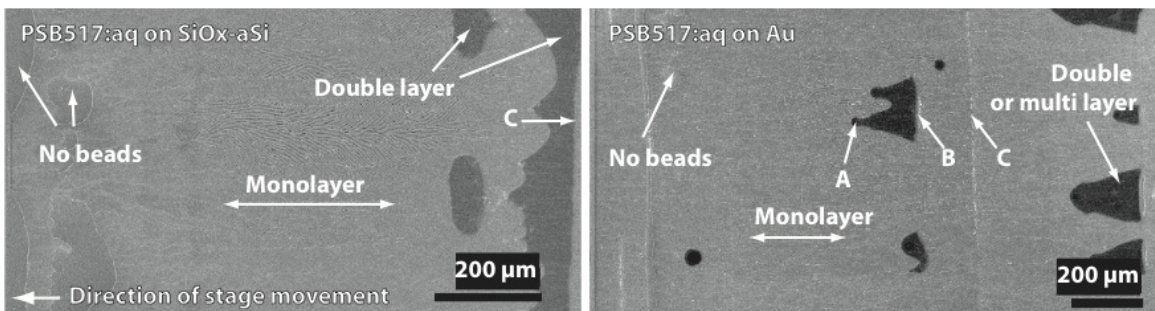


Figure 2.17: Typical SEM images of PSB517 beads deposited onto SiO_x -aSi (left) and gold (right) substrates. Explanations in the text.

low magnification SEM images of PSB517 beads deposited onto SiO_x -aSi and sputtered gold substrates. The bead layer was grown towards the right of the images, the stage was withdrawn towards the left. The stage speed was varied between $1 \mu\text{m}/\text{sec}$ and $2.5 \mu\text{m}/\text{sec}$; the stage temperature was varied between 20°C and 26°C . These external parameters were adapted dynamically with the goal to obtain a dense monolayer of beads. For example, an increase of the stage speed will influence both the shape of the meniscus between the bottom substrate and the glass slide edge. The bead pump speed is influenced by the substrate temperature due to change of the liquid evaporation rate.

On the very left side of the images, the onset of the bead deposition can be seen (“No beads”). On both types of substrates, a continuous bead monolayer could be grown for several $100 \mu\text{m}$. Disturbances due to substrate contamination (dust) or local roughness peaks (gold granular structure) caused the growth of double or multilayers. **A** in figure 2.17 (right) indicates such a disturbance point with a broadening tail of bead double layers (dark grey area). From **A** to **B**, the deposition conditions were kept constant.

To terminate the double layer deposition, the stage speed was slightly increased which caused a break-up of the bead array (**B**). When the convective flow of particles was lowered at constant stage speed by decreasing the stage temperature and thus reducing the liquid evaporation rate, the deposited bead layer became sparse (**C** in both images). After adapting the stage speed to the decreased convective particle transport, the deposition of a continuous bead monolayer was reinitiated.

It was observed that the deposition of the PSB517 beads in aqueous suspension is very similar on both types of substrates. This confirms that the substrate specific interactions are dominated by the capillary immersion forces (c.f. section 2.1).

With respect to CAPA-tool controlled CSA, the above described manipulations show the flexibility and control options of CSA using the CAPA tool which allow a dynamic adjustment of the bead deposition parameters. Below, assembled bead layers are described in more detail for beads deposited onto the SiO_x -aSi substrate

Figure 2.18 shows SEM images of typical PSB517 layer formations. Arrows **A**, **B**, **C** point to specific locations described below. The directional growth of the bead array

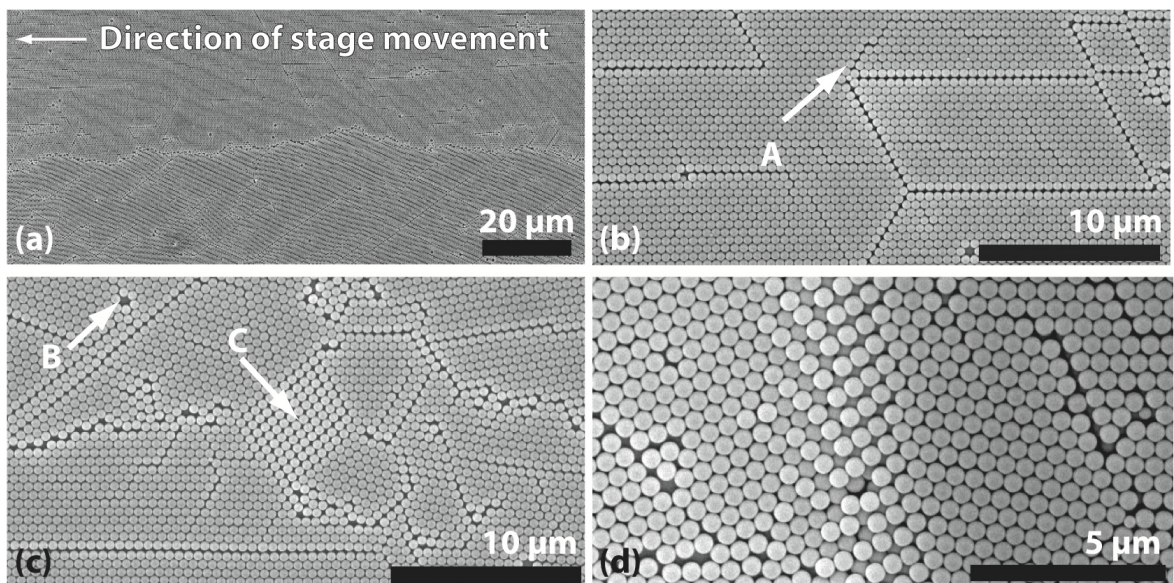


Figure 2.18: SEM images of PSB517 beads on a SiO_x -aSi substrate. Deposition from aqueous suspension. Explanations in the text.

can be seen; crystalline domains have a tendency to orient along the growth direction (figure 2.18 (a)). The perfect growth of large crystalline regions is hindered by the bead size distribution. For example, the integration of small beads into the array may cause line defects **A**. A void point defect is indicated by **B**. **C** indicates a 2-dimensional defect, the beads are arranged in an almost square rather than in a hexagonal lattice. This is

stimulated by two joining crystal domains, which open up a cone whose width vertical to the growth direction does not match a multiple of the bead diameter. As the deposition in a square lattice is not energetically favorable, the square lattice domain is terminated soon and the layer growth continues in a hexagonal fashion. The onset of such a double layer growth with a transition from a square to a hexagonal arrangement is shown in figure 2.18 (d)

Deposition of PSB281 beads

In the following experiments, PSB281 beads were deposited. The first deposition was done on sputtered Au substrates with the lower surface roughness. Compared to PSB517:aq suspension on the same substrate type, a drastic difference in behavior of the bead suspension was observed. The PSB281:aq wetted the substrate surface to an extent that no pinning of beads to the substrate surface, which is necessary for the formation of an initial bead layer, could be achieved. The second deposition on evaporated Au substrates with a higher surface roughness showed the same wetting behavior. An initial wetting film contact line was formed upon halting the stage, accumulating a large amount of beads beneath the glass slide edge and depositing a bead multilayer which subsequently acted as a barrier to the liquid flow opposite the array growth direction.

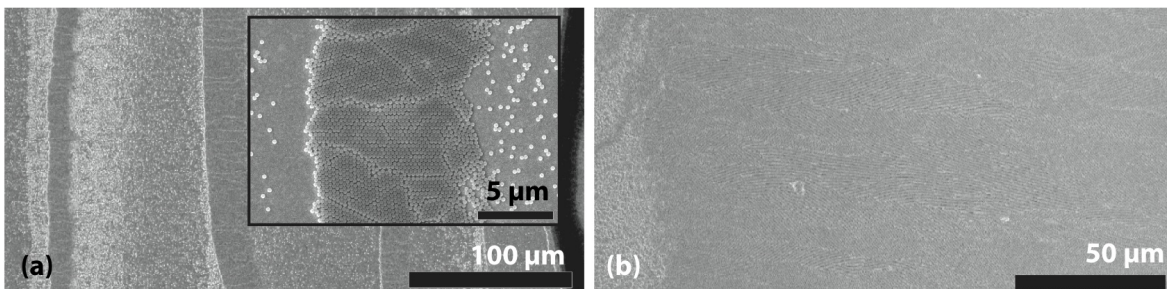


Figure 2.19: SEM images of PSB281 beads on an evaporated gold substrate. Deposition from aqueous suspension. Explanations in the text.

The continuous monolayer deposition remained very difficult to achieve, the stage speed and temperature needed to be finely tuned to find an equilibrium between no deposition and multilayer deposition of beads. This typically resulted in stripe patterns as shown in figure 2.19 (a). Figure 2.19 (b) shows an SEM image of a large monolayer region after successful tuning of the deposition conditions. These results show that different bead sizes can be deposited with the same experimental setup if the deposition parameters are finely tuned to the suspensions wetting properties.

Deposition of PSB508 beads from ethanolic suspension

PSB508 beads were deposited onto sputtered gold substrates from an ethanolic suspension⁹. The evaporation rate of ethanol is higher compared the one of water under the

⁹Drop-coating CSA deposition of PSB508 and PSB517 beads gave the same results. Thus one can

same ambient conditions (temperature, relative humidity). Consequently, also the convective particle flow of beads in ethanolic suspension to the wetting film contact line is higher. Consequently, an increased and turbulent particle flow rate was observed during the deposition of the beads. Additionally, the lower surface tension of ethanol promotes wetting of the substrate surface and lowers the meniscus slope angle at the wetting film contact line.

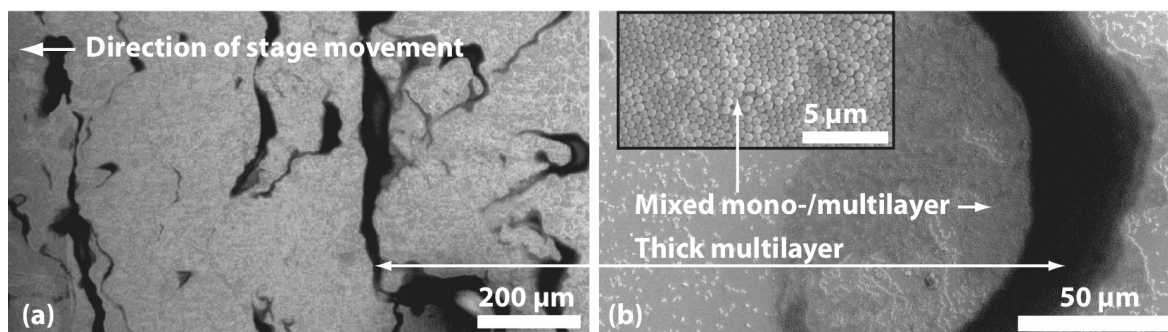


Figure 2.20: SEM images of PSB508 beads on a sputtered gold substrate. Deposition from ethanolic suspension. Explanations in the text.

Figure 2.20 shows typical depositions obtained for ethanolic suspensions. The majority of the bead arrays were either multi- or sparse layers. The multilayer deposition reflects the chaotic flow within the ethanolic suspension. Unlike in the case of beads deposited from aqueous suspensions, the multilayer starting line is not perfectly straight and parallel to the glass slide edge, but rather distorted. Locally, the deposition of a monolayer was observed (figure 2.20 (b)). However, the bead ordering was less good as compared to the one observed for beads deposited from aqueous suspension, and frequently beads were locally deposited in a multilayer configuration. To better control the bead convective flow, the stage temperature was lowered to 10°C. This did not significantly improve the bead deposition process; turbulences in the bead flow remained high. Further lowering of the stage temperature was not feasible as this would have resulted in water condensation. These results show that beads in ethanolic suspension can not be deposited in a controlled manner under standard ambient conditions.

Deposition from aqueous suspension with EG

Surfactants are an alternative to ethanol to lower the surface tension and thus tune the meniscus slope at the wetting film contact line. In the experiments below, a small amount of ethylene glycol (EG) was added to the PSB517:aq suspension, which is hence termed PSB517:EG (c.f. table 2.3).

assume that differences in the CAPA-assisted CSA are not related to the different type of beads used.

It was observed that the wetting of the substrate surface was enhanced as compared to the pure water suspension. The convective flow of the particles in the PSB517:EG suspension was similar to the one in the PSB517:aq suspension, and beads were deposited under similar stage speed and temperature settings ($0.75 \mu\text{m}/\text{sec}$ and 23°C).

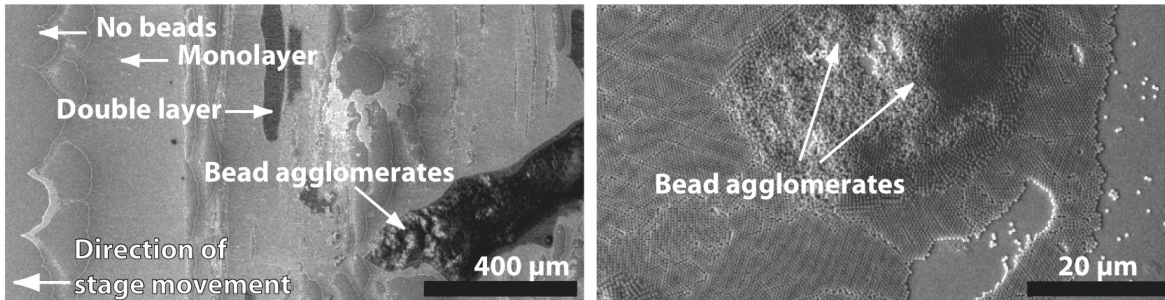


Figure 2.21: SEM images of PSB517 beads on a sputtered gold substrate. Deposition from aqueous suspension with EG. Explanations in the text.

Figure 2.21 shows the resulting bead layers obtained from a PSB517:EG suspension. Over the first $\approx 100 \mu\text{m}$, a continuous monolayer was deposited. The bead arrangement in this monolayer region has the same characteristics as shown in figure 2.18. After a few minutes of deposition, agglomerates formed in the bead suspension and were deposited onto the substrate, preventing further monolayer growth.

The pre-formation of the agglomerates in the suspension means that the addition of EG reduces the colloidal stability. Originally, the aqueous PS bead suspensions are stabilized by the presence of an electric double layer (c.f. section 2.1). However, EG is a non-ionic molecule with two hydrophilic chain ends. Thus, molecular chain end interactions are likely to cause the agglomeration. A non-ionic amphiphilic molecule, such as Triton-X, is an alternative to EG.

Preliminary conclusions

PS beads were deposited in a controlled manner using the CAPA tool. This has been shown for different bead sizes in different suspension compositions, and on different types of substrates. The stage speed and temperature have an important influence on the deposition process. In order to obtain a continuous bead monolayer, both parameters have to be finely tuned. As a result, large polycrystalline bead monolayers could be obtained (figure 2.18). Importantly, large monolayer were also obtained for bead sizes which could not be deposited successfully by the drop-coating CSA method (figure 2.19). The experiments showed that the bead deposition process is very sensitive, e.g. to local roughness variation on the substrate surface or fluctuations in the water evaporation rate. Both variations can cause the formation of sparse or multilayers. Thus, the monolayer coating of larger areas will be a challenging task. Different bead suspensions require different

deposition parameters. This is because both the wetting properties of the suspensions and the dynamics of the convective bead flow differ. For example, smaller beads are easier to transport to the wetting film contact line by convective drag forces as compared to large beads. Also, the capillary immersion forces that drive the integration of beads into an already existing layer are stronger for larger beads (c.f. section 2.2). This explains why it is more straight forward to obtain continuous bead monolayers for PSB517 beads than for PSB281 beads. The deposition of beads from ethanolic and surfactant modified aqueous suspensions was investigated. In both cases, the deposition process was inferior as compared to deposition from pure water suspensions. Especially, bead agglomeration in suspension was observed when using EG as surfactant.

The most stringent limitation of CSA using the CAPA-tool is the substrate area that can be coated in a controlled way. It is limited by the size of the glass slide used to control the wetting film meniscus and the area observable by the microscope mounted camera. Also, the deposition speed is rather low (between 1.0 to 2.0 $\mu\text{m}/\text{sec}$). Therefore, a third method, bead deposition by spin-coating, was investigated and is described in the following section.

2.3.3 Spin-coating

Spin-coating is a well known technique commonly employed in silicon micromachining or by the semiconductor industry to deposit polymer layers of controlled thickness onto a wafer^{1,218}. In a standard spin-coating procedure, the substrate is fixed to a rotating substrate holder (chuck) by vacuum. Then, the liquid to be deposited is dispensed. After spreading of the liquid on the wafer, the chuck is accelerated to its final spin-speed. The substrate is kept rotating until most of the solvent has evaporated.

For the spin-coating of viscous liquids, the resulting film thickness is determined by the centrifugal force which is counteracted by the viscous force (c.f. Emslie²¹⁹):

$$\rho\omega^2r = -\eta\frac{\delta^2v}{\delta z^2}, \quad (2.18)$$

where ρ is the liquid density, ω is the rotational speed, r is the radial position on the substrate with the center $r = 0$, η is the liquid viscosity, v is the shear flow velocity as a function of vertical position z . Applying no-slip and no-shear boundary conditions at $z = 0$ (substrate surface) and $z = h$ (liquid surface), respectively, allows to determine the shear flow. By integration, the radial flow per unit volume can thus be determined. Applying an equation of continuity leads to the following relation between film thickness h and ω and spin time t :

$$h \propto \frac{1}{\omega\sqrt{t}}. \quad (2.19)$$

Interestingly, for Newtonian fluids and neglected liquid evaporation, the film thickness is independent of the radial position. Also it has been shown that thicker films become thinner faster²¹⁹, which means that thickness variations are leveled out during the spin-coating procedure.

Spin-coating of photo-resist Depending on the kind of liquid spin-coated, the layer formation process is very different. Photo-resist spin-coating is most widely known in the MEMS community. In that case, a thin, almost solid crust forms at the resist-air interface that inhibits further solvent evaporation. More resist is then ejected from in between the substrate-resist and resist-air interface due to the centrifugal force. Thus (within a certain viscosity range) the resulting layer thickness is solely determined by the spin-speed and spin-time, as predicted by equation 2.19.

Spin-coating of colloidal suspensions However, in case of spin-coating of colloidal suspensions, not only the film thickness (or the number of colloidal array layers), but also the arrangement of the colloidal particles, is influenced by the spin-coating parameters. Moreover, one needs to distinguish the spin-coating of colloidal suspensions in volatile and non-volatile media. In the latter case, shear-induced ordering plays an important role when the Peclet-number is > 1 (c.f. Ackerson²²⁰, Britten²²¹, Vermant²²² and Shereda²²³). The dimensionless Peclet number Pe is a measure for shear-thickening of non-Newtonian fluids^{181,222}:

$$Pe = \frac{\dot{\gamma}\eta a^3}{k_B T}, \quad (2.20)$$

where $\dot{\gamma}$ is the shear rate, η is the medium viscosity, and a is the particle radius. $Pe > 1$ means that convective forces associated with e.g. the shear flow dominate Brownian diffusion. An approximation is given by²²³ $Pe \approx \frac{6\pi\rho\omega^2 r(h-z)a^3}{k_B T}$. Highly ordered wafer-scale arrays of non-close packed (ncp) colloidal crystal templates could thus be fabricated (for example Jiang and McFarland²²⁴, Venkatesh²²⁵ and Min²²⁶).

When the colloidal suspension is rather dilute (low effective η at low particle volume concentrations below $\approx 15\%$) and/or in the case of volatile solvents (fast thinning of the liquid layer due to evaporation), the particle assembly is dominated by inter-particle and particle-substrate interactions^{204,212,227,228} and by capillary immersion forces (section 2.1). For $\Delta\rho = \rho_{colloid} - \rho_{solvent} \ll 1$, inhomogeneous particle distribution within the liquid film due to centrifugal forces can be neglected. In this way, Deckman and Dunsmuir obtained hexagonally close-packed (hcp) monolayers of sub- μm PS beads on small size substrates (c.f. their original article on *Natural lithography*¹³³). In subsequent works, researchers have chosen different experimental conditions with respect to the choice of solvent, particle concentration, use of surfactants or substrate pre-treatment. For all the different cases, a good reproducibility of the spin-coated layers could be ob-

tained^{134,229,230,165}. Mono- as well as multilayers with different stacking order (e.g. face-centered-cubic or body-centered-cubic) have been fabricated by tuning the spin-speed, colloidal suspension concentration or solvent composition (e.g. Ozin¹⁷⁹ and Mihi²³¹). By adjusting for example the electrostatic inter-particle interaction, also ncp monolayers can be obtained (e.g. Peng²³²).

Drying and array formation process The array formation process observed in this thesis was comparable to previous results reported by Ogi²¹³ and Giuliani¹³⁸. Both suggest a substrate-induced array formation during the drying process, that is when the liquid film thickness is on the order of the bead size. Giuliani et al. observed a wafer border to center progression of the drying front. They could fit their experimental observations with a linear decrease of the evaporation rate and an increase of the dried colloidal layer thickness towards the substrate center. This is similar to what was observed in this thesis.

A schematic of the spin-coating of PS beads from a volatile solvent suspension is shown in figure 2.22. The suspension is dispensed statically. Spreading of the bead

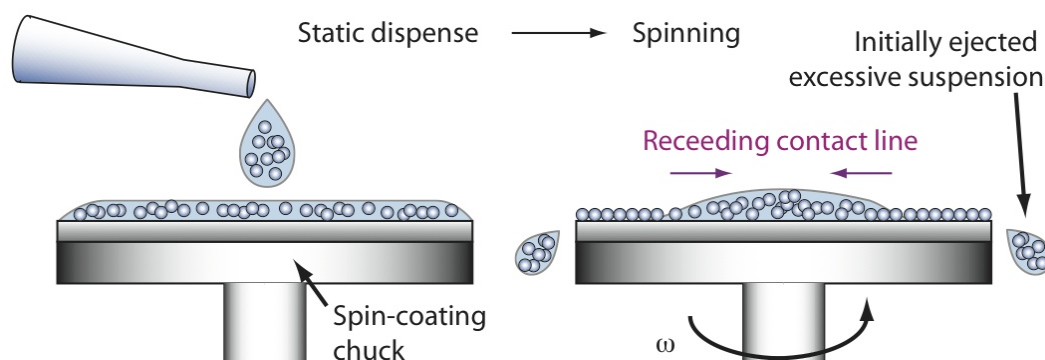


Figure 2.22: Spin-coating of PS beads.

suspension across the whole wafer surface can be enforced by a manual tilt and rotation of the substrate. This allows to reduce the amount of suspension needed. Then, wafer rotation is initiated and liquid is ejected from the wafer due to the centrifugal force. The ejected volume depends on the spin-speed, acceleration, and liquid viscosity, but also on ambient conditions such as temperature and relative humidity. For example, at high relative humidity, the liquid evaporation rate and thus the drying process are slower compared to under low humidity conditions. Consequently, more colloidal suspension will be ejected from the wafer, leaving less beads for deposition on the substrate. The drying front moves inwards from the wafer border. From the onset of drying, the amount of beads on the substrate is fixed. This will ultimately determine whether sparse, mono- or multilayer bead arrays will be formed on the substrate. Within a certain range,

the parameters suspension concentration, spin-speed and humidity are interchangeable. Thus, obtaining a homogeneous bead distribution across the wafer surface is feasible but not trivial and requires careful balancing of the inter-dependent parameters²³³.

Ultimate limitations to obtain long-range array order There are two main limitations to obtain perfect 2D, hexagonally close-packed crystals by spin-coating: First, as pointed out in chapter 2.3.2 and illustrated in figure 2.18, the size distribution of the beads inherently limits perfect array order due to the creation of point and line defects. Secondly, for evaporation induced array formation starting at the substrate border, crystals with different principal orientation merge and domain boundaries are created. However, for the target applications in this thesis, only short-range order over ≈ 10 periodicities is required.

Experimental

Suspension compositions

PSB284 5%w/v, PSB535 10%w/v and PSB836 10%w/v aqueous suspensions were used as delivered. PSB428 and PSB535 suspensions with higher or lower bead concentration were prepared by dilution with Di-H₂O or centrifugation and solvent extraction. Characterization of the colloidal suspension properties such as surface tension and ζ -potential was not conducted. However, it could be observed that the PSB284 suspension foamed when agitated, PSB535 and PSB836 suspensions did not. This may be linked to particle induced foam-stabilization, which is more promoted for smaller beads and at lower particle concentrations (c.f. Fujii²³⁴). Centrifugation of the PSB284 suspension in order to increase the bead concentration to 10%w/v was not feasible as this led to a permanent bead agglomeration. Just before use, the suspensions were filtered with a 5 μ m fluoroethylene filter to remove agglomerates.

Substrates

Test-grade 4" Si wafers with a thermal oxide of 100 nm thickness were used as substrates in the systematic spin-coating experiments. Different types of substrates were used to show the influence of varying the spin-coating conditions, such as Si wafers with native oxide only, coated with 100 nm thermal oxide or 100 nm of SiN, and on Pyrex wafers. Prior to the bead spin-coating, the wafers were treated in an oxygen plasma, either in a barrel etcher for 10 min at 1000 W or in O₂-RIE for 2 min at 100 W and then stored in air. The time delay between the bead deposition and the plasma treatment was limited to 30 min. For comparison, wafers were alternatively treated with Piranha ca. 5 hrs prior to bead deposition.

Procedure

Spin-coating was done under standard, class 1000 or better, clean-room conditions. The wafers were positioned on a spin-coating chuck integrated into a laminar flow hood. 900 μl of bead suspension¹⁰ was statically dispensed into the middle of the wafer and let spread for 1 to 2 seconds before spinning. In case of incomplete wetting of the wafer surface, the suspension was manually dispersed across the wafer surface by either a gentle tilt and rotation of the wafer or by a careful spread with a clean pipette tip. The wafer was spun until all solvent had evaporated. Typically after at most 60 sec, the wafer was dry. The wafer edge was cleaned of beads with a piece of clean-room wipe soaked in acetone held with tweezers and pressed to the wafer border of the rotating wafer.

Bead array analysis

Optical microscope images were taken along the wafer diagonal. The percentage of sparse, mono- and multilayers of beads was analyzed as described in the appendix [A.2](#).

Results and discussion

Substrate dependent wetting behavior

Different wetting behavior was observed for identical suspensions on different substrate types and substrate pre-treatment, namely Si with native oxide, Si without native oxide where the bead suspension was dispensed only a few minutes after removing the thermal oxide in an HF etch, Si with 100 nm thermally grown oxide, Si with 100 nm low-stress silicon nitride (LS-SiN), and pyrex glass wafers. These substrates have different Hamaker constants, and a different wetting behavior is expected (c.f. section [2.1](#) and Seemann¹⁸⁷).

In the following, *good* wetting behavior will be defined as the case when 900 μl of suspension spreads on the 4" wafer surface either autonomously or by gentle tilting of the wafer; *insufficient* means that the suspension had to be forced to spread with the use of a horizontally held pipette tip; *de-wetting* means that the suspension recoils into small droplets on the wafer surface. In summary, the following was observed:

- PSB284 suspensions spread well on any kind of substrate.
- PSB535 and PSB836 suspensions wetting was good on Si wafers with native oxide or 100 nm of LS-SiN and pyrex wafers, but insufficient on Si wafers with 100 nm thermal oxide.
- PSB535 suspension wetting on Piranha treated 100 nm SiO₂ wafers was less good than on O₂-plasma treated wafers.

¹⁰Note that this corresponds to 30 to 40 $\times V_{calc}$ (c.f. [2.3.1](#)).

- PSB836 suspensions on bare Si wafers without native oxide de-wetted completely.

The above observations were confirmed by dynamic advancing θ_a and receding θ_r contact angle measurements performed on O₂-plasma pre-treated wafers. The plasma treatment was done to make the measurements comparable to the spin-coating conditions. On Si wafers with 100 nm thermal oxide, $\theta_a \approx 20$ to 30° for 10%w/v aqueous suspensions of PSB428, PSB535 and PSB836, but it was significantly lower for PSB284 5%w/v aqueous suspension with $\theta_a \approx 17 \pm 5^\circ$. θ_r was less than 10° in all cases and could not be measured accurately. In the case of Si wafers with native oxide only, both θ_a and θ_r were below 10° .

The different wetting properties did however not translate into significant differences of the deposited bead layer (apart from the total de-wetting case). This is explained by the fact that bead assembly driven by capillary immersion forces takes place under receding contact angle conditions which were identical both for *good* and *insufficient* substrate wetting. This is consistent with early results reported by Denkov¹³⁶ that capillary immersion forces dominate over suspension surface tension modifications, which is similar to changing the wetting properties by changing the substrate type.

Suspension dependent drying behavior¹¹

Shortly after the wafer rotation was initiated, interference rings indicated liquid film thinning. In case of the PSB535 and PSB836 suspensions, with one exception, the interference rings moved from the wafer border towards the center. This is due to a linear increase in evaporation rate with the radial distance from the wafer center. PSB535 spin-coated at 2000 rpm revealed an oscillatory interference ring movement. Air flow fluctuations in the laminar flow hood and solvent evaporating from the liquid accumulated in the spin-coater basin can not be excluded as a contributing factor to this un-expected behaviour. Another factor is the competition between centrifugal forces driving the suspension to the wafer edge and the radially increasing evaporation rate driving the drying front in the opposite direction.

The PSB284 suspension showed a totally different drying behavior. At all spin-speeds, the interference rings moved from the center to the border of the wafer. This is related to the lower bead concentration (5%w/v as compared to 10%w/v in case of the PSB535 and PSB836 suspensions). Shear thinning or thickening varying with the radially increasing shear flow rate can be another factor. Also, the smaller bead size and lower suspension concentration is lowering and retarding the capillary immersion forces: (i) because they are proportional to the particle size, and (ii) as they become effective only once the liquid film height has dropped below the particle diameter. Finally, as mentioned above, the PSB284 suspension showed different wetting behavior and produced foam, which is

¹¹Observations made during the systematic spin-coating study.

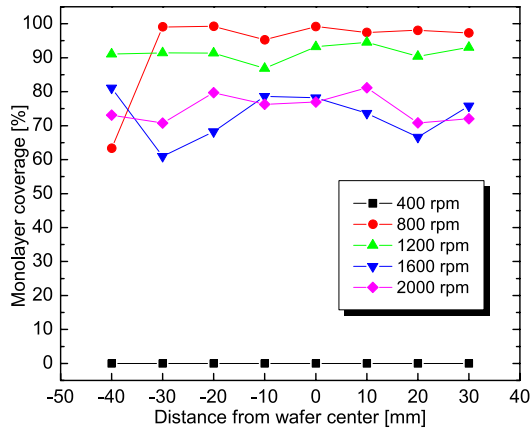
due to a different and/or stronger suspension stabilization mechanism. This influences the particle-substrate and inter-particle interactions as well as the suspension viscous flow behavior.

Bead layers as a function of spin-speed and bead size

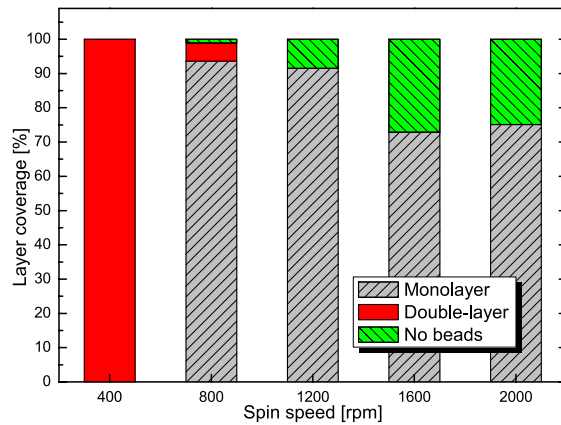
PSB284, PSB535 and PSB836 aqueous suspensions were spin-coated onto O₂-plasma treated Si wafers with 100 nm thick thermally grown SiO₂ as described above. The spin-speed was increased from 400 rpm to 2000 rpm in steps of 400 rpm with an acceleration of 500 rpm/s. No spread-step was used. The bead layers were analyzed by optical microscopy. The bead-substrate contrast was enhanced with a differential interference filter (c.f. appendix A.2). Figures 2.23a, 2.23c and 2.23e show the monolayer coverage for radial distances Δx from the wafer center for different spin-speeds. No measurements are available for $\Delta x = +40$ mm due to limitations of the microscope x-y table. Figures 2.23b, 2.23d and 2.23f are the corresponding radially averaged percentages of sparse, mono- and double-layers as a function of spin-speed, the sum of which is 100%.

Radial distribution Overall, the bead layer distribution was homogeneous across the wafer surface. Only in case of PSB535 beads deposited at speeds ≥ 1600 rpm, a monolayer coverage decreasing with increasing Δx could be observed, indicated by dashed lines in figure 2.23c. This can be correlated with the oscillatory movement of the drying front when spin-coating PSB535 suspensions at high spin-speeds as follows: The outward directed drying drives beads away from the wafer center. These beads accumulate at the wafer border and are eventually ejected from the wafer, increasingly depleting the bead concentration with increasing Δx . In some cases, a scattered distribution of data points can be observed, e.g. for PSB284 coated at 800 rpm or PSB535 coated at 400 rpm. This can be explained by local defects due to satellite formation during spin-coating and the limited amount of microscope images analyzed. Also, in some cases, the imaged area was on the order of the size of one continuous bead layer region, which explains jumps from 0% to 40-50% monolayer coverage in figure 2.23c for 400 rpm (also c.f. figure A.5 in the appendix).

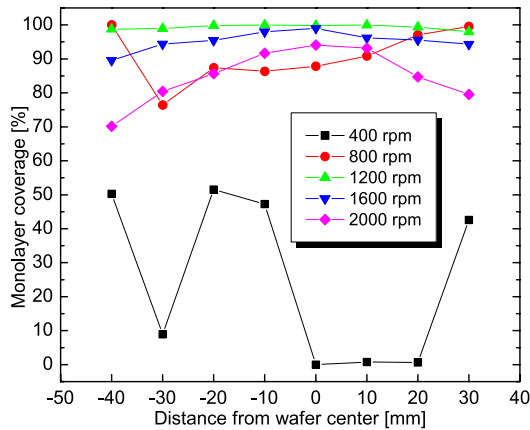
Bead layer types For identical spin-speeds, different bead layers were obtained for different colloidal suspensions (figures 2.23b, 2.23d and 2.23f). A high bead monolayer coverage $> 90\%$ could be obtained for both PSB284 and PSB535 spun at 800 rpm and 1200 rpm, despite their different volume concentration (5%w/v vs. 10%w/v, respectively). Another characteristic similar for PSB284 and PSB535 beads is the transition from mainly multilayers at low spin-speed to increasingly empty areas with no beads at high spin-speeds. These transitions are sharper for PSB284 than for PSB535 suspensions, e.g. at 400 rpm and 800 rpm, PSB284 yielded 100% and then 5% bead multilayers



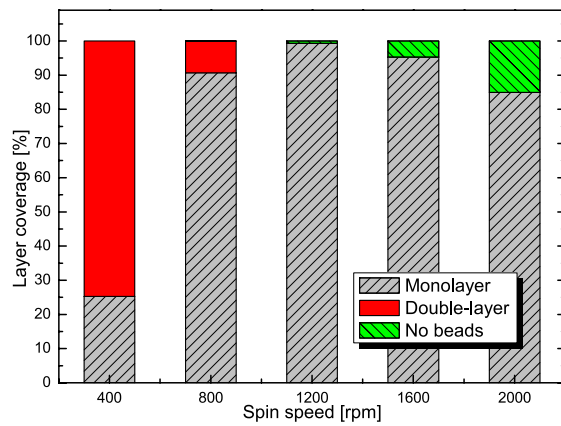
(a) PSB284 5%w/v Monolayers



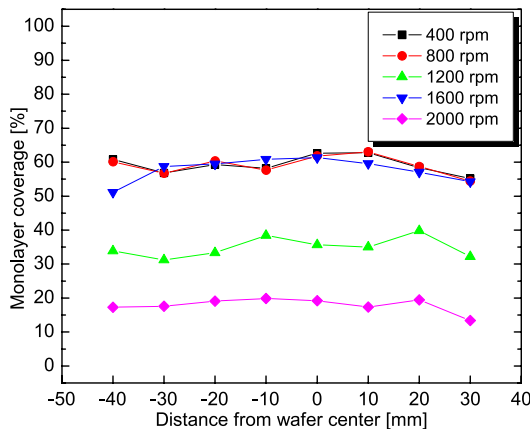
(b) PSB284 spin-speed



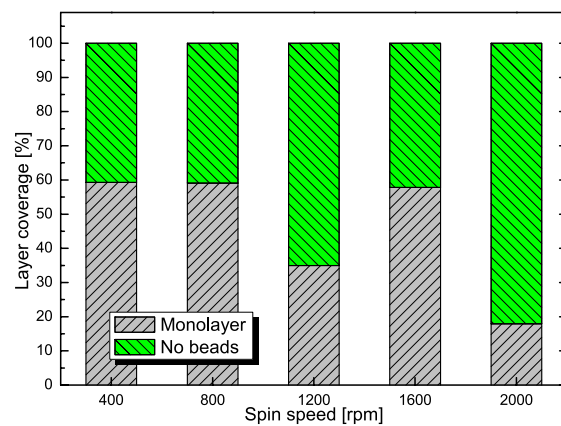
(c) PSB535 10%w/v Monolayers



(d) PSB535 spin-speed



(e) PSB836 10%w/v Monolayers



(f) PSB836 spin-speed

Figure 2.23: PSB284, PSB535 and PSB836 aqueous suspensions spin-coated at different spin-speeds. The left columns shows the radial monolayer distribution for different spin-speeds. The right column shows the wafer-averaged percentage of mono- and double-layers (multilayers) and areas not covered with beads as a function of spin-speed.

with the remaining area covered with bead monolayers, while PSB535 transitioned from 75% to 10% multilayers.

In case of the 10%w/v PSB836 suspensions, the bead layer coverage, parted between bead monolayers and no beads, is almost constant for a wide range of spin-speeds from 400 rpm to 1600 rpm. The low monolayer percentage at 1200 rpm is not in line with the data, which is explained by an experimental error (e.g. wrong spin-speed settings). The monolayer coverage remains $< 60\%$ even at the lowest spin-speed.

Optimization of spin-coating on different substrates by changing spin-speed and suspension concentration

Increasing or decreasing the suspension concentration is to some extent identical to decreasing or increasing the spin-speed²³¹. Thus, both parameters can be tuned in order to optimize spin-coating on different substrates, for different bead sizes or under different temperature and humidity conditions, as long as critical low or high values are not surpassed¹². The inter-dependence of the parameters suspension concentration, spin-speed and substrate are shown with the example of PSB428 beads spin-coated onto O₂-plasma pre-treated Si wafers coated with either 100 nm SiO₂ or 100 nm LS-SiN and onto pyrex wafers.

Variation of suspension concentration and spin-speed Figure 2.24 shows the results obtained by spin-coating PSB428 aqueous suspensions of different concentration and at different spin-speeds onto Si wafers with 100 nm thermal oxide. For clarity, the monolayer distribution as a function of radial position Δx is shown in three different graphs for suspension concentrations of 10%, 8.3% and 7%. Figure 2.24d shows the wafer averaged relative amount of bead mono- and double-layers and areas not covered with beads.

The radial bead layer type distribution was inhomogeneous, unlike the results obtained for PSB284, PSB535 and PSB836 beads. The monolayer ratio varies by up to 40% from the wafer border to its center (figure 2.24a). This radial variation was observed for all suspension concentrations and for mono-/double-layer as well as for mono-layer/no beads coatings; for 7% suspension concentrations coated at 1200 rpm, the radial variation was lowest with $\approx 20\%$. In all cases, the bead density increases towards the wafer center (figure 2.24b). This means that the centrifugal force driving beads to the wafer border is not well balanced with the bead concentration. Non-Newtonian viscous behavior may also cause a shear-flow that is different from the one for PSB284, PSB535 or PSB836 beads and disadvantageous for a homogeneous distribution.

¹²For example, homogenization of the liquid film can not be achieved at very low spin-speeds²¹⁹. The upper limit is set by the spin-coater specifications and the amount of beads affordable to waste when high suspension concentrations are coated at high speeds.

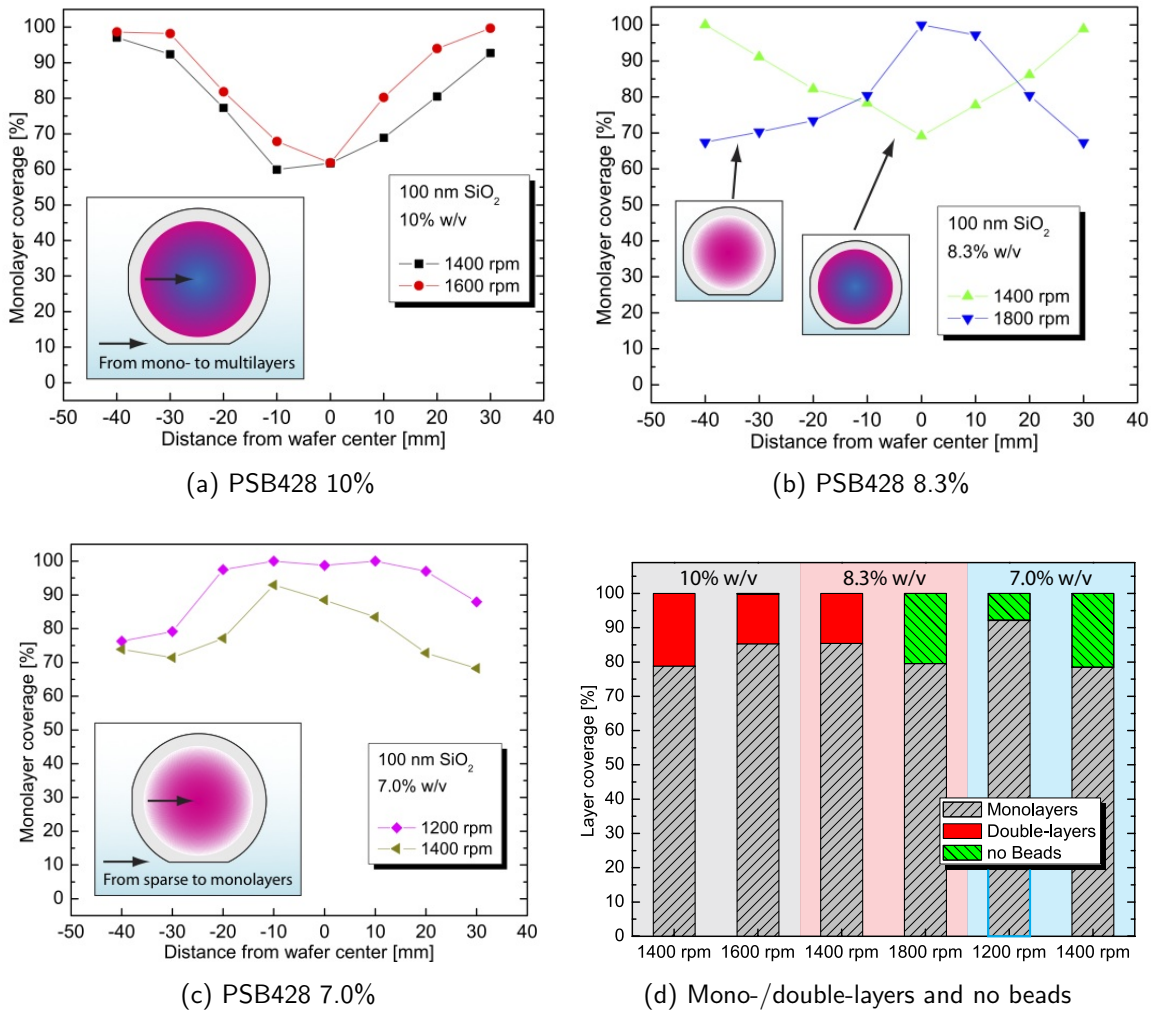


Figure 2.24: PSB428 aqueous suspensions spin-coated onto Si wafers with 100 nm thermal oxide. Both suspension concentration and spin-speeds were varied.

By adapting the suspension concentration, also for PSB428 beads a homogenization of the radial bead layer distribution was achieved (a wafer border to center variation of $\approx 20\%$ in case of the 7% suspension, figure 2.24c).

Spin-coating PSB428 beads from 10% suspensions at 1400 rpm and 1600 rpm produced mono- and double-layers. Reducing the concentration to 8.3% increased the ratio of multi- to double-layers for the same spin-speed (1400 rpm), while empty areas appeared upon an increase of the spin-speed to 1800 rpm. The best monolayer coverage was obtained for spin-coating a 7% concentration suspension at 1200 rpm. The ratio of mono- to double-layers is almost identical for 8.3% and 7% concentration suspensions coated at 1800 rpm and 1400 rpm, respectively, showing that spin-speed and suspension concentration are to some extent interchangeable.

Spin-coating on SiN and Pyrex wafers Si wafers coated with 100 nm LS-SiN and pyrex wafers were spin-coated with PSB428 aqueous suspensions. In case of the LS-SiN wafers, the suspension concentration was kept constant at 8.3% and the spin-speed was varied from 1200 rpm to 1600 rpm. In case of the Pyrex wafers, the spin-speed was not further lowered but kept constant at 1200 rpm. Instead, the suspension concentration was 8.3% and 10%.

The radial monolayer distribution is shown in figures 2.25a and 2.25b for LS-SiN and pyrex wafers, respectively. The monolayer coverage varied in a range of 20% and was thus much less pronounced than in case of the 100 nm SiO₂ coated wafers (c.f. above). Under different conditions, monolayer coverages $> 85\%$ were obtained. The substrate influence manifests itself by significant differences in the bead layer coverages obtained under identical conditions. For example, spin-coating 8.3% suspensions at 1200 rpm yielded a wafer-averaged 80% monolayer coverage on pyrex wafers, while it was close to 90% on LS-SiN wafers. A similar difference is seen by comparing the results obtained on 100 nm SiO₂ wafers and LS-SiN wafers coated from 8.3% suspensions at 1400 rpm (compare figures 2.24d and 2.25c). While the monolayer coverage is in both cases $\approx 80\%$, the remaining area is occupied by double-layers on SiO₂ and empty areas on LS-SiN wafers.

Finally, a linear dependence of the monolayer coverage on spin-speed not observed before was found in case of the the LS-SiN wafers. For this bead and substrate type, this greatly facilitates an optimization of the spin-coating conditions.

Aqueous vs. Triton-X and ethanolic suspensions

The spin-speed influences the centrifugal forces and the liquid evaporation rate, both of which determine the amount of beads present on the wafer at the onset of the drying process. Therefore, instead of increasing the suspension concentration or lowering the spin-speed, water was exchanged for a solvent with a higher vapor pressure. (This is only a valid approach if the colloidal suspension remains stable, at least for the duration

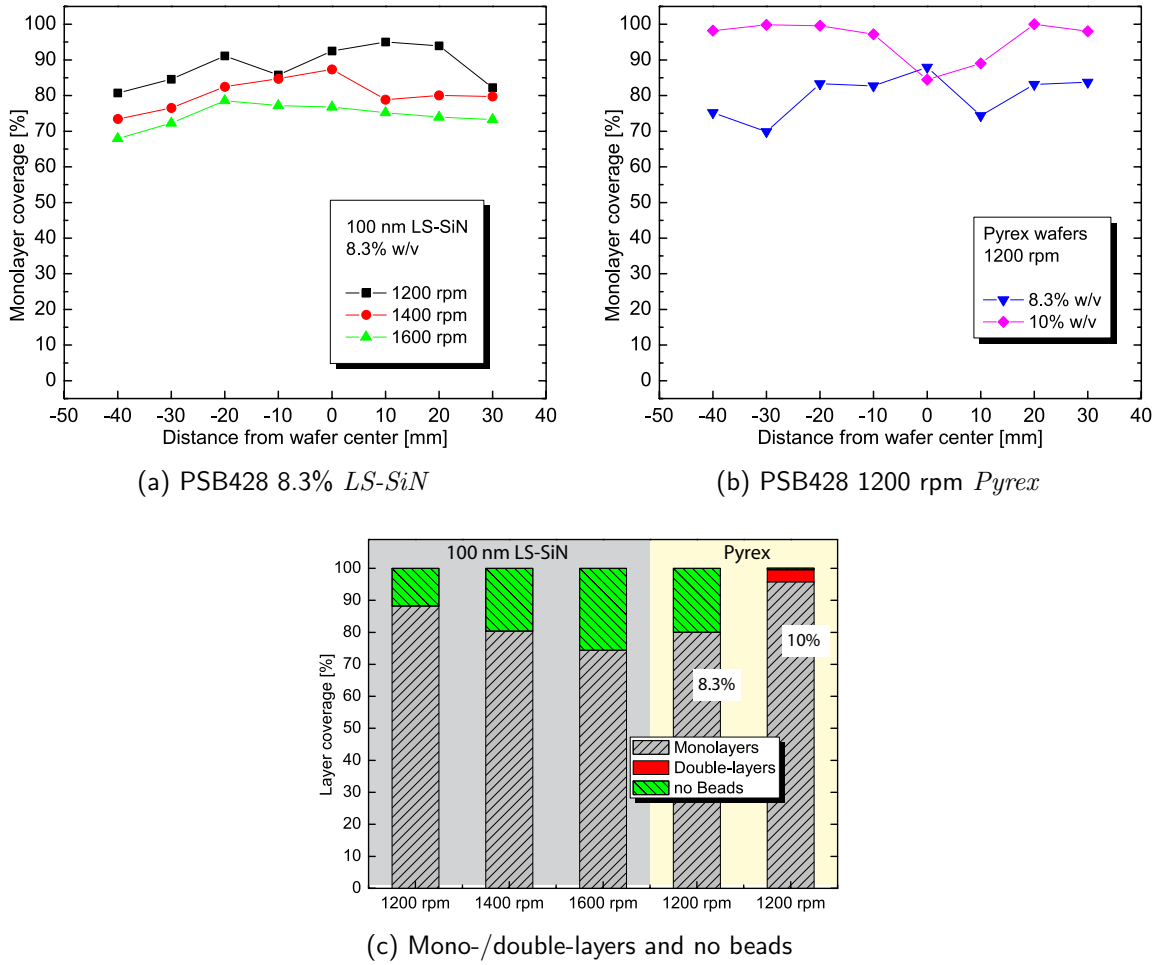


Figure 2.25: PSB428 aqueous suspensions spin-coated onto (a) Si wafers coated with 100 nm LS-SiN and onto (b) Pyrex wafers. In (a) the spin-speed was varied, in (b) the suspension concentration was varied; (c) shows the relative amount of bead mono- and double-layers and areas without beads.

of the experiment.)

PSB836 beads were spin-coated onto hydrophilic pre-treated 100 nm oxide wafers at 400 rpm from 10%w/v suspensions of different solvent compositions: (a) aqueous (c.f. above) (b) 3:7 v/v H₂O:1%Triton-X 100 and (c) 3:7 v/v H₂O:Ethanol. The addition of Triton-X lowers the surface tension and is thus expected to enhance the wetting properties without a major influence on the evaporation rate. The addition of ethanol enhances both the wetting of the wafer surface and the solvent evaporation.

The Triton-X suspension foamed strongly when being agitated, and the wetting of the substrate was slightly enhanced as compared to wetting by aqueous suspensions. Mono- and multilayers were obtained with multilayers increasing towards the wafer center. Thus, the percentage of monolayers decreased from 90% to 34% at $\Delta x = 40$ mm to 0 mm. This radial dependence was not observed in case of aqueous suspensions (figure 2.23e). The higher bead density (mono- and multilayers instead of monolayers and no beads) as well as the radial dependence show that the addition of a large amount of surfactant does influence the viscous flow properties and the bead array formation mechanism. Spin-coating experiments at different spin-speeds with the same H₂O:Triton-X composition are foreseen.

The ethanolic suspension completely wetted the substrate surface. During spinning, an oscillatory movement of the drying front could be observed (c.f. above: PSB535 aqueous suspensions spun at 2000 rpm). The resulting bead layer is dominated by multilayers of ≥ 2 layers. This is explained by the enhanced evaporation rate of ethanol. The domain sizes are smaller as compared to the ones obtained by spin-coating from aqueous or Triton suspensions, which is caused by instabilities of the ethanol evaporation and the lower surface tension as compared to water.

Preliminary conclusions

Close-packed monolayers covering $\geq 90\%$ of the wafer surface were realized on different substrates (100 nm SiO₂ or LS-SiN, Pyrex) by spin-coating aqueous suspensions of PSB284, PSB535 and PSB428 beads and adapting the suspensions concentration and spin-speed. In case of PSB836 suspensions, the monolayer coverage did not exceed 60%. First shot experiments by spin-coating PSB836 Triton-X modified suspensions suggest that lowering the liquid surface tension, and thus obtaining an initially more homogenous bead distribution across the substrate surface, will improve the deposition results. A radially homogeneous monolayer distribution was obtained by fine-tuning the suspension concentration and spin-speed. Different drying behaviors were observed. Radially homogeneous coatings were obtained when the drying front progressively moves inwards from the wafer border to its center (c.f. PSB284 and PSB535 coated on 100 nm

SiO₂). The substrates' dielectric properties considerably influence the wetting of the substrate by the bead suspension^{188,187}, and thus the array formation process. A low receding contact angle favors the formation of well-ordered and radially homogeneous bead layers. Spin-speed and suspension concentration were partially inter-changeable parameters, facilitating an optimization of the spin-coating parameters. All experiments were conducted under standard clean-room conditions; coating of one wafer took less than 2 min. The dispensed volume was kept constant at 900 μ l. For identical substrate types and bead suspensions, the results were reproducible and consistent.

Comments on the chosen spin-coating methodology and suggestions for further improvements

The bead deposition approach taken in this thesis is empiric and the objective of the current work was to use such 2D colloidal crystals as an initial pattern template. For the formation of large-area ($\gg 10$ μ m in domain size) hexagonally close-packed 2D colloidal crystals by means of spin-coating necessitates are more thorough theoretical and experimental investigation of the influence of the bead size, suspension stabilization mechanism (e.g. charge-stabilized or steric), particle-substrate as well as particle-particle interactions, suspension viscous behavior as a function of solvent and bead concentration.

As mentioned in chapter 2.3.3, highly ordered colloidal crystals can be obtained by spin-coating of high viscosity, non-volatile solvent where shear-induced ordering of sterically stabilized particles, treated as hard spheres, plays a crucial role. In particular, this requires a high Peclet number (equation 2.20). Therefore, for applications where good long-range order is needed, spin-coating of particles from non-volatile viscous solvents should rather be used²²².

On the other hand, spin-coating from aqueous suspensions has several advantages, the most obvious one being the complete evaporation of the solvent during the spin-coating process that alleviates a post-deposition process step to remove suspension components in dry state (e.g. either O₂-plasma etching of a polymeric matrix or dissolution of silica beads²²⁴). Secondly, suspensions are relatively easy to manipulate and readily available from various manufacturers. To optimize the ordering and gain a better understanding of the influencing parameters, the spin-coating process can be analyzed with respect to the following parameters: 1) wetting of the substrate and distribution of the colloidal suspension on the substrate surface, 2) progression of the liquid evaporation, 3) liquid film thinning profile, 4) distribution of particles within the bulk suspension and in the vicinity of the wetting film contact line, 5) inter-particle and particle-substrate interactions that favor or inhibit the formation of close-packed arrays, and 6) an analysis of the different competing forces (c.f. page 043302-7 in Zhao et al.²²⁷). For such an analysis, the following theoretical investigations and experiments are appropriate:

- Zhao and Marshall²²⁷ proposed a discrete-element method to model the time-resolved distribution of colloidal particles within the liquid and on the substrate surface during spin-coating. Although the method is limited to the non-evaporative phase of the spin-coating process, it could yield useful insight to obtain the optimum amount and distribution of bead suspension before the onset of the evaporation induced array formation (c.f. 1) above). Furthermore, the influence of particle-substrate interactions on bead mobility, and thus on the formation of highly ordered bead arrays, can be investigated for different substrate and suspension types (c.f. 5) above). A different model should be used to tackle the questions concerning 2), 3), 4), and 6) (c.f. above). To my knowledge, however, models to adequately simulate the spin-coating of *aqueous* colloidal suspensions have not yet been proposed.
- Experimentally, 1), 2), 3) and eventually 4) (using e.g. fluorescent beads) can be analyzed using high speed camera observation with varying illumination settings¹³⁸ and/or laser interferometry²³⁵. Such experiments yield the information necessary to quantify the influence of substrate type, suspension composition, and spin-coating conditions (spin-speed, ambient as well as substrate temperature, ambient humidity) on the progression of the array formation, correlated with the liquid film thinning. Dynamic contact angle measurements with different bead suspensions on different substrate types reveal the liquid film profile at various receding contact line speeds.
- Assessing the influence, lest be the magnitude, of the competing forces (c.f. 6) above) is challenging. Indirect observation methods could be used based on a crude analysis of the obtained particle coatings for e.g. different spin-speeds (varying the centrifugal force), different bead sizes or densities (varying the capillary immersion force, brownian motion, and to which extent beads are subject to centrifugal and gravitational forces), or different colloidal suspension stabilization methods and magnitudes (varying inter-particle and particle-substrate interactions). Priority should be given with respect to the target colloidal crystal and application. For example, in the present case, this means that only polystyrene beads stabilized as provided by the manufacturer should be used.

Despite the complexity of the spin-coating process, a feature that makes it so popular for the uniform deposition of various suspensions and solutions, was evident: Good parameters can be found quickly and spin-coating proves to be a reliable and reproducible coating method.

2.4 Summary and conclusions

Three different bead deposition methods, namely drop-coating convective self-assembly (CSA), CSA controlled with the CAPA-tool (capillary assisted particle assembly), and spin-coating, have been investigated. The goal was to obtain a wafer-scale monolayer coverage. Table 2.4 compares the different methods with respect to the monolayer coverage that could be obtained, deposition time, cost, and complexity of the experimental setup.

Criterion	Drop-coating CSA Section 2.3.1	Controlled CSA Section 2.3.2	Spin-coating Section 2.3.3
Bead layers	Mainly sparse or multi-layers, especially in the center wafer region.	Monolayer deposition locally well controlled.	Mono- and/or multilayers can be deposited.
Monolayer coverage	Poor.	Good within the controlled region.	Up to 90% of the wafer surface. Can vary with radial position on the wafer.
Time	1 hr to 1 day.	Couple of hours for cm-size substrates.	Few minutes.
Cost	Cheap. No bead waste.	Expensive. Requires presence of operator. Bead waste low.	Moderate. Bead waste most important factor.
Experimental setup	Very easy. Good for laboratory conditions.	Rather sophisticated.	Very easy. Compatible with standard clean room equipment.

Table 2.4: Comparison of the employed bead deposition methods.

For all deposition methods, a significant influence of the bead size, solvent composition, substrate type, surface chemistry, and ambient conditions was observed. This means that, for example, for the deposition of different bead sizes or coating of different substrate types, the coating conditions need to be adjusted.

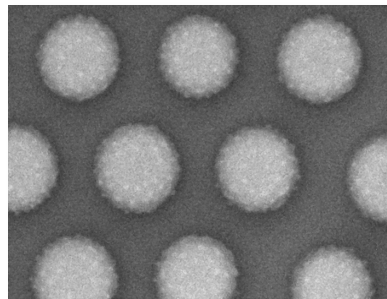
For bead spin-coating, good parameters were found quickly, also owing to the short deposition time itself. By spin-coating, uniform close-packed bead monolayers were realized with a coverage $\geq 90\%$ on a 4" wafer scale. As the final devices targeted in this thesis, based on arrays of sub- μm holes in thin films and membranes, do not require long-range ordering nor precise hole positioning, these criteria can be neglected. Thus, in the remainder of this thesis, bead layer templates were always obtained by spin-coating.

3 Bead size reduction

In this chapter, it will be shown how the size of PS bead can be tuned after deposition of the beads onto the substrate.

In this way, starting from an identical bead template, different dot sizes are obtained without changing the spacing between the dots. Size reduction is done by etching the PS beads in an oxygen plasma. The etch behavior depends on the machine setup and etching conditions. Roughening of the bead surface and bead displacement during the etching process was observed.

First, typical etch conditions and characteristics as reported in the literature are briefly reviewed. Then, the main results on etching PS beads by O₂-RIE are presented and discussed.



3.1 Etching of PS beads in oxygen plasma

PS is a hydrocarbon molecule and thus can be decomposed by reactive oxygen species into CO_2 and water. Depending on the plasma setup and conditions, the etching process may be either isotropic, or have an additional anisotropic etch component. Figure 3.1a schematically shows cross-sections of beads and how they shrink in case of 100% isotropic etching; figure 3.1b shows the 100% anisotropic etching situation. In the following paragraphs, the results reported in the literature will be briefly summarized. Table 3.9 at the end of this section puts in relation these previously reported results with the ones obtained in this thesis.

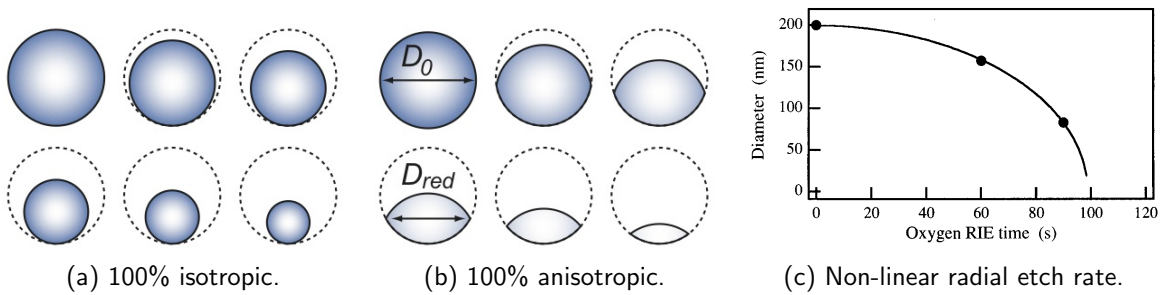


Figure 3.1: (a) and (b) Schematic showing the cross-sectional views of the bead shrinkage under either 100% isotropic or anisotropic etch conditions. (c) Non-linear radial etch rate. Figure reproduced from Haginoya et al.¹⁴⁹.

O_2 -RIE

Haginoya et al.¹⁴⁹ etched PS beads by oxygen reactive ion etching (O_2 -RIE) with a radio-frequency (RF) source. They report a non-linear relationship between the bead diameter d and O_2 -RIE etch time t : $D = D_0 \cos(\arcsin(kt/2D_0))$. Here, D_0 is the initial bead diameter and k is a constant depending on the experimental conditions. This means that the radial etch rate increases with increasing etch time in a non-linear fashion, in this case from 50 nm/min to ca. 150 nm/min. The highest etch rate increase occurs once the bead diameter is less than 50% of its initial diameter (c.f. figure 3.1c).

Other works employing a similar RIE setup report a constant radial etch rate, i.e. a linear relationship between the bead diameter and etch time^{236,165,170}. Minor non-linearities are explained by a preferential exposure of the top part of the beads to the plasma^{165,236} or a gradient in “softness” of the particles²³⁶. In the case of Cheung et al¹⁷⁰, it should be mentioned that for the results shown, their beads are at most reduced to 80% of their initial diameter, which is above the bead size where the non-linearity reported by¹⁴⁹ becomes effective. All works employing O_2 -RIE state an average radial etch rate in the range of 50 to 80 nm/min, despite varying etch gas compositions (O_2 or O_2 with

CF₄), gas flows, chamber pressures (40 mT, 50 mT or 200 mT) and machines used (c.f. table 3.9).

Another common observation is a roughening of the bead surface. Lohmueller et al report it to be increasing linearly with etch time¹⁶⁵. Also, beads exposed to O₂-RIE were found to be difficult to remove from the substrate; bead traces remained on the substrate^{170,165}. The exact origin of these effects remains unclear. It may be related to an inhomogeneous bead stiffness or composition, possibly further enhanced by additional UV radiation induced polymerization during the etch process. Difficult to remove bead traces could be an indication of inorganic compounds which serve for stabilization of the beads in aqueous suspension (e.g. sulfonate groups in this case c.f. figure 2.8). These do not form volatile etch compounds with reactive oxygen species.

UVO

To alleviate the roughening of the PS beads surface during O₂-RIE, Reimhult et al¹⁵¹ etched beads using an ozone cleaner. In this setup, UV light is used to create the oxygen radicals. Beads with a diameter of 200 nm and 100 nm were reduced to less than 50% of their original size without significant roughening of the bead surface. The UVO radial etch rates were linear and on the order of 10 nm/min. Both the low etch rate and the reduced surface roughening are advantageous for the size reduction of small beads with diameters less than 300 nm.

Low temperature ICP-RIE

Plettl et al¹⁵² observed that beads tend to “tip-over” when being etched by anisotropic O₂-RIE. This is attributed to etching induced changes in the viscosity of the PS particles: small polymer chains are created that diffuse into the particle and act as plasticizer²³⁷. Another possible explanation is stress-induced mobility, as reported by Lee and coworkers²³⁸. Furthermore, it was observed that the beads preferentially dislocate towards lattice defects. A locally higher etch rate was excluded as an explanation. According to Plettl et al, it is more likely that induced polarization charges in the beads follow local strong electric field gradients.

They solved these issues by combining an initial room-temperature RIE etch step with further etching at -150°C in an inductively coupled plasma. The initial RIE etch step serves to cut inter-particle polymer connections (also c.f. section 3.2.4). This was followed by an almost perfectly isotropic etch in ICP mode. The ICP plasma was stabilized with a small amount of RIE power, but the self-bias was kept above -8V at all times. At -150°C with an ICP power of 60 W and a chamber pressure of 55 mT, the etch rate was very low with approx. 1 nm/min. However, the beads retained their spherical shape and dislocation of the beads could be avoided.

3.2 Experimental

Here, the results obtained for O₂-RIE size reduction of PS beads are described. As an example, figure 3.2 shows PSB428 etched by O₂-RIE. The spherical beads are transformed into oblate, elliptical particles. This is caused by the anisotropy of the etch process, which was investigated as a function of etch time, RIE self-bias and RIE system used. An increase of the bead surface roughness and dislocations of the PS beads during O₂-RIE was also observed.

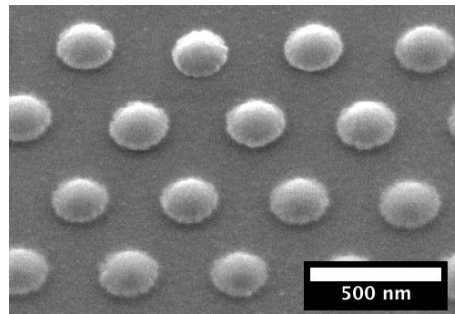


Figure 3.2: 40° tilt SEM image of PSB428 beads etched for 2 min at 50 mT and an oxygen flow of 20 sccm. The RF input power was 80 W, resulting in a self-bias voltage of -400 V. The machine used was *O₂-RIE (B)*.

Two different Oxford Plasmalab 80Plus machines were used, in this text referred to as *O₂-RIE (B)* and *O₂-RIE (N)* (c.f. the etch recipes in A.3).

3.2.1 Anisotropic etch characteristics

O₂-RIE (B)

Figure 3.3 shows etch results obtained for PSB428 and PSB535 beads deposited by spin-coating onto 4" silicon wafers. The chamber pressure was 200 mT at 50 sccm O₂ gas flow; the RIE incident power was 80 W, resulting in a self-bias voltage of -300 V. Four etch runs were done on each wafer by shading 3/4 of the substrate with a dummy silicon wafer, rotating the etch protection by 90°, and performing another etch. The etch times for the quarter wafers were 120 sec / 140 sec / 120 sec / 100 sec and 150 sec / 170 sec / 150 sec / 130 sec for PSB428 and PSB535 wafers, respectively. Thus, the data points at 120 sec and 150 sec are the mean values of two etch runs.

SEM images of beads were taken with a Philips XL30 ESEM-FEG at 10 kV acceleration voltage and a source-substrate distance of 10 mm. The beads had not been coated with a conductive layer. Image analysis was done in two ways, first using the Olympus software analySIS, and secondly by a manual procedure using Gimp and ImageJ. The measured average bead diameter obtained by the two different analysis procedures

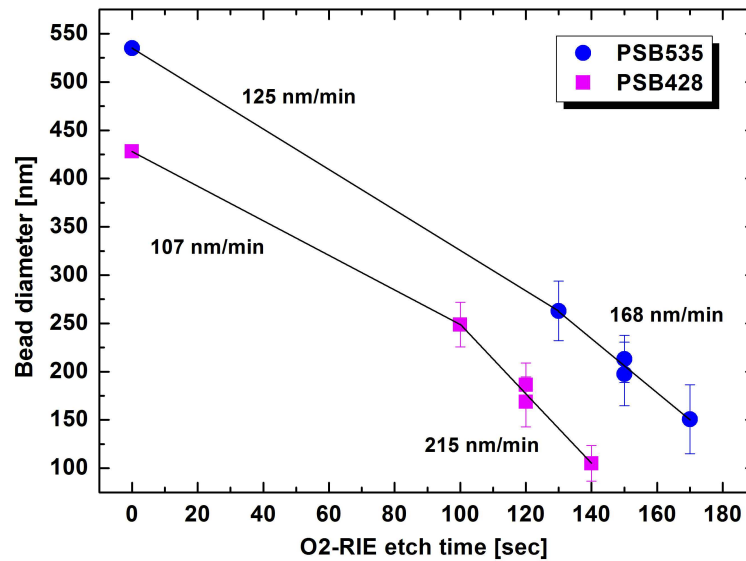


Figure 3.3: Size reduction of PSB428 and PSB535 using O_2 -RIE (B) at 80 W and a resulting self-bias of -300 V. The continuous lines are linear fits within a limited data range, the error bars correspond to 2σ . The corresponding etch rate is indicated in the figure.

differed within a range of ± 10 nm. Thus, in the following, when threshold setting was impossible due to an insufficient contrast between the beads and the silicon substrate, the particle size analysis was done manually.

Figure 3.3 shows that the etch rate is increasing with increasing etch time. Dashed lines in figure 3.3 are linear interpolations for a selected data range. The first range is from the initial bead diameter to the first measured data point which lies at half the initial bead diameter; the second range is over the three following data points. The etch rates increase with increasing etch time from 107 nm/min and 125 nm/min to 215 nm/min and 168 nm/min for PSB428 and PSB535 beads, respectively. This means that the spherical beads are etched anisotropically (c.f. O_2 -RIE 3.1).

O_2 -RIE (N)

Figure 3.4 shows etch results obtained for PSB508 and PSB281 beads deposited by spin-coating onto small silicon chips. The chamber pressure was 200 mT at 50 sccm O_2 gas flow and thus identical to the conditions used in the O_2 -RIE (B) experiments shown above. However, the RIE incident power was 100 W, which resulted in a self-bias voltage of -253 V. Four etch runs were done for each bead size and for each chip separately. The etch times were 60 sec / 90 sec / 120 sec / 180 sec. In this case, the bead diameter measurements were done during image acquisition using the measurement tool of the SEM software.

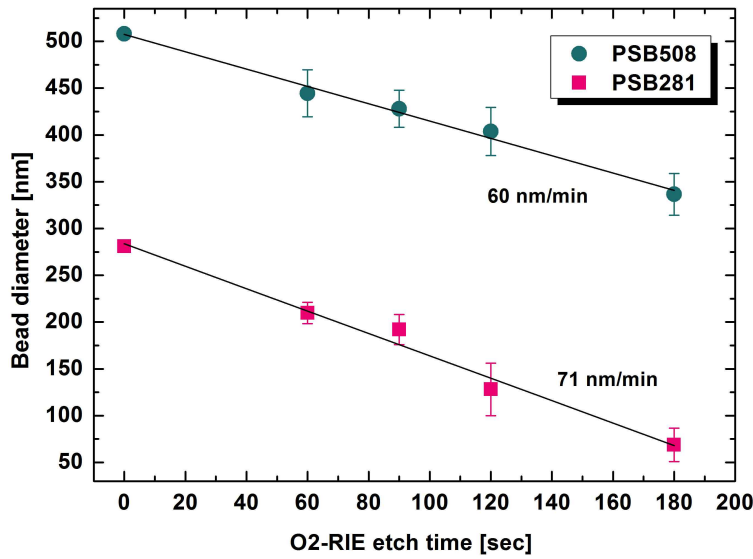
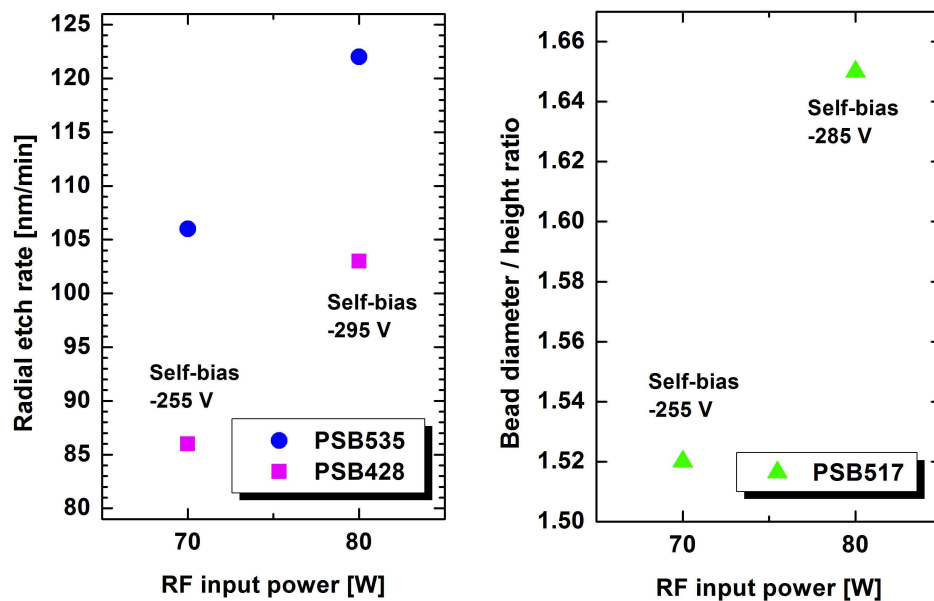


Figure 3.4: Size reduction of PSB508 and PSB281 using O_2 -RIE (N) at 100 W and a resulting self-bias of -253 V. The continuous lines are linear fits over the complete data set, the error bars correspond to 2σ . The corresponding etch rate is indicated in the figure.

Other than in the O_2 -RIE (B) experiments, the etch rate stays constant with increasing etch time, which means that the etch process is less anisotropic. Despite the higher RF input power, the etch rates are considerably lower: 60 nm/min and 71 nm/min for PSB508 and PSB281 beads, respectively. The more isotropic etch behavior and the lower etch rates is due to the lower self-bias voltage. A lower self-bias reduces the physical, anisotropic component relative to the chemical, isotropic etch component. Another factor could be that the machines are differently pre-conditioned, as O_2 -RIE (N) is also used for RIE processes employing etch gases other than O_2 .

Influence of self-bias voltage

The etch results described above show that the self-bias voltage has an important influence on the etch characteristics. This was verified in etch experiments performed with O_2 -RIE (B) using two different RF input power settings, 70 W and 80 W, which induced a self-bias voltage of -255 V and -295 V, respectively. PSB428 and PSB535 beads on silicon chips were etched for 100 sec and 120 sec, respectively. Figure 3.5a shows the radial etch rates as a function of RF input power. At 70 W, the radial etch rates were 86 nm/min and 106 nm/min; at 80 W the etch rates were 103 nm/min and 122 nm/min for PSB428 and PSB535, respectively. This significant increase in etch rate is explained by the lower self-bias voltage (absolute higher value), which augments the physical sputter-etch component of the O_2 -RIE etch process.



(a) PSB428 and PSB535 etch rates as a function of RF input power.

(b) PSB517 diameter/height ratio as a function of RF input power.

Figure 3.5: Dependence of etch rate and anisotropy on RF power and self-bias voltage. Beads etched with O_2 -RIE (B).

Shown in figure 3.5b is a plot of the diameter to height ratio as a function of RF input power. PSB517 beads on small silicon chips were etched for 125 sec at 80 W and for 130 sec at 70 W. Top-view and cross-sectional SEM images were taken with a LEO Zeiss SEM at 3 kV electron acceleration voltage and a working distance of 4 mm. The diameter to height ratios were measured to be 1.52 and 1.65 for etching at 70 W (-255 V self-bias) and at 80 W (-285 V self-bias), respectively. This is a further manifestation that a lower self-bias increases the anisotropic, physical etch component.

Reproducibility

Reproducible radial etch rates could not always be obtained. This is related to the variation of the self-bias voltage with the machines used in this thesis. The self-bias varied ± 10 V for identical RF power and pressure settings. It was observed that the resulting self-bias is sensitive to the pre-conditioning and prior type of use of the machine, requiring conditioning runs to obtain reproducible etch rates. Another factor is the loading factor, i.e. how much polymeric material is etched and thus how many reactive species are consumed. For example, this needs to be considered when changing from chip-size to wafer-scale substrates.

3.2.2 Bead surface roughening

Roughening of the bead surface during O_2 -RIE has been reported before¹⁶⁵. Similar observations were made in this thesis. An example is shown in figure 3.6, which shows PSB428 beads etched for different etch times. The etch conditions are indicated in the figure caption. For better contrast of the SEM images, the samples were coated with a few nm of gold prior to SEM imaging. After 100 sec of etching, the particles have lost their spherical shape. The crumbly residues kept a constant shape and did not disappear from the surface if the etching continued for ≥ 60 sec. This means that these residues are of inorganic nature and stem from the bead synthesis process (c.f. 2.3).

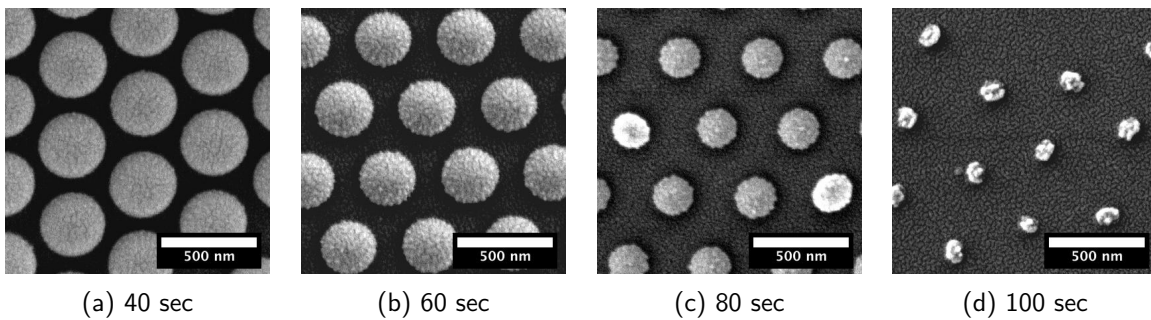


Figure 3.6: The bead surface roughness is increasing with increasing etch time. PSB428 beads were etched with O_2 -RIE (*B*) at 200 mT O_2 at 50 sccm flow, 80 W, and a resulting self-bias voltage of -300 V.

3.2.3 Bead dislocation

Plettl et al.¹⁵² observed a preferential tilting of beads away from domain boundaries. The beads tilt if they give way to external forces, or due to plasma induced changes of their properties, such as viscosity changes or local stress-gradients. External forces, such as electric field gradients, are responsible for preferential tilt directions, while changes in the beads material properties cause random dislocations.

In the present case, both random and preferential dislocations were observed. Figure 3.7a shows an SEM image of PSB535 beads after etching for 120 sec in O_2 RIE (*N*) at 200 mT with 50 sccm oxygen gas flow and an RF input power of 100 W, resulting in a self-bias of -260 V. During SEM imaging, selected beads preferentially located at line defects of the bead array charged. They are encircled in figure 3.7a. The bead charging is explained by a reduced contact to the silicon substrate. An actual dislocation can be seen in in figures 3.7b and 3.7c. They are different SEM images of beads shown in figure 3.6c. Preferential dislocations can be identified in figure 3.7b, while a random tilt of beads is indicated by the arrows in figure 3.7c.

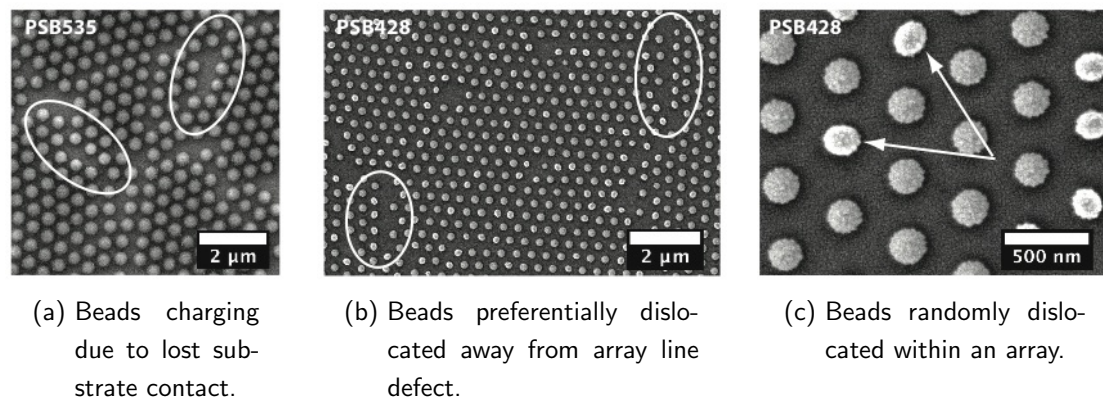


Figure 3.7: Beads tilting in random or preferential directions when etched by O_2 -RIE. (a) shows beads charging in the SEM due to lost contact to the silicon substrate. (b) and (c) Beads tilt both in preferential and random directions.

3.2.4 Cutting polymeric links between beads

The results from the paragraphs above show that O_2 -RIE for size reduction has limitations due to a non-linear radial etch rate, bead surface roughening and dislocation of beads. However, a strong bridging was found for the PSB535 charge obtained from *microparticles GmbH*. In that case, directional etching shows its usefulness to break polymer bridges connecting neighboring particles.

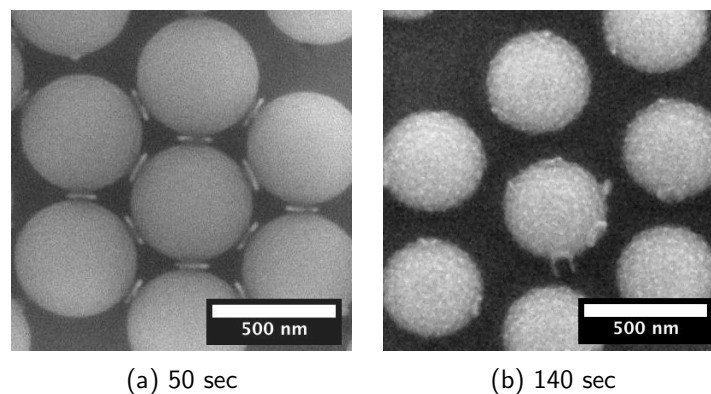


Figure 3.8: PSB535 beads etched in O_2 -RIE (N) at 200 mT with 50 sccm oxygen gas flow and an RF input power of 100 W, resulting in a self-bias of -244 V.

Figure 3.8 shows SEM images of PSB535 beads etched for a 50 sec and 140 sec. After 50 sec of etching, the particles are bridged. Continuing the etching process breaks these bridges. These initial bridges need to be broken at an early stage of the bead size reduction process. Otherwise, beads are dislocated, being pulled towards each other as some links will be cut earlier than others.

3.3 Summary and conclusions

PS beads were etched by O₂-RIE after bead deposition. In this way, the bead size was reduced in a controlled way down to 0.3× the original bead diameter. The obtained results are in accordance with results previously reported in the literature, as summarized in table 3.9.

The influence of different plasma conditions on the bead shrinkage process was investigated. A low self-bias voltage leads to an anisotropic etching, and consequently a non-linear radial etch rate. The etch process can be tuned to be more isotropic by increasing the self-bias voltage. The self-bias voltage depends on the RF input power settings, but also on the machine configuration and pre-conditioning of the machine.

Morphological changes of the beads such as a roughening of the bead surface or bead dislocations were observed. Due to non-linearly increasing radial etch rates and roughening of the bead surface, the reduced bead size is limited to ca. 30% of the initial bead size. In some cases, the formation of inter-particle polymeric links was observed. There, the directional sputter-etch component of an RIE system is necessary to make sure these links are cut at the very beginning of the size reduction process¹⁵².

Previous works have shown that substrate temperature¹⁵², electric field gradients¹⁵² and the type of oxygen reactive species¹⁵¹ play an important role during size reduction of polystyrene beads by plasma etching. In addition, as found in this work, the etch behavior is not identical for beads from different delivery charges. This is explained by minor differences in polymerization state and surface groups that are also affected by UV irradiation²³⁹ and reaction with the oxygen reactive species²⁴⁰, respectively.

The above partially illustrates the actual complexity of the bead size reduction process that deserved a more thorough investigation. This is out of the scope of the current thesis work. Nevertheless, a few indication shall be mentioned that could lead to a better understanding of the PS bead O₂-plasma etching process:

First of all, size reduction experiments, correlated with a detailed chemical analysis (e.g. ζ-potential measurements, X-ray photoelectron spectroscopy), need to be conducted. Information on the influence of the substrate temperature on the etch behavior could be accelerated by placing PS beads on membranes with different sizes (and thus different membrane-to-bulk heat transfer coefficients). Heat measurements with integrated thermo-resistive sensors could provide experimental information on the membrane temperature. A theoretical anticipation of the heat generated during the etch process is challenging due to the different possible decomposition pathways²³⁹.

UV induced cross-linking during etching can be avoided by separating the plasma source from the etching chamber, e.g. using an ICP-RIE setup with a long diffusion cylinder. In an alternative approach, the etch behavior of only partially cross-linked PS

beads (that are commercially available) could be compared to those of 100% cross-linked PS beads²⁴¹.

Reference	Plasma setup	Gas flow [sccm]	Chamber pressure [mT]	Incident RF power [W]	Self-bias voltage [V]	Radial etch rate [nm/min]	Radial etch rate	Bead surface roughening ?
Haginoya 1997	RIE	N.A.	40	80 W*	N.A.	50 to 150	Non-linear	Yes
Hanarp 2003	PlasmaTharm Batchtop VII RIE/PE	N.A.	250	50	N.A.	75	Approx. linear	N.A.
Cheung 2006	Parallel plate RIE	O2: 200 CF4: 8.4	200	100	N.A.	60	Linear	Yes
Reimhult 2007	UVO	--	atm.	--	--	20	Linear	No
Lohmüller 2008	Oxford plasmalab 80 plus RIE	O2 : 30 Ar : 10	50	50	-150	60	Linear	Yes
Plettl 2009	Oxford Plasmalab 80Plus RIE-ICP	15	55	60 W (ICP) 1 W (RIE)	> -8	1	Linear	No
In this work	<i>O₂-RIE (B)</i>	50	200	100	-285 to -300	PSB428 : 110 to 225 PSB535 : 130 to 190	Non-linear	Yes
	<i>O₂-RIE (N)</i>	50	200	80	-250 to -260	PSB428 : 61 PSB535 : 76	Linear	Yes

* 160 mW/cm² → 80 W for a round electrode with a diameter of 20 cm.

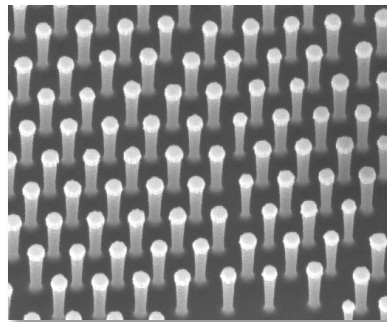
Figure 3.9: Comparison of oxygen plasma etching of PS beads. Top row data extracted from [149,236,170,151,165,152](#).

4 Bead pattern transfer

In this chapter, two process options of nanosphere lithography (NSL), to generate either a “hole” or a “dot” pattern, are described.

The processes will be briefly outlined in the first section. The experimental results for both pattern transfer options are shown in the second part. The related process issues and limitations will be discussed.

In the third section, the combination of wafer-scale nanosphere with UV lithography for micro-patterning of the nanostructures is shown.



4.1 Nanosphere lithography

In the introduction 1.2.2, the principles of nanosphere lithography have been outlined briefly. In this work, size-reduced PS beads were used either as a lift-off template or as an etch mask for a pattern transfer by dry-etching as shown in figure 4.1. Using the *lift-off* routine, a thin holey metal layer is fabricated on top of a silicon substrate. Using the *etching* routine, an array of silicon oxide dots is produced.

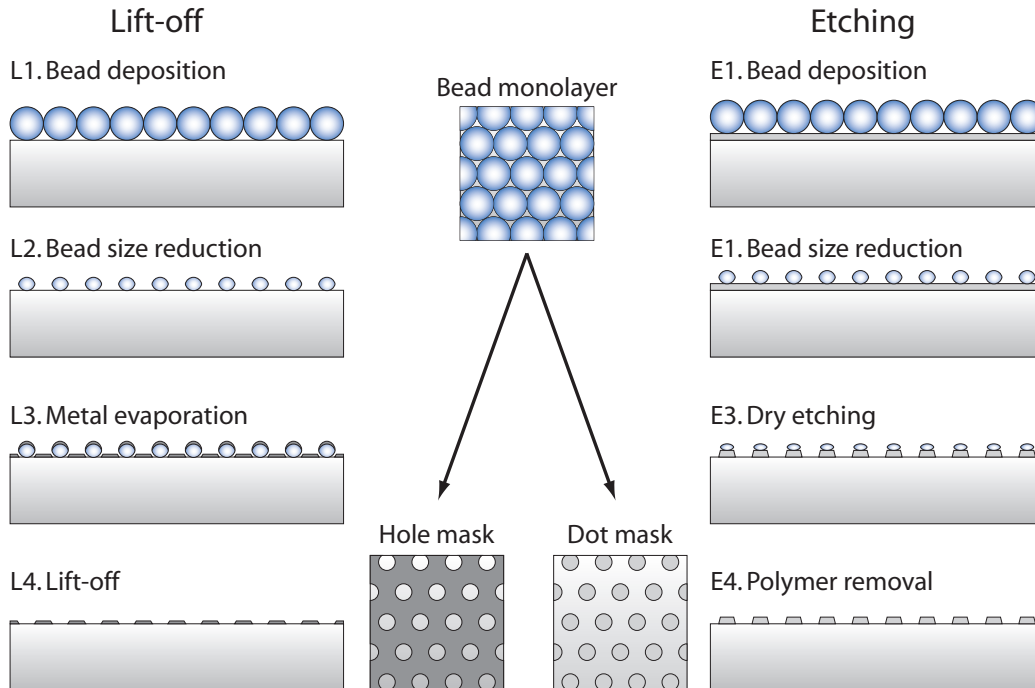


Figure 4.1: Schematic of nanosphere lithography. The beads are either used as lift-off template or etch mask, respectively resulting in a hole or dot mask on the substrate. Explanations in the text.

In both cases, the first two bead processing steps are identical: a layer of beads is deposited onto the substrate. Then, optionally, the bead size is reduced to the desired diameter. To obtain a holey metal layer, metal is evaporated directionally onto the beads. Lift-off is done by removing the beads, for example by sonication of the wafer in organic solvents. This produces a thin metal film with an array of holes on the silicon substrate. To obtain an array of dots, e.g. in a thin silicon oxide layer, the beads are used as a mask in a dry-etch procedure. Removal of the beads after dry-etching is optional and depends on the subsequent process steps, if any.

The patterned material layer, a hole mask as obtained by the *lift-off* routine or a dot mask as obtained by the *etching* routine, can be used as a functional device layer. This is appropriate if only thin layers with low aspect-ratio are needed. If high aspect-ratio

structures are needed, NSL in its simplest form faces limitations.

In case of the *lift-off* routine, the thickness of the metal film is limited by the cross-sectional bead dimensions. Under optimum conditions (high source-substrate evaporation distance, low pressure), lift-off can be performed for metal film thicknesses $t_m \leq 0.2D_{red}$, where D_{red} is the reduced bead diameter. Typical evaporated film thicknesses are usually lower^{133,134,156}. The characteristics of the *lift-off* routine are discussed in more detail in section 4.2.1.

In the *etching* routine, the PS bead template is used as a dot mask directly. The etch rate selectivity between the polymeric dot mask and the inorganic material to be etched can be rather good in chemically driven dry-etch processes. This is for example the case in silicon dry-etch processes based on a SF₆ chemistry¹⁷⁰.

In this case, however, the bead shading cross-section of the beads which turns from spherical to elliptical after O₂-RIE size-reduction needs to be considered. This causes early mask failure at the bead edge (section 4.2.2), which makes it difficult to obtain high aspect ratio pillars with a well-controlled and smooth side-wall shape.

The use of an intermediate mask is an alternative approach. This can be either a holey metal film produced by NSL *lift-off*, or a dot array produced in a thin oxide layer by NSL *etching*. The advantage is that the inorganic intermediate masking layer has a homogeneous thickness and a higher etch-rate selectivity to the substrate material (depending on the substrate material and etch process used). In this thesis, such an intermediate masking layer was used for the etching of holes into thin metal films and for the etching of high aspect-ratio silicon pillars with controlled side-wall shape (c.f. chapter 5).

4.2 Experimental

4.2.1 Holey thin metal films by NSL *lift-off*

Optimum lift-off results

Figure 4.2 shows low and high magnification SEM images of a chromium thin film patterned by NSL using the *lift-off* routine (c.f. figure 4.1). 4" silicon wafers with a 100 nm thick silicon nitride film served as substrates. PSB428 beads were deposited by spin-coating; afterwards the size of the beads was reduced in by O₂-RIE as described in chapter 3 (O₂-RIE conditions: 80 W at 200 mT O₂ for 1 min 5 sec, self-bias voltage -300V). The diameter of the beads after size-reduction was 260 nm, the bead rim height h_{rim} can be estimated to be ca. 110 nm based on cross-sectional SEM images of beads after size-reduction. After bead size reduction, a 15 nm thick Cr film was evaporated directionally onto the wafers. Lift-off was performed by sonicating the wafers for 1 min

each in THF, acetone, and isopropanol, followed by a thorough rinse with flowing Di-water. The wafers were left for drying under a flow hood.

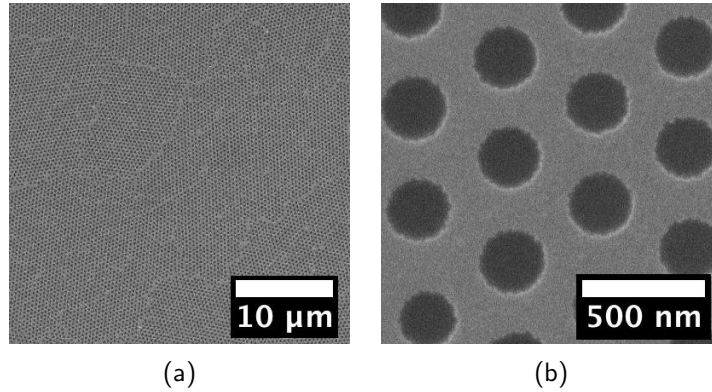


Figure 4.2: SEM images of a holey metal film produced by NSL *lift-off*. All beads and metallic bead caps were removed from the substrate, the hole shape is perfectly circular.

The low magnification image in figure 4.2a shows that a 100% lift-off yield can be obtained over a large area. All beads have been removed, leaving behind a hole in the thin metal film. Figure 4.2b shows that the round shading cross-section of the beads has been perfectly copied into the metal film. The edges of the circular holes in the mask pattern are smooth without any indication of ripped-off metal film. This result shows that metal films much thinner than the bead rim height h_{rim} can be easily patterned by NSL.

Lift-off limitations

Using O_2 -RIE size reduced PS beads as a lift-off template is subject to two main limitations: (a) The evaporated metal film thickness should not exceed $\approx 0.66 h_{rim}$, even if a highly directional evaporation process is used, and (b) room-temperature O_2 -RIE can induced tilting of the beads and thus produce elliptical holes in the metal mask (section 3.2.3). These two limitations are illustrated in figure 4.3.

Note that $0.66 h_{rim}$ translates into $\approx 0.2D_{red}$ for beads reduced to about half their initial diameter under anisotropic etch conditions.

In case (a), deposition of the metal under a small angle, e.g. due to a small misalignment of the substrate relative to the evaporation source, or local thickness variations due to columnar grain growth, may result in closing of the gap between the metal on top of the bead and the metal on the substrate. This will make a lift-off impossible (if not mechanically induced by e.g. rubbing the wafer surface), which is shown in the left-hand side SEM images in figure 4.3. The images were taken after the lift-off procedure. The

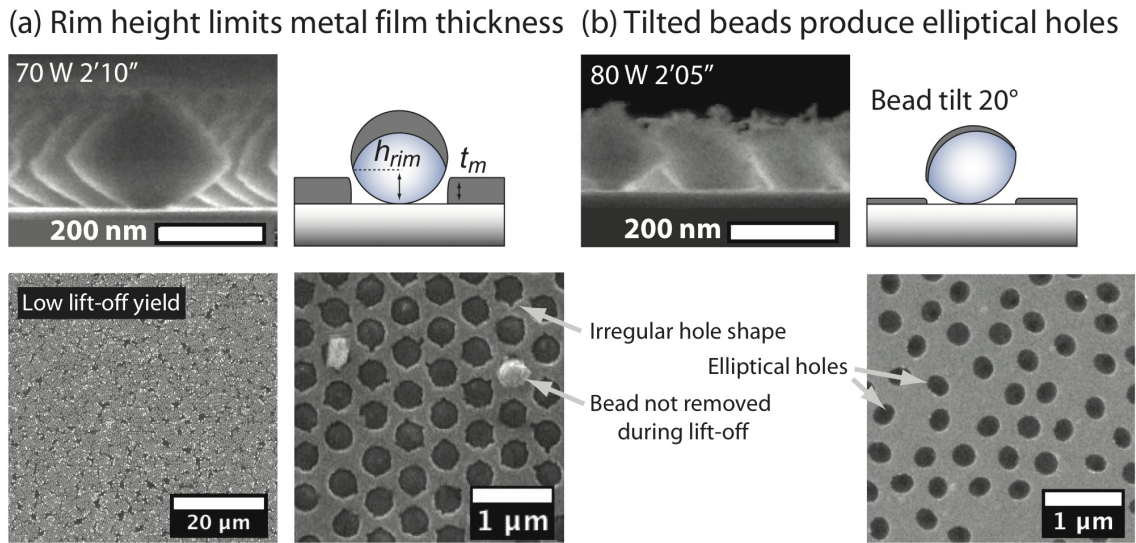


Figure 4.3: (a) Using beads as a lift-off template, the metal film thickness t_m for which a successful lift-off can be achieved is limited by the rim height h_{rim} . In the example shown, h_{rim} and t_m are both 100 nm. (b) Tilting of the beads induced by O_2 -RIE size reduction results in elliptical hole shapes after lift-off. In this example, $t_m = 15$ nm and thus much lower than $h_{rim} = 70$ nm. Cross-sectional SEM images were taken prior to metal evaporation. Top-view SEM images were taken after the lift-off procedure.

rim height h_{rim} and the evaporated metal film thickness t_m both were 100 nm. The low magnification SEM images shows many white speckles, which represent beads that still adhere to the surface after lift-off; the lift-off yield is low. The high magnification SEM image shows a zoom into one of those bead still attached to the surface. The irregular hole shape is due to roughening of the bead surface during O_2 -RIE (section 3.2.4). In case (b) (right-hand side images in figure 4.3), the beads tilted during O_2 -RIE. This results in elliptical hole shapes after lift-off. The lift-off yield was still successful because t_m was chosen much lower than h_{rim} (15 nm and 70 nm, respectively). Tilting of the beads is another factor that limits the metal film thickness as, on one side, the bead edge will be closer to the substrate surface than the nominal h_{rim} .

While the film thickness limitation by h_{rim} is inherent to the lift-off process, a bead dislocation could be avoided by using a different bead size reduction procedure (c.f. section 3.1).

4.2.2 Si pillars by NSL etching

In the above section, the bead pattern was used as a lift-off template to create holes in thin metal films. The inverse structure - dots or pillars - can be obtained by using the

beads as an etch mask instead (c.f. figure 4.1). Using only beads as etch mask limits the control over the Si pillar sidewall shape and the attainable aspect-ratio (height/width). Thus an intermediate oxide layer is introduced. In this way, Si pillars with an aspect-ratio $> 3:1$ and controlled sidewall shape were realized by Si deep reactive ion etching (Si-DRIE).

Beads as etch mask

Example Si pillar arrays using PSB535 beads as an etch mask in Si-DRIE are shown in figure 4.4. A continuous silicon etch procedure was used based on a SF_6 chemistry. The beads have not been removed after Si-DRIE. This kind of procedure has a very good etch rate selectivity to polymeric masking materials; it is usually better than 10:1. The pillars in figure 4.4a and figure 4.4b are 600 nm and 800 nm high, respectively;

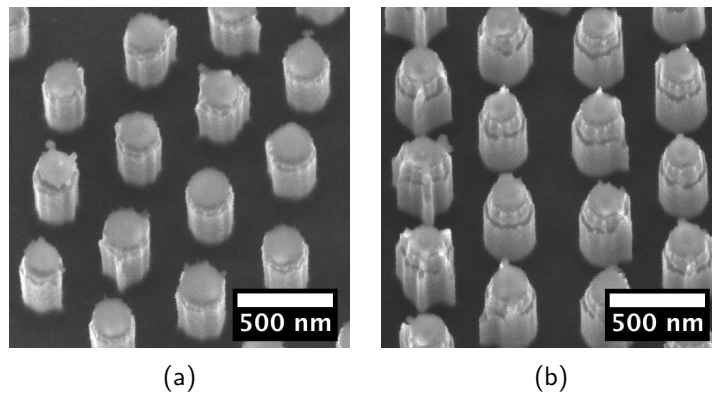


Figure 4.4: SEM images of silicon pillars etched using size-reduced PS beads as a polymeric etch mask. The aspect ratio of the structures is limited by finite etch selectivity and elliptical bead shape.

they were obtained with the same bead etch mask by partially shading the wafer during Si-DRIE. The etch gas ratio was different in the two cases, thus the different resulting pillar diameter. This does not obscure the main observation that the bead mask fails after attaining a pillar aspect ratio of approximately 1:3. Mask failure starts at the border of the circular shading cross-section because this is where the mask thickness is lowest. The onset of the bead mask failure is already visible in figure 4.4a. The resulting terraced pillar shape becomes obvious after continued etching (figure 4.4b). It is undesirable where high aspect ratio pillars with a controlled sidewall shape are needed.

Intermediate silicon oxide etch mask

Fabrication of the intermediate oxide dot mask

The oxide dot mask is fabricated using the beads as an etch mask during SiO₂-RIE with C₄F₈ chemistry. This process step is shown in figure 4.1. Figure 4.5 shows PSB428 and PSB517 beads after size reduction and the corresponding resulting dot mask after etching of 100 nm of silicon oxide. Indicated in the figure caption are the mean bead and oxide dot diameters. While the size of the PSB517 beads is well retained in the oxide mask, a loss in dimension of 20 nm in diameter can be observed in case of the PSB428 beads. There are two possible reasons: First, the reduced diameter of the PSB428 beads is less than $\frac{1}{2}$ the original bead diameter. At this size, the particles have become oblate due to the anisotropy of the O₂-RIE bead size reduction. The PSB517 are still relatively “thicker” as their reduced diameter is still above half the original bead diameter.

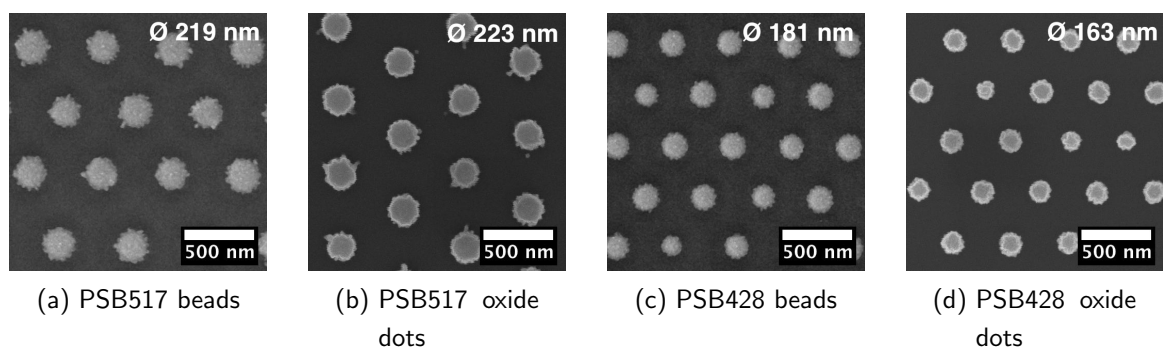


Figure 4.5: Size comparison between the diameter of the PS bead template and the diameter of the oxide dots obtained by SiO₂-RIE into 200 nm silicon oxide. (a,b) shows the results for PSB535 beads, (c,d) the ones for PSB428 beads.

Secondly, although the etch rate selectivity of polymeric masking material to silicon oxide is at most 2:1, 200 nm thick oxide was patterned without major loss in dimensions for reduced bead sizes larger than approximately $\frac{1}{2}$ the original bead diameter and with a bead thickness of less than 200 nm. This can be explained by a softening of the PS beads when the temperature rises above the melting temperature (100°), re-flowing on the substrate, and thus a redistribution of the polymer from the center of the bead to the border. Such a deformation of beads was observed by SEM imaging of pillars after Si-DRIE, prior to stripping of the beads in organic solvents or O₂-plasma. Temperature anneal experiments had revealed that such a reflow occurs only for beads that are still relatively large. This is the second reason why the loss in dimension occurs for beads smaller than $\frac{1}{2}$ the original bead diameter.

Etching of high aspect-ratio silicon pillars

Using the silicon oxide dots as an etch mask, high aspect ratio pillars were fabricated. Figure 4.6 shows several schematics that explain the terminology used to describe etch profiles.

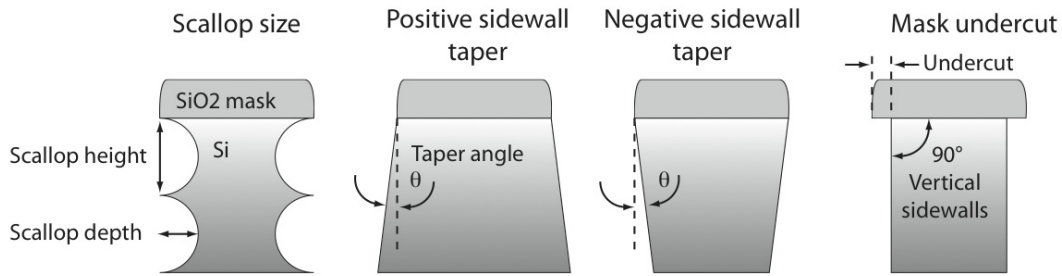


Figure 4.6: Schematic etch profiles with corresponding terminology.

A well-known process for the etching of high aspect-ratio silicon structures is the Bosch-process^{1,218,242}. With a selectivity greater than 70:1, it has an extremely high etch rate selectivity for silicon oxide as a masking material. In a Bosch-type process, an isotropic etch cycle is followed by a passivation cycle. This results in a scalloped sidewall profile. A reduction of the etch cycle time will reduce both the lateral as well as the vertical etch depth; the scallop dimensions can thus be reduced. However, depending on the machine condition and pillar density on the wafer, significant variations of the scallop size were observed. The variations could also happen within one continuous etch run, possibly related to thermal variations (e.g. loss of vacuum clamping of the wafer to the substrate), or simply instabilities in the fast switching gas flow. Such an

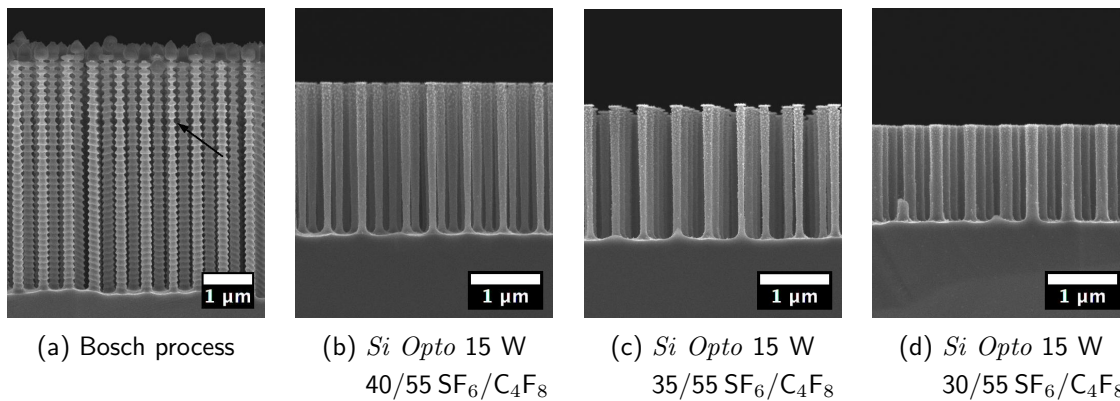


Figure 4.7: Silicon pillars etched by a Bosch-type process and by the continuous etch process *Si Opto*. In case of *Si Opto*, the etch rate and mask undercut was investigated as a function of SF_6 gas flow.

example is shown in figure 4.7a, obtained using the ICP-RIE AMS200 DSE system. The $\text{SF}_6/\text{CH}_4/\text{O}_2$ gas flows and cycle conditions were 300 sccm/200 sccm/100 sccm for 2.5 sec/2 sec/1 sec. The chamber pressure was flow-controlled with a constant butterfly valve setting and varied from 2×10^{-2} to 9×10^{-3} mbar. The ICP power was constant at 1500 W, with a low-frequency RIE pulsation only during the SF_6 etch cycle. The chuck

temperature was controlled at 0°C. As etch mask, 100 nm thick silicon oxide dots with a diameter of 210 nm in diameter were used. The etching was performed continuously for 4 min, during which the scallop size varies. The change in scallop shape at the top of the pillars is explained by a non-zero etch rate of the sidewall passivation layer at the top, thus smoothing out the scallop shape with increasing etch time. However, the scallop size variations as indicated by the arrow can not be explained other than by uncontrolled gas or wafer temperature fluctuations. Due to such fluctuations, it was regularly observed that silicon pillars with an aspect ratio > 10 and a diameter < 200 nm were “cut-off” at some point during the etching process.

For this reason and for a better control of the sidewall slope angle, a continuous etch procedure was used. The etch rate selectivity Si:SiO₂, and thus the attainable aspect-ratio, is then reduced to 20:1. This remains a sufficient aspect-ratio for the target applications. The continuous etch process *Si Opto* is tuned for the etching of high aspect ratio structures in silicon with vertical sidewalls and small mask undercut.¹ SF₆ and C₄F₈ are used as etch gases. Fluorine radicals provide the chemical etch component, reacting with silicon to SiF. C₄F₈ decomposes into carbon and fluorine radicals, thus providing both an etch and a passivation component thanks to the in-situ deposition of thin fluorocarbon polymer film. The plasma is generated by an ICP-RIE system with low frequency pulsation. The ICP input power determines the plasma density. The chuck coupled RIE power stabilizes the system and allows to tune the self-bias voltage independently from the plasma density. A certain self-bias voltage is needed to preferentially remove the passivation layer at the bottom of the etched silicon surface by ion impact. Thus, tuning the process involves balancing of the etch gas ratio, flow, and ICP and RIE input powers²⁴².

Figures 4.7b, 4.7c and 4.7d show typical etch results using the same oxide dot mask as in figure 4.7a. The ICP and RIE input powers were 1500 W and 15 W, respectively. The SF₆/C₄F₈ gas flows were varied from 40 sccm/55 sccm to 30 sccm/55 sccm as indicated in the figure captions. The chamber pressure was stabilized at 3×10^{-3} mbar. All samples were etched continuously for 4 min. The etch rate decreases from 545 nm/min to 345 nm/min. While the pillar sidewall shape is vertical in all cases, the mask undercut is reduced from 40 nm to 20 nm with decreasing SF₆ gas flow. This is because the passivation component related to the C₄F₈ gas is relatively increased. This shows how the mask undercut can be controlled by changing the etch gas ratio. A minimum mask undercut can not be avoided as the silicon oxide dot mask fabricated by the NSL *lift-off* routine produces dot patterns with an irregular border shape and slightly slanted sidewalls. On the other hand, by using a higher SF₆ flow, the pillar diameter can be reduced. This is an option for tuning of the pillar dimensions without the necessity to

¹The process had been optimized by the staff of the Center for Micronanotechnology (CMI) at EPFL.

change the oxide dot mask dimensions.

Figure 4.8 shows *Si Opto* etch results that show how the pillar sidewall taper can be tuned from negative (undercut) to positive (broadening towards the pillar base). Again, 100 nm thick silicon oxide dots were used as a mask pattern; all samples were etched for 3 min. The dot diameter was 215 nm in this case. The conical toppings on top of the pillars are remains of the PS bead mask that was not totally removed after etching of the silicon oxide dot mask. The ICP input power was 1500 W. The RIE input power was 30 W instead of 15 W. This increases the physical etch component, thus reducing the Si:SiO₂ etch rate selectivity, consequently inducing an earlier mask failure.

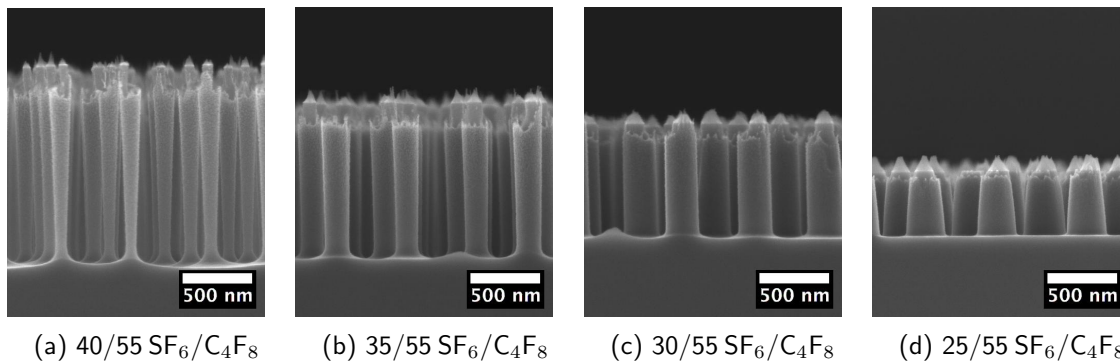


Figure 4.8: The silicon pillar sidewall shape is controlled by changing the gas flow ratios SF₆/C₄F₈ of the etch process *Si Opto*. The ICP input power was 30 W.

The etch gas ratio was changed, this time from 40 sccm/55 sccm SF₆/C₄F₈ to a SF₆ flow as low as 25 sccm. This has a major influence on the pillar sidewall shape: it is changed from negative for a high SF₆ ratio to a positive sidewall slope for the lowest SF₆ gas ratio. Simultaneously, as in the above case, the etch rate decreases with decreasing SF₆ gas ratio: from 470 nm/min to 160 nm/min. This is in accordance with the observations above that a lower SF₆ gas ratio reduces the etch rate.

4.2.3 Micro-patterning of holes and dots/pillars

For the integration of the sub- μm structures into functional devices, they need to be placed within specific areas on the wafer substrate. Commonly, top-down nanopatterning methods such as electron beam lithography, nano-imprint lithography or nano-stenciling, but also some bottom-up methods such as template-assisted assembly^{147,148} intrinsically have this option. Other bottom-up methods, especially those based on self-assembly, often do not. This is also the case for NSL using spin-coated beads. Therefore, the structures obtained by NSL need to be micro-patterned in an additional process step.

UV photolithography

Standard UV photolithography was used for the purpose of micro-patterning. Both hole arrays as well as dot masks were patterned in this way. Figure 4.9 shows a standard UV photolithography process using positive tone photoresist. The wafer surface is pre-

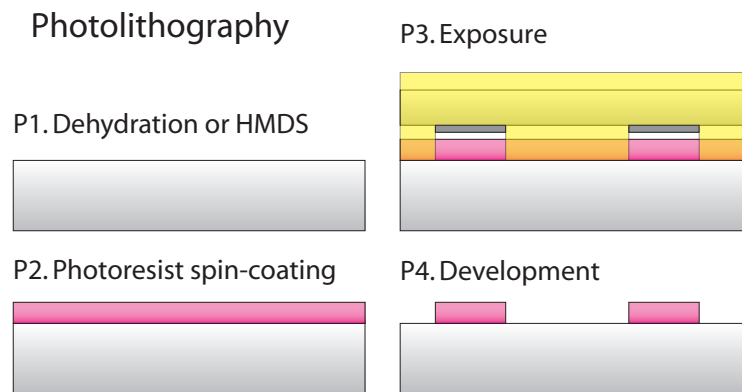


Figure 4.9: Schematic of positive-tone photoresist UV photolithography.

treated to enhance the adhesion of the photoresist to the substrate. The pre-treatment depends on the wafer surface chemistry. Silicon substrates are generally pre-treated with a silane (hexamethyldisilazane) in an oven process. This dehydrates the wafer surface and renders it hydrophobic. For oxidized wafers or noble metal surfaces, better results are obtained by only dehydrating the wafer in a convection oven for 1 hr at 150 °C. Generally, the pre-treatment becomes important for small isolated patterns, e.g. thin photoresist lines, with critical mask dimensions of a few μm . After wafer pre-treatment, a thin resist layer of typically 2 to 10 μm is spin-coated onto the wafer. Here, a spread-step at low speed is followed by a spin-step at high speed which determines the final film thickness. Remaining solvent is removed during a bake step. The photoresist is exposed through a photoresist mask using a mask aligner. Standard photoresist masks consist of quartz plates with a patterned chromium layer. The mask is aligned and placed in contact to the photoresist coated wafer. The exposure dose depends on the photoresist thickness and wafer surface, typical values are in the 100 mJ/cm^2 range. In the case of positive tone photoresist, the photoresist exposed by UV light is removed in the subsequent development step (figure 4.9). The inverse is the case for negative tone photoresist. Ususally, a short descum step in a barrel type oxygen plasma finishes the photolithography. This is done to remove any possible photoresist remains in the open areas.

Thus, the process of UV photolithography involves wet chemistry and temperature steps which may potentially influence pre-patterned nanostructures. For example, bake steps can reach a temperature of up to 120°C, and commonly used developers con-

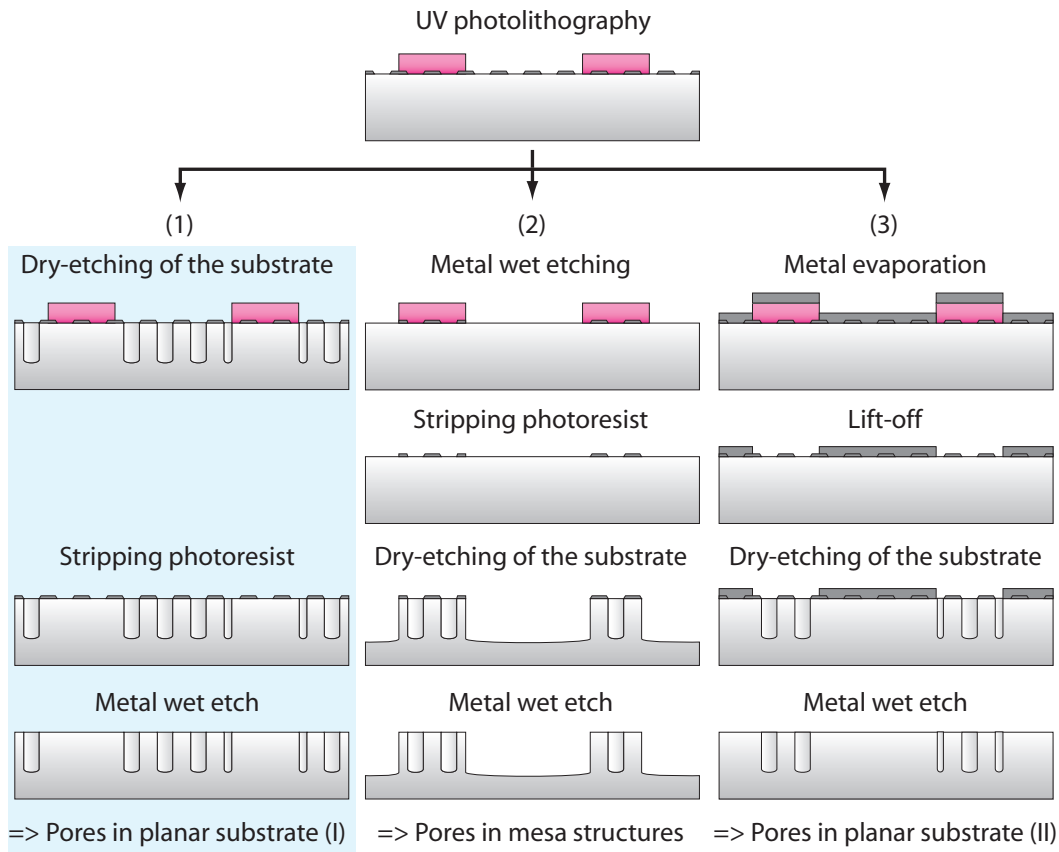


Figure 4.10: Schematic patterning of metallic hole masks and the resulting micropatterned nanostructures. Process option (1) was used in the fabrication of thin SiN membranes with sub- μm holes (c.f. chapter 5).

tain KOH. The KOH content of the developer needs to be considered when patterning metallic surfaces (c.f. below). Spin-coating and wet-processing steps may threaten fragile, free-standing structures already present on the wafer. In other cases, the device functionality may critically depend on the materials purity, and contamination by photolithography with organic molecules may pose a problem. In such cases, stencil lithography can be a convenient alternative.

Patterning of NSL hole and dot masks by UV photolithography

The photoresist pattern can be used for the micropatterning of nanostructures in different ways. In general, three different types of topographies can be obtained using the identical photolithographic mask. It depends on whether the photoresist pattern itself, or in combination with subtractive or additive methods is used. The three options are shown in figure 4.10 for metallic hole masks, and in figure 4.11 for oxide dot masks.

As mentioned above, for the photolithographic patterning of thin nanostructured

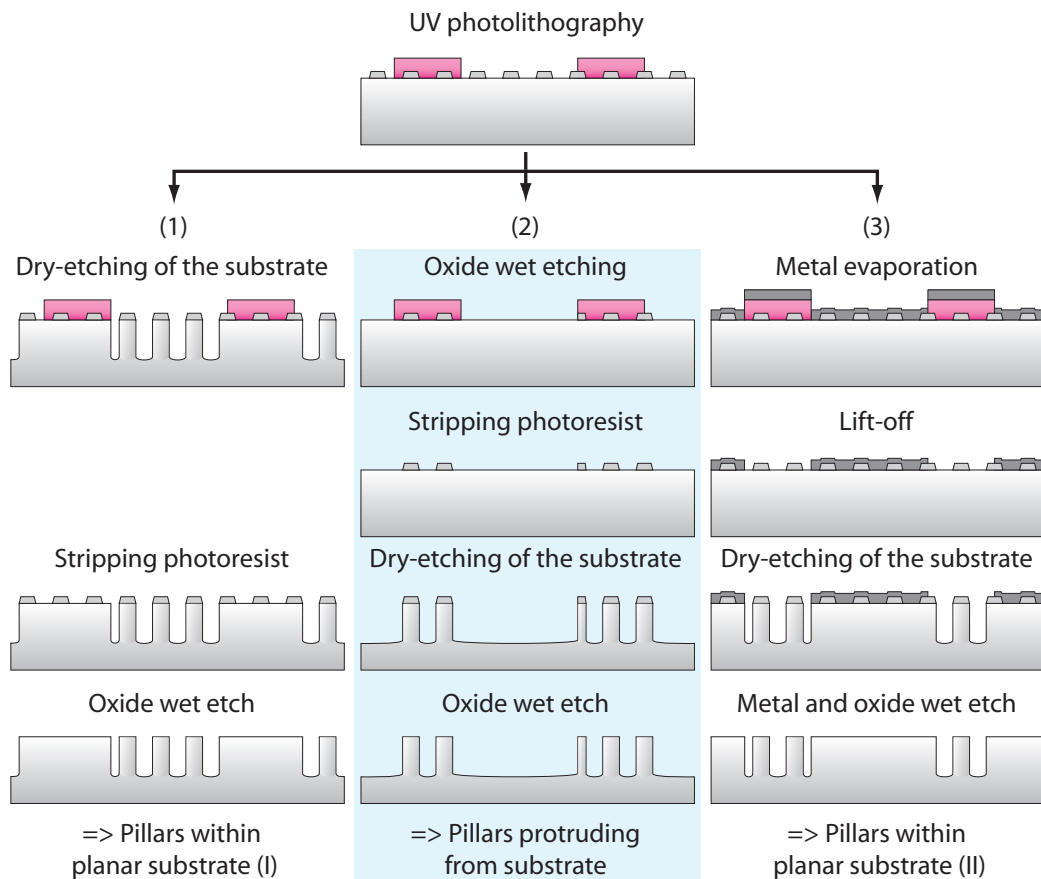


Figure 4.11: Schematic patterning of oxide dot masks and the resulting micropatterned nanostructures. Process option (2) was used in the fabrication of thin gold films and membranes with sub- μm holes (c.f. chapter 5).

metal surfaces, the metal needs to be highly resistant to the developer. In this case, it contained KOH, and developing an exposed photoresist on 15 thick Al hole masks led to the complete removal of the aluminum layer. Therefore, Cr was used when compatible with subsequent process steps.

Micro-patterned holes

Hole masks in 15 nm thick Cr were fabricated on 4" Si wafers coated with a 100 nm thick layer of low-stress PECVD SiN by employing the NSL *lift-off* routine. The Cr hole mask was additionally patterned by UV photolithography. In this way, sub- μm holes were locally etched into the SiN film. This process is schematically shown for the case of a bare Si substrate in process option (1) in figure 4.10. Figure 4.12 shows SEM images of photolithographically patterned holes in 100 nm thick SiN layers. The SEM images were taken after SiN-RIE and after stripping of the photoresist, but prior to the final Cr mask wet-etch removal. SiN etching was done at room temperature for 40 sec using

the LS SiN 5:1 etch recipe (c.f. etch recipes in A.3); the etch progress was monitored using an endpoint detection laser-interferometry system.

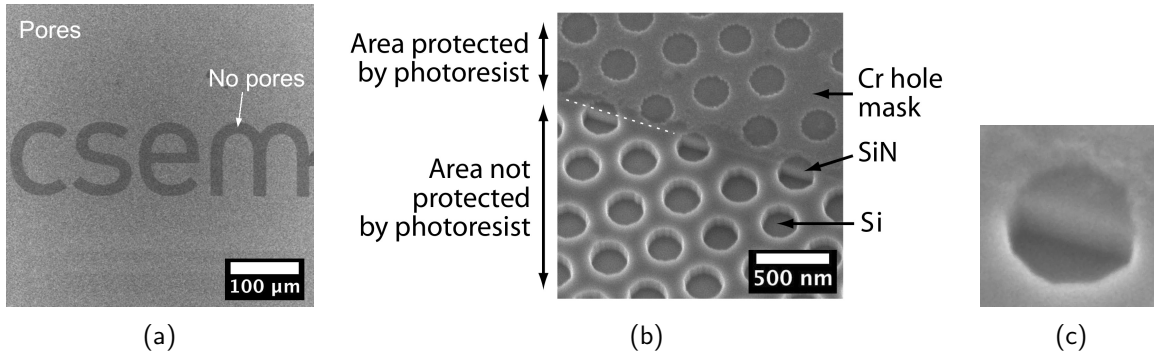


Figure 4.12: SEM images of micro-patterned holes etched into 100 nm thick SiN after stripping of the photoresist mask, but before Cr wet-etching. (a) shows the homogeneity of the hole etch. (b) shows that the Cr hole mask has been nicely transferred into the SiN layer. (c) is a zoom into (b).

Figure 4.12a shows a low magnification SEM image of homogeneously etched holes surrounding the CSEM logo. The logo area was protected with photoresist during dry-etching. A zoom into such a transition region from an etched to a non-etched area is shown in figures 4.12b and 4.12c. The transition border is indicated by a white dotted line. The Cr hole mask pattern has been nicely transferred into the underlying SiN layer. The top surface is left undamaged, which means that a Cr mask thickness of 15 nm is sufficient for the etching of 100 nm SiN.

Micro-patterned oxide dot masks

An example of an oxide dot mask patterned according to process option (2) in figure 4.11 is shown in figure 4.13. The photograph and SEM images were taken immediately after HF wet-etching and stripping of the photoresist. The photograph in figure 4.13a was taken with a flash, thus the colored light diffraction effects at the patterned nanoscale dot arrays. Figure 4.13b shows a low magnification SEM image of patterned oxide dots. The light grey areas represent the oxide dot arrays. Areas without oxide dots within the otherwise continuous dot array are indicated by arrows. The absence of oxide dots in those areas are due to empty areas in the original bead template. Such empty areas are not an issue for the subsequent processing steps (c.f. chapter 5), though not desirable.

Figure 4.13c is a zoom into a transition region. Photoresist covered the dots on the right hand side during HF etching (arrow **A** in figure 4.13c). Two observations can be made: Although the oxide on the left hand side was removed by HF wet-etching, circular patterns remain (arrow **B** in figure 4.13c). This is due to a small over-etch on the order

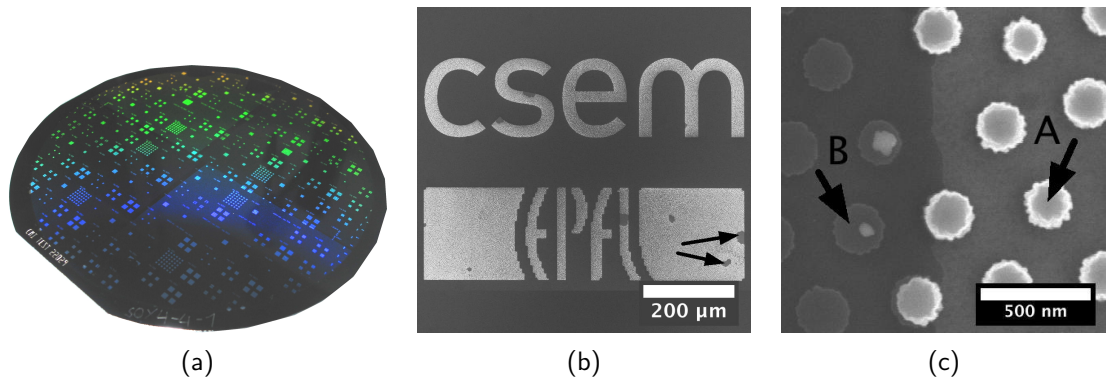


Figure 4.13: Oxide dots patterned by UV photolithography and HF wet-etching. The SEM images were taken after stripping of the photoresist. PSB428 beads with $D_{red} = 290$ nm served as a template for the oxide dot mask etching.

of 5 to 10 nm during the SiO_2 -RIE etching of the oxide dots that partly transfers the pattern into the Si substrate, caused by the finite SiO_2 :Si etch selectivity (also c.f. the AFM height image in figure 4.14a). This over-etching was done on purpose to ensure a complete removal of the oxide layer around the beads. An insufficient removal can have undesirable consequences for subsequent the substrate etchings, e.g. for the fabrication of micro-patterned high aspect-ratio Si pillars. The Si pillars would be placed upon a small substrate mesa due to a residual continuous oxide layer (c.f. below). A residual oxide layer is shown in the AFM height images in figure 4.14b.

Another important observation is that the right half in figure 4.13c (region with arrow **A**) has a lighter grey substrate background. The border between the darker and lighter background shade on the silicon substrate corresponds to the photoresist border. Indeed, AFM phase imaging after HF etching and stripping of the photoresist showed a phase change when crossing this transition region (figure 4.14a). Such a phase change is an indication the the surface chemistry is different.

This can be due to damage of the Si substrate surface by ion impact during SiO_2 -RIE which can enhance the re-growth of native oxide. Then, when the wafer is photolithographically patterned and oxide dots are locally removed by HF wet-etching, the regrown native oxide is also removed. As chemical wet-etching in HF does not deeply damage the Si substrate, enhanced re-growth of the native oxide is not the case. The presence of this comparatively thick native oxide in some wafer regions has to be considered in subsequent processing steps where it acts as a masking layer.

As a preliminary conclusion, transferring nanoscale patterns by processes designed for micro-machining applications is technologically involved. Short etch times make the dry-etching process very sensitive to small variations, e.g. with respect to plasma stabilization time, self-bias build-up and substrate temperature¹.

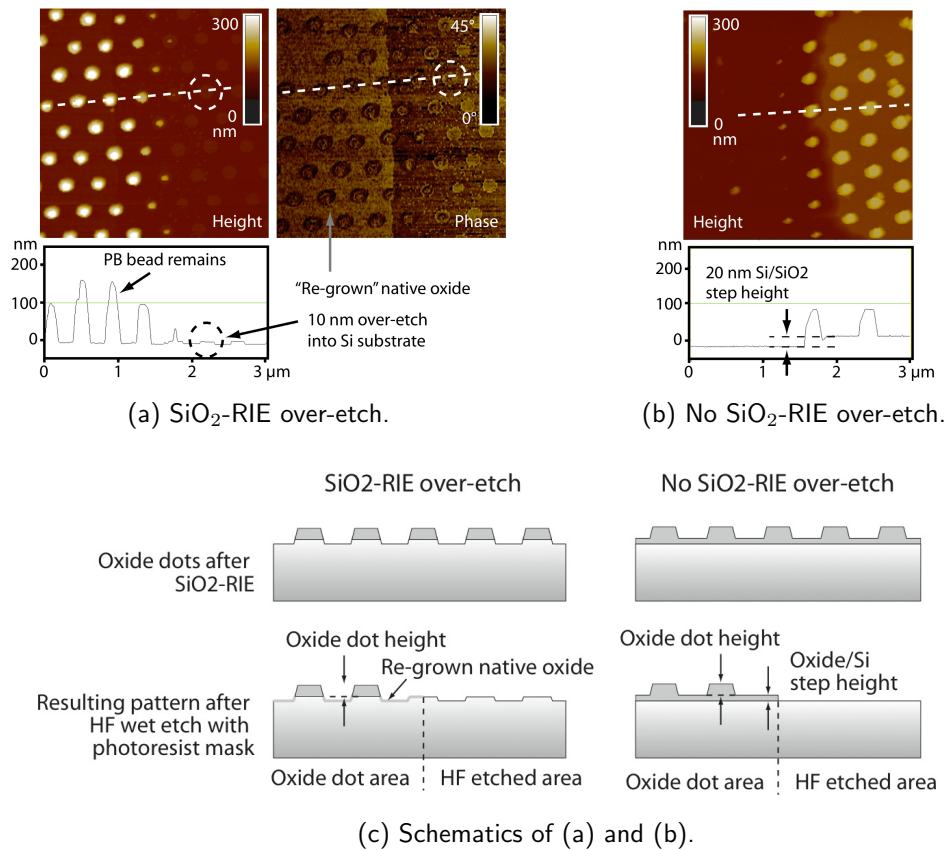


Figure 4.14: Height and phase AFM images of oxide dots patterned by HF wet-etching. The SiO_2 -RIE and HF wet-etch conditions were identical (30 sec SiO_2 PR 5:1 (old) at 0°C (c.f. A.3) and 5 min BHF wet etch), but conducted in different batches. Below an illustration of the resulting micropatterned oxide dot arrays in case of a small SiO_2 over-etch and when the oxide is not completely etched .

Micro-patterned high aspect-ratio silicon pillars

Figure 4.15 shows an example of micro-patterned high aspect-ratio Si pillars. Figure 4.15b is a zoom into figure 4.15a. It shows a transition region from the Si plain substrate to an area structured with Si pillars. Figure 4.15c shows a similar transition region on a different wafer. The wafers were obtained from the same batch and processed in the same manner. Oxide dots were etched into 100 nm SiO₂ using size-reduced PSB535 ($D_{red} = 225$ nm) and PSB428 ($D_{red} = 150$ nm) as a polymeric etch mask (30 sec at 0°C SiO₂ PR 5:1 (old), c.f. etch recipes in A.3). The oxide dot mask was then patterned by UV photolithography and HF etching. This was followed by Si-DRIE to locally realize high aspect-ratio Si pillars (process option (2) in figure 4.11). Si-DRIE was done for 4 min at 0°C using a continuous etch procedure (MK Si Opto type recipe with a 40/55 etch gas ratio and 15 W RIE source power).

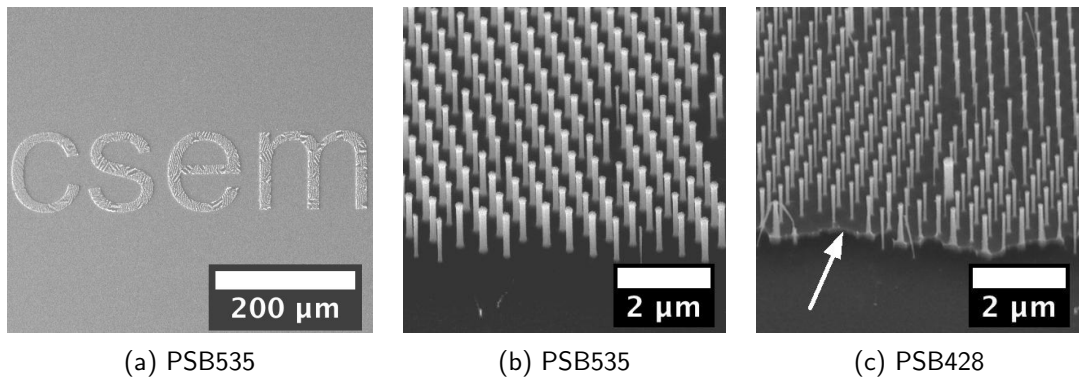


Figure 4.15: SEM images of micro-patterned high aspect-ratio Si pillars using UV photolithographically patterned oxide dot masks. The same SiO-DRIE procedure was employed in all images. (b,c) images were taken at a 30° tilt angle.

On both wafers, Si pillars with a vertical sidewall shape and high aspect ratio >10 were successfully etched in pre-defined areas on the Si substrate. The pillars' height is ~ 1.6 μm with a diameter of 155 nm (PSB535) and 100 nm (PSB428). The diameter is smaller than the diameter of the oxide dot mask before Si-DRIE due to an early mask failure at the border of the oxide dot masks, in addition to a ca. 20 nm mask undercut.

In case of the PSB535 wafer, the Si substrate is etched homogeneously. In case of the PSB428 wafer, a small step pattern can be observed as indicated by the arrow in figure 4.15c. Thus the pillars are placed on top of a Si mesa structure. As described in the previous section, a thin residual oxide layer remains within the oxide dot area when the SiO₂-RIE is insufficient. Indeed, a Si/SiO₂ step height of 10 nm could be measured in case of the PSB428 wafer. As a conclusion, for a reliable and reproducible Si pillar etching, the process flow has to account for such fabrication process related variations.

In the present case, this was successfully achieved by (i) monitoring the SiO₂-RIE etch progress with a laser interferometric end-point-detection system and over-etching for 5 sec, and (ii) performing a 2 sec SiO₂-RIE etch prior to Si-DRIE.

4.3 Summary and conclusions

Size-reduced PS beads were used for the wafer-scale fabrication of holey thin metal films. This is done by a nanosphere lithography *lift-off* routine. The metal film thickness is limited by the vertical dimensions of the beads, for a high yield lift-off result, the metal film thickness should be less than the bead rim height h_{rim} . Typical metal film thicknesses in this thesis are in the range of 10 to 20 nm for hole diameters of 150 to 400 nm. Bead tilt induced by the anisotropic O₂-RIE bead size-reduction results in elliptical rather than spherical holes.

Employing a nanosphere lithography *etching* routine, the PS beads were used as direct etch mask to transfer pillars into the underlying substrate. However, the attainable aspect-ratio is limited due to the elliptical cross-sectional shape of the beads, inducing an early mask failure at the border of the pillars.

To obtain high aspect-ratio pillars, an intermediate oxide dot mask was used. This allowed to realize silicon pillars with an aspect-ratio greater than 10:1. By tuning the Si-DRIE etching conditions, the sidewall taper of the pillars tuned in a controlled way.

Finally, standard UV photolithography was used for the micro-patterning of hole and pillar arrays. Two process options were demonstrated for (a) the local etching of holes into a thin SiN layer, and (b) the local etching of SiO₂ dots and Si pillars. The latter is technologically involved as the dry-etch times are extremely short and sensitive to various process conditions. The micro-patterning of metallic hole masks is less sensitive to process condition variations, but puts limitations with respect to the nanostructured metal. In both cases, the process flow was adapted accordingly and micro-patterned holes and pillars were fabricated reproducibly.

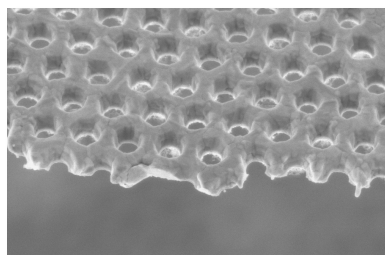
5 Device fabrication

In this chapter, the fabrication of thin films and membranes perforated with sub- μm holes is described.

Holes were transferred into thin gold (Au) and silicon nitride (SiN) films by etching into the device layer. In another approach, holey gold films and membranes were fabricated using Si or SiO₂ pillars as lift-off template. The hole etch masks were fabricated by the nanosphere lithography (NSL) lift-off routine, whereas the high-aspect ratio silicon pillars were fabricated using the NSL etch routine.

Hole arrays in $2.4 \times 2.4 \text{ mm}^2$ large SiN membranes and $1.2 \times 1.2 \text{ mm}^2$ large Au membranes were fabricated on 4" wafer substrates, as well as in Au films on 2" glass wafers .

First, the fabrication of porous SiN membranes is shown. This is followed by a description of the fabrication of hole arrays in thin Au films on glass substrates, and then the fabrication of holey Au membranes either supported by a Si frame or transferred to a transparent parylene layer.



5.1 Holey SiN membranes by etching through Cr hole mask

There is a demand in industrial and academic applications for thin holey SiN membranes of large size with sub- μm holes of narrow size distribution.

Using the NSL *lift-off* routine, 100 nm thick SiN membranes of up to 2.4 mm in side-length with a hole density on the order of 10^6 holes/ cm^2 were fabricated in a collaboration with Dr. Veronica Savu in the group of Prof. Brugger at EPFL.

Membranes with holes of narrow size distribution having a 2σ standard deviation is $< 8\%$ were fabricated. This size distribution corresponds to the size distribution of the beads used in the NSL process step. The fabrication process was designed in a way to allow the simultaneous fabrication of membranes of different size on one wafer. Furthermore, high density arrays of membranes can be realized thanks to the anisotropic membrane release procedure. Also, the process has the flexibility to realize membranes with different holes sizes on the same wafer.

After an outline of the fabrication process, the crucial steps will be described in more detail in the results and discussion section. For more details on the bead deposition, bead size reduction and NSL *lift-off* routine process steps, c.f. chapters 2, 3 and 4, respectively. The mask layouts can be found in the appendix A.7.

5.1.1 Process outline

The schematic fabrication process is shown in figure 5.1. 4" single-side (SSP, 525 ± 25 μm thick) or double-side (DSP, 380 ± 10 μm thick) polished (100) Si wafers served as the base substrate. The process on SSP and DSP wafers was identical with the only difference that final membrane release on DSP wafers was accomplished faster. 100 nm of low stress Si nitride (LS-SiN) was deposited by LPCVD (low pressure chemical vapor deposition). The nominal residual tensile stress of the deposited LS-SiN is less than 200 MPa. 200 nm of Al were deposited by PVD onto the wafer backside and later served as an etch mask during Si-DRIE. Process steps H3 to H5 show the NSL *lift-off* routine as described in detail in previous chapters: a monolayer of beads was deposited by spin-coating. The size of the PS beads was reduced by O_2 -RIE and then served as a lift-off template for the fabrication of a 15 nm thick Cr hole mask on top of the SiN layer. Process steps H6 and H7 show the fabrication of micro-patterned hole areas by standard UV photolithography and SiN RIE. The photoresist on the wafer frontside was stripped. Backside photolithography was performed to define etch windows in the Al and SiN layer aligned to the frontside patterns. The Al was patterned by wet-etching. At this stage, also the Cr hole mask on the wafer frontside was stripped in a Cr wet-etch. After

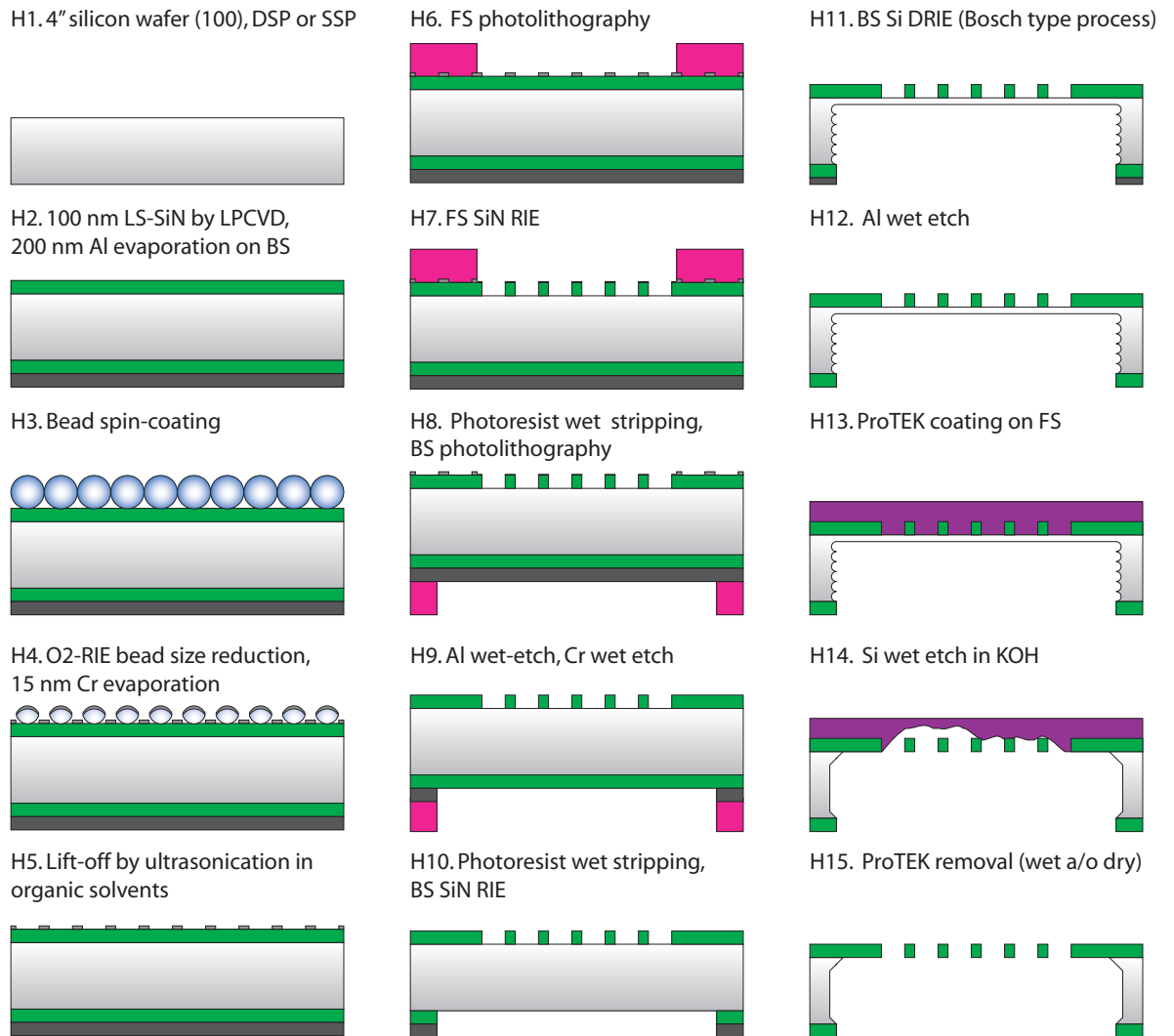


Figure 5.1: Process flow for the fabrication of SiN membranes with sub- μm holes.

stripping of the photoresist in a combination of O₂-plasma and organic solvents, windows in the backside SiN layer were opened by dry etching using the Al layer as mask.

H11 through H15 show the membrane release procedure. First, the Si substrate was etched from the backside in an anisotropic Bosch-type Si-DRIE procedure with a high etch rate on the order on the order of 10 μm/min. This etching was done until a ≈ 50 μm thick Si membrane was produced. Then, the Al backside mask was stripped by wet-etching and the wafer frontside was coated with a protective coating (c.f. ProTEK® in section A.5). Membranes release was performed by wet-etching in KOH. Afterwards, the protective coating was removed either in organic solvents and/or by stripping in an O₂-plasma.

5.1.2 Results and discussion

Fabrication of the hole etch mask by the NSL *lift-off* routine

PSB428 and PSB535 beads in 10% w/v aqueous suspension were spin-coated onto 4" wafers coated with 100 nm LS-SiN. The wafers were pre-treated in an oxygen plasma, at most 30 min before bead deposition, to render the substrate surface hydrophilic. For the plasma pre-treatment, no difference was observed whether e.g. 2 min of 100 W O₂-RIE in a parallel platen reactor, or an isotropic etch for 10 min in a 1000 W barrel reactor was used.

The spin-coating was done under non-clean room conditions with an ambient temperature controlled to 21°C, but fluctuating relative humidity. Therefore, the spin-coating parameters were adjusted to the daily conditions using plain Si wafers as test wafers, analyzing the obtained bead layer by optical microscopy and adjusting the spin-coating parameters accordingly. As the goal was to obtain a homogeneous monolayer, advantage was given to monolayers with small empty spaces rather than monolayers with patches of multilayers. This ensured that the final holey membranes would not have micron-size holes (NSL process steps H3 to H5 in figure 5.1). On average, three test wafers were sufficient to find the good spin-coating conditions. 1 ml of bead suspension were used per 4" wafer; the suspensions were passed through a 5 μm filter just before use to remove bead agglomerates. Ultrasonication of the bead suspension at room temperature was not successful to disperse such agglomerates.

The wafers were centered on a spin-coating chuck and the bead suspension was pipetted in the middle of the wafer. If necessary, the suspension was spread across the whole wafer surface by manually tilting the wafer and/or distributing the suspension with a horizontally held pipette tip. (For more details on the bead spin-coating and related issues, please refer to the corresponding section in the bead deposition chapter 2.3.3.) After a short dwell time between 5 to 10 sec, wafer rotation was initiated. Homogeneous

monolayer coatings with a radially uniform distribution and a coverage of 86% were obtained with the following parameters:

- PSB428: 60 sec at 1800 rpm, acceleration 500 rpm/sec, dwell time 10 sec, at a relative humidity of 20%
- PSB535: 60 sec at 1100 rpm, acceleration 300 rpm/sec, dwell time 60 sec, at a relative humidity of 36%

The beads were removed at the wafer edge after all solvent had evaporated to avoid contamination of subsequently used equipment.. This was done under wafer rotation, using an acetone-soaked tissue held with tweezers and gently pressed to the wafer border.

In the next step, the bead size was reduced by O₂-RIE using O₂-RIE *B* at the standard conditions of 200 mT O₂, sustained at a flow of 100 sccm, 80 W RF input power resulting in a self-induced DC bias of -300 V. The first column in figure 5.2 shows size-reduced PSB535 (first row) and PSB428 (second and third row) beads. (Bead size analysis was done software based but using manual threshold settings; the same holds true for the subsequent size analysis of the Cr mask hole size and the holes etched into the SiN layer.)

Beads on the PSB535 wafer were etched for 1 min 20 sec, resulting in an average bead size of 310 ± 32 nm. The 2σ standard deviation of the measured bead size was ± 32 nm. Two different bead sizes were obtained on the same PSB428 wafer by shading the other wafer half during O₂-RIE using a half Si dummy wafer. On the one wafer half (L), beads were etched for 1 min 5 sec, resulting in a bead size of 257 ± 21 nm; on the other wafer half (R), beads were etched for 1 min 15 sec, resulting in a bead size of 207 ± 22 nm. The bead radial etch rates thus were 169 nm/min (PSB535), 158 nm/min (PSB428 L) and 177 nm/min (PSB428 R). The higher etch rate in case of PSB428 (R) is explained by the anisotropy of the etch process (c.f. chapter 3). In case of the PSB428 wafer, the 2σ standard deviation is on the order of 7%, which is only slightly larger than the size distribution of the original beads (3% for both PSB428 and PSB535 beads). The 2σ standard deviation of up to 14% in case of the PSB535 wafer is comparatively large. Reasons for this are bead tilting and bead surface roughening induced by the O₂-RIE etch procedure. Due to bead surface roughening makes, the diameter can not be measured accurately and broadens the measured bead and hole diameter size distributions.

The second column in figure 5.2 shows the 15 nm thick Cr hole etch mask realized using the size-reduced beads as lift-off template in the NSL *lift-off* routine (chapter 4). The Cr was evaporated directionally onto the beads. A 100% lift-off yield was obtained by ultrasonication of the wafers in THF, acetone and isopropanol for 2 min each, followed by a thorough rinse in Di-H₂O and drying in air. After lift-off, the Cr mask thickness was

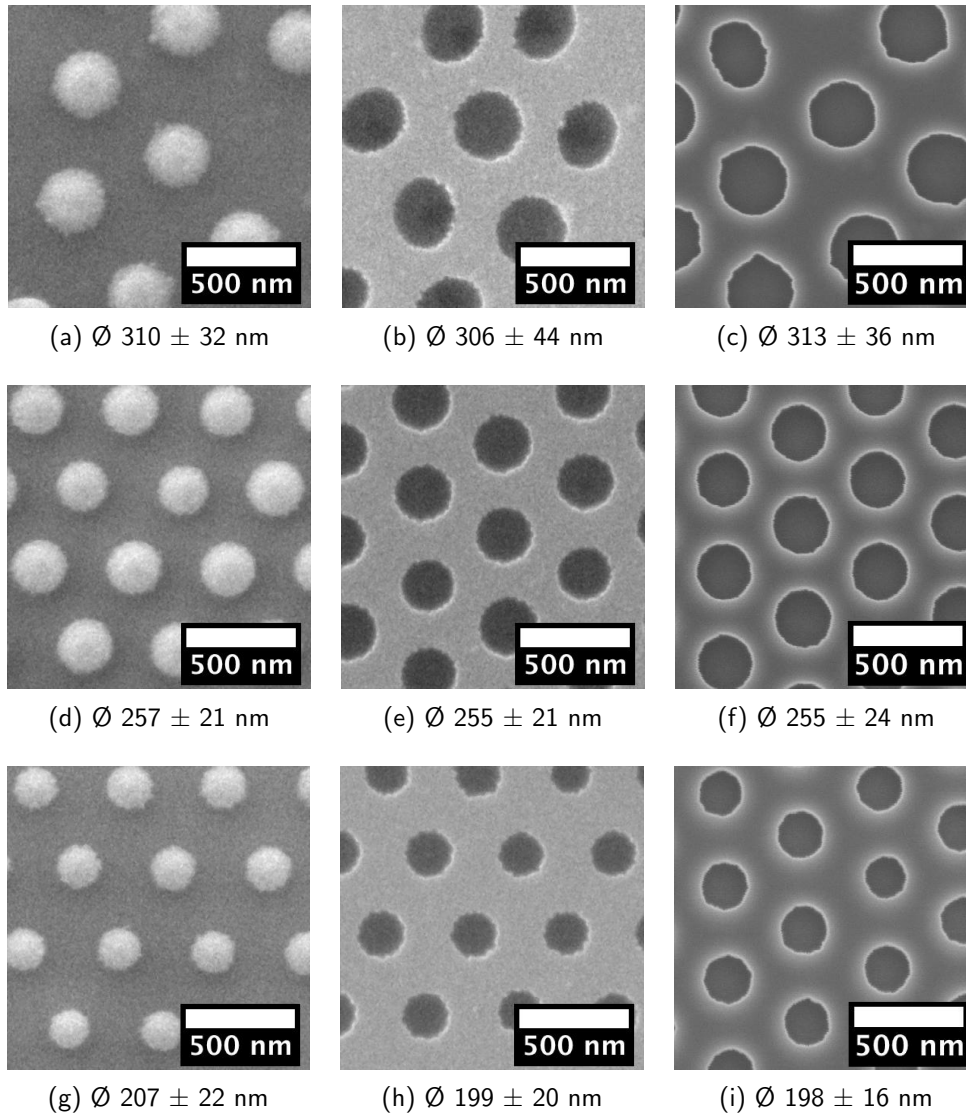


Figure 5.2: By using different bead templates, different hole densities and sizes can be fabricated without changing major fabrication process parameters. The first row and the second/third rows show SEM images on a wafer where PSB535 and PSB428 beads were used as template, respectively. PSB428 beads were reduced to different sizes on the same wafer. The diameter of the size-reduced beads transfers exactly into the later hole size. The indicated range corresponds to 2σ . The columns from left to right show the size-reduced beads, the holey Cr mask, and the holes etched into 100 nm thick SiN.

confirmed by AFM imaging. For different evaporations, the mask thickness deviated by ± 2 nm off the set value. The Cr mask hole sizes were 306 ± 44 nm (PSB535), 255 ± 21 nm (PSB428 L) and 199 ± 20 nm (PSB428 R). They correspond well to the reduced bead size and confirm the accuracy of the pattern transfer by the NSL *lift-off* routine. The AFM images taken after lift-off revealed that a small amount of PS bead remains where the bead was attached to the substrate surface. In order to minimize the masking effect of these polymer remains in the subsequent hole etching process, 1 min O₂-RIE was performed. Not all of the polymer could be removed, though. The remaining scum is inorganic and stems from the PS bead synthesis process.

Etching of micro-patterned holes

After fabrication of the Cr hole mask, holey membrane areas were defined by UV photolithography (H6 in figure 5.1). The critical mask dimensions were on the order of a few μm and thus the lithography process had not to be optimized. Mask alignment was done with respect to the wafer flat. The lithography process plays a crucial role in the fabrication procedure as it ensures a controlled membrane release by KOH wet-etching and well defined membrane sizes. Furthermore, the micro-patterning is necessary to render the holey membranes more stable by placing the holes away from the Si frame within the inner membrane area (section 1.1.3).

The micro-patterned Cr hole mask was transferred into holes in the underlying LS-SiN by SiN-RIE (H7 in figure 5.1)). Etching was done at room temperature; 40 sec of etching were sufficient to etch through the 100 nm of SiN. The standard recipe SiN LS 5:1 was used (c.f. etch recipes in A.3). Simultaneously, the progress of the etching progress was monitored with an endpoint detection system; over-etching was done for ≈ 5 sec to ensure that the SiN was cleared at the bottom of the holes. The photoresist was stripped after hole etching in a combined dry/wet etch procedure, first performing ≥ 1 min of O₂-plasma in a microwave barrel reactor at 500 W. This induces damages in the photoresist top layer which is hardened by the SiN-RIE. Then, the photoresist was cleanly removed by stripping at 60°C in photoresist remover provided by the photoresist supplier. The remover contains a high content of NMP (1-methyl-2-pyrrolidone, c.f. solvents²⁴³), which is a good organic solvent.

The third column in figure 5.2 shows holes in 100 nm LS-SiN, etched using the Cr hole mask that is shown in the second column. The SEM images were taken before stripping of the Cr mask. The hole diameters were 313 ± 36 nm (PSB535), 255 ± 24 nm (PSB428 L) and 198 ± 16 nm (PSB428 R). Within a range of ± 10 nm, they correspond well to the previously measured bead and Cr hole mask diameters.

At this fabrication step, micro-patterned SiN layers with holes have been obtained with different hole densities and porosities: The hole densities are 6.3×10^8 and 4.0×10^8 holes/cm²

for PSB428 and PSB535 beads, respectively. The respective porosities for holes of 313 nm (PSB535) and 255 nm as well as 198 nm (PSB428) in diameter are 31%, 32% and 19%.

Membrane release by Si-DRIE and KOH wet-etching

Schematically, the membrane release process is shown in process steps H8 to H15 in figure 5.1). First, membrane openings were defined in the Al/SiN double layer by means of photolithography, Al wet-etching and SiN-DRIE. Two different frontside/backside mask layouts were used as described in the appendix A.7. After the Al wet-etch procedure to define the membrane opening on the wafer backside, the frontside holey Cr mask was removed in a Cr-etch. Then, the patterned Al mask served as a dry-etch mask to open windows in the backside SiN. This was done with the same etch parameters that were used for the frontside hole etching.

The membrane release process was done in a combination of Si dry- and wet-etching. The dry-etch using a Bosch-type etch procedure has the advantage of having a higher etch rate as compared to standard KOH wet-etching at 60°C (Si-DRIE ≥ 10 $\mu\text{m}/\text{min}$ vs. KOH ≈ 0.33 $\mu\text{m}/\text{min}$ in $\langle 100 \rangle$ direction). Also, the Bosch-process allows the deep anisotropic Si etching with vertical sidewalls and thus is not accompanied by a lateral loss in dimensions. The sidewalls obtained by etching a (100) Si wafer in KOH have a tapered angle of 54.7° ¹, thus e.g. etching through a 500 μm thick Si wafer results in a lateral mask opening shrinkage by 353 μm . This limits the attainable membrane integration density. As the Si-DRIE has only limited etch selectivity between Si and SiN, the final release step was done in KOH, which has an almost infinite Si/SiN etch selectivity.

Si-DRIE using a Bosch-type process was done until ≈ 50 μm of Si were left to etch before SiN membrane release. For the etch recipe conditions, c.f. AMS etch parameters in A.3. The Si-DRIE was subject to aspect-ratio dependent etching (ARDE). This means that the large membrane openings are etched faster than the small ones. The Si-DRIE was stopped when the largest membranes were thinned down to the desired Si membrane thickness.¹ As a consequence of ARDE, KOH etch times to release small membranes were considerably longer than those for large membranes. This means that KOH etch solution could penetrate through the already released, larger membranes, and start etching the Si through the holes in the not-yet released, smaller membranes (figure 5.3). The use of a sealed KOH etch chuck would not solve this problem.

However, etching of the Si substrate through the frontside holes should be avoided in

¹An attempt to compensate for ARDE by integrating grill structures in the large membrane windows was not successful and repeatedly lead to Si remaining in the membrane middle (more explanations are given in A.7).

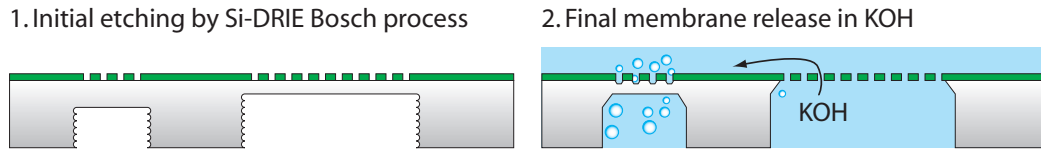


Figure 5.3: Due to aspect-ratio dependent etching in Si-DRIE, the Si to be etched is less thick in case of larger membranes. In the following wet-etch release step, KOH solution may penetrate through the larger membrane holes. This leads to undesirable etching of the Si substrate through frontside holes.

any case. As has been reported by Kuiper⁴², pressure build-up due to H₂ gas generation associated with the KOH etching process causes SiN films with sub- μm holes to break. While Kuiper et al. employed a front-side dry-etch procedure through the SiN holes, in this thesis, a temporary protective front-side coating during wet-etch release, ProTEK[®], that can be applied by spin-coating, was used. This is shown in process step H13 in figure 5.1. (For more information on ProTEK and the applied coating procedure, please c.f. A.5.)

Although ProTEK is not etched in KOH, it was found that it tends to delaminate from the perforated SiN layer (H14 in 5.1 and figure 5.5). Therefore, additional micro-patterning of the holes is needed that restricts the holey area to within the inner membrane region. This shall be explained with an illustrative example of a membrane where the holes were *not* micro-patterned. A photograph of a wafer after the membrane release in KOH is shown in figure 5.4a. In that case, holes were etched into the SiN layer all across the wafer (no micro-patterning of holes) apart from some membranes which had no holes at all. These non-hole membranes appear dark because the smooth surface does not diffract the camera flash light. Shown in the inset is a photograph taken under ambient light. The non-hole membranes are intact and have well defined square borders; the holey membranes are broken and have rounded, enlarged corners.

The enlargement of the membrane area can be explained by the delamination of ProTEK, after which the Si frontside was attacked by KOH in the open hole areas (figure 5.5). An optical microscope image of an intact, but enlarged holey membrane is shown in 5.4b. The dashed square indicates the membrane area as defined by photolithography. The arrow points to SiN with holes that has been under-etched by KOH attack from the frontside. A transition region of this under-etch is shown in the SEM micrograph 5.4c. The arrows indicate holes through which the Si frontside was attacked by KOH; the typical pyramidal KOH etch groove pattern can be identified. As the KOH etch rate in $\langle 111 \rangle$ direction is slow but non-zero, the etch pyramids of closely spaced holes will eventually join (dashed square in figure 5.4c).

Thus, the micro-patterning of the holes serves two purposes: (a) it is viable during the

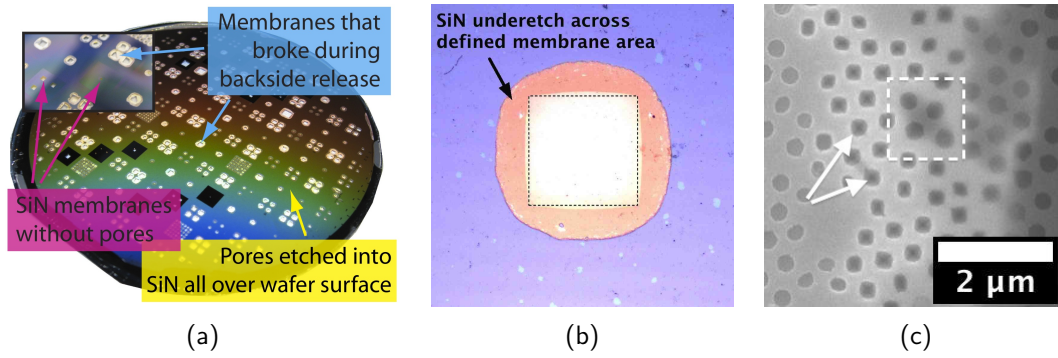


Figure 5.4: (a) Photograph of a wafer with holey and non-holey membranes. (b) Optical microscope image illustrating the KOH underetch through the frontside holes. (c) SEM image of a membrane/substrate transition region showing the attack of the Si substrate through the frontside holes.

combined dry-etch/wet-etch release procedure to avoid H_2 gas pressure build-up beneath the holes and to obtain well-defined membrane sizes (figure 5.5), and (b) it renders the holey membranes more stable by placing the mechanically weaker, perforated membrane region away from the high-stress inflection points towards the Si frame.²

As last fabrication step (HS15 in figure 5.1), the ProTEK was removed. This can be done either by O_2 -plasma ashing or by wet-etching in acetone and isopropanol. For the plasma ashing, it should be noted that the choice of the plasma asher plays an important role. It was found that plasma ashers with a microwave powered source had a destructive influence on the membranes, while ProTEK removed by RF generated O_2 plasmas did not damage the membranes. The etch rate in a 1000 W RF barrel type O_2 etcher was $\approx 1 \mu\text{m}/\text{min}$ at a temperature of 62°C . For the piecewise ProTEK removal on chips cleaved after KOH backside release, the wet-etch procedure was preferred. The chips were carefully immersed in acetone and isopropanol for 10 min each, then left for drying in air. Residual polymer scum was removed on the membrane front- and backside by 1 min etching at 100 W in an RF powered O_2 -RIE parallel platen reactor.

²For a thin, low stress membranes, the location of the inflection point (τ) away from the support frame can be approximated by $\tau = l/2 \pm l/(2\sqrt{3})$. As an example, $\tau \approx 25 \mu\text{m}$ for a square SiN membrane of sidelength $l = 1 \text{ mm}$ and a Young's modulus on the order of 290 GPa⁴⁸.

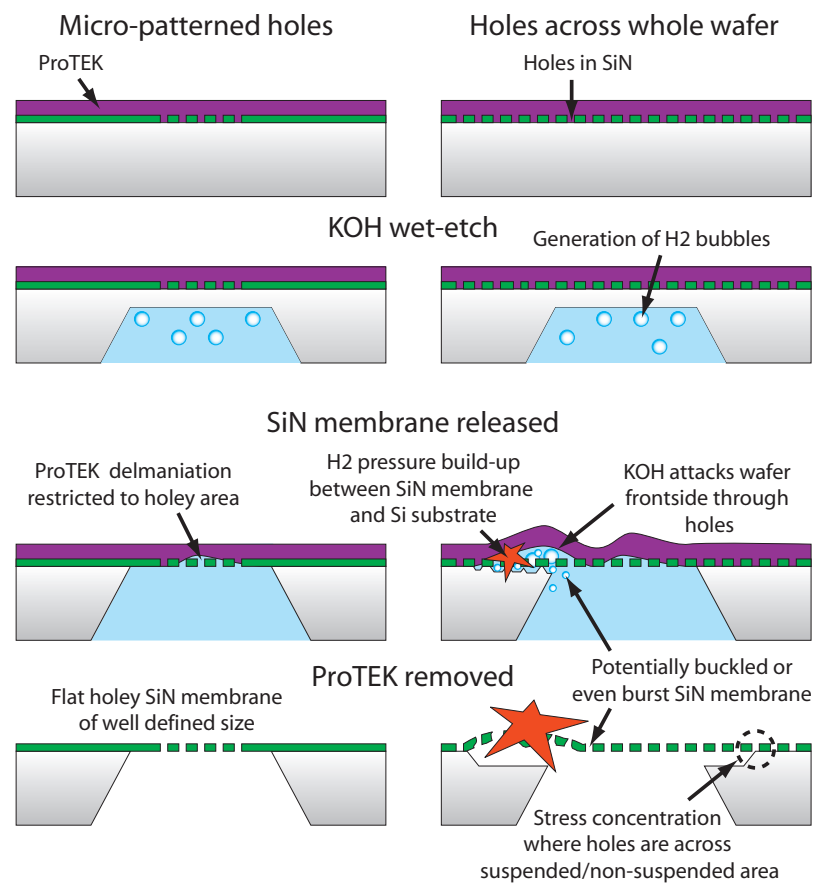


Figure 5.5: Schematic illustration of the need for hole micro-patterning and the use of ProTEK when the final membrane release is done by KOH wet-etching.

Released membranes

By the combined use of a protective coating and micro-patterning of the holes, differently sized membranes were successfully fabricated on the same wafer. Figure 5.6a shows photographs of holey and non-hole released membranes. The SiN is 100 nm thick, and the membranes have a side-length of 400, 800, 1200 and 2400 μm . Thus the largest size membrane have an aspect ratio (membrane width/thickness) of 24000. Chips with 6×6 arrays of 400 μm large membranes were fabricated on the same wafer. All membranes within the array were intact, showing that the fabrication process is suitable for the fabrication of high density membrane arrays. Non-hole membranes were integrated on the same wafer for comparison of the mechanical strength of holey vs. non-hole membranes (c.f. chapter 6.1).

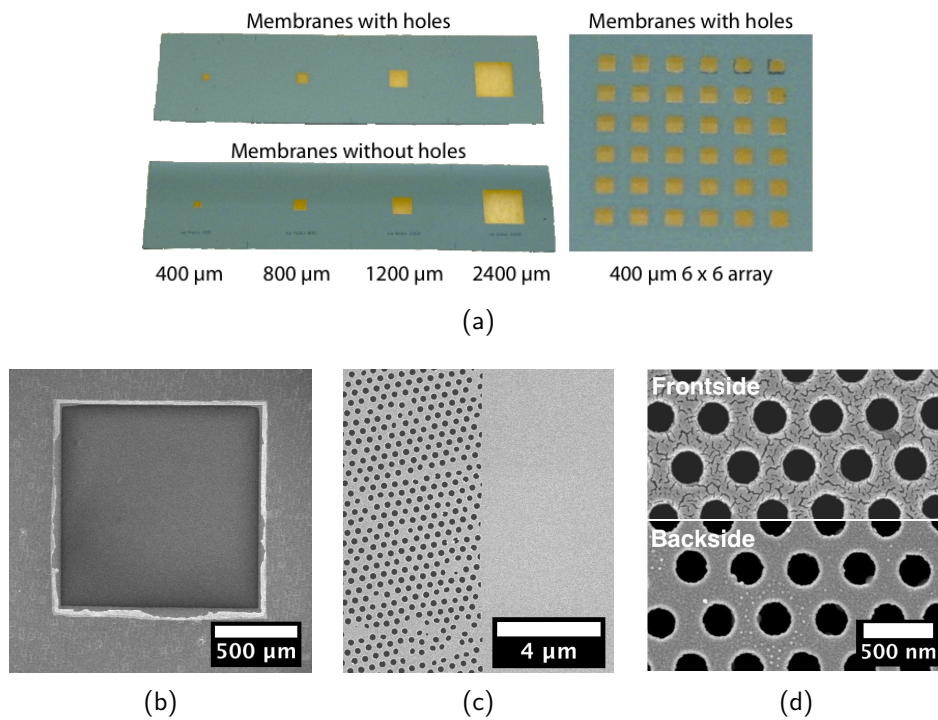


Figure 5.6: Successfully fabricated 100 nm thick SiN membranes. The photographs in (a) show that membranes of different sizes were fabricated on one wafer. (b-c) show SEM micrographs of micro-patterned holey membranes.

Figure 5.6b shows a low magnification SEM micrograph of the backside of a holey membrane with a side-length of 1200 μm . The backside opening is only slightly enlarged by the final KOH etch procedure. Thus, membranes released by the combined SiDRIE/KOH procedure can be densely integrated. Figure 5.6c shows a SEM micrograph of the transition region from the holey to the non-hole membrane area. The image was taken on the backside of the membrane, showing that the holey area is limited to the free-standing membrane region. The hole shape and openness of the holes was confirmed

by SEM imaging of both the membrane frontside and backside. To avoid charging of the membranes during SEM imaging, they were coated with a thin Au layer. The size of the holes as measured from the frontside and from the backside was 212 ± 40 nm and 220 ± 24 nm, respectively.

An explanation for this difference remains speculative. Rather the inverse, larger hole openings on the frontside and smaller ones on the backside, is expected from the SiN-RIE etch process. It has a strong physical etch component, which results in positive tapered sidewalls rather than negative sidewall tapers¹.

5.1.3 Preliminary conclusions

NSL has been successfully employed for the wafer-scale fabrication of 100 nm thick SiN membranes with sub- μm size holes.

The hole density depends on the size of the bead template used and was 6.3×10^8 and 4.0×10^8 holes/cm² for PSB428 and PSB535 beads, respectively. Within a range of 10 nm, the SiN hole size corresponds precisely to the diameter of the size-reduced PS beads. SiN holes in the range of 200 to 320 nm in diameter were realized by using a different NSL bead template.

By developing a membrane release procedure that combines Si-DRIE with KOH wet-etching and employing a temporary protective coating, square membranes of different size were fabricated on the same wafer. Here, micro-patterning of the hole area plays a crucial role.

The smallest membranes had a side-length of 400 μm , the largest ones had a side-length of 2400 μm . The membranes can be integrated into dense arrays thanks to the vertical etch profile of the Si-DRIE etch process.

5.2 Hole arrays in Au films on glass substrates by sputter-etching

In this section, the fabrication of arrays of sub- μm size holes in 200 nm thick Au films on glass substrates is described. The process combines NSL using spin-coated PS beads with a sputter-etching process. This allows the batch fabrication of several $1000 \mu\text{m}^2$ large hole arrays in 200 nm thick Au films without the use of an adhesion layer for the Au film. The hole size and lattice period can be tuned independently with this method. This allows a tuning of the optical properties of the hole arrays for the desired application.

First, the process outline is described; the important tuning parameters are briefly stated. In the results section, the experimental observations for each crucial process step will be discussed. The results are summarized at the end of this chapter in 5.4..

5.2.1 Process outline

Figure 5.7 shows the schematic of the process flow for the sputter-etch fabrication of hole arrays in thin Au films on glass substrates.

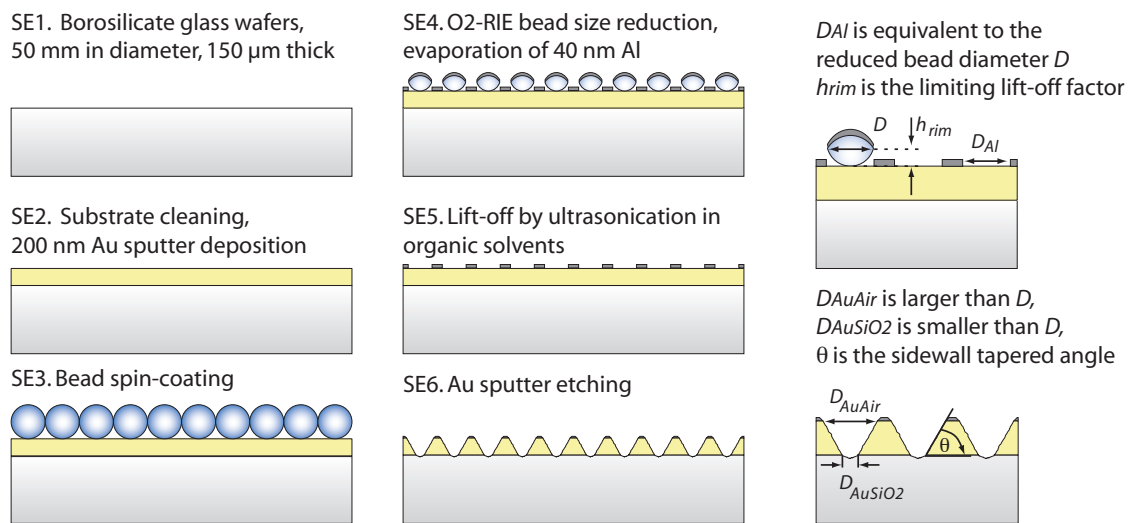


Figure 5.7: Process flow for the fabrication of thin Au films with sub- μm holes on glass substrates.

Preparation of Au substrates

The preparation of the Au coated glass wafers corresponds to process steps SE.1 and SE.2 in figure 5.7. As base substrates, 150 μm thick borosilicate glass wafers of 50 mm in diameter obtained from Karl Hecht Assistent GmbH (Germany) were used. The wafers

were cleaned in organic solvents assisted by sonication and blown dry in a stream of nitrogen. Prior to the Au deposition, the wafer surface was exposed to an argon plasma for 5 min. Then, a 200 nm thick Au film was DC sputtered onto the wafers in a Balzers BAS450 at a rate of 10 Å/s at room temperature. Under these deposition conditions, the adhesion of the Au film to the glass substrate is good, despite the lack of an adhesion layer such as Cr or Ti for the Au. No delamination has been observed after sonication in organic solvents for more than 30 min. This can be attributed to a mechanical adhesion mechanism²⁴⁴ as Atomic Force Microscope (AFM) characterization showed that the glass wafers are decorated with small indentations of ca. 2 nm in depth and width, with a density of ca. 90 indentations/ μm^2 , despite the overall smoothness of the glass substrates ($R_{rms} = 0.5$ nm). For comparison, Au films deposited under the same conditions onto glass substrates of similar R_{rms} , but without the small indentations, delaminated immediately when sonicated in organic solvents.

NSL fabrication of a hole etch mask

The NSL *lift-off* routine was used to fabricate a holey Al film on top of the Au substrates (process steps SE.3, SE.4 and SE.5 in figure 5.7). Two different sizes of polystyrene beads, PSB419 and PSB517, were used. In the remainder of this section, wafers of type **A** and **B** are meant when 419 nm size and 517 nm size beads were used in the NSL process step, respectively. This naming rule also holds for the figures shown.

For spin-coating of the beads, the suspensions were diluted with ethanol just before use (1.5% (v/v) and 2.0% (v/v) for PSB419 and PSB517 beads, respectively). The dilution with ethanol improves the wetting of the wafer surface and speeds up the solvent evaporation. Thus only 100 μl of bead suspension were necessary for the coating of one wafer. The spin-coating was done at room temperature and the relative humidity was controlled between 30 to 40%. To obtain a dense monolayer of beads, the spin-coating parameters (speed, acceleration, dwell time) were determined experimentally and are shown in table 5.1. The quality of the bead layers with respect to the arrangement of the beads (e.g. hexagonally close-packed (hcp) or non-close packed (ncp)) as well as the overall coverage of the wafer surface was analyzed by optical microscopy.

Note that these conditions differ from the optimum conditions found for spin-coating beads onto 4" Si wafers. At the same time, this shows that the bead spin-coating parameters such as spin-speed and humidity can be optimized for the coating of different substrate types and sizes. It also shows that the amount of beads needed for wafer spin-coating can be reduced by adapting the solvent composition and concentration.

After deposition of the beads, the size of the beads was reduced by etching by O_2 -RIE (c.f. O_2 -RIE (N) in chapter 3). The incident RF power was set to 100 W. At a pressure of 200 mTorr, the resulting self-bias voltage was -260 V in this case. As described in

Beads	Spin speed [rpm]	Acceleration [rpm/sec]	time [sec]
A PSB419	500	300	2
	100	100	1
	1500	500	60
B PSB517	500	300	5
	100	300	1
	1500	500	60

Table 5.1: Spin-coating conditions for bead monolayers deposited onto Au coated glass wafers.

chapter 3, the etching of the beads is slightly anisotropic with a faster etch-rate in the vertical than in the lateral direction. The beads on type **A** and **B** wafers were etched in the oxygen plasma for 2 min 40 sec and 3 min 35 sec, respectively, resulting in reduced bead diameter of a D of 195 ± 5 nm and 225 ± 5 nm, respectively.

In the next step, the size-reduced PS beads were used as a lift-off template to fabricate a holey Al mask on top of the Au layer. A 40 nm thick Al film was evaporated at a rate of 4 \AA/s in a Leybold-Optics LAB600H evaporator with a source-substrate distance of approximately 1 m. Lift-off of the PS beads was done by overnight swelling in tetrahydrofuran (THF), followed by sonication in THF and rinsing in organic solvents. Gentle manual polishing during the rinsing process was applied on type **A** wafers to increase the lift-off yield to almost 100%. The size of the holes in the Al layer, D_{Al} was confirmed to be identical to D .

Sputter etching of holes

Finally, holes were etched into the Au film by sputter-etching using the holey Al film as a hard mask (c.f. process step SE.6 in figure 5.7). The etching was done in an Alcatel SCM600 sputtering machine operated in reverse mode. The pressure was set to 5 mTorr and the plasma is sustained under an incident RF power of 400 W, resulting in a self-bias voltage of -190 V. Wafers of type **A** and **B** were sputter etched in a continuous (Cont.) and intermittent (Int.) etching procedure (see 5.2). The continuous etching was done for 30 min, the intermittent etching was done in four steps from 20 to 50 min of cumulative etch time. The resulting hole geometry was analyzed after each etch run by Scanning Electron Microscope (SEM) and AFM imaging.

Wafer type	Procedure Cont./Int.	Etch time [min]
A	Cont.	30
B	Cont.	30
A	Int.	20
		+10 = 30
		+10 = 40
		+10 = 50
B	Int.	20
		+10 = 30
		+10 = 40
		+10 = 50

Table 5.2: Etch protocols used for the continuous and intermittent sputter-etching of holes.

5.2.2 Results and discussion

Spin-coating results

Both **A** and **B** type wafers were homogeneously coated with a monolayer of PS beads by spin-coating. A photograph of a wafer after spin-coating is shown in figure 5.8 (a) (wafer type **A**). Regions of hcp and ncp bead monolayers can be found on the wafer surface. Those regions can be distinguished as shown in figure 5.8 (b) (wafer type **B**). The typical domain size of hcp regions is on the order of several 1000 μm^2 .

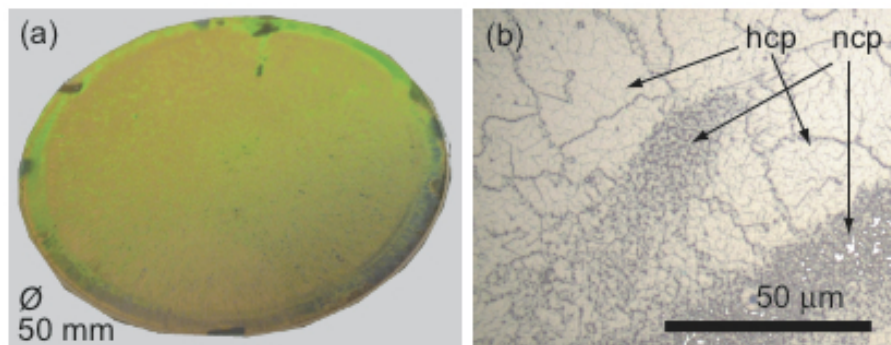


Figure 5.8: (a) Photograph of a 200 nm Au coated glass wafer spin-coated with PSB419 beads. (b) Optical microscope image of a typical region of the wafer shown in (a). Hcp and ncp bead monolayers are indicated by arrows.

Low magnification optical microscope images were taken at several locations across the wafer surface. They reveal long-range order defects in the bead monolayer such as areas not covered by beads or bead multilayers. Image analysis revealed that the

overall defect area occupies less than 10% of the wafer surface. Again, this shows that NSL provides a flexible method for wafer-scale nanopatterning that can be adapted to different bead sizes, bead suspension compositions and substrate types.

Bead size reduction

The bead size reduction has been discussed extensively in chapter 3. No special etch behavior differing from the previously described one has been observed in this case.

Al hole mask

Figure 5.9 shows SEM images of both type wafers after completion of the NSL *lift-off* routine. The holes in the 40 nm thick Al layer precisely reproduce the top-view shading cross-section of the size reduced beads. The size of the Al mask holes is 195 nm on type **A** and 225 nm on type **B** wafers. As the bead surface is roughened during the size-reduction, this roughening translates into small notches in the overall circular holes in the Al mask.

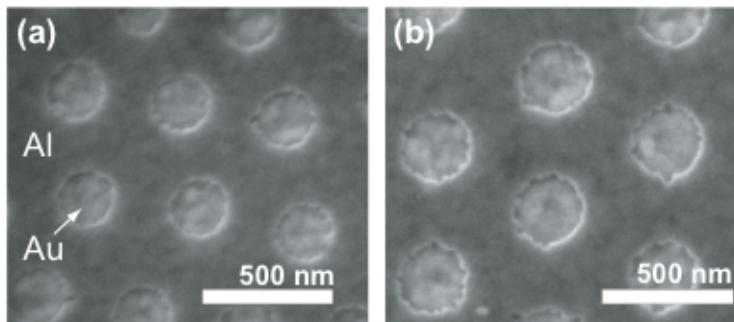


Figure 5.9: SEM images of the holey Al mask fabricated by the NSL *lift-off* routine on Au coated glass substrates using PSB419 (a) and PSB517 (b) beads.

On the type **B** wafers, the lift-off yield was 100% after swelling and sonication in THF. In case of the **A** wafers, the yield had to be increased by applying a gentle manual polishing procedure. This difference in lift-off behavior can be explained by the fact that the rim height h_{rim} of the 419 nm size beads after size reduction is only 50 nm, as compared to 70 nm in case of the 517 nm size beads. h_{rim} is the bead height at the bead's outer diameter(c.f. figure 5.7).

Large arrays of holes by sputter-etching

The advantage of sputter-etching is that it is a parallel process allowing hole fabrication on a full wafer in a single etching step. Figure 5.10 shows SEM images of a type **B** wafer after continuous etching for 30 min. The uniformity of the etching procedure and of the

distribution of holes is shown in figure 5.10 (a). Two distinct areas can be identified in figure 5.10 (a) - regions of a hexagonally close-packed (hcp) and non-close packed (ncp) holes. Domains of good short-range order in the hcp region appear as a Moiré pattern.

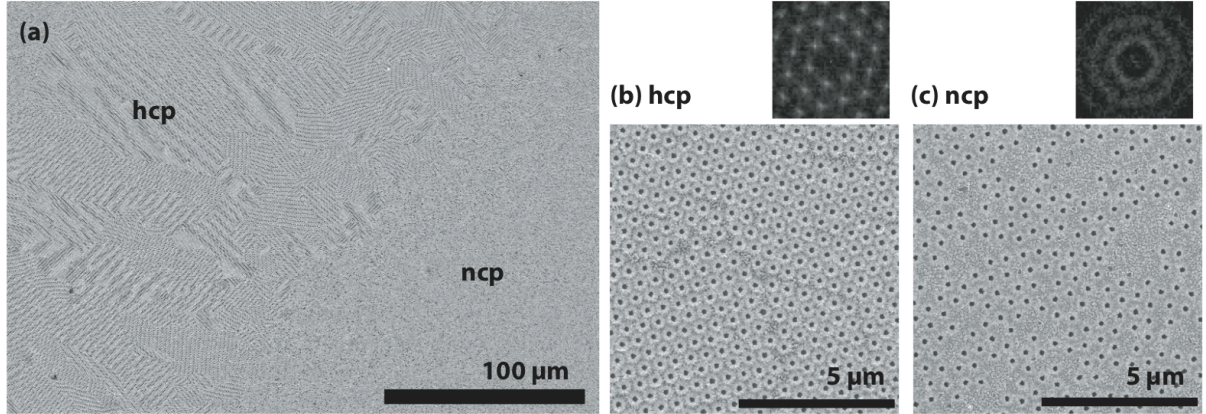


Figure 5.10: SEM images of hole arrays etched into 200 nm thin Au films using PSB517beads as NSL *lift-off* template. (a) Low magnification image showing the homogeneity of the etch result. (b) and (c) are zooms into regions marked as hcp and ncp in (a). The insets above (b) and (c) show the corresponding FFTs.

Figures 5.10 (b) and (c) show a zoom into the areas marked as hcp and ncp in figure 5.10 (a). The insets show the corresponding Fast-Fourier-Transform (FFT) images of figures 5.10 (b) and (c). The FFT of the hcp image shows the peaks of a hexagonal crystal structure, while the FFT of the ncp region shows a ring pattern typical for the absence of long-range order. In the latter case, the radius of the inner ring corresponds to the characteristic distance between the holes in the absence of array order.

Sputter-etch selectivity and widening of the mask holes

Sputter-etching is a purely physical etching process. Therefore, the etch rate mainly depends on the materials hardness. While the bulk hardnesses of Au and Al are similar, Al oxide is much harder than both Au or Al²⁴⁵. The etch rate selectivity Au:Al for plain 20 nm thick films was measured to be ≥ 10 . This may be explained by the presence of a thin Al oxide layer on top of the Al film. Oxidation of the Al mask also has a significant influence on the etch results obtained by either the continuous or the intermittent etching procedure (c.f. below for more details).

For dense patterns with sub- μm features, faceting¹, which erodes the masking layer at the pattern edges, may lead to an early mask failure. In the present case, the masking layer consists of closely spaced holes in a thin Al film. Thus, faceting leads to a widening of the mask holes until they start to merge, eventually resulting in a complete removal of

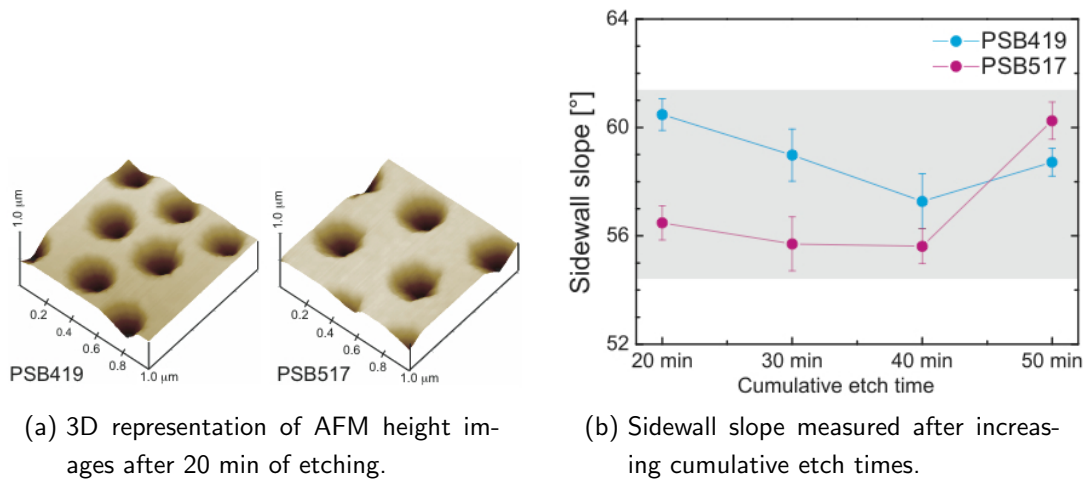


Figure 5.11: AFM analysis of the hole sidewall slope of sputter etched holes.

the masking layer. Thus, in order to obtain a certain hole size for a given hole spacing, it is important to take into account the continuous widening of the mask holes.

When etching the holes into the Au film, the hole will eventually reach the glass substrate and the glass substrate will start to be etched. The etch rate selectivity of Au:SiO₂ was measured to be ≥ 2 for plain substrates. Therefore, although the glass substrate is etched, it is at a much lower etch rate than the Au.

Conical hole cross-section

Figure 5.11 illustrates the cross-sectional hole profile obtained by sputter-etching. Figure 5.11a shows AFM images of both type wafers after 20 min of etching. Figure 5.11b shows the measured sidewall slope for different cumulative etch times when the intermittent etch procedure was used. The data shown in figure 5.11b were obtained by combining AFM height with SEM topography measurements. An image analysis software was used to extract the hole diameters $D_{AuGlass}$ and D_{AuAir} from the SEM images (software: analySIS by OLYMPUS). $D_{AuGlass}$ and D_{AuAir} are sketched in figure 5.7.

For varying cumulative etch times, the sidewall slope is constant around $58 \pm 3^\circ$. This value is in good agreement with theory, according to which the highest etch rate is obtained for ions incident under an angle of 60° to 70° ^{246,218}. Mask faceting, the ion angular distribution and redeposition of non-volatile etch products may explain the slightly lower value of 58° .

Continuous versus intermittent etching procedure

Figure 5.12 shows SEM images of holes on type **A** and **B** wafers after 30 min of *continuous* etching. The hole diameter at the Au-glass interface, $D_{AuGlass}$, is 80 nm and

170 nm on type **A** and type **B** wafers, respectively. This corresponds to a hole filling factor ff of 3% (**A**) and 10% (**B**), where the ff is the hole area at the Au-glass interface divided by the area of a hcp unit cell. The diameter at the Au-air interface, D_{AuAir} is 280 nm (**A**) and 320 nm (**B**). Originally, the diameter of the Al mask holes D_{Al} was 195 nm (**A**) and 225 nm (**B**). Thus the widening of the mask holes diameter during the etching is about 90 nm on both types of wafers. This may be explained by faceting at the mask edges.

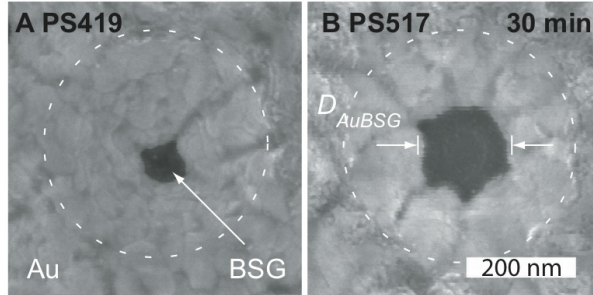


Figure 5.12: Holes in 200 nm thick Au films obtained on type **A** and **B** wafers by the continuous etching procedure. (BSG = borosilicate glass)

The Al masking layer is used up after 30 min of continuous etching. The absence of a residual Al mask was confirmed by energy dispersive X-ray spectroscopy measurements taken before and after the etching procedure and compared to bare 200 nm thick Au films on glass substrates. This shows how an in-situ removal of the masking layer is possible, eliminating the need for a post-treatment to remove the masking layer.

On the other hand, further etching would result in a thinning of the Au layer and in a continuous widening of $D_{hole,AuGlass}$. This limits the attainable $D_{AuGlass}$, and thus the ff , to rather small values. A possible approach to increase $D_{AuGlass}$ and reduce the effect of the mask hole widening would be to use a thicker Al mask. A thicker Al mask, however, may only be realized at the trade-off of accepting a larger D_{Al} as the lift-off metal film thickness is limited by h_{rim} . Using a larger $D_{hole,Al}$, however, faceting would pose a problem as the holes in the Al mask will merge even sooner. Despite a thicker masking layer, early mask failure could be the case. Thus, a more practical solution is either to have a more resistant etch mask, or to modify the etching process.

Figure 5.13 shows SEM images of holes on type **A** and **B** wafers after each step of the *intermittent* etching procedure. The hole size increases with increasing cumulative etch time due to faceting of the mask holes. The relationship between etch time and hole diameter is shown in figure 5.14. With the cumulative etch time increasing from 20 to 50 min, $D_{AuGlass}$ increases from 65 nm to 195 nm and from 105 nm to 250 nm for type **A** and type **B** wafers, respectively. The corresponding hole filling factor can thus be tuned from 2% to 19% (**A**) and 4% to 20% (**B**). This shows how the continuous

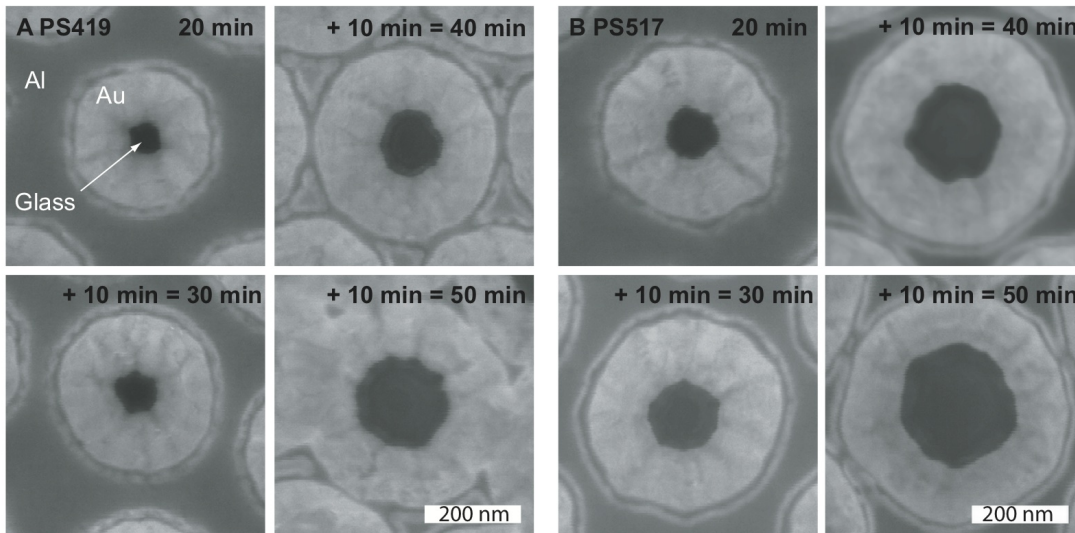


Figure 5.13: Holes in 200 nm thick Au films obtained on type **A** and **B** wafers by the intermittent etching procedure.

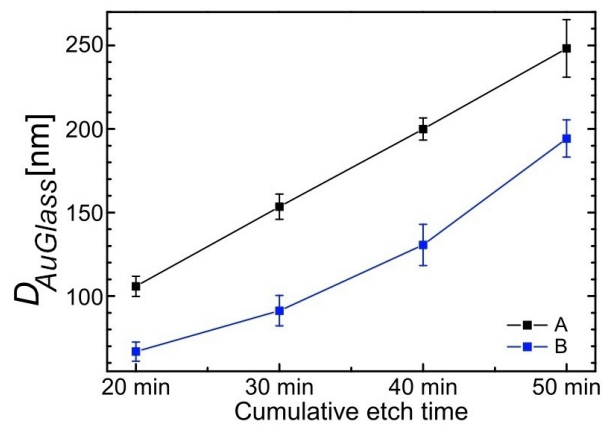


Figure 5.14: The hole diameter at the Au-glass interface as a function of increasing cumulative etch time.

widening of the holes in the Al mask provides a convenient way to obtain different hole diameters for originally identical mask dimensions.

Another observation from figure 5.13 is that the Al mask is still valid even after 50 min of cumulative etch time, while it was completely removed after only 30 min of continuous etching. Two factors contribute to the prolonged mask lifetime: a) a re-oxidation of the Al masking layer in between the consecutive etch runs and b) reduced heating during the etching process. The prolonged mask lifetime allows to use a thinner masking layer and still achieve a large hole size without reducing the Au film thickness. A thinner masking layer also allows to realize smaller mask hole diameters which are limited by the height of the PS bead lift-off template in the NSL process step.

5.2.3 Preliminary conclusions

By combining NSL using spin-coated PS beads with a sputter-etching process, nanoscale hole arrays in 200 nm thick Au films were fabricated on 50 mm in diameter glass wafers. All process steps are wafer-based and thus allow a low-cost, high throughput fabrication. The hole array periodicity is determined by the original size of the PS beads (419 nm and 517 nm in the present case). The order of the arrays is dependent on the spin-coating parameters and can be optimized. By O₂-RIE size-reduction of the deposited PS beads, the hole size in the Al etch mask can be tuned. Sputter-etching is then used to transfer the Al hole mask into the Au layer. The resulting holes have a conical cross-section with a sidewall slope of ca. 58°. By adapting the sputter-etch parameters, different hole sizes in the Au film can be realized without the need to modify the Al mask. For example, the hole size in 200 nm thick Au films was tuned from 65 to 195 nm for a mask hole diameter of 195 nm, or from 105 to 250 nm for a mask hole diameter of 225 nm.

5.3 Gold thin films and membranes with sub- μm holes using Si and oxidized Si pillars as lift-off template

200 nm thick Au membranes with sub- μm holes were fabricated using Si and oxidized Si pillars as inorganic lift-off template. The high aspect ratio of the pillars allows the fabrication of holes with almost vertical sidewalls and an aspect-ratio > 1 . The pillars are fabricated using wafer-scale NSL with PS beads. In this way, up to 1200 μm large holey membranes were fabricated in a parallel process. The hole size and spacing depends on the initial bead template and can be varied by choosing beads of a different size and adjusting the bead size reduction parameters. Here, membranes with hole sizes in the range of 150 nm to 300 nm in diameter with a spacing of 428 nm and 535 nm were fabricated. Two process schemes have been developed: (1) Free-standing membranes supported by a Si frame were fabricated, and (2) holey thin Au films were realized on a Si substrate and then transferred to a transparent, flexible layer.

One application of the holey Au membranes are surface plasmon resonance based sensors (c.f. chapter 1). Therefore, one criterion was the realization of Au membranes either totally without the use of a lossy metal adhesion layer such as Cr or Ti, or with the option to remove the adhesion layer within the process flow. Other important criteria were that the attainable Au film thickness be at least 200 nm and that the hole arrays cover an area of at least $100 \times 100 \mu\text{m}^2$. All of these specifications were met successfully.

First, the developed process flows are briefly described. Then, the use of Si and oxidized Si pillars as an inorganic lift-off template is described. The fabrication of the pillar etch mask and pillar etching are described in chapters 3 and 4, respectively. The fabrication of the holey free-standing Au membranes and membranes on a flexible substrate are described in two separate sections.

5.3.1 Process outline

Figures 5.15 and 5.16 show the schematic process flows for the fabrication of Au membranes with sub- μm holes supported by a Si frame and transferred to a thin flexible substrate, respectively. The first two process steps are identical. The initial substrate was a Si wafer with arrays of oxide dots. These dots served as a mask in the subsequent Si-DRIE process and were fabricated using the NSL *lift-off* routine in combination with photolithographic micro-patterning. This as well as the fabrication of high aspect-ratio Si pillars with controlled sidewall shape is described in chapter 4.

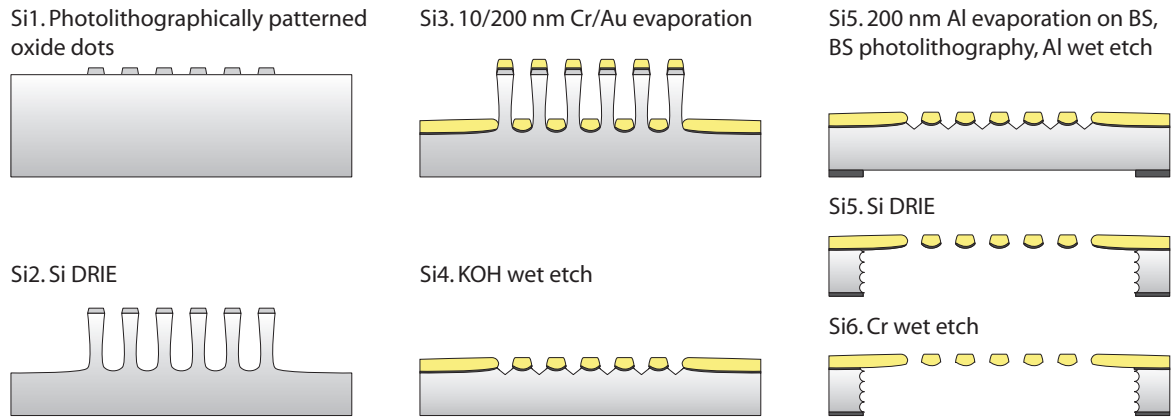


Figure 5.15: Process flow for the fabrication of Au membranes with sub- μm holes.

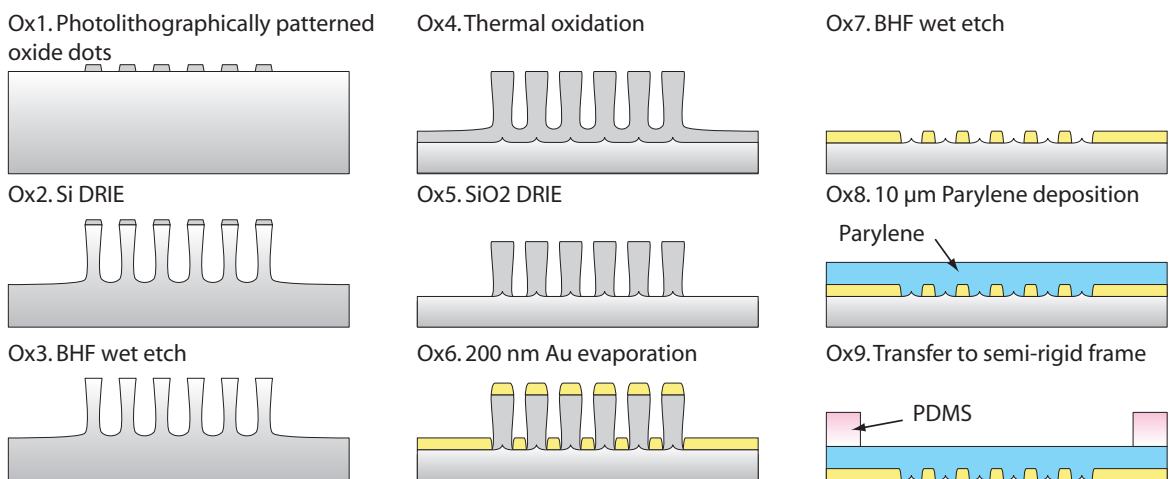


Figure 5.16: Process flow for the fabrication of thin Au films with sub- μm holes on flexible substrates.

After etching of the Si pillars, the two process flows differ. For the fabrication of the free-standing holey Au membranes, the Si pillars were used as they were. A 10/200 nm thick Cr/Au layer was deposited onto the wafers in a highly directional evaporation procedure. Then, the pillar template was removed by wet-etching in KOH. The membranes were released by Si-DRIE. For the backside mask, 200 nm of Al were deposited onto the wafer backside and windows aligned to the frontside micro-patterns were defined by photolithography and Al wet-etching. An alternative backside patterning procedure using a SiO₂/SiN etch mask is briefly described in the appendix A.6. Finally, the Cr was removed in the membrane area by wet-etching.

In case of the fabrication of holey Au membranes transferred to a flexible substrate, the Si pillars were first thoroughly cleaned and the intermediate oxide dot mask was removed by BHF wet-etching (buffered hydrofluoric acid²⁴⁷). Then, the pillars were thermally oxidized with an oxidation depth $\geq 1/2$ of the maximum pillar diameter. This was followed by anisotropic SiO₂-DRIE until the Si substrate around the pillars is reached. The shape of the oxidized pillars is not majorly affected by this. Then, 200 nm of Au were directionally evaporated onto the substrates. By careful HF wet-etching, the oxidized Si pillars were removed, resulting in a micro-patterned holey Au film. 10 μ m of Parylene-C (c.f. A.4) were conformally deposited onto the substrates. Then, the parylene was carefully peeled-off. As the adhesion of parylene to Au is superior to the one of Au to Si, the holey Au films could be leveled off and were glued to a PDMS (polydimethylsiloxane) frame.

5.3.2 (Oxidized) Si pillars as lift-off templates

Choice of Si-DRIE etch process: Bosch-type or continuous

Initial tests were performed to validate that the shape of high aspect-ratio Si and oxidized Si pillars are suitable as lift-off template for Au films with a thickness ≥ 200 nm. Two types of Si-DRIE etch procedure were used: a cycled Bosch-type process and a continuous etch procedure. For both types of etch process, an aspect ratio ≥ 5 was achieved.

Dot arrays were written by e-beam lithography into thin nLOF-photoresist on double-side polished Si wafers with a 100 nm thick thermal oxide. The photoresist pattern was transferred into the oxide layer by SiO₂-DRIE. After stripping of the photoresist, the oxide dots were used as hard mask in either continuous or Bosch-type Si-DRIE etching. In the continuous Si-DRIE etch procedure, the SF₆/C₄F₈ gas ratio was 40/55 sccm with an ICP/RIE power of 1500/15 W. In the Bosch-type process, SF₆/CH₄/O₂ cycle times were 2.5/2/1 sec with an ICP power of 1500 W and a pulsed RIE coupling of 90 W only during the SF₆ cycle. The gas flows were 300/200/100 sccm, respectively. A Bosch-type

process has the advantage to surely provide undercut patterns due to scalloping. On the other hand, the lateral scallop depth is difficult to control at nanoscale dimensions due to the extremely short cycle times and singular large scallops may result in a pillar cut-off. When tuning the etch gas and ICP/RIE electrode settings appropriately, the continuous etch type procedure is suitable for the vertical etching of Si structures²⁴². Here, it was to be investigated if the verticality of Si pillars and under-cut of the oxide dot mask is sufficient to provide a reliable lift-off template, and whether this is maintained after oxidation of the pillars. Thus, one half of the test-wafer was thermally oxidized after etching of the Si pillars with a nominal oxide thickness of 100 nm.

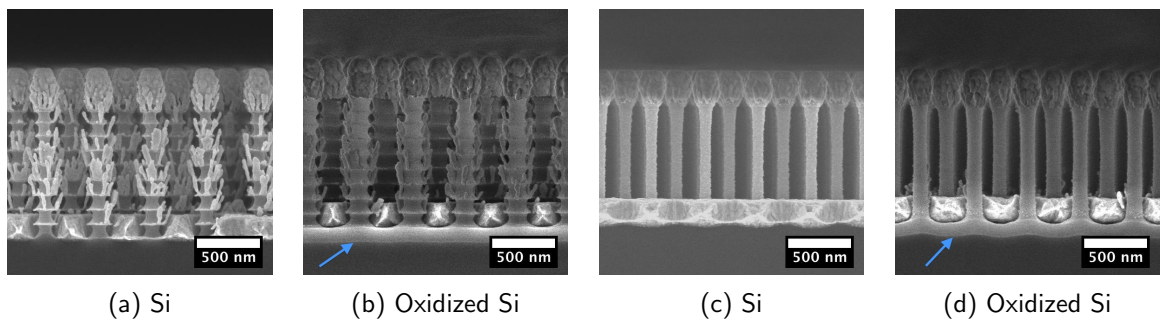


Figure 5.17: Cross-sectional SEM images of Si (a,c) and oxidized Si (b,d) pillars etched by Bosch-type (a,b) or continuous (c,d) Si-DRIE. 10/200 nm Cr/Au and 200 nm Au were evaporated onto the Si and oxidized Si pillars, respectively. The dot mask for those initial tests was patterned by EBL.

10/200 nm Cr/Au and 200 nm Au were directionally evaporated onto Si and oxidized Si pillars, respectively. Cross-sectional SEM images after evaporation are shown in figure 5.17. The pillars shown in 5.17a and 5.17b were etched by a Bosch-process, those shown in 5.17c and 5.17d were etched by continuous etch procedure. The latter ones (b and d) were oxidized; the transition from the Si base substrate to the oxide top-layer is indicated by blue arrows.

In all cases, the directional evaporation was successful, the metal layer at the bottom of the pillars is disconnected from the pillar tops and thus will provide a suitable lift-off template. Volume growth due to oxidation does not have a significantly negative influence, the under-cut is preserved in all cases.

The scallops of Bosch-type Si-DRIE etched pillars pose a problem, however. Columnar vertical growth of metal from the outmost extension of the scallops is observed. This means a reduced material deposition at the bottom of the pillars, making a controlled film deposition difficult. Also, the columnar growth threatens to form an interconnected network for thicker films, thus limiting the applicability as a lift-off template for thick Au films. Therefore, in the following, Si pillars etched by the continuous type Si-DRIE were used as a lift-off template.

Lift-off in KOH and BHF

In the next step, the lift-off procedure was validated. Si and oxidized Si pillars served as inorganic lift-off template. Figure 5.18 shows the pillar templates after metal evaporation and the resulting holey metal films after lift-off. In both cases, PSB428 beads were used for the initial dot mask patterning. The micro-patterning and transfer into high aspect ratio pillars is described in chapter 4.

Si pillars shown in figure 5.18a were etched for 1 min in a continuous type Si-DRIE at 10°C with a 40/50 sccm SF₆/C₄F₈ etch gas ratio. The ICP/RIE RF power was 1500/15 W, resulting in a low self-bias of ca. -8 V. The pillar aspect-ratio was 7. The pillars shown in figure 5.18c were etched under the same conditions except for a different etch gas ratio. Here, the ratio was set to 35/55 sccm SF₆/C₄F₈ and etching was done for 2 min 30 sec; the pillar aspect-ratio was 4. The gas ratio was adapted after calibrating the resulting pillar shape with test samples. The etch rate could be lowered by reducing the ratio of the etch gas SF₆ to the passivation gas C₄F₈. In this way, the desired pillar shape was obtained.

After pillar etching, the substrates were thoroughly cleaned by treatment in an oxygen plasma, Piranha and an HF dip. Then, the wafer was thermally oxidized with a nominal oxide thickness of 200 nm. After oxidation, the bottom SiO₂ was etched directionally by SiO₂-DRIE for 1 min at 10°C. The etch progress was monitored with an endpoint detection system and removal of the SiO₂ at the bottom of the pillars was confirmed by SEM imaging.

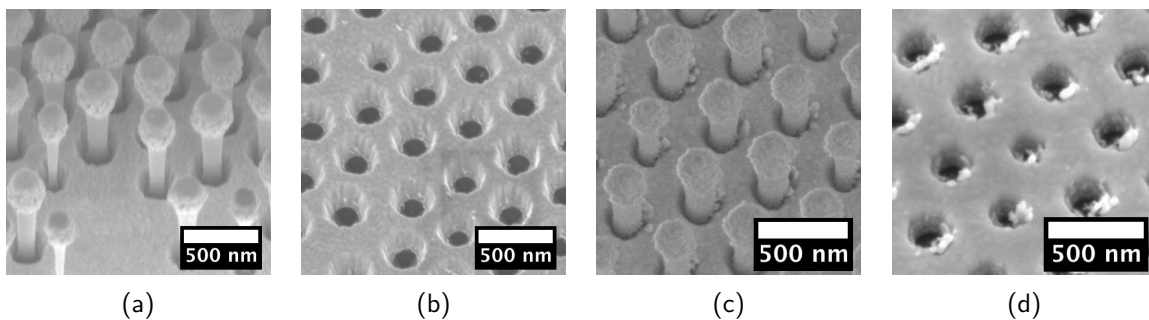


Figure 5.18: SEM images after metal evaporation and lift-off. (a,b) Si pillars with 10/200 nm Cr/Au and after lift-off in KOH. (c,d) Oxidized Si pillars with 200 nm Au and after lift-off in BHF. All SEM images were taken under a tilt angle of 30°.

10/200 nm Cr/Au and 200 nm Au were evaporated directionally onto wafers with Si and oxidized Si pillars, respectively (figures 5.18a and 5.18c). The metal was deposited only onto the pillar tops and at the bottom of the pillars, no metal was deposited onto the pillar sidewalls. A small columnar growth was observed towards one side at the

base of the oxidized Si pillars. This is due to a slight inclination of the wafer during evaporation, i.e. the wafer was not perfectly aligned at a right angle with respect to the evaporation source. The metal caps on top of the pillars also grew in the horizontal direction, thus increasingly shading the bottom substrate, which is a limiting factor for lift-off of thick metal films when holes of vertical sidewalls are desirable.

Figures 5.18b and 5.18d show the holey metal films after lift-off in 40% KOH at 60°C and in a 1:1 by volume mixture of BHF and water at room-temperature, respectively. (Note that the use of this harsh base and acid limits the lift-off procedure to metals not attacked or deteriorated by these chemicals, such as Au and Cr.) KOH etching was done for 1 min, the onset of the etching process was observed by eye as it was linked to a strong H₂ gas bubble generation. Equally, once the Si pillars were etched, the etch process naturally slowed down when facing (111) Si planes. At that point, the wafer was removed from the KOH etch solution, immersed in water and sonicated at room temperature. The sonication was necessary to level up metal caps attached to the wafer surface (also c.f. below). The leveling off of these caps was observed by eye as milky clouds dispersing into the water. Also, the micro-patterned areas changed their optical impression from dark (due to incoherent light diffraction by the metal caps) to bright golden color. In order to remove the caps from the Au surface across the whole wafer surface, the wafer had to be rotated and placed in different locations in the sonication bath as the sonication power had local concentration points in the bath. The overall sonication process took \approx 2 min. Afterwards, the wafer was rinsed under flowing water and left for drying in air.

BHF etching of the oxidized Si pillars was done in a similar way, first etching the inorganic pillar template and then removing the metal caps from the surface by sonication of the wafer in water. Pillar etching was done for 1 min. Here, the etch progress could not be as easily observed as it does not involve gas generation. The security issues associated with HF etching hindered observation of color changes on the substrate as an indication of the etch process. After HF etching, sonication in water was done in a similar way as described in the KOH lift-off procedure. However, in this case, care had to be taken due to the weak adhesion of the Au film to the Si substrate. Rinsing was done by carefully immersing the wafer several times in fresh Di-H₂O. The wafer was left for drying in air.

Figure 5.19 shows photographs of wafers after KOH (a) and BHF (b) lift-off. The Cr/Au surface in the KOH lift-off case is intact. On the other hand, the problem related to a delamination of the Au film during sonication is visible in the BHF lift-off case. Arrows in the middle of the wafer in figure 5.19b indicate areas where the Au film peeled off. At the border of the wafer, damage is primarily due to handling of the wafer with tweezers.

While the KOH lift-off result was overall uniform also on large micro-patterned areas

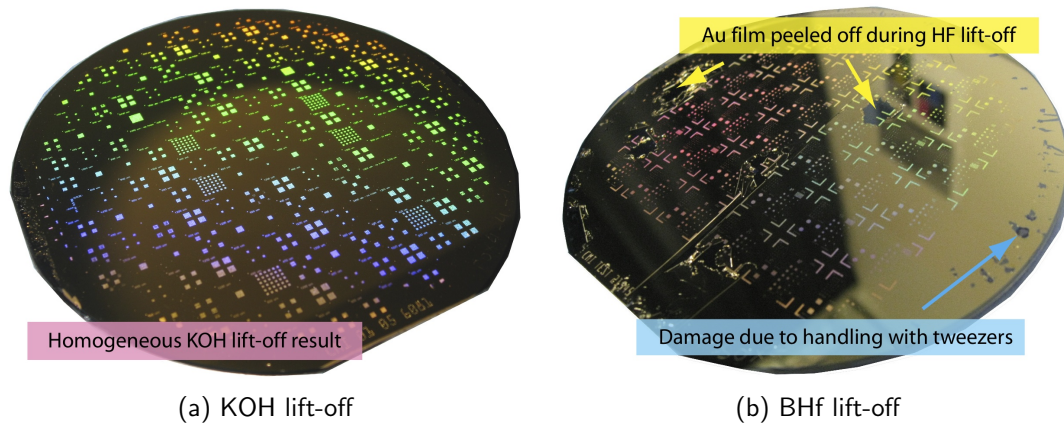


Figure 5.19: Wafer photographs taken after lift-off of 10/200 nm Cr/Au and 200 nm Au in KOH and BHF, respectively. The corresponding SEM images are shown in figure 5.18.

and across the whole wafer surface, the limited sonication time in the case of BHF lift-off lead to many holey areas still covered with Au caps. This is shown in figure 5.20. Figure 5.20a shows an optimum result where a large micro-patterned area was rendered almost free of Au caps. In a less optimum case, the result was as shown in figure 5.20b where almost all Au caps remained on the surface. A zoom of such a Au cap is shown in figure 5.20c. Initial trials to prevent the Au layer from delamination by protecting it with photoresist did not prove to be successful. Other remedies to solve this issue are under investigation. Improvements can be made by using a pillar template with even higher aspect ratio, modifying the BHF etch procedure (e.g. under continuous laminar flow), or performing the lift-off on small chips.

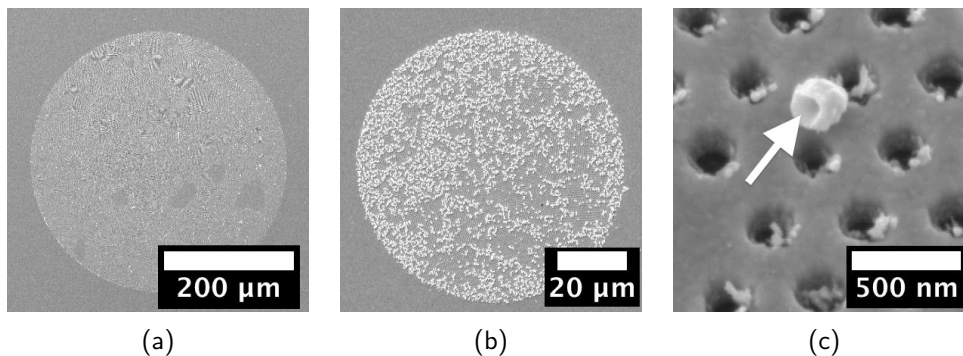


Figure 5.20: Ultra-sonication of full wafers in Di-H₂O was restricted by Au delamination. Thus, while in some areas the lift-off was successful (a), in others (b,c), the holey layers remained covered with Au caps (arrow in (c)).

5.3.3 Au membranes with sub- μm holes

The following process steps involve the backside release of the micro-patterned layer by Si-DRIE and removal of the Cr adhesion layer by wet-etching. This concerns fabrication steps Si5 and Si6 in figure 5.15. Full 4" wafers were processed to the end of this fabrication procedure. Figure 5.21 shows the same wafer, first after spin-coating with the PSB428 bead template, then after micro-patterning of the oxide dot mask, and finally after Si-DRIE membrane release. Only few membranes were broken. This is related to over-etching in the Si-DRIE as the etch rate radially increased towards the wafer border. Another factor was aspect-ratio dependent etching (ARDE), although this was partially compensated by integrating grill structures in the larger membrane openings (c.f. appendix A.7).

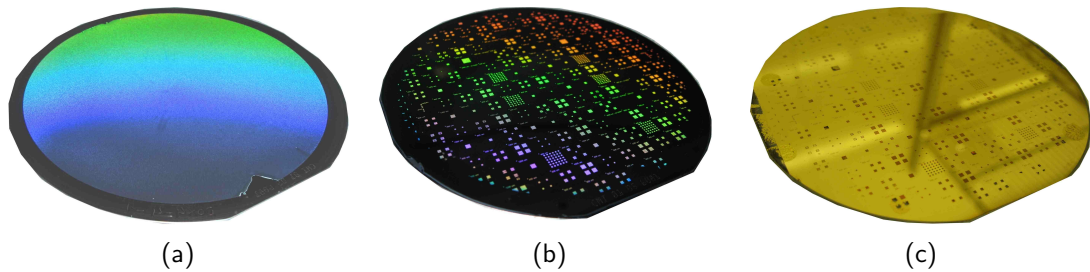


Figure 5.21: Photographs of DOX4-4-1 at different processing steps: (a) after spin-coating of PSB428. (b) After patterning the oxide dot mask by BHF wet-etching. (c) After backside release of 20/200 nm thick Cr/Au holey membranes by Si-DRIE.

For the backside release by Si-DRIE, the $380 \pm 10 \mu\text{m}$ thick double-side-polished wafer was glued to a handle wafer with a solid resin dissolvable in acetone and a melting temperature of 135°C (Quickstick QS135). A 200 nm thick Al layer on the wafer backside was patterned and served as Si-DRIE etch mask; the Cr layer served as an etch-stop layer. Anisotropic etching using a Bosch-type process with 7/2 sec etch/passivation cycle times and an etch rate on the order of $4 \mu\text{m}/\text{sec}$ was used (“SOI accurate ++++”), in conjunction with an isotropic etch process with a vertical/lateral etch rate on the order of $4/2 \mu\text{m}/\text{sec}$ (“Si release”).

After etching $100 \mu\text{m}$, an isotropic etch was performed to partially remove the ARDE compensation structures. The detached ARDE Al grill was removed by blowing the wafer in a stream of nitrogen. Etching was continued anisotropically, the etch depth was regularly controlled with an optical microscope equipped with a micrometer measurement gauge. The onset of the release was also observed visually (transparency of the etch windows). At that point, only the Si release procedure was used in steps of 1 min. Etching was stopped when larger membranes started to break due to over-etching. At

that point, ca. 80% of all membranes had been released. In some cases, remains of the ARDE structures were left.

Before wet-etching of the Cr adhesion layer, electron-dispersive X-ray (EDX) spectra were taken on the membranes for comparison of the membranes material composition before and after wet-etching. In the material analysis, Au, Cr, Al and Si were compared. A strong Al peak was visible, while a Cr peak was only found on some of the membranes. This is due to the comparatively small amount of Cr present. (As shown in chapter 7, the Cr removal by wet-etching was confirmed by comparing the optical transmission spectra before and after Cr wet-etching.) The presence of Al is attributed to the use of the Al backside etch mask and the ARDE structures. An Al wet-etch was thus performed in addition to a Cr wet-etch. (Standard wet-etchants were used, such as CR-7 with Iodine and Al etch type A²⁴⁷). The relative amount of Al as measured by EDX was reduced. Due to the thinness of the membranes, it can not be excluded that the Al peak stems from the wafer substrate holder used during EDX spectra recoding in the SEM. A different analysis technique is thus required.

Both Al and Cr etches were done at room temperature, the etch progress was observed visually. Etching was done by immersing the wafers horizontally in laboratory glass ware petri dishes (c.f. figure 5.22a). Rinsing was done by multiple vertical immersions in Di-H₂O. The etched wafers were left for drying in air.

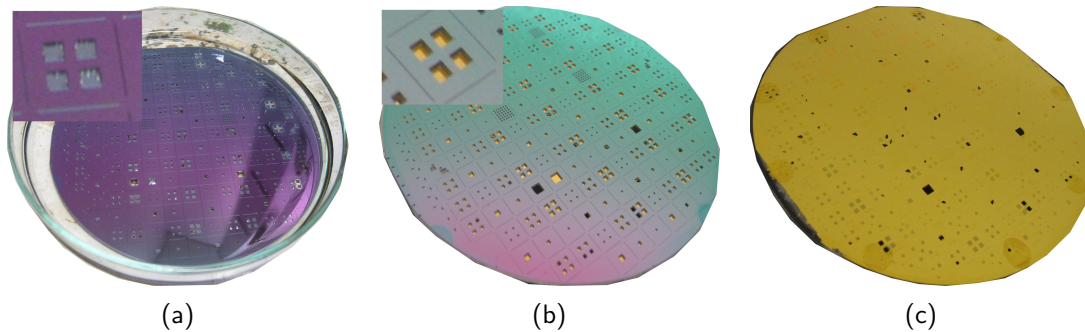


Figure 5.22: Photographs of DOX4-5-1 immersed in Al wet-etch (a) and in dry state after completion of the Cr wet-etch: backside (b) and frontside (c).

The wet-etch procedures caused additional harm to the membranes, and the yield at this final stage of the fabrication process was $\approx 30\%$. This can be improved by using vertical etch setups as most membranes broke during horizontal immersion of the wafers into the etch solution, especially in case of the rather viscous Al etchant.

The removal of the Cr adhesion layer was visible as the membrane backside changes from grey to golden. This is shown in the insets of figures 5.22a and 5.22b. The green-purple color in of the Si wafer backside is due to the presence of a 650/200 nm thick SiO₂/SiN layer. A photograph of the wafer frontside is shown in figure 5.22c. Here, the

broken membranes can be distinguished as black holes.

In the following, it will be described how initial bead template was preserved throughout the process. In summary, this is shown in figure 5.23. Shown are top-view SEM

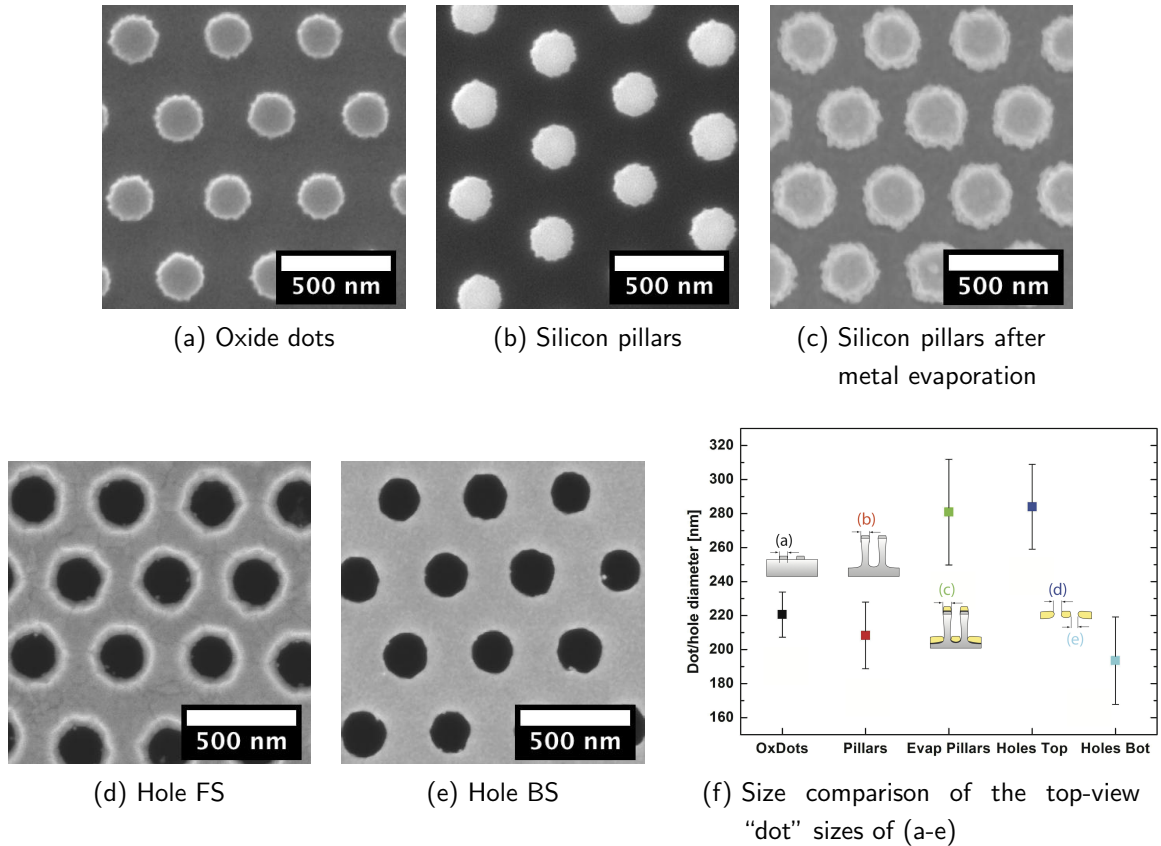


Figure 5.23: SEM images of the DOX4-4-1 wafer at different processing steps (a-e). The evaporated metal film thickness was 20 nm Cr + 200 nm Au. (f) Comparison of the “dot” sizes.

images of the same wafer. From (a) through (e), it shows the oxide dot mask, the Si pillars, the Si pillars with 20/200 nm Cr/Au evaporated on top, and a frontside and backside image after membrane release. Figure 5.23f is a graph with the measured dot/hole diameters, the error bars correspond to the 2σ standard deviation. The oxide dots, Si pillars and backside hole dimensions are of similar size with average diameters of 220 nm, 208 nm and 197 nm, respectively.

The decrease in size is explained as follows: The oxide dot mask is “used” during Si-DRIE, particularly at the edge. This results in a reduced Si pillar diameter. Then, the cross-sectional sidewall shape of the Si pillars was etched to be negative, i.e. having an under-cut (also c.f. the tilted SEM image in figure 5.18a). Au has a high mobility and thus, even if evaporated directionally, it diffuses closer to the pillar bottom and thus narrows the hole diameter as compared to the pillar top.

The evaporated pillars and the frontside hole diameter are 80 nm wider as compared to the pillars before evaporation. This is due to a horizontal growth of the metal caps formed on top of the Si pillars.

The holes have a sidewall cross-section which is almost vertical. For a 200 nm thick Au film, a difference in hole size from the bottom to the top of 80 nm in diameter yields a sidewall taper of 11° (90° corresponds to vertical sidewalls).

5.3.4 Au films with sub- μm holes transferred to parylene

The process chart for the transfer of thin holey Au films to parylene, a flexible transparent polymer, is shown in figure 5.16. The main differences as compared to the fabrication of holey Au membranes (figure 5.15) is that (1) the Si pillars are oxidized after Si-DRIE etching, (2) Au is evaporated without the use of an adhesion layer, (3) the lift-off is done in BHF, and (4) the holey films are not released from the backside, but transferred to a transparent flexible polymer film. The use of oxidized Si pillars as lift-off template and the lift-off procedure have been described in the above section 5.3.2. Here, the transfer of the holey Au film to parylene will be described. (Also c.f. Parylene® in section A.4 which also contains the description of an initial experiment to validate the adhesion of Au to parylene.)

Two transfer options were investigated as shown schematically in figure 5.24. In one case, the parylene was left as deposited and the parylene/holey Au composite layer was peeled off and transferred to a rigid support frame. In the other case, photolithography was done after parylene deposition to define windows accessible for etching by O_2 -RIE. The etch windows were aligned to the micro-patterned holey Au areas. By choosing an appropriate photoresist thickness, the parylene can be locally removed. Simultaneously, this etches the photoresist. Then, the patterned parylene/holey Au composite layer was attached to a semi-rigid frame, e.g. made from a thin PDMS sheet (poly-dimethylsiloxane), and peeled off.

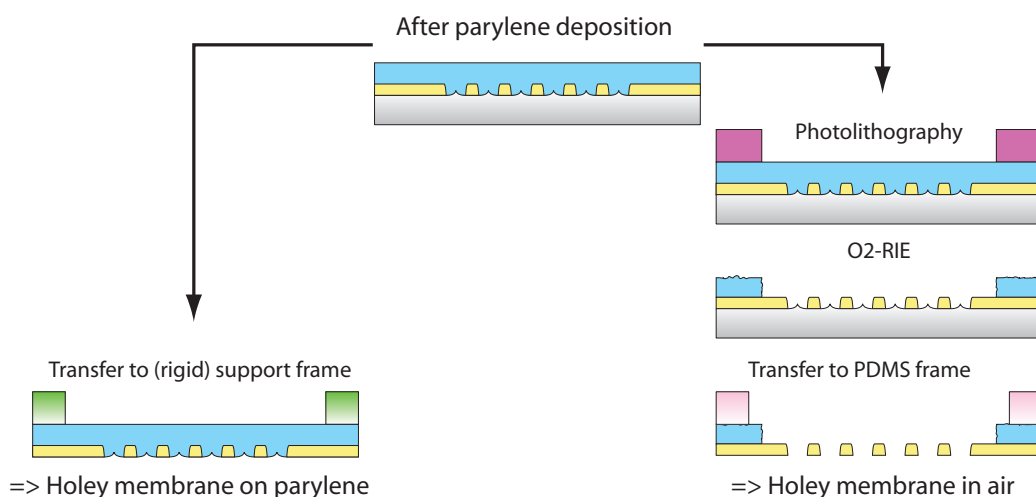


Figure 5.24: Two options for the transfer of holey Au films to a flexible substrate. Leaving the parylene unpatterned renders the Au/parylene composite layer more rigid. For some applications and characterizations, however, it may be interesting to locally remove the parylene by etching in an oxygen plasma.

Figure 5.25 shows photographs of the chips prepared for the two processing options. Figure 5.25a shows the un-patterned parylene/Au layer before peeling it off the Si chip. For that purpose, the conformally deposited parylene was cut with a scalpel. Holey Au regions can be identified by eye. Figure 5.25b shows a patterned parylene/Au composite layer after peeling it off using a PDMS frame. In the middle of the PDMS frame, holey Au membranes are free-standing in air.

After peeling off the parylene/Au composite layers and transferring them to a transport substrate, the samples were analyzed by optical microscopy and SEM imaging. Figure 5.26a and 5.26d are optical microscope images of holey Au films on parylene and free standing holey Au membranes in air surrounded by parylene, respectively. In the images shown, the structures are flat without wrinkles or cracks. This shows that parylene/Au composite layers can be peeled-off without damaging the holey Au layer. It also shows that large holey Au films can be produced by the technologically involved BHF lift-off procedure (c.f. section 5.3.2) and be further processed (parylene deposition, photolithography, dry-etching). In figure 5.26a, arrows indicate small bumps on the parylene surface. Such bumps were not observed for parylene deposited onto Si blank wafers. The origin of these bumps may be related to surface structures acting as deposition nucleation sites. For some applications, e.g. in optics when light is transmitted through the membranes, these bumps cause undesirable light focussing or diffraction effects.

Figure 5.26b shows an SEM image of a parylene/Au composite layer where the holey Au film was torn apart. The Au film was still supported by the parylene film. This

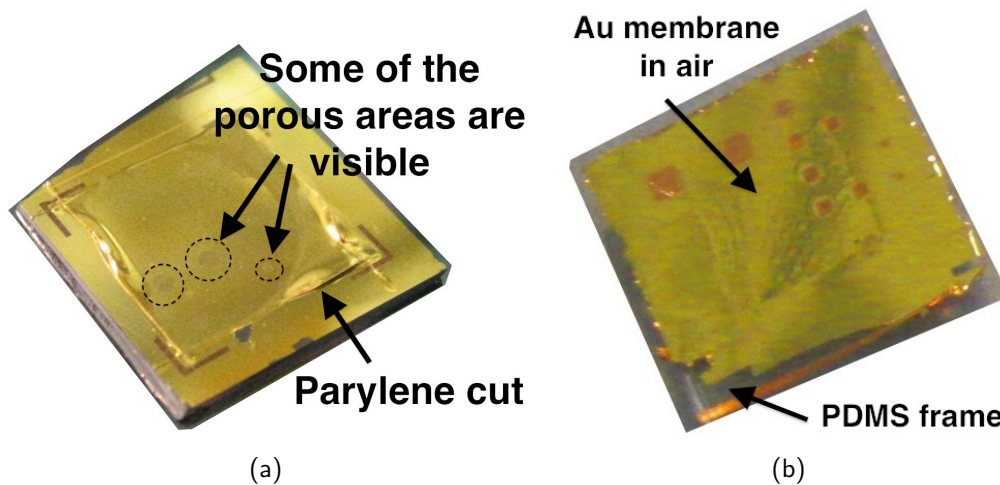


Figure 5.25: (a) The unpatterned parylene/Au layer prepared for peel-off. A parylene square is cut. (b) A patterned parylene/Au layer has been peeled off using a PDMS frame.

damage occurs when the Au film undergoes excessive stress when being pulled off the substrate. The stress is caused by locally good adhesion of the Au film to the substrate, e.g. due to mechanical stiction to the structured surface. Another reason is distortion of the peel-off frame during pull-off. The latter can be amended by improving on the design of the semi-rigid transfer frame used for pulling off the parylene/Au composite layer. At the same time, this example shows the advantage of having a continuous flexible film to support the holey Au layer. Depending on the application, the device would still be functional. The arrow in the inset in figure 5.26b points to a protrusion in the parylene layer. This stems from the parylene being “molded” into the holes in the Au film. This exemplifies the conformal deposition of parylene also into sub- μm size features.

A high magnification image of a holey Au film supported by parylene is shown in figure 5.26c. It shows the smoothness of the Au film surface that was molded from the Si substrate. The impression is that hillocks exist between the holes. (This, however, remains to be confirmed by AFM imaging.) An explanation for these hillocks would be the rounded interstitial space at the bottom of the initial Si pillars.

Figure 5.26e and figure 5.26f show SEM images of a micro-patterned holey Au layer surrounded by a micro-patterned parylene layer. The image was taken before peeling off the parylene/Au composite layer. Figure 5.26f is a zoom into the transition regions from the holey Au layer to the non-hole Au layer, and from there to the Au layer coated with parylene. In the region exposed to the RF coupled O_2 -plasma, the parylene has been cleanly removed from the Au surface. No obvious damage has been done to the Au surface (high magnification SEM images not shown). This is noteworthy because holey Au membranes in air fabricated by the Si pillar templating procedure (c.f. section 5.3.3)

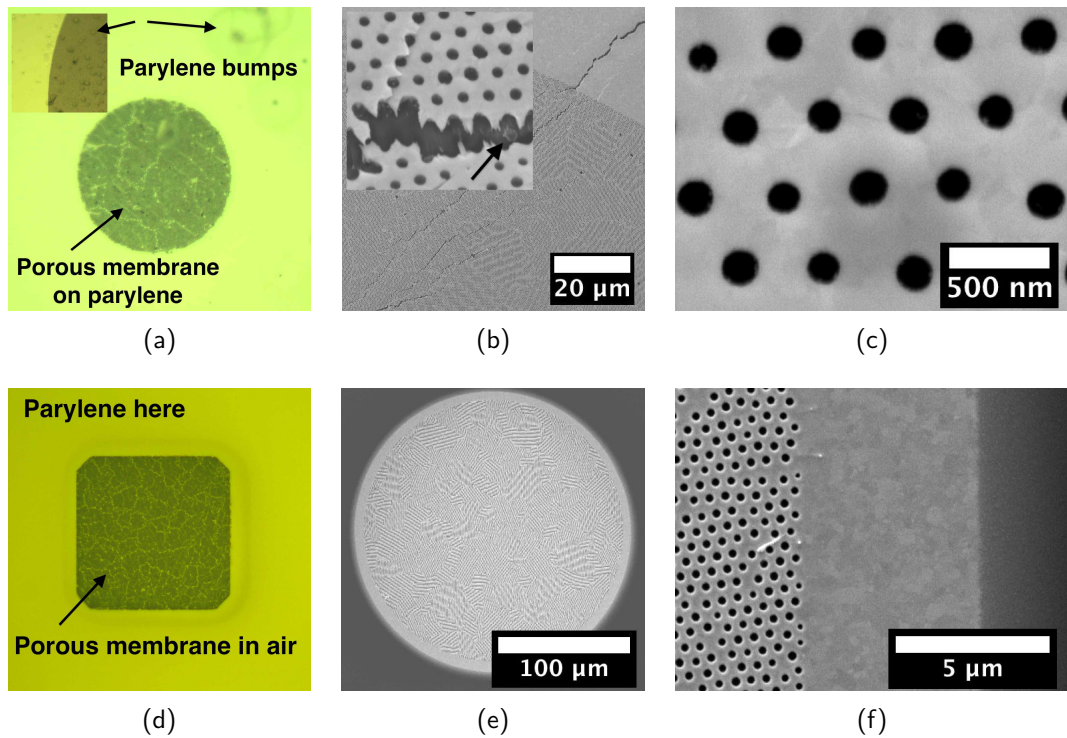


Figure 5.26: Optical microscope and SEM images of holey Au films and membranes transferred to parylene as a flexible substrate. (a-c) Continuous parylene layer, (d-f) parylene locally removed on top of holey Au film. (a) Holey Au layer coated with parylene. (b) A crack in the Au film supported by parylene. (c) The Au layer molded from the Si/oxidized Si pillar template is smooth. (d) Holey Au membrane in air supported by a parylene frame. (e) Parylene has been etched on the patterned holey Au film. (f) The parylene has been cleanly removed from the Au surface.

were severely damaged after 1 min exposure to a 500 W microwave generated O₂-plasma in a barrel reactor^{1,218}.

A size comparison of the dot/hole diameters as done in the previous section will not be described here. It can be assumed that the relationship between the oxidized Si pillar diameter and the resulting holes is the same as in case of the Si pillars used as a lift-off template in KOH.

5.3.5 Preliminary conclusions

Micro-patterned oxide dot arrays were fabricated by the NSL *etch* routine and photolithography. These dot masks were then used to create high aspect-ratio Si pillar with a negative side-wall profile. A pillar aspect ratio ≥ 5 was obtained. Si pillars and oxidized Si pillars were then used as inorganic lift-off template for the fabrication of 200 nm thick Au membranes and films on a flexible polymer substrate. The oxidized pillars underwent an additional SiO₂-DRIE in order to remove the SiO₂ at the bottom of the pillars. Cr/Au and pure Au films were directionally evaporated onto the pillars. In this way, holes with a sidewall taper of 80° were realized.

Au membranes with hole arrays using Si pillars as lift-off template were released by Si-DRIE and the Cr adhesion layer was removed by wet-etching. Holey membranes with a diameter of 1200 μm were fabricated. Au films with hole arrays using oxidized Si pillars as lift-off template were transferred to a transparent flexible substrate. Parylene was used for its good adhesion to Au, its mechanical stability and for its conformal deposition properties. By photolithographically patterning the parylene layer, holey Au membranes in air were also realized.

5.4 Summary and conclusions

Wafer-scale nanosphere lithography (NSL) using spin-coated PS beads was used either in its' *lift-off* or *etching* form to produce sub- μm hole and dot array pattern templates on various kinds of substrates. Additionally, the hole or pillar templates were micro-patterned by standard UV photolithography, defining specific device regions on the wafer surface and potentially enhancing the device properties (e.g. improvement of the holey membrane stability).

Different processes were developed to produce wafer-scale arrays of holes of sub- μm dimension in different types of material: (i) 100 nm thick, 2400 μm large SiN membranes (5.1), (ii) 200 nm thick Au films on glass substrates (5.2), (iii) 200 nm thick Au membranes with a sidelength of 1200 μm and in 200 nm thick Au films transferred to a flexible, transparent substrate (5.3).

This shows the flexibility of NSL based patterning of sub- μm hole arrays. Both Si-based and metallic thin films and membranes can be patterned. The dimensions of the holes can be easily varied by adapting the size-reduction parameters, while the hole density and spacing can be varied by choosing a different initial bead size. Furthermore, as compared to standard top-down fabrication methods, the cost-of-ownership of the employed process equipment is comparatively low.

6 Characterization of SiN and Au films and membranes

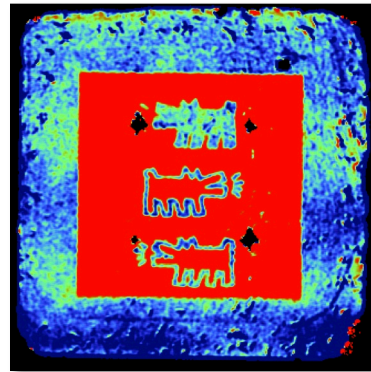
In this chapter, test and characterization of the fabricated holey SiN membranes and Au films and membranes is described.

SiN membranes with and without holes were bulge-tested. They withstood differential pressures up to 5 bar.

The transmission of visible light through hole arrays in Au films and membranes was measured.

Reproducible optical properties were obtained by sputter-etching hole arrays into Au films on glass substrates.

Au membranes with sub-wavelength hole arrays were characterized with and without a thin Cr adlayer. After Cr removal, a light transmission enhancement of 2.4 was measured.



6.1 Bulge tests of holey SiN membranes

The mechanical robustness of 100 nm thick, $400 \times 400 \mu\text{m}^2$ large, holey SiN membranes was tested in a bulge test. The hole diameter was 200 nm with an average spacing of 428 nm and a hole fraction $ff \approx 20\%$.

Experimental

A schematic of the experimental setup used is shown in figure 6.1. The pressure p exerted on the membrane was controlled by sealing the membrane chips in a gasket and pressurizing them from below. A typical 3D representation of a membrane under pressure taken with a Veeco optical interference microscope is shown in figure 6.1b.

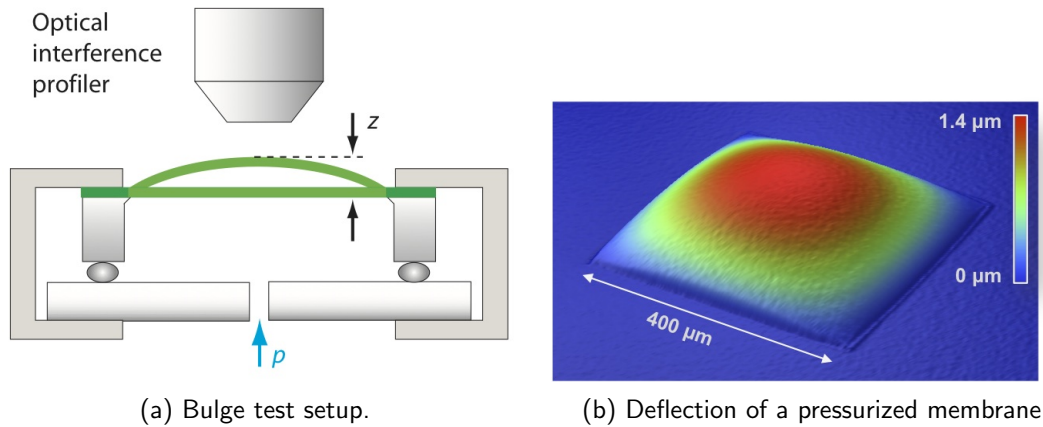


Figure 6.1: The mechanical properties of holey and non-hole SiN membranes were characterized in a bulge test setup (a). An example 3D representation of a bulged membrane recorded with the optical interference profiler (b).

After each stepwise pressure increase, the membrane deflection was recorded with the interference microscope. The center deflection z was manually extracted from the cross-sectional membrane profiles. A plot of the relation of p and z is shown in figure 6.2. For the maximum $p = 2.7 \text{ bar}$, $z = 12 \mu\text{m}$.

After the stepwise increase, the pressure was augmented to 5 bar. Neither the membranes without, nor the membranes with holes broke at that point.

Results and discussion

Pressurizing the membranes to 5 bar showed that mechanically robust membranes can be fabricated using the nanosphere lithography based fabrication approach.

Still, in order to draw a conclusion with respect to the influence of the holes on the mechanical membrane properties, more statistically valid measurements are needed. For

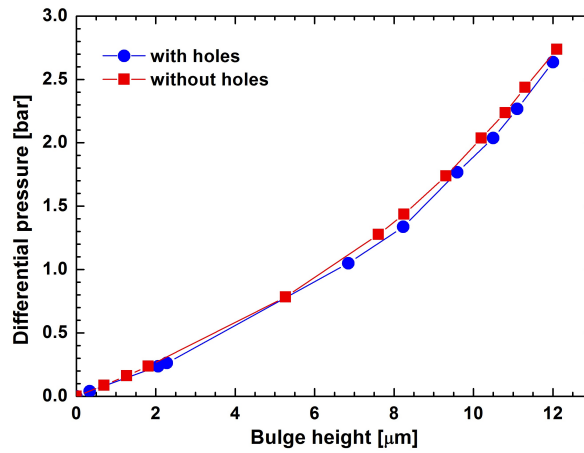


Figure 6.2: Results of the bulge test measurements. The applied differential pressure is plotted over the center membrane deflection height z .

example, the pressure-deflection curves in figure 6.2 are very similar. This is surprising as, compared to the unperforated membranes, a larger deflection of the holey membranes is expected due to a lower effective Young's modulus E_{eff} . In the present case, a small difference in l can explain the similarity as, for large deflections, z scales approximately as $z \propto l\sqrt[3]{l/h}$.⁴³ (A difference in h can be excluded as the membranes were fabricated on the same wafer.)

6.2 Light transmission through hole arrays in Au films and membranes

Au thin films and membranes decorated with sub-wavelength hole arrays are interesting for a variety of optical applications linked to the excitation of surface plasmons (SPs) (c.f. sections 1.1.1 and 1.1.4). For device application, it is crucial to obtain reproducible optical characteristics. This will be shown with the example of sputter-etched hole arrays. Secondly, plasmon-mediated transmission enhancements were obtained that are similar to those reported for focused ion beam milled hole arrays.

Experimental setup

For all light transmission experiments, the same measurement setup was used. A schematic is shown in figure 6.3. It is based on an inverted optical microscope with a low numerical aperture ($NA < 0.1$) with a white light illumination source. The light is collected through a $40\times$ objective ($NA = 0.6$) and analyzed using a spectrometer coupled with a liquid nitrogen cooled CCD camera. The imaged area at a spectrometer slit opening of 0.5 mm is approximately $40\times 5 \mu\text{m}^2$. The light intensity I transmitted through the hole arrays was normalized to the light intensity transmitted through a glass slide, I_0 .

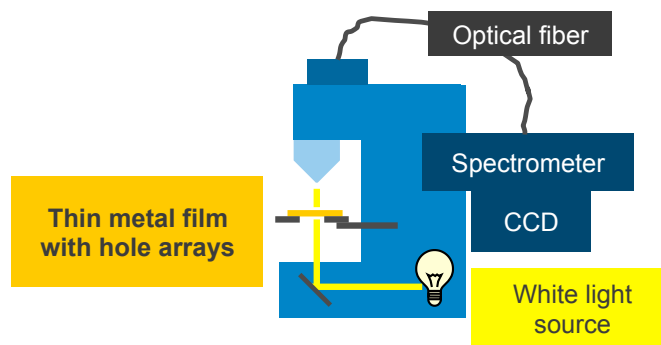


Figure 6.3: Schematic of the optical transmission measurement setup.

6.2.1 Sputter-etched hole arrays in Au films on glass substrates

In section 5.2, the fabrication of hole arrays in 200 nm thick Au on glass films was described. All the fabricated samples were also characterized optically. Here, a typical example is given which shows that using NSL as the hole patterning method, and sputter-etching to transfer the holes into the Au film, reproducible optical properties can be obtained.¹

Experimental

Hole arrays were intermittently sputter-etched for 40 min (i.e. 4×10 min of etching) in two different etch runs 1 and 2. The average hole diameter at the Au-glass interface was 130 nm. For a $p \approx 419$ nm (type **A** wafer), this corresponds to a ff of 9%.

For each run, the optical transmission was measured at two different locations. SEM imaging and FFT confirmed that the hole arrays were of high short-range order across the the light collection region ($40 \times 5 \mu\text{m}^2$).

Figure 6.4 shows the normalized light intensity as a function of wavelength. The SP

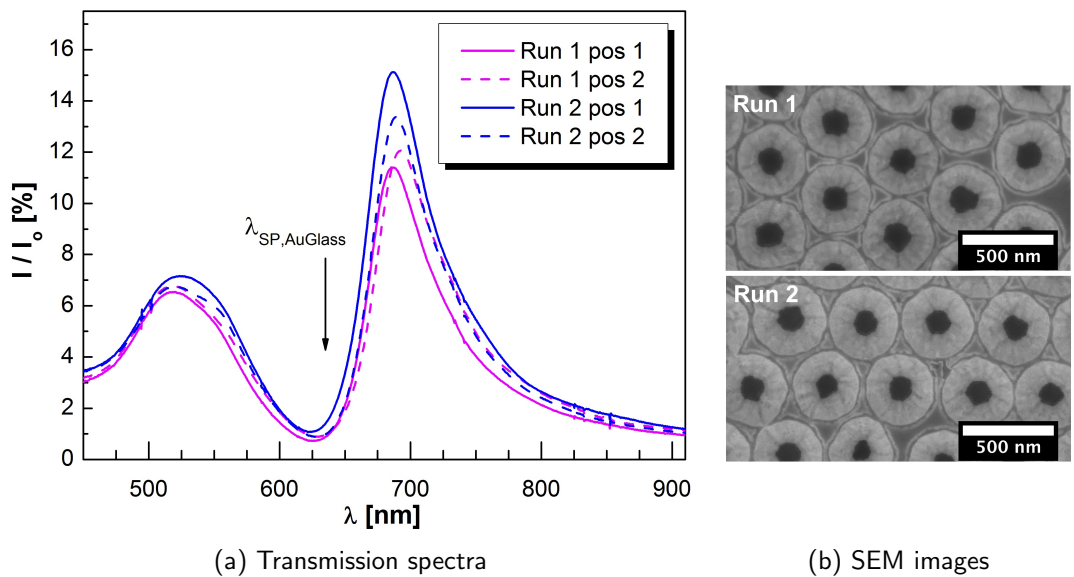


Figure 6.4: (a) Spectra of optical transmission through sputter-etched hole arrays fabricated in different etch runs 1 and 2. For each run, measurements were taken at two different locations on the wafer surface (pos 1 and pos 2).

(b) Typical SEM images of hole arrays from run 1 and run 2.

Hole array parameters: $p \approx 419$ nm, $D_{hole, AuGlass} \approx 130$ nm, $ff = 9\%$.

excitation wavelength for SPs propagating along the Au-glass interface, $\lambda_{SP, AuGlass} =$, is

¹The optical characteristics, as determined by p and thus λ_{SP} , were not only reproducible for hole arrays of similar diameter, but also for holes of varying diameter. Measured spectra can be found in the appendix A.8.

indicated by an arrow. One dip at 650 nm and two transmission peaks around 515 nm and 690 nm are observed in the transmission spectra. The corresponding transmissions for the two etch runs are given in table 6.1.

λ		515 nm	650 nm	690 nm
I/I ₀	Run 1 pos 1	6.5 %	1 %	11.5 %
	Run 1 pos 2	6.5 %	1 %	12 %
	Run 2 pos 1	6.5 %	1 %	13.5 %
	Run 2 pos 2	7 %	1 %	15 %

Table 6.1: Normalized light transmission at dip and peak wavelengths rounded to 0.5%. The corresponding spectra are shown in figure 6.4.

Results and discussion

For different etch runs and different measurement locations, the measured spectral locations of the transmission dip and peak wavelengths are in good agreement. This shows that reproducible optical properties can be obtained hole arrays by fabricated by sputter-etching. The hole array short-range order of the NSL hole pattern is sufficient.

The dip in transmission is due to light diffraction at a grazing angle (Wood-Rayleigh (WR) anomaly). The short-wavelength peak is located within the transparency window of Au and is thus not linked to SP mediated light transmission²⁴⁸. The high transmission around 690 nm is due to resonant excitation of propagating SPs at the smooth Au-glass interface. For higher transmission (Run 2 pos 1), the peak is slightly red-shifted as it is blocked by the WR anomaly.

For samples of Run 2, the long-wavelength transmission is up to 3.5% higher as compared to the one for Run 1 samples. This is explained by minor differences in hole diameter, which can not be precisely defined due to the irregular hole shape (c.f. the SEM images in figure 6.4b).

The last question is whether extraordinary optical transmission (EOT) is observed or not. For large hole arrays, the enhancement factor η is calculated by dividing the transmitted light in [%] by the ff . EOT requires that $\eta > 1$. However, the $ff = 9\%$ given above is based on topographical measurements only, and not taking into account the conical hole shape and the Au skin-depth δ of 30 nm. This means that some amount of light is directly transmitted through the tapered hole sidewalls, and the “optical”, effective hole diameter D_{eff} is actually larger than the topographically measured $D_{AuGlass}$ of 130 nm. Assuming a worst case situation, D_{eff} is set to 170 nm, which is where the Au film attains a thickness of 30 nm (the hole sidewall taper is $\approx 58^\circ$, figure 5.11).²

²Transmission measurements through thin CrAu films (≤ 1 nm Cr and 15 nm Au) showed that about

Consequently, the effective ff becomes 15% and $\eta = 1$ (Run 2 pos 1). Thus, EOT is not observed in the present case.

EOT is caused by the coupling of SP modes on one side of the metal-dielectric interface, with other propagating surface waves on the other side of the metal film. The Au-air interface of the sputter-etched hole arrays is extremely rough, reducing the SP decay length drastically. This explains why η is limited to 1.

6.2.2 Sub-wavelength hole arrays in Au membranes

Arrays of sub- μm holes in Au membranes were fabricated by a Si-pillar lift-off procedure (c.f. section 5.3 and figure 5.15). 200 nm Au was evaporated onto a 10 nm thick Cr adhesion layer. After membrane release by Si-DRIE, the Cr was removed by wet-etching. The hole array periodicity p was ≈ 419 nm. With a hole diameter $D = 130$ nm, the hole fractional area ff is 9% (figure 6.5b).

(Transmission measurements through hole arrays in Au membranes and Au membranes on parylene fabricated using SiO_2 pillars revealed similar results. The spectra can be found in the appendix A.9.)

Experimental

Optical transmission spectra were taken before and after Cr removal by wet-etching. Different spectra were taken at arbitrary membrane locations. The spectra in figure 6.5 show typical examples. The spectra were taken over a range from $\lambda = 450$ nm to 950 nm. Beyond 700 nm, light transmission dropped to zero and thus for clarity, only the interesting region around the observed transmission peak is shown. $\lambda_{SP,AuAir}$ is located at 360 nm and thus not indicated in the graph.

Before Cr etch, a transmission maximum of 3% is located at 540 nm. Upon Cr removal, a red-shift occurs to 540 nm where 22% of the incident light is transmitted.

Results and discussion

First of all, an interesting comparison can be made between the hole arrays fabricated by sputter-etching (c.f. the section above) and the membranes fabricated by the lift-off type procedure. Neglecting the effective increase of $D_{hole,AuGlass}$ in case of the sputter-etched hole arrays, the hole array parameters are identical. However, no light is transmitted through the membrane hole arrays at $\lambda = 510$ nm. This confirms that the short-wavelength transmission peak observed for the sputter-etched hole arrays is due to direct light transmission.

45% of incident light is transmitted at $\lambda = 700$ nm. Thus, widening D_{eff} to 170 nm where the Au film attains a thickness of 30 nm can be considered safe.

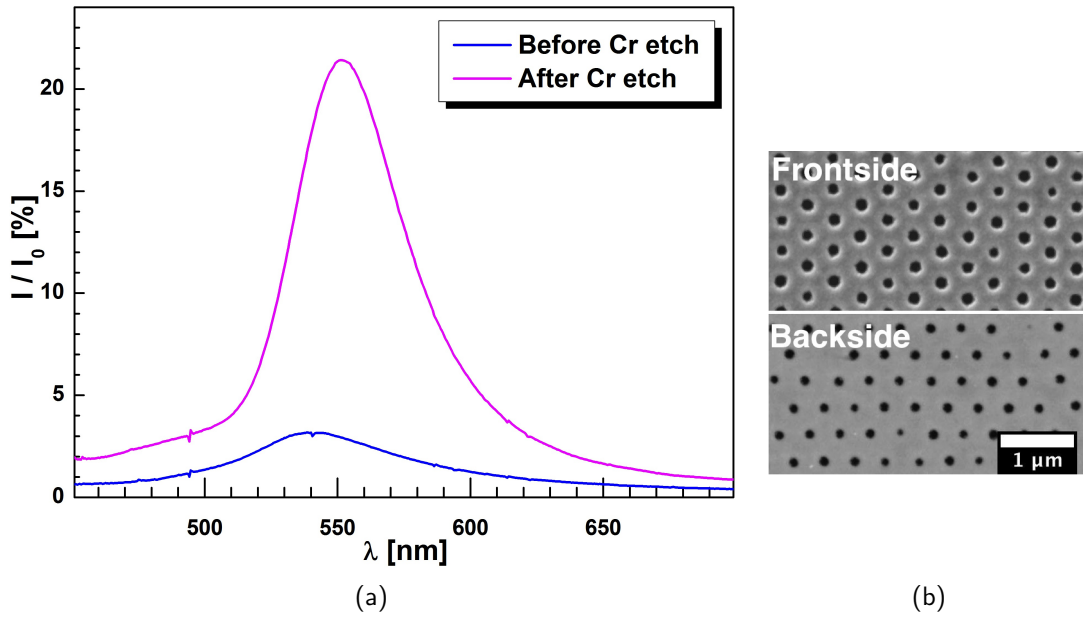


Figure 6.5: (a) Optical transmission through hole arrays as shown in (b) before and after wet-etching of Cr. (b) SEM images of the front- and backside of the characterized Au membrane.

Hole array parameters: $p \approx 419$ nm, $D = 130$ nm, $ff = 9\%$.

Upon Cr removal, a drastic increase in light transmission occurs through the membranes. Before Cr removal, propagating SP do only exist at the top Au-air interface. After Cr removal, SPs are excited at both sides of the membrane, and resonant coupling of these top and bottom SP modes leads to the high transmission. This explicitly shows the destructive effect of strongly absorbing metals such as Cr (large ϵ''_m) on SP mediated transmission.

In this case, a contribution of direct light transmission can be excluded as the high transmission occurs far above the cut-off wavelength of 260 nm, the Au film is optically thick, and the holes have almost vertical sidewalls. Thus, 22% light transmission through holes with a ff 9% means that EOT with an enhancement factor $\eta = 2.4$ is observed.

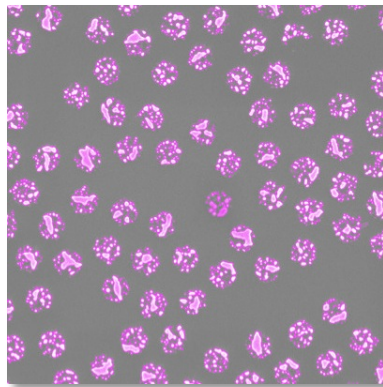
This EOT is on the same order of magnitude as reported for hole arrays fabricated by focused ion beam milling²⁰. This shows the suitability of the developed Si pillar templated fabrication approach for plasmonic applications such as the collection of light through sub-wavelength hole arrays.

7 Stenciling and refractive index sensing

In this chapter, the application of the fabricated devices is demonstrated.

Thin holey SiN membranes were used as stencil masks for the deposition of Au and Ag dot arrays. In a second stencil experiment, similar membranes were used as an etch mask to transfer the hole pattern into a 500 nm thick SiN membrane.

Refractive index sensing was demonstrated by measuring the optical transmission through sputter-etched hole arrays immersed in water-glycerine solutions.



7.1 Deposition through holey stencils

Arrays of sub- μm metallic particles are interesting for a variety of applications, such as surface enhanced raman scattering (SERS)²³ or as masks in dry etch processes.

Experimental

100 nm thick holey SiN membranes with an array periodicity $p \approx 419$ nm and a hole size of 245 nm were used as stencil masks for the deposition of Au and Ag dot arrays. The evaporated film thicknesses were nominally 20 nm (Au) and 35 nm (Ag). The stencils were fixed to Si substrates using Kapton tape. Evaporation was done in an electron-beam evaporator (Leybolds LAB600) with a high source-substrate distance of ≈ 1 m. The substrates were placed directly above the source.

Results and discussion

First, striking differences can be observed with respect to the morphology of the Au and Ag deposited onto the stencils (figures 7.1c and 7.1e) and onto the Si substrates (figures 7.1d and 7.1f): The gold film shows a granular, almost discontinuous structure, while the Ag thin film is continuous. Au is known to have a very high surface mobility as compared to other metals²⁴⁴, and under certain conditions, thin films of high mobility metals may exhibit a de-wetting behaviour²⁴⁹. This is what is observed in case of the Au deposition.

Also, nanoscale Au grains form a broad halo around the main dots. In case of the Ag dots, such granular deposits are limited to within a few nanometers from the main dot. This difference is explained by (a) a different stencil-substrate gap height G in the Au and Ag depositions and thus a difference in geometric blurring (c.f. equation 1.1 in the introduction), and (b) a more important blurring due to surface diffusion in the case of Au²⁸.

An overview of the measured hole and (main) dot sizes is shown in figure 7.1b. The stencil hole diameter before use as a stencil mask is 245 nm (figure 7.1a). After evaporation of Au and Ag through the stencil, the stencil holes have been reduced to 230 nm (figures 7.1c (Au) and 7.1e (Ag)). The reduction of the stencil hole diameter is due to clogging of the stencil aperture (also c.f. figure 1.2 in the introduction). Figures 7.1d and 7.1f show the resulting Au and Ag dot arrays on the Si substrate obtained by evaporation through the stencil. The Au and Ag main dot diameters are ≈ 230 nm and thus correspond well to the reduced stencil hole sizes. For such aperture dimensions, this is an excellent result.

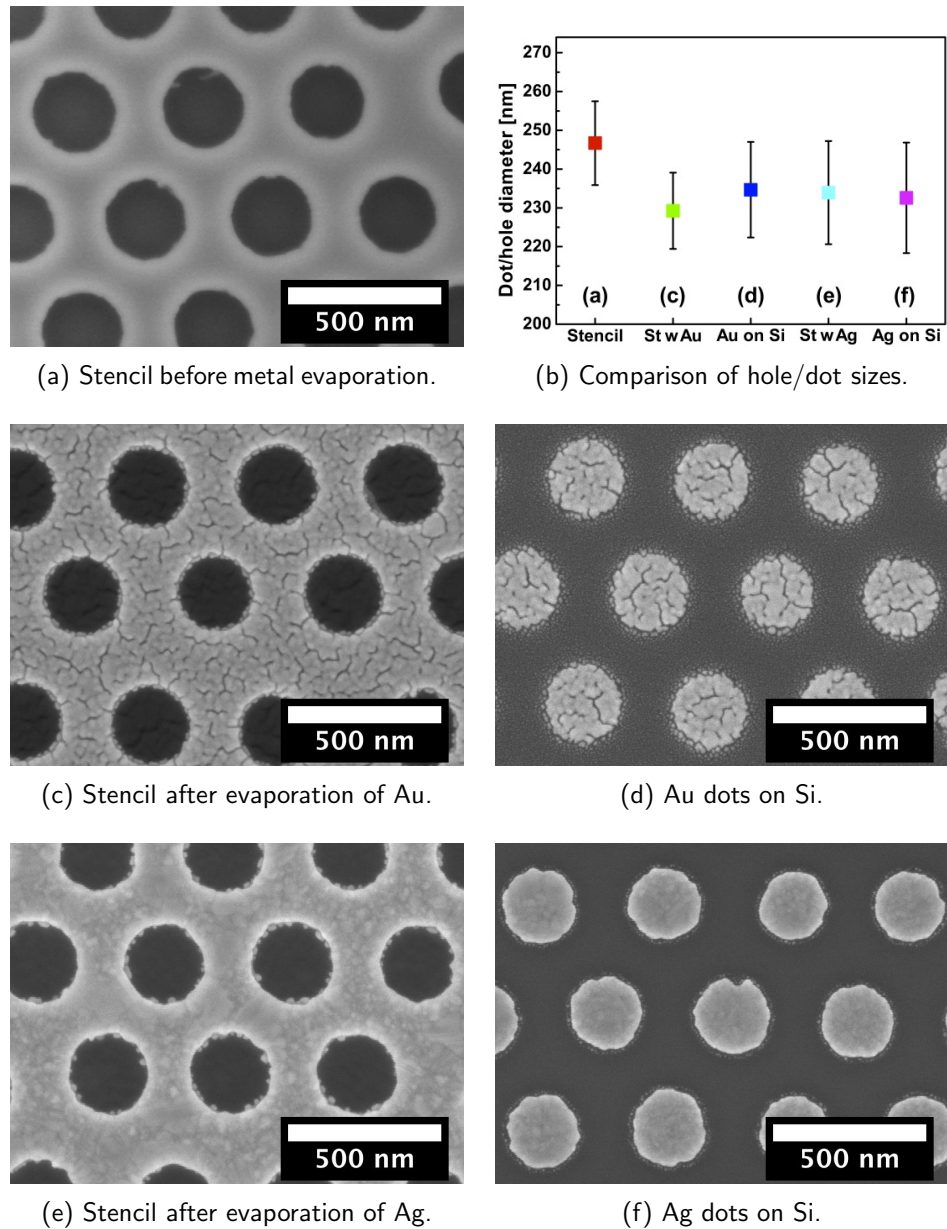


Figure 7.1: Use of thin SiN membranes with sub- μm holes as stencil masks for metal evaporation. (a) Stencil backside before evaporation. (c) and (e) stencil backside after evaporation Au and Ag, respectively. (d) and (f) corresponding Au and Ag dot arrays on a Si wafer. (b) shows the mean size of holes/dots for (a) and (c) through (f) with a 1σ error bar.

7.2 Etching through holey stencils

The sub- μm pattern transfer into thick SiN films is technologically involved due to the low etch rate (ER) selectivity of commonly used masking materials to SiN (e.g. photoresist commonly has an ER selectivity $\approx 1:1$). This requires thick masks, which in turn are challenging to pattern at sub- μm resolution. The following experiments will show how thin holey SiN membranes can be used as dry-etch masks for the etching of holes with an aspect-ratio of ≈ 2 into 500 nm thick SiN membranes²⁵⁰. These etchings were done by Dr. Veronica Savu from the group of Prof. Brugger at EPFL.

Experimental

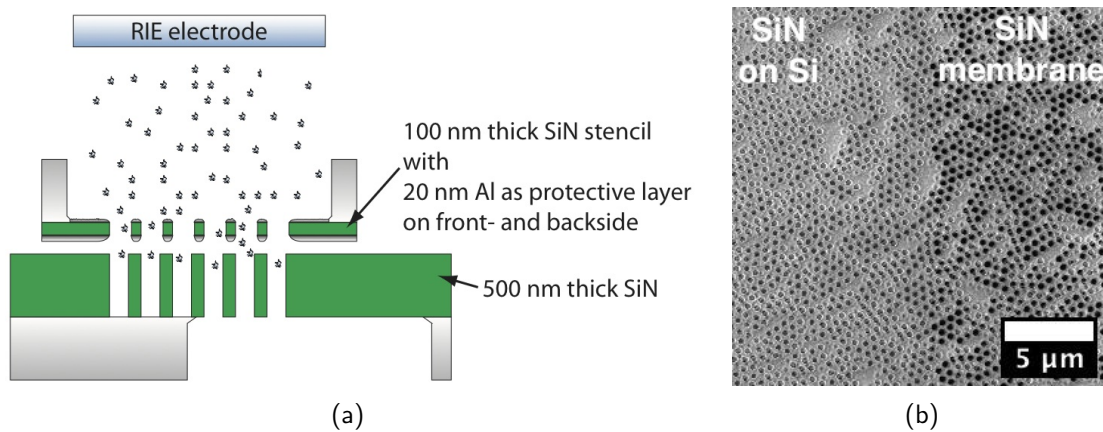


Figure 7.2: (a) Experimental setup for etching holes into 500 nm thick SiN using a 100 nm thick SiN stencil. An SEM image across the SiN on Si to the SiN membrane area after hole etching is shown in (b).

The SiN membranes used in this experiment had an average hole diameter of 325 nm with a hole spacing of $p \approx 535$ nm. The stencil holes had small notches linked to bead surface roughening during bead size reduction process (section 3.2.4).

First, a protective 100 nm thick Al layer was evaporated onto the top and bottom of the holey stencils. Then, the stencil was fixed with an organic resin to a 500 nm thick SiN membrane in a configuration as shown in figure 7.2. SiN dry-etching was done for 4 min at room temperature in an Alcatel 601E ICP-DRIE system. The recipe used is based on a $\text{C}_4\text{F}_8/\text{CH}_4$ chemistry. Under such process conditions, an Al mask thickness of 100 nm is usually sufficient for the etching of 500 nm SiN. Figure 7.2b shows a low magnification SEM image of the obtained etch result.

Results and discussion

Figure 7.3a shows an SEM image of the stencil after evaporation of 100 nm Al onto it, reducing the stencil hole size to ≈ 265 nm. Figure 7.3b shows the same stencil after it has been used as an etch mask during 4 min of SiN dry-etching. The holes in the stencil are slightly enlarged, measuring ≈ 270 nm. Thus Al mask abrasion is very low. And therefore, coating the stencil with a thin Al layer is an efficient way to protect the stencil membrane during dry-etching.

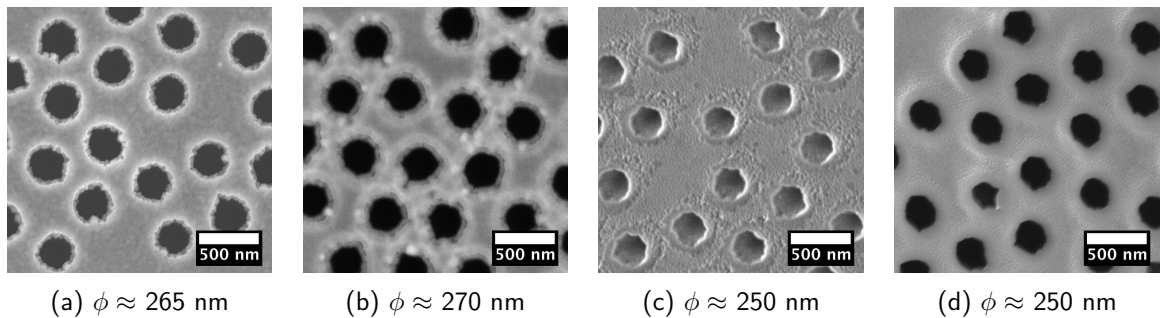


Figure 7.3: Holes in the stencil after evaporation of a 100 nm thick protective Al layer (a) and after use as an etch mask for 4 min of SiN etching (b). Holes etched into 500 nm thick SiN on Si (c) and into the SiN membrane (d). Indicated in the figure captions are the measured hole diameters ϕ .

Figures 7.3c and 7.3d show SEM images of holes etched into the SiN on Si layer and etched into the SiN membrane, respectively. A comparison of the images shows that the hole pattern has been transferred throughout the 500 nm thick SiN membrane in an unprecedented manner. It is a proof-of-concept that using holey SiN membranes as a stencil etch mask, sub- μm holes can be transferred into device layers, even such that are otherwise difficult to pattern.

The holes in the 500 nm thick SiN layer and membrane were measured to be ≈ 250 nm in diameter, and thus about 20 nm smaller as compared to the holes in the stencil mask. Also, a halo of granular appearance can be seen around the holes in the 500 nm thick SiN layer and membrane. Both are explained by a deflection of ions at the stencil aperture and sidewalls, spreading the angular distribution of the reactive etch species. This concentrates highly energetic etchants to within a region smaller than the stencil holes, while low energetic etchants are widely spread and damage the top SiN surface.

In addition to surface damage, the halo is caused by Al mask erosion, depositing non-volatile Al etch products onto the SiN surface beneath the stencil.

7.3 Refractive index sensing

The transmission of light through hole arrays in thin metallic films is sensitive to changes of the refractive index (RIX) in the surrounding dielectric environment (equation 1.7). In the following, this was used to detect RIX changes in glycerine-water-solutions using sputter-etched hole arrays (c.f. section 5.2).

Experimental

Hole arrays in 200 nm thick Au films on a glass substrate were immersed in glycerine-water-solutions. The glycerine concentration was increased from 0 vol% to 1, 2, 3, 5, 20, and 50 vol%, corresponding to a change of the RIX from $n = 1.333$ to $n = 1.3898$ ($\Delta n = 0.0568$). In this experiment, sputter etched hole arrays with $p \approx 517$ nm and $ff = 10\%$ were used. Figure 7.4 (left panel) shows the normalized transmission spectra for hole arrays in water-glycerine solutions. All spectra show a dip in transmission at $\lambda = 721$ nm. For hole arrays in glycerine-water-solutions, two transmission peaks are observed. At 0% glycerine concentration, these are located at 661 nm and 827 nm. For increasing glycerine-concentration, these peaks are red-shifted with a maximum shift to 50 nm at 50% glycerine concentration. The SP excitation wavelengths for a Au-glass and Au-water interface, $\lambda_{AuGlass}$ and $\lambda_{AuWater}$, are indicated by vertical lines. The arrows indicate the increase in glycerine concentration.

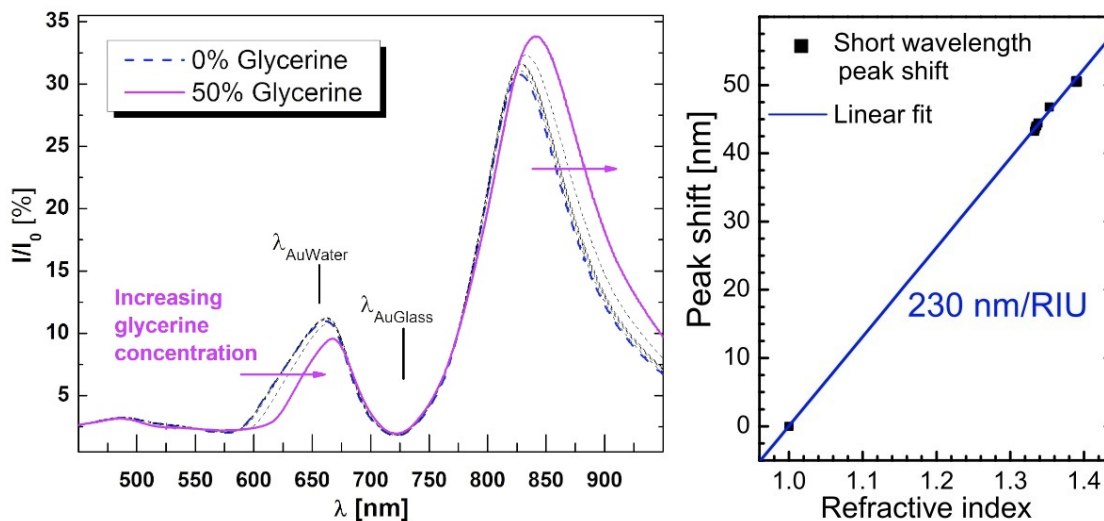


Figure 7.4: Transmission spectra for hole arrays in water-glycerine solutions (left). The glycerine concentrations were increased from 0% to 1, 2, 3, 5, 20, and 50 vol%, resulting in a RIX change of $\Delta n = 0.0568$. The sensitivity, measured as a peak wavelength shift, is 230 nm/RIX unit (RIU) (right).

Results and discussion

The dip in transmission at 721 nm is due to a Wood-Rayleigh anomaly. The long-wavelength transmission peak is caused by SP excitation at the Au-glass interface. Both are not sensitive to changes of the RIX at the top hole array surface.

The short wavelength peak is due to SP excitation at the top surface. It is sensitive to RIX changes. $\lambda_{AuWater}$ is therefore red-shifted with increasing glycerine concentrations. As the SP mediated transmission is caused by coupling of SPs at both metal-dielectric interfaces, the shift in $\lambda_{AuWater}$ induces both a shift of the short-wavelength and the long-wavelength peak. Thus, both peak shifts can be correlated to a change of the RIX. An analysis of the long-wavelength peak shift as a function of the RIX yields a RIX sensitivity of 230 nm/RIU unit (RIU) (figure 7.4 right panel).

In the literature, sensitivities larger than 500 nm/RIU have been reported for VIS transmission measurements and hole arrays of similar p ⁷⁰. A higher RIX sensitivity can be achieved by optimizing the hole array parameters, and thus the interference of different surface waves involved in the light transmission mechanism²⁵¹.

Precise tuning of the hole array parameters is challenging for sputter-etched hole arrays. p is linked to the size of the beads used in the nanosphere lithography process step. But commercial beads are not available for arbitrary sizes. The hole shape is determined by the fabrication process.

On the other hand, sputter-etched hole arrays have some advantages compared to hole arrays fabricated by e.g. FIB, e-beam lithography or PEEL¹:

- (i) They provide a sensitive hole array area on a full wafer-scale. They are directly attached to transparent substrates that are compatible with micro-fabrication post-processing.
- (ii) High light transmission with an efficiency η on the order of 1 is possible owing to the excitation of SPs at the Au-glass interface. This is not the case if a Cr adhesion layer is used, such as needed in the case of lift-off based hole array fabrication (either using an e-beam pattern or NSL).

This makes sputter-etched hole arrays a suitable substrate for the facile integration with microfluidics²⁵², where the large hole array area alleviates the problem of precise positioning of the measurement window. Also, the total amount of light transmitted is high, for example as compared to FIB arrays that only extend over a few tens of periods, increasing the signal-to-noise ratio.

¹A combination of phase-shifting photolithography, etching, electron-beam deposition, lift-off⁹⁹.

8 Conclusions and outlook

8.1 Conclusions

The goal of this thesis was the fabrication of sub- μm hole arrays in SiN and Au thin films and membranes on a 4" wafer scale. This has been achieved by developing two different processes, both of which are initially based on a nanosphere lithography (NSL) pattern template. The principle process parameters were characterized, and solutions to fabrication related issues were found by tuning the process or choosing an alternative method. The most out-standing results of this thesis are the fabrication of 100 nm thick, $2400 \times 2400 \mu\text{m}^2$ large SiN, and 200 nm thick, $1200 \times 1200 \mu\text{m}^2$ large Au membranes with arrays of sub- μm holes. Beyond fabrication of the devices, characterization and test for applications in the targeted fields of stenciling, filtration and plasmonics was done successfully.

The conclusions below contain a critical statement, as well as future directions for further improvements.

Bead deposition (chapter 2)

Different methods were investigated for the deposition of close-packed polystyrene (PS) bead monolayers onto 4" wafers, namely drop-coating convective self-assembly (CSA), controlled CSA with the CAPA-tool¹, and spin-coating.

The influence of the parameters governing bead self-assembly was underestimated in the beginning, and drop-coating CSA using only a simple experimental setup did not yield suitable monolayer coatings. With the CAPA-tool², important parameters such as the liquid evaporation rate or the wetting film contact line were controlled in experiments on chip-size substrates.

For the coating of 4" wafers, spin-coating of beads from aqueous suspensions was used.

¹capillary assisted particle assembly

²The experiments were done in collaboration with Heiko Wolf and Cyrill KÜmin at the IBM Rüschlikon research labs, where the CAPA-tool is used as a powerful tool for the precise particle placement on pre-patterned surfaces^{148,147}

The spin-speed and suspension concentration was varied in systematic experiments. In this way, homogeneous monolayer coatings covering up to 90% of the wafer surface were obtained on different substrate types and for different bead diameters D .

However, both a better understanding of the parameters influencing the bead deposition results, and further process optimization to reduce bead waste and avoid the deposition of bead multilayers, are needed. Bead multilayers result in large hole defects in the later, holey device layer. In case of the NSL *lift-off* based process, a possible solution would circumvent this problem by depositing the lift-off metal by conformal atomic layer deposition¹⁵⁹. For the fabrication of pillar templates, however, a different solution needs to be found.

Bead size reduction (chapter 3)

Tuning of the hole diameter in the holey films and membranes was achieved by size-reduction of the PS beads by O_2 -reactive ion etching (RIE). The results were reproducible up to reduced bead diameter $D_{red} = 0.3D$.

This limitation is imposed by the anisotropy of the etch process and due to the negative self-bias voltage in conjunction with the spherical bead shape. At low self-bias voltage (high absolute value), the bead diameter etch rate increased non-linearly once $D_{red} < 0.5D$. An increase of the self-bias voltage reduces the anisotropy, but also the etch rate and the ability to break polymeric links between the beads.

An unsolved challenge remains roughening of the bead surface and bead tilt or dislocation. This is an issue for filtering or plasmonic applications where round holes with a small size distribution are needed. Cryogenic plasma etching is a possibility to amend the bead surface roughening and bead tilt¹⁵².

Micro-patterned holey metallic etch masks and Si pillar templates (chapter 4)

The size-reduced PS beads served as a template for two kinds of nanosphere lithography (NSL) options, either (a) as a *lift-off* template for the fabrication of holey metal etch masks, or (b) as an *etch* mask for the fabrication of high aspect-ratio Si pillars.

By directional evaporation of a thin metal layer onto the beads and subsequent lift-off in organic solvents, holey metallic films were realized on different substrate types. A 100% lift-off yield was achieved for metal film thicknesses $\leq 0.2 \times D_{red}$.

For the second NSL option, the bead template was transferred into an intermediate SiO_2 mask. The influence of the Si-DRIE parameters on the pillar sidewall shape and mask undercut was characterized. By balancing the etch gas ratio, Si pillars with an aspect ratio ≥ 5 and a negative sidewall profile were reproducibly fabricated.

Micro-patterning of the hole and oxide dot masks was a crucial next step with respect to the subsequent processes and final device properties. Several challenges were

encountered when combining standard micro-machining techniques with bottom-up self-assembly based patterning. By adapting the process sequence, choosing a different masking material, or providing for over-etch margins, reliable micro-patterning was achieved. Thus, arrays of sub- μm holes in SiN and Si pillar arrays were successfully integrated with sub-sequent micro-fabrication process steps.

Fabrication of holey SiN membranes (chapter 5.1)

100 nm thick holey SiN membranes with dimensions up to $2400 \times 2400 \mu\text{m}^2$ were fabricated by locally etching holes into the SiN layer and releasing the membrane in a combined dry-/wet-etch procedure.

The hole fractional area (ff or porosity) were as high as 50%. The loss in dimension from D_{red} to the holes in the device layer was $< 0.05D_{red}$. Issues in the membrane release procedure due to the small hole size and high ff were solved by combining a temporary protective frontside coating during KOH with micro-patterning of the holes. Both the obtained ff and the loss in dimension are superior to values reported for similar holey SiN membranes patterned by interference lithography⁹⁶.

Compared to membrane release by anisotropic wet-etching, the combined dry-/wet-etch procedure has two distinct advantages. It increases the membrane array integration density, owing to the vertical sidewalls of the Si frame, and speeds up the release time, thanks to the high etch-rates that can be obtained with Si-DRIE. Other options to attain a high membrane density are the use of (110)-oriented Si wafers, or designing for recessed Si prismatic bars resulting from KOH under-etch on (100) Si wafers.

Fabrication of holey Au films on glass substrates (chapter 5.2)

By sputter-etching, wafer-scale hole arrays were fabricated in 200 nm thick Au films on glass substrates. First, using the NSL *lift-off* approach, holey metal etch masks were fabricated on 2" glass wafers sputter-coated with 200 nm of Au. Au deposition without the use of an adhesion layer was a pre-requisite for the targeted plasmonic applications. Good adhesion of the Au to the glass substrate was obtained owing to the deposition process and substrate used. Then, by sputter-etching, the hole mask was transferred into conical holes in the Au layer.

Using an intermittent etch procedure, the Au hole diameter was tuned from tens to a few hundred nm without changing the holey etch mask.

This process showed that large hole arrays in optically thick Au films can be fabricated in a relatively simple way, especially as compared to other commonly used serial writing methods such as focussed ion beam milling (FIB) or electron beam lithography. The process has further potential to obtain holes of vertical sidewalls, for example by using an ion beam etch setup and/or providing for a rotation-and-tilt substrate holder.

Fabrication of holey Au membranes with Si pillars as lift-off template (chapter 5.3)

In a conceptually different approach, 200 nm thick holey Au membranes with sizes up to $1200 \times 1200 \mu\text{m}^2$ were fabricated.

Micro-patterned oxide dots fabricated using the NSL *etch* approach served as an etch mask for Si pillar etching. A continuous Si-DRIE (deep RIE) etch procedure was characterized and optimized. By tuning the $\text{SF}_6/\text{C}_4\text{F}_8$ etch gas ratio, pillars with an aspect-ratio > 5 and a negative sidewall profile were fabricated reproducibly. This was a crucial achievement as the pillars served as a lift-off template in the following process step, in which Cr and Au was directionally evaporated onto the pillars. The pillars were then removed by KOH wet-etching, leaving behind sub- μm holes with almost vertical sidewalls in the 200 nm thick Au layer. Those micro-patterned hole arrays were aligned to a backside mask and released by Si-DRIE dry-etching. The membrane yield was on the order of 30%.

An issue not accounted for yet in the mask layouts was aspect-ratio dependent etching and the radially non-uniform etch-rate. For membranes of varying size on one wafer, this resulted in early release of the larger membranes, which broke if the etching was continued.

To my knowledge, this is an unprecedented way to fabricate wafer-scale arrays of sub-wavelength holes (in the visible wavelength regime) in 200 nm thick free-standing membranes of millimeter-size. The only alternative to fabricate such membranes supported on a Si frame is FIB. Fabrication of the same number of hole arrays (based on the above 30% yield) is very unfeasible. Using average values for a calculation (≈ 1 hr write time for a 40×40 hole array in 200 nm Au), FIB would take about 2 years (including night and day and week-ends).

Fabrication of holey Au films on parylene with oxidized Si pillars as lift-off template (chapter 5.3)

In a similar way as described above, oxidized Si (SiO_2) pillars were used as a lift-off template in HF. This has the advantage of being applicable also to other metal than Au. For the purpose of transferring the holey Au layer to a transparent, flexible parylene film, only Au was evaporated, without the use of an adhesion layer.

The lift-off process was very delicate, but by careful handling, hole arrays in 200 nm thick Au films could be realized. Then, parylene was deposited, and with this as a flexible support layer, the holey Au films could be peeled off. Optionally, windows were etched into the parylene covering the hole arrays, resulting in free-standing Au membranes on a flexible support.

The SiO₂ pillar templating process in its current form does not yield reproducible results. Nevertheless, it remains interesting as it offers the possibility to create sub-wavelength hole arrays also in other metals interesting for plasmonic applications, such as Ag.

Bulge tests and optical transmission measurements (chapter 6)

Primary bulge tests revealed an excellent mechanical stability of holey SiN membranes. 400×400 μm² large membranes with a f of 20% withstood differential pressures up to 5 bar. Systematic tests with holey membranes of different f or different membrane sizes have not been conducted yet.

Optical transmission measurements through sputter-etched hole arrays showed the optical properties of the Au arrays were reproducible. The high surface roughness of the top metal-dielectric interface is the reason that the light transmission enhancement, η , is limited to values on the order of 1.

Au membranes with sub-wavelength hole arrays fabricated by the Si pillar lift-off procedure were optically characterized before and after Cr removal. High, surface plasmon mediated light transmission with an η of 2.4 was measured upon Cr removal. That means that extraordinary optical transmission (EOT, $\eta > 1$) was obtained with enhancements on the same order of magnitude as reported for hole arrays fabricated by focused ion beam milling²⁰. This is an excellent result as it shows that the developed fabrication process is not only faster and more suitable for large-scale fabrication than FIB, but also produces hole arrays that have comparable optical qualities.

Stenciling and refractive index sensing (chapter 7)

The suitability of the fabricated holey SiN membranes for use as a high resolution shadow masks was successfully demonstrated. Au and Ag dot arrays with dots of well defined dimensions were deposited onto Si substrates by evaporation through the holey SiN stencil membrane. By dry-etching through the stencil, the hole pattern in the SiN membrane was transferred into pores in a 500 nm thick SiN membrane.

Sputter-etched hole arrays in Au films were used for refractive index sensing. The sensitivity was low as compared to values reported in the literature, and improvements require optimization of the hole array geometry. An advantage as compared to hole arrays fabricated by other methods is the wafer-scale dimension of the hole arrays, providing the possibility for on-wafer micro-fluidic integration without the need for a precise

placement of the measurement windows.

8.2 Outlook

The achievements attained in this have brought about a significant contribution to the field of nano- and microfabrication. New pathways were opened for interesting future work with respect to continued fundamental and application studies in the realm of maskless nanopatterning, plasmonic sensing, filtration, material science, photovoltaics, or functional surfaces. Below, a few examples of future work are given.

Filtration

The fabricated porous SiN membranes have excellent mechanical properties. This makes them a suitable tool for filtration applications. At CSEM S.A., nanoporous SiN membranes have been developed¹²⁹ and are tested for filtration applications. The membranes fabricated in this thesis close the gap from nanoporous to standard, micro-machined microporous membranes.

Flow through plasmonic sensing

A large hole array area is viable for fast and low-noise refractive index sensing based on the excitation of surface plasmons at structured, metallic surfaces. The group of Hattice Altug has shown that plasmonic sensing using a microfluidic flow-through setup can further improve the sensor speed and sensitivity⁷⁶. They used porous SiN membranes coated with a thin Au layer. However, the fabrication throughput of their devices is limited by the hole patterning step which is based on expensive and slow e-beam lithography. The holey, millimeter-size SiN membranes developed in this thesis provide an excellent, low-cost platform for similar flow-through setups.

Transparent electrodes

Photovoltaic and light-emitting applications require at least one transparent electrode. Transparent, conducting indium-tin-oxide (ITO) electrodes are threatened by a worldwide decrease in indium supply and rising cost^{253,254}. Thin holey metals films are a potential alternative to ITO²⁵⁵. In a first-shot experiment within an internal collaboration at CSEM S.A., thin holey Au films were fabricated by the NSL *lift-off* routine. The films had a low sheet resistance $< 40 \Omega/\text{square}$ and high broad-band transmission $\approx 70\%$ of visible light, in accordance with electrical and full-wave optical simulations. These promising first results justify continued research on the topic.

Material properties of holey Au membranes

Dense arrays of small holes in thin metallic membranes have an important influence on the membrane mechanical and optical properties. To date, a systematic investigation is limited by the time- and cost-intensive fabrication method, e.g. focused ion beam milling. In the domain of thin film material science, the influence of the holes, in combination with different deposition methods, on grain growth and film morphology has not been exhaustively studied yet. Such studies could yield important results as the film morphology influences the electrical, mechanical, and optical properties^{244,21}.

Using NSL and Si pillar lift-off templating, holey Au membranes of varying film thickness, hole diameter and hole spacing can be fabricated on a full wafer-scale, providing substrates for a systematic material characterization.

Replication of sub- μm pillars

In this thesis, short-range ordered arrays of high aspect-ratio Si pillars were fabricated at an intermediate process step. There exists a wide range of applications for such sub- μm size surface textures, e.g. physical colors²⁵⁶, cell growth substrates¹⁶⁷, or tuning of the surface wettability²⁵⁷. For large surface applications, replication via imprinting is a convenient method for high throughput micro- and nanopatterning. Replication of similar, larger Si pillar structures has been demonstrated at CSEM S.A. The fabrication of positive-sidewall pillars with sub- μm diameter, and replication thereof, will be a challenging task, but with many potential applications.

The end.

Bibliography

- [1] M J Madou. *Fundamental of Microfabrication - The Science of Miniaturization Second Edition*. CRC Press LLC, 2002.
- [2] 4M Network of Excellence. Nanomembrane roadmap: Nanomembrane technology and devices based on nanomembrane technology, 2006.
- [3] J. Koehler, M. Albrecht, C. R. Musil, and E. Buchers. Direct growth of nanostructures by deposition through an Si_3N_4 shadow mask. *Physica E: Low-dimensional Systems and Nanostructures*, 4(3):196 – 200, 1999.
- [4] J. Brugger, J.W. Berenschot, S. Kuiper, W. Nijdam, B. Otter, and M. Elwenspoek. Resistless patterning of sub-micron structures by evaporation through nanostencils. *Microelectronic Engineering*, 53(1-4):403 – 405, 2000.
- [5] E. A. Speets, P. T. Riele, M. A. F. van den Boogaart, L. M. Doeswijk, B. J. Ravoo, G. Rijnders, J. Brugger, D. N. Reinhoudt, and D. H. A. Blank. Formation of metal nano- and micropatterns on self-assembled monolayers by pulsed laser deposition through nanostencils and electroless deposition. *Advanced Functional Materials*, 16(10):1337–1342, 2006.
- [6] E. M. Renkin. Filtration, diffusion, and molecular sieving through porous cellulose membranes. *Journal of General Physiology*, 38(2):225–243, 1954.
- [7] S Kuiper, C J M van Rijn, W Nijdam, and M C Elwenspoek. Development and applications of very high flux microfiltration membranes. *Journal of Membrane Science*, 150:1–8, 1998.
- [8] C. J. M. van Rijn, W. Nijdam, S. Kulper, G. J. Veldhuis, H. van Wolferen, and M. Elwenspoek. Microsieves made with laser interference lithography for micro-filtration applications. *Journal of Micromechanics and Microengineering*, 9(2):170–172, 1999.
- [9] A Thormann, N Teuscher, M Pfannmoeller, U Rothe, and A Heilmann. Nanoporous aluminum oxide membranes for filtration and biofunctionalization. *Small*, 3:1032 – 1040, 2007.
- [10] Chuyang Y. Tang, Young-Nam Kwon, and James O. Leckie. Probing the nano- and micro-scales of reverse osmosis membranes—a comprehensive characterization of physiochemical properties of uncoated and coated membranes by xps, tem, atr-ftir, and streaming potential measurements. *Journal of Membrane Science*, 287(1):146 – 156, 2007.
- [11] H. Bayley and C. R. Martin. Resistive-pulse sensing - from microbes to molecules. *Chemical Reviews*, 100(7):2575–2594, 2000.
- [12] S. P. Adiga, C. M. Jin, L. A. Curtiss, N. A. Monteiro-Riviere, and R. J. Narayan. Nanoporous membranes for medical and biological applications. *Wiley Interdisciplinary Reviews-Nanomedicine and Nanobiotechnology*, 1(5):568–581, 2009.

- [13] H. J. Lee, P. D. Beattie, B. J. Seddon, M. D. Osborne, and H. H. Girault. Amperometric ion sensors based on laser-patterned composite polymer membranes. *Journal of Electroanalytical Chemistry*, 440(1-2):73–82, 1997.
- [14] K. Healy, B. Schiedt, and A. P. Morrison. Solid-state nanopore technologies for nanopore-based dna analysis. *Nanomedicine*, 2(6):875–897, 2007.
- [15] J. J. Kasianowicz, E. Brandin, D. Branton, and D. W. Deamer. Characterization of individual polynucleotide molecules using a membrane channel. *Proceedings of the National Academy of Sciences of the United States of America*, 93(24):13770–13773, 1996.
- [16] M Liley. Microtools for toxicology and pharmacology. Technical report, CSEM S.A., 2009.
- [17] J. Norman and T. Desai. Methods for fabrication of nanoscale topography for tissue engineering scaffolds. *Annals of Biomedical Engineering*, 34(1):89–101, 2006. 76.
- [18] Reinhard Ulrich. Interference filters for the far infrared. *Appl. Opt.*, 7(10):1987–1996, 1968.
- [19] Carsten Winnewisser, Frank Lewen, Jochen Weinzierl, and Hanspeter Helm. Transmission features of frequency-selective components in the far infrared determined by terahertz time-domain spectroscopy. *Appl. Opt.*, 38(18):3961–3967, 1999.
- [20] C. Genet and T.W. Ebbesen. Light in tiny holes. *Nature*, 445(7123):39–46, JAN 4 2007.
- [21] H Raether. *Surface Plasmons on Smooth and Rough Surfaces and on Gratings*. Springer, 1988.
- [22] de A Leebeeck, L K Swaroop Kumar, V de Lange, D Sinton, R Gordon, and A G Brolo. On-chip surface-based detection with nanohole arrays. *Analytical Chemistry*, 79:4094–4100, 2007.
- [23] M. E. Stewart, C. R. Anderton, L. B. Thompson, J. Maria, S. K. Gray, J. A. Rogers, and R. G. Nuzzo. Nanostructured plasmonic sensors. *Chemical Reviews*, 108(2):494 – 521, 2008.
- [24] H. Rigneault, J. Capoulade, J. Dintinger, J. Wenger, N. Bonod, E. Popov, T. W. Ebbesen, and P. F. Lenne. Enhancement of single-molecule fluorescence detection in subwavelength apertures. *Physical Review Letters*, 95(11), 2005.
- [25] D Sinton, R Gordon, and A G Brolo. Nanohole arrays in metal films as optofluidic elements: progress and potential. *Microfluid Nanofluid*, 4, 2008.
- [26] J Dintinger, S Klein, and T W Ebbesen. Molecule–surface plasmon interactions in hole arrays: Enhanced absorption, refractive index changes, and all-optical switching. *Advanced Materials*, 18:1267–1270, 2006.
- [27] J. Y. Laluet, E. Devaux, C. Genet, T. W. Ebbesen, J. C. Weeber, and A. Dereux. Optimization of surface plasmons launching from subwavelength hole arrays: modelling and experiments. *Optics Express*, 15(6):3488–3495, 2007.
- [28] O. Vazquez-Mena, L. G. Villanueva, V. Savu, K. Sidler, P. Langlet, and J. Brugger. Analysis of the blurring in stencil lithography. *Nanotechnology*, 20(41):415303, 2009.

-
- [29] M J K Klein, F Montagne, N Blondiaux, O Vazquez-Mena, H Heinzelmann, R Pugin, J Brugger, and V A Savu. Nanoporous sin membranes patterned by wafer-scale nanosphere lithography. *Journal of Vacuum Science and Technology*, 2010. submitted.
- [30] X-M Yan, A M Contreras, M M Koebel, J A Liddle, and G A Somorjai. Parallel fabrication of sub-50-nm uniformly sized nanoparticles by deposition through a patterned silicon nitride nanostencil. *Nano Letters*, 5:1129–1134, 2005.
- [31] V A Savu, S Neuser, and J Brugger. Bismuth nanowires with stencil lithography. In *Proceedings 34th International Conference on Micro & Nano Engineering (Athens)*, 2008.
- [32] T N Tun, M H T Lwin, H H Kim, N Chandrasekhar, and C Joachim. Wetting studies on au nanowires deposited through nanostencil masks. *Nanotechnology*, 18:335301, 2007.
- [33] P. Weber, E. Guibert, S. Mikhailov, J. Brugger, and G. Villanueva. Ion beam etching: Replication of micro nano-structured 3d stencil masks. *Application of Accelerators in Research and Industry*, 1099:539–541, 2009.
- [34] S. W. Pang, M. W. Geis, W. D. Goodhue, N. N. Efremow, D. J. Ehrlich, R. B. Goodman, and J. N. Randall. Pattern transfer by dry etching through stencil masks. *Journal of Vacuum Science & Technology B: Microelectronics and Nanometer Structures*, 6(1):249–252, 1988.
- [35] G Villanueva, O Vazquez-Mena, M A F van den Boogaart, K Sidler, K Pataky, V Savu, and J Brugger. Etching of sub-micrometer structures through stencil. *Journal of Microelectronic Engineering*, 85:1010–1014, 2008.
- [36] Y. X. Zhou, Alan T. Johnson, James Hone, and Walter F. Smith. Simple fabrication of molecular circuits by shadow mask evaporation. *Nano Letters*, 3(10):1371–1374, 2003.
- [37] J Arcamone, M A F van den Boogaart, F Serra-Graells, J Fraxedas, J Brugger, and F Perez-Murano. Full-wafer fabrication by nanostencil lithography of micro/nanomechanical mass sensors monolithically integrated with cmos. *Nanotechnology*, 19(30):305302, 2008.
- [38] K. Sidler, O. Vazquez-Mena, V. Savu, G. Villanueva, M.A.F. van den Boogaart, and J. Brugger. Resistivity measurements of gold wires fabricated by stencil lithography on flexible polymer substrates. *Microelectronic Engineering*, 85(5-6):1108 – 1111, 2008. Proceedings of the Micro- and Nano-Engineering 2007 Conference - MNE 2007.
- [39] G. Villanueva, O. Vazquez-Mena, C. Hibert, and J. Brugger. Direct etching of high aspect ratio structures through a stencil. In *Micro Electro Mechanical Systems, 2009. MEMS 2009. IEEE 22nd International Conference on*, pages 144 –147, 25-29 2009.
- [40] Maryna Lishchynska, Victor Bourenkov, Marc A.F. van den Boogaart, Lianne Doeswijk, Juergen Brugger, and James C. Greer. Predicting mask distortion, clogging and pattern transfer for stencil lithography. *Microelectronic Engineering*, 84(1):42 – 53, 2007.
- [41] 2010. This argument is supported by the long-time experience in the group of Prof. J. Brugger (EPFL-STI-IMT-LMIS1).
- [42] S Kuiper. *Development and application of microsieves*. PhD thesis, University of Twente, Enschede, The Netherlands, 2000.

- [43] C van Rijn, W van der Wekken, Nijdam W, and M Elwenspoek. Deflection and maximum load of microfiltration membrane sieve made with silicon micromachining. *Journal of Microelectromechanical Systems*, 6(1):48–54, 1997.
- [44] C J M van Rijn and M C Elwenspoek. Micro filtration membrane sieve with silicon micro machining for industrial and biomedical applications. In *IEEE MEMS proceedings 1995*, pages 83–87, 1995.
- [45] NL-1072 VP Amsterdam NL) Van Rijn, Cornelis J. M. (Gerard Doustraat 10. Inorganic membrane for microfiltration, and a process for production of such an inorganic membrane, August 1996.
- [46] Cornelis Johannes Maria Van Rijn. Membrane filter and a method of manufacturing the same as well as a membrane, May 1998.
- [47] G. Belfort, R. H. Davis, and A. L. Zydney. The behavior of suspensions and macromolecular solutions in cross-flow microfiltration. *Journal of Membrane Science*, 96(1-2):1–58, 1994.
- [48] C.J.M. van Rijn, editor. *Nano and Micro Engineered Membrane Technology*. Elsevier B.V., 2004.
- [49] A Karimi, O R Shojaei, T Kruml, and J.-L. Martin. Characterisation of tin thin films using the bulge test and the nanoindentation technique. *Thin Solid Films*, 308-309:334–339, 1997.
- [50] A Kovacs, A Kovacs, M Poganya, and U Mescheder. Mechanical investigation of perforated and porous membranes for micro- and nanofilter applications. *Sensors and Actuators B*, 127:120–125, 2007.
- [51] F J de Abajo Garcia. Colloquium: Light scattering by particle and hole arrays. *Reviews of Modern Physics*, 79:1267, 2007.
- [52] R. W. Wood. On a remarkable case of uneven distribution of light in a diffraction grating spectrum. *Philosophical Magazine*, 4(19-24):396–402, 1902.
- [53] Lord Rayleigh. On the dynamical theory of gratings. *Proc. R. Soc. Lond. A*, 79:399–416, 1907.
- [54] T. W. Ebbesen, H. J. Lezec, H. F. Ghaemi, T. Thio, and P. A. Wolff. Extraordinary optical transmission through sub-wavelength hole arrays. *Nature*, 391(6668):667–669, 1998.
- [55] W. L. Barnes, A. Dereux, and T. W. Ebbesen. Surface plasmon subwavelength optics. *Nature*, 424(6950):824–830, 2003.
- [56] C Kittel. *Introduction to Solid State Physics*. Wiley-VCH, 2002.
- [57] H A Bethe. Theory of diffraction by small holes. *Phys. Rev.*, 66:163–182, 1944.
- [58] T. Thio, H. F. Ghaemi, H. J. Lezec, P. A. Wolff, and T. W. Ebbesen. Surface-plasmon-enhanced transmission through hole arrays in cr films. *Journal of the Optical Society of America B-Optical Physics*, 16(10):1743–1748, 1999.
- [59] A. Degiron, H. J. Lezec, W. L. Barnes, and T. W. Ebbesen. Effects of hole depth on enhanced light transmission through subwavelength hole arrays. *Applied Physics Letters*, 81(23):4327–4329, 2002.

-
- [60] K. L. van der Molen, K. J. Klein Koerkamp, S. Enoch, F. B. Segerink, N. F. van Hulst, and L. Kuipers. Role of shape and localized resonances in extraordinary transmission through periodic arrays of subwavelength holes: Experiment and theory. *Physical Review B*, 72(4), 2005.
- [61] E Laux, C Genet, and T W Ebbesen. Enhanced optical transmission at the cutoff transition. *Optics Express*, 17:6920–6930, 2009.
- [62] L. Martin-Moreno, F. J. Garcia-Vidal, H. J. Lezec, K. M. Pellerin, T. Thio, J. B. Pendry, and T. W. Ebbesen. Theory of extraordinary optical transmission through subwavelength hole arrays. *Physical Review Letters*, 86(6):1114–1117, 2001.
- [63] C. Genet, M. P. van Exter, and J. P. Woerdman. Fano-type interpretation of red shifts and red tails in hole array transmission spectra. *Optics Communications*, 225(4-6):331–336, 2003.
- [64] F. Przybilla, A. Degiron, J. Y. Laluet, C. Genet, and T. W. Ebbesen. Optical transmission in perforated noble and transition metal films. *Journal of Optics a-Pure and Applied Optics*, 8(5):458–463, 2006.
- [65] A Krishnan, T Thio, T J Kim, H J Lezec, T W Ebbesen, P A Wolff, J Pendry, L Martin-Moreno, and F J Garcia-Vidal. Evanescently coupled resonance in surface plasmon enhanced transmission. *Optics Communications*, 200, 2001.
- [66] A. G. Brolo, R. Gordon, B. Leathem, K. L. Kavanagh, and Rk. Surface plasmon sensor based on the enhanced light transmission through arrays of nanoholes in gold films. *Langmuir*, 20(12):4813–4815, 2004.
- [67] A. Dahlin, M. Zach, T. Rindzevicius, M. Kall, D. S. Sutherland, F. Hook, and Lq. Localized surface plasmon resonance sensing of lipid-membrane-mediated biorecognition events. *Journal of the American Chemical Society*, 127(14):5043–5048, 2005.
- [68] A. Lesuffleur, H. Im, N. C. Lindquist, K. S. Lim, and S. H. Oh. Laser-illuminated nanohole arrays for multiplex plasmonic microarray sensing. *Optics Express*, 16(1):219–224, 2008.
- [69] A. Lesuffleur, H. Im, N. C. Lindquist, and S. H. Oh. Periodic nanohole arrays with shape-enhanced plasmon resonance as real-time biosensors. *Applied Physics Letters*, 90(24), 2007.
- [70] R. Gordon, A. G. Brolo, D. Sinton, and K. L. Kavanagh. Resonant optical transmission through hole-arrays in metal films: physics and applications. *Laser & Photonics Reviews*, 4(2):311–335, 2010.
- [71] K. A. Tetz, L. Pang, and Y. Fainman. High-resolution surface plasmon resonance sensor based on linewidth-optimized nanohole array transmittance. *Optics Letters*, 31(10):1528–1530, 2006.
- [72] H. Im, A. Lesuffleur, N. C. Lindquist, and S. H. Oh. Plasmonic nanoholes in a multichannel microarray format for parallel kinetic assays and differential sensing. *Analytical Chemistry*, 81(8):2854–2859, 2009.
- [73] A. Dhawan, J. F. Muth, D. N. Leonard, M. D. Gerhold, J. Gleeson, T. Vo-Dinh, and P. E. Russell. Focused ion beam fabrication of metallic nanostructures on end faces of optical fibers for chemical sensing applications. *Journal of Vacuum Science and Technology B*, 26:2168–2173, 2008.

- [74] J. Ferreira, M. J. L. Santos, M. M. Rahman, A. G. Brolo, R. Gordon, D. Sinton, and E. M. Girotto. Attomolar protein detection using in-hole surface plasmon resonance. *Journal of the American Chemical Society*, 131(2):436, 2009.
- [75] M. J. K. Klein, M. Guillaumee, B. Wenger, L. A. Dunbar, J. Brugger, H. Heinzelmann, and R. Pugin. Inexpensive and fast wafer-scale fabrication of nanohole arrays in thin gold films for plasmonics. *Nanotechnology*, 21(20), 2010.
- [76] A A Yanik, M Huang, A Artar, T-Y Chang, and H Altug. Integrated nanoplasmonic-nanofluidic biosensors with targeted delivery of analytes. *Applied Physics Letters*, 96, 2010.
- [77] F Y Li, L Zhang, and R M Metzger. On the growth of highly ordered pores in anodized aluminum oxide. *Chemistry of Materials*, 10:2470–2480, 1998.
- [78] Napa - emerging nanopatterning methods: An eu integrated project consortium. online, 2006.
- [79] H. D. Tong, H. V. Jansen, V. J. Gadgil, C. G. Bostan, E. Berenschot, C. J. M. van Rijn, and M. Elwenspoek. Silicon nitride nanosieve membrane. *Nano Letters*, 4(2):283–287, 2004.
- [80] Y. Q. Fu, N. K. A. Bryan, and L. T. Fatt. Fabrication and characterization of nanopore array. *Journal of Nanoscience and Nanotechnology*, 6(7):1954–1960, 2006.
- [81] F Eftekhari, C Escobedo, J Ferreira, X Duan, E M Girotto, A G Brolo, R Gordon, and D Sinton. Nanoholes as nanochannels: Flow-through plasmonic sensing. *Analytical Chemistry*, 81, 2009.
- [82] K J Klein Koerkamp, S Enoch, F B Segerink, N F van Hulst, and L Kuipers. Strong influence of hole shape on extraordinary transmission through periodic arrays of subwavelength holes. *Physical Review Letters*, 92, 2004.
- [83] N. C. Lindquist, A. Lesuffleur, and S. H. Oh. Lateral confinement of surface plasmons and polarization-dependent optical transmission using nanohole arrays with a surrounding rectangular bragg resonator. *Applied Physics Letters*, 91(25), 2007.
- [84] L A Dunbar, M Guillaumee, F de Leon-Perez, C Santschi, E Grenet, R Eckert, F Lopez-Tejeira, F J Garcia-Vidal, L Martin-Moreno, and R P Stanley. Enhanced transmission from a single subwavelength slit aperture surrounded by grooves on a standard detector. *Applied Physics Letters*, 95:011113, 2009.
- [85] Fabrication of nano-sized gold dot array using bi-layer nano imprint lithography. In *Eco-Materials Processing & Design VII*, volume 510-511 of *Materials Science Forum*, pages 446–449. Trans Tech Publications Ltd, Zurich-Uetikon, 2006.
- [86] J. Brian Leen, Paul Hansen, Yao-Te Cheng, and Lambertus Hesselink. Improved focused ion beam fabrication of near-field apertures using a silicon nitride membrane. *Opt. Lett.*, 33(23):2827–2829, 2008.
- [87] S Aksu, A A Yanik, R Adato, A Artar, M Huang, and H Altug. High-throughput nanofabrication of infrared plasmonic nanoantenna arrays for vibrational nanospectroscopy. *Nano Letters*, 10:2511–2518, 2010.

-
- [88] O M Piciu, M W Docter, M C van der Krogt, Y Garini, T Young, P M Sarro, and A Bossche. Fabrication and optical characterization of nano-hole arrays in gold and gold/palladium films on glass. *Proceedings of the Institution of Mechanical Engineers, Part N: Journal of Nanoengineering and Nanosystems*, 221:107–114, 2007.
- [89] N. Gadegaard and D. McCloy. Direct stamp fabrication for nil and hot embossing using hsq. *Microelectronic Engineering*, 84(12):2785 – 2789, 2007.
- [90] D Stolwijk, E F C Driessen, M A Verschuuren, G W 't Hooft, M P van Exter, and M J A de Dood. Enhanced coupling of plasmons in hole arrays with periodic dielectric antennas. *Optics Letters*, 33, 2008.
- [91] P Apel. Track etching technique in membrane technology. In *Radiation measurements*, 20th International Conference on Nuclear Tracks in Solids, 2001.
- [92] I. Vlassiuk, P. Y. Apel, S. N. Dmitriev, K. Healy, and Z. S. Siwy. Versatile ultrathin nanoporous silicon nitride membranes. *Proceedings of the National Academy of Sciences of the United States of America*, 106(50):21039–21044, 2009.
- [93] M A F van den Boogaart, G M Kim, R Pellens, J-P van den Heuvel, and J Brugger. Deep-ultraviolet-microelectromechanical systems stencils for high-throughput resistless patterning of mesoscopic structures. *Journal of Vacuum Science & Technology B*, 22:3174, 2004.
- [94] J.M. Carter, R.C. Fleming, T.A. Savas, M.E. Walsh, and T.B.kk O'Reilly. Interference lithography. Technical report, MTL Annual Report, 2003.
- [95] J. H. Jang, C. K. Ullal, M. Maldovan, T. Gorishnyy, S. Kooi, C. Y. Koh, and E. L. Thomas. 3d micro- and nanostructures via interference lithography. *Advanced Functional Materials*, 17(16):3027–3041, 2007.
- [96] S. Kuiper, H. van Wolferen, G. van Rijn, W. Nijdam, G. Krijnen, and M. Elwenspoek. Fabrication of microsieves with sub-micron pore size by laser interference lithography. *Journal of Micromechanics and Microengineering*, 11(1):33–37, 2001.
- [97] T W Odom, J C Love, D B Wolfe, K E Paul, and G M Whitesides. Improved pattern transfer in soft lithography using composite stamps. *Langmuir*, 18:5314–5320, 2002.
- [98] E-S Kwak, J Henzie, S-H Chang, S K Gray, G C Schatz, and T W Odom. Surface plasmon standing waves in large-area subwavelength hole arrays. *Nano Letters*, 5, 2005.
- [99] J Henzie, J Lee, M H Lee, W Hasan, and T W Odom. Nanofabrication of plasmonic structures. *Annual Review of Physical Chemistry*, 60:147–165, 2009.
- [100] H Schiff. Nanoimprint lithography: An old story in modern times? a review. *Journal of Vacuum Science and Technology B*, 26, 2008.
- [101] Y. N. Xia and G. M. Whitesides. Extending microcontact printing as a microlithographic technique. *Langmuir*, 13(7):2059–2067, 1997.
- [102] H Wolf. Soft lithography & self-assembly. EPFL Doctoral School, 2008.

- [103] J L Skinner, L L Hunter, A A Talin, J Provine, and D A Horsley. Large-area subwavelength aperture arrays fabricated using nanoimprint lithography. *IEEE Transactions on Nanotechnology*, 7:527–531, 2008.
- [104] J Chen, J Shi, D Decanini, E Cambril, Y Chen, and A-M Haghiri-Gosnet. Gold nanohole arrays for biochemical sensing fabricated by soft uv nanoimprint lithography. *Microelectronic Engineering*, 86:632–635, 2009.
- [105] L. J. Heyderman, B. Ketterer, D. Bachle, F. Glaus, B. Haas, H. Schiff, K. Vogelsang, J. Gobrecht, L. Tiefenauer, O. Dubochet, P. Surbled, and T. Hessler. High volume fabrication of customised nanopore membrane chips. *Microelectronic Engineering*, 67-8:208–213, 2003.
- [106] www.csem.ch. Tooling for replicated nanostructures. Technical report, CSEM S.A., Thin Film Optics, 2009.
- [107] www.csem.ch. Replicated color filters. Technical report, CSEM S.A., Thin Film Optics, 2009.
- [108] Y Xia and G M Whitesides. Soft lithography. *Annu. Rev. Mater. Sci.*, 28:153–184, 1998.
- [109] T Ozaki, K Sugano, and Oscar Tsuchiya, Tans Tabata. Versatile method of sub-micro particle pattern formation using self-assembly and two-step transfer. In *Proceedings IEEE MEMS 2007*, 2007.
- [110] T. Kraus, L. Malaquin, H. Schmid, W. Riess, N. D. Spencer, and H. Wolf. Nanoparticle printing with single-particle resolution. *Nature Nanotechnology*, 2:570–576, 2007.
- [111] A Kumar, H A Biebuyck, and G M Whitesides. Patterning self-assembled monolayers: Applications in materials scienc. *Langmuir*, 10:1498–1511, 1994.
- [112] HA Biebuyck, NB Larsen, E Delamar, and B Michel. Lithography beyond light: Microcontact printing with monolayer resists. *IBM JOURNAL OF RESEARCH AND DEVELOPMENT*, 41:59–170, 1997.
- [113] B A Grzybowski, C E Wilmer, J Kim, and K J M Browne, K P aand Bishop. Self-assembly: from crystals to cells. *Soft Matter*, 5:1110–1128, 2009.
- [114] I.W. Hamley. Ordering in thin films of block copolymers: Fundamentals to potential applications. *Progress in Polymer Science*, 34(11):1161–1210, November 2009.
- [115] S.B. Darling. Directing the self-assembly of block copolymers. *Progress in Polymer Science*, 32(10):1152 – 1204, 2007.
- [116] A P Marencic and R A Register. Controlling order in block copolymer thin films for nanopat- terning applications. *Annual Review of Chemical and Biomolecular Engineering*, 1:277–97, 2010.
- [117] C T Black, R Ruiz, G Breyta, Y Y Cheng, M E Colburn, H-C Kim, and Y Zhan. Polymer self assembly in semiconductor microelectronics. *IBM J. RES. & DEV.*, 51, 2007.
- [118] S. A. Jenekhe and X. L. Chen. Self-assembly of ordered microporous materials from rod-coil block copolymers. *Science*, 283(5400):372–375, 1999.

-
- [119] G. Arya, J. Rottler, A. Z. Panagiotopoulos, D. J. Srolovitz, and P. M. Chaikin. Shear ordering in thin films of spherical block copolymer. *Langmuir*, 21(24):11518–11527, 2005.
- [120] S. Krishnamoorthy, R. Pugin, J. Brugger, H. Heinzelmann, A. C. Hoogerwerf, and C. Hinderling. Block copolymer micelles as switchable templates for nanofabrication. *Langmuir*, 22(8):3450–3452, 2006.
- [121] S. Krishnamoorthy, R. Pugin, J. Brugger, H. Heinzelmann, and C. Hinderling. Tuning the dimensions and periodicities of nanostructures starting from the same polystyrene-block-poly(2-vinylpyridine) diblock copolymer. *Advanced Functional Materials*, 16(11):1469–1475, 2006.
- [122] S. Krishnamoorthy, C. Hinderling, and H. Heinzelmann. Nanoscale patterning with block copolymers. *Materials Today*, 9(9):40–47, 2006.
- [123] K. W. Guarini, C. T. Black, Y. Zhang, H. Kim, E. M. Sikorski, and I. V. Babich. Process integration of self-assembled polymer templates into silicon nanofabrication. *Journal of Vacuum Science & Technology B*, 20(6):2788–2792, 2002. 27.
- [124] I. W. Hamley. Nanostructure fabrication using block copolymers. *Nanotechnology*, 14(10):R39–R54, 2003.
- [125] M. Haupt, S. Miller, A. Ladenburger, R. Sauer, K. Thonke, J. P. Spatz, S. Riethmuller, M. Moller, and F. Banhart. Semiconductor nanostructures defined with self-organizing polymers. *Journal of Applied Physics*, 91(9):6057–6059, 2002.
- [126] S. Brieger, O. Dubbers, S. Fricker, A. Manzke, C. Pfahler, A. Plettl, and P. Ziemann. An approach for the fabrication of hexagonally ordered arrays of cylindrical nanoholes in crystalline and amorphous silicon based on the self-organization of polymer micelles. *Nanotechnology*, 17(19):4991–4994, 2006.
- [127] A.-M. Popa. *Stimuli-responsive nanostructured surfaces*. PhD thesis, Swiss Federal Institute of Technology Lausanne, 2009.
- [128] C. T. Black, K. W. Guarini, G. Breyta, M. C. Colburn, R. Ruiz, R. L. Sandstrom, E. M. Sikorski, and Y. Zhang. Highly porous silicon membrane fabrication using polymer self-assembly. *Journal of Vacuum Science & Technology B*, 24(6):3188–3191, 2006.
- [129] A. M. Popa, P. Niedermann, H. Heinzelmann, J. A. Hubbell, and R. Pugin. Fabrication of nanopore arrays and ultrathin silicon nitride membranes by block-copolymer-assisted lithography. *Nanotechnology*, 20(48):485303, 2009.
- [130] M. Haupt, S. Miller, R. Glass, M. Arnold, R. Sauer, K. Thonke, M. Moller, J. P. Spatz, and Dt. Nanoporous gold films created using templates formed from self-assembled structures of inorganic-block copolymer micelles. *Advanced Materials*, 15(10):829, 2003.
- [131] J. Vadrine, Y. R. Hong, A. P. Marencic, R. A. Register, D. H. Adamson, and P. M. Chaikin. Large-area, ordered hexagonal arrays of nanoscale holes or dots from block copolymer templates. *Applied Physics Letters*, 91(14), 2007.
- [132] U. C. Fischer and H. P. Zingsheim. Sub-microscopic pattern replication with visible-light. *Journal of Vacuum Science & Technology*, 19(4):881–885, 1981.

- [133] H. W. Deckman and J. H. Dunsmuir. Natural lithography. *Applied Physics Letters*, 41(4):377–379, 1982.
- [134] J. C. Hulthen and R. P. Van Duyne. Nanosphere lithography - a materials general fabrication process for periodic particle array surfaces. *Journal of Vacuum Science & Technology a-Vacuum Surfaces and Films*, 13(3):1553–1558, 1995.
- [135] S. M. Yang, S. G. Jang, D. G. Choi, S. Kim, and H. K. Yu. Nanomachining by colloidal lithography. *Small*, 2(4):458–475, 2006.
- [136] N. D. Denkov, O. D. Velev, P. A. Kralchevsky, I. B. Ivanov, H. Yoshimura, and K. Nagayama. Mechanism of formation of 2-dimensional crystals from latex-particles on substrates. *Langmuir*, 8(12):3183–3190, 1992.
- [137] A. S. Dimitrov and K. Nagayama. Continuous convective assembling of fine particles into two-dimensional arrays on solid surfaces. *Langmuir*, 12(5):1303–1311, 1996.
- [138] M. Giuliani, W. Gonzalez-Vinas, K. M. Poduska, and A. Yethiraj. Dynamics of crystal structure formation in spin-coated colloidal films. *Journal of Physical Chemistry Letters*, 1(9):1481–1486, 2010.
- [139] B. G. Prevo and O. D. Velev. Controlled, rapid deposition of structured coatings from micro- and nanoparticle suspensions. *Langmuir*, 20(6):2099–2107, 2004.
- [140] G. H. Jeong, J. K. Park, K. K. Lee, J. H. Jang, C. H. Lee, H. B. Kang, C. W. Yang, and S. J. Suh. Fabrication of low-cost mold and nanoimprint lithography using polystyrene nanosphere. *Microelectronic Engineering*, 87(1):51–55, 2010.
- [141] P. Jiang and M. J. McFarland. Wafer-scale periodic nanohole arrays templated from two-dimensional nonclose-packed colloidal crystals. *Journal of the American Chemical Society*, 127, 2005.
- [142] K. D. Barbee, A. P. Hsiao, M. J. Heller, and X. H. Huang. Electric field directed assembly of high-density microbead arrays. *Lab on a Chip*, 9(22):3268–3274, 2009.
- [143] M. Alberti, E. Yacoub-George, W. Hell, C. Landesberger, and K. Bock. Biomolecular self-assembly of micrometer sized silica beads on patterned glass substrates. *Applied Surface Science*, 255(17):7759–7765, 2009.
- [144] K. Lee, M. Duchamp, G. Kulik, A. Magrez, J. W. Seo, S. Jeney, A. J. Kulik, L. Forro, R. S. Sundaram, and J. Brugger. Uniformly dispersed deposition of colloidal nanoparticles and nanowires by boiling. *Applied Physics Letters*, 91, 2007.
- [145] W. K. Lee, Z. Dai, W. P. King, and P. E. Sheehan. Maskless nanoscale writing of nanoparticle-polymer composites and nanoparticle assemblies using thermal nanoprobles. *Nano Letters*, 10:129–133, 2010.
- [146] J. Park and J. Moon. Control of colloidal particle deposit patterns within picoliter droplets ejected by ink-jet printing. *Langmuir*, 22(8):3506–3513, 2006.
- [147] Y. N. Xia, Y. D. Yin, Y. Lu, and J. McLellan. Template-assisted self-assembly of spherical colloids into complex and controllable structures. *Advanced Functional Materials*, 13(12):907–918, 2003.

-
- [148] L Malaquin, T Kraus, H Schmid, E Delamarche, and H Wolf. Controlled particle placement through convective and capillary assembly. *Langmuir*, 23, 2007.
- [149] C. Haginoya, M. Ishibashi, and K. Koike. Nanostructure array fabrication with a size-controllable natural lithography. *Applied Physics Letters*, 71(20):2934–2936, 1997.
- [150] J. Y. Shiu, C. W. Kuo, P. L. Chen, and C. Y. Mou. Fabrication of tunable superhydrophobic surfaces by nanosphere lithography. *Chemistry of Materials*, 16(4):561–564, 2004.
- [151] E. Reimhult, K. Kumar, and W. Knoll. Fabrication of nanoporous silicon nitride and silicon oxide films of controlled size and porosity for combined electrochemical and waveguide measurements. *Nanotechnology*, 18:275303, 2007.
- [152] A Plettl, F Enderle, M Saitner, A Manzke, C Pfahler, S Wiedemann, and P Ziemann. Non-close-packed crystals from self-assembled polystyrene spheres by isotropic plasma etching: Adding flexibility to colloid lithography. *Advanced Functional Materials*, 19:3279–3284, 2009.
- [153] C. Gigault, K. Dalnoki-Veress, and J. R. Dutcher. Changes in the morphology of self-assembled polystyrene microsphere monolayers produced by annealing. *Journal of Colloid and Interface Science*, 243(1):143–155, 2001.
- [154] H. Agheli and D. S. Sutherland. Nanofabrication of polymer surfaces utilizing colloidal lithography and ion etching. *Ieee Transactions on Nanobioscience*, 5(1):9–14, 2006.
- [155] H. Fredriksson, Y. Alaverdyan, A. Dmitriev, C. Langhammer, D. S. Sutherland, M. Zaech, and B. Kasemo. Hole-mask colloidal lithography. *Advanced Materials*, 19(23):4297–4302, 2007.
- [156] C. L. Haynes and R. P. Van Duyne. Nanosphere lithography: A versatile nanofabrication tool for studies of size-dependent nanoparticle optics. *Journal of Physical Chemistry B*, 105(24):5599–5611, 2001.
- [157] C. M. Zhou and D. Gall. Surface patterning by nanosphere lithography for layer growth with ordered pores. In *34th International Conference on Metallurgical Coatings and Thin Films*, pages 433–437, San Diego, CA, 2007.
- [158] G Duan, W Cai, Y Luo, F Lv, J Yang, and Y Li. Design and electrochemical fabrication of gold binary ordered micro/nanostructured porous arrays via step-by-step colloidal lithography. *Langmuir*, 25:2558–62, 2009.
- [159] J. R. Oh, J. H. Moon, H. K. Park, J. H. Park, H. Chung, J. Jeong, W. Kim, and Y. R. Do. Wafer-scale colloidal lithography based on self-assembly of polystyrene nanospheres and atomic layer deposition. *Journal of Materials Chemistry*, 20(24):5025–5029, 2010.
- [160] A Kosiorek, W Kandulski, H Glaczynska, and M Giersig. Fabrication of nanoscale rings, dots, and rods by combining shadow nanosphere lithography and annealed polystyrene nanosphere masks. *Small*, 1:439–444, 2005.
- [161] Alyson V. Whitney, Benjamin D. Myers, and Richard P. Van Duyne. Sub-100 nm triangular nanopores fabricated with the reactive ion etching variant of nanosphere lithography and angle-resolved nanosphere lithography. *Nano Letters*, 4(8):1507–1511, 2004.

- [162] C. F. Chau and T. Melvin. The fabrication of macroporous polysilicon by nanosphere lithography. *J. Micromech. Microeng.*, 18:064012, 2008.
- [163] V A Savu, M J K Klein, F Montagne, O Vazquez-Mena, J Brugger, H Heinzlmann, and R Pugin. Nanoporous sin membranes patterned by wafer-scale nanosphere lithography. In *Conf. Proceedings EIPBN 2010, Anchorage*, 2010.
- [164] A. Ladenburger, A. Reiser, J. Konle, M. Feneberg, R. Sauer, K. Thonke, F. Yan, and W. A. Goedel. Regular silicon pillars and dichroic filters produced via particle-imprinted membranes. *Journal of Applied Physics*, 101(3):034302, 2007.
- [165] T. Lohmueller, U. Muller, S. Breisch, W. Nisch, R. Rudolf, W. Schuhmann, S. Neugebauer, M. Kaczor, S. Linke, S. Lechner, J. Spatz, and M. Stelzle. Nano-porous electrode systems by colloidal lithography for sensitive electrochemical detection: fabrication technology and properties. *Journal of Micromechanics and Microengineering*, 18(11):115011, 2008.
- [166] T H Reilly-Ill, J van de Lagemaat, R C Tenent, and A J Morfa. Surface-plasmon enhanced transparent electrodes in organic photovoltaics. *Applied Physics Letters*, 92:243304, 2008.
- [167] G Weder, N Blondiaux, M Giazzon, N Matthey, M J K Klein, R Pugin, H Heinzlmann, and M Liley. Use of force spectroscopy to investigate the adhesion of living adherent cells. *Langmuir*, 26:8180–8186, 2010.
- [168] Y. C. Jung and B. Bhushan. Contact angle, adhesion and friction properties of micro- and nanopatterned polymers for superhydrophobicity. *Nanotechnology*, 17(19):4970–4980, 2006.
- [169] W. Wu, D. Dey, O. G. Memis, A. Katsnelson, and H. Mohseni. A novel self-aligned and maskless process for formation of highly uniform arrays of nanoholes and nanopillars. *Nanoscale Research Letters*, 3(3):123–127, 2008.
- [170] C. L. Cheung, R. J. Nikolic, C. E. Reinhardt, and T. F. Wang. Fabrication of nanopillars by nanosphere lithography. *Nanotechnology*, 17(5):1339–1343, 2006.
- [171] W Wu, D Dey, A Katsnelson, O G Memis, and H Mohseni. Large areas of periodic nanoholes perforated in multistacked films produced by lift-off. *Journal of Vacuum Science and Technology B*, 26:1745, 2008.
- [172] Y. H. Kang, S. S. Oh, Y. S. Kim, and C. G. Choi. Fabrication of antireflection nanostructures by hybrid nano-patterning lithography. *Microelectronic Engineering*, 87(2):125–128, 2010.
- [173] X Zhang, Z Zhu, C Sun, F Zhu, Z Luo, J Yan, and B Mao. Colloidal lithography-based fabrication of suspended nanoporous silicon nitride membranes. *Microchim Acta*, 167:135–140, 2009.
- [174] C Acikgoz, X Y Ling, I Y Phang, M A Hempenius, D N Reinhoudt, J Huskens, and G J Vancso. Fabrication of freestanding nanoporous polyethersulfone membranes using organometallic polymer resists patterned by nanosphere lithography. *Advanced Materials*, 21:1–4, 2009.
- [175] G. Decher. Fuzzy nanoassemblies: Toward layered polymeric multicomposites. *Science*, 277(5330):1232–1237, 1997.
- [176] G. M. Whitesides, J. P. Mathias, and C. T. Seto. Molecular self-assembly and nanochemistry - a chemical strategy for the synthesis of nanostructures. *Science*, 254(5036):1312–19, 1991.

-
- [177] M. Mastrangeli, S. Abbasi, C. Varel, C. Van Hoof, J. P. Celis, and K. F. Bohringer. Self-assembly from milli-to nanoscales: methods and applications. *Journal of Micromechanics and Microengineering*, 19(8):083001, 2009.
- [178] Y. H. Wang and W. D. Zhou. A review on inorganic nanostructure self-assembly. *Journal of Nanoscience and Nanotechnology*, 10(3):1563–1583, 2010.
- [179] G. A. Ozin and S. M. Yang. The race for the photonic chip: Colloidal crystal assembly in silicon wafers. *Advanced Functional Materials*, 11(2):95–104, 2001.
- [180] P A Kralchevsky and K Nagayama. Capillary forces between colloidal particles. *Langmuir*, 10:23–36, 1994.
- [181] J Ducree and R Zengerle. Microfluidics. Course book on Microfluidics, IMTEK, University of Freiburg, 2001.
- [182] P Schurtenberger. Soft matter - colloids. Course on Colloidal Chemistry.
- [183] K Tauer. *Colloids and colloid assembled - Latex particles Ch.1*. Wiley-VCH, 2004.
- [184] M R Pashley and M E Karaman. *Applied Colloid and Surface Chemistry*. Wiley-VCH, 2004.
- [185] N V Churaev and V D Sobolev. *Nanoscience - Colloidal and Interfacial Aspects Ch.1 Surface Forces in Nanostructures*. CRC Press, 2010.
- [186] D Myers. *Surfaces, Interfaces, and Colloids - Principles and applications*. Wiley-VCH, 2 edition, 1999.
- [187] R Seemann, S Herminghaus, and K Jacobs. Gaining control of pattern formation of dewetting liquid films. *Journal of Physics: Condensed Matter*, 13:4925–4938, 2001.
- [188] L Bergstroem. Hamaker constants of inorganic materials. *Advances in Colloid and Interface Science*, 70:125–169, 1997.
- [189] Harald Fiedler. Zeta potential ps forschungspartikel im grossenbereich 300 - 800 nm. Personal correspondence, July 2010.
- [190] P. A. Kralchevsky, V. N. Paunov, I. B. Ivanov, and K. Nagayama. Capillary meniscus interaction between colloidal particles attached to a liquid-fluid interface. *Journal of Colloid and Interface Science*, 151(1):79–94, 1992.
- [191] V. N. Paunov, P. A. Kralchevsky, N. D. Denkov, and K. Nagayama. Lateral capillary forces between floating submillimeter particles. *Journal of Colloid and Interface Science*, 157(1):100–112, 1993.
- [192] O. D. Velev, N. D. Denkov, V. N. Paunov, P. A. Kralchevsky, and K. Nagayama. Direct measurement of lateral capillary forces. *Langmuir*, 9(12):3702–3709, 1993.
- [193] E. Adachi, A. S. Dimitrov, and K. Nagayama. Stripe patterns formed on a glass-surface during droplet evaporation. *Langmuir*, 11(4):1057–1060, 1995.

- [194] P. A. Kralchevsky and N. D. Denkov. Capillary forces and structuring in layers of colloid particles. *Current Opinion in Colloid & Interface Science*, 6(4):383–401, 2001.
- [195] P A Kralchevsky and K D Danov. *Nanoscience - Colloidal and Interfacial Aspects Ch.15 Interactions between Particles at a Fluid Interfaces*. CRC Press, 2010.
- [196] K. D. Danov and P. A. Kralchevsky. Interaction between like-charged particles at a liquid interface: Electrostatic repulsion vs. electrocapillary attraction. *Journal of Colloid and Interface Science*, 345(2):505–514, 2010.
- [197] H. Nishikawa, S. Maenosono, Y. Yamaguchi, and T. Okubo. Self-assembling process of colloidal particles into two-dimensional arrays induced by capillary immersion force: A simulation study with discrete element method. *Journal of Nanoparticle Research*, 5(1-2):103–110, 2003.
- [198] S. Maenosono, C. D. Dushkin, and Y. Yamaguchi. Direct measurement of the viscous force between two spherical particles trapped in a thin wetting film. *Colloid and Polymer Science*, 277(10):993–996, 1999.
- [199] R. McGorty, J. Fung, D. Kaz, and V. N. Manoharan. Colloidal self-assembly at an interface. *Materials Today*, 13(6):34–42, 2010.
- [200] P. A. Kralchevsky and K. Nagayama. Capillary interactions between particles bound to interfaces, liquid films and biomembranes. *Advances in Colloid and Interface Science*, 85(2-3):145–192, 2000.
- [201] Y Cui, M T Bjork, J A Liddle, C Sonnichsen, B Boussert, and A P Alivisatos. Integration of colloidal nanocrystals into lithographically patterned devices. *Nano Letters*, 4:1093–1098, 2004.
- [202] P A Kralchevsky, V N Paunov, I B Ivanov, and K Nagayama. Capillary meniscus interaction between colloidal particles attached to a liquid-fluid interface. *Journal of Colloid and Interface Science*, 151:79–94, 1991.
- [203] D. Y. C. Chan, J. D. Henry, and L. R. White. The interaction of colloidal particles collected at fluid interfaces. *Journal of Colloid and Interface Science*, 79(2):410–418, 1981.
- [204] S. C. Rodner, P. Wedin, and L. Bergstrom. Effect of electrolyte and evaporation rate on the structural features of dried silica monolayer films. *Langmuir*, 18(24):9327–9333, 2002.
- [205] E Sirotkin, J D Apweiler, and F Y Ogrin. Macroscopic ordering of polystyrene carboxylate-modified nanospheres self-assembled at the water-air interface. *Langmuir*, 26:10677–10683, 2010.
- [206] P H F Hansen, S Roedner, and L Bergstroem. Structural characterization of dense colloidal films using a modified pair distribution function and delaunay triangulation. *Langmuir*, 17:4867–75, 2001.
- [207] T. Okubo, S. Chujo, S. Maenosono, and Y. Yamaguchi. Microstructure of silica particle monolayer films formed by capillary immersion force. *Journal of Nanoparticle Research*, 5(1-2):111–117, 2003.
- [208] F. Q. Fan and K. J. Stebe. Assembly of colloidal particles by evaporation on surfaces with patterned hydrophobicity. *Langmuir*, 20(8):3062–3067, 2004.

-
- [209] M. Himmelhaus and H. Takei. Self-assembly of polystyrene nano particles into patterns of random-close-packed monolayers via chemically induced adsorption. *Physical Chemistry Chemical Physics*, 4(3):496–506, 2002.
- [210] Q. Yan, L. Gao, V. Sharma, Y. M. Chiang, and C. C. Wong. Particle and substrate charge effects on colloidal self-assembly in a sessile drop. *Langmuir*, 24(20):11518–11522, 2008.
- [211] Y. D. Yin, Y. Lu, B. Gates, and Y. N. Xia. Template-assisted self-assembly: A practical route to complex aggregates of monodispersed colloids with well-defined sizes, shapes, and structures. *Journal of the American Chemical Society*, 123(36):8718–29, 2001.
- [212] D. Y. Wang and H. Mohwald. Rapid fabrication of binary colloidal crystals by stepwise spin-coating. *Advanced Materials*, 16(3):244, 2004.
- [213] T. Ogi, L. B. Modesto-Lopez, F. Iskandar, and K. Okuyama. Fabrication of a large area monolayer of silica particles on a sapphire substrate by a spin coating method. *Colloids and Surfaces a-Physicochemical and Engineering Aspects*, 297(1-3):71–78, 2007.
- [214] R. D. Deegan, O. Bakajin, T. F. Dupont, G. Huber, S. R. Nagel, and T. A. Witten. Capillary flow as the cause of ring stains from dried liquid drops. *Nature*, 389(6653):827–829, 1997.
- [215] Particle synthesis. Technical report, microparticles GmbH, May 2007.
- [216] www.cpsinstruments.com. The cps disc centrifuge, 2010.
- [217] T. Kraus, L. Malaquin, E. Delamarche, H. Schmid, N. D. Spencer, and H. Wolf. Closing the gap between self-assembly and microsystems using self-assembly, transfer, and integration of particles. *Advanced Materials*, 17(20):2438, 2005.
- [218] R Zengerle. Mst t&p skript teil 1&2. Slides for course in microsystems engineering IMTEK - Freiburg University, Germany., 2006.
- [219] A. G. Emslie, F. T. Bonner, and L. G. Peck. Flow of a viscous liquid on a rotating disk. *Journal of Applied Physics*, 29(5):858–862, 1958.
- [220] B. J. Ackerson and N. A. Clark. Shear-induced partial translational ordering of a colloidal solid. *Physical Review A*, 30(2):906–918, 1984.
- [221] J. A. Britten and I. M. Thomas. Non-newtonian flow effects during spin coating large-area optical coatings with colloidal suspensions. *Journal of Applied Physics*, 71(2):972–979, 1992.
- [222] J. Vermant and M. J. Solomon. Flow-induced structure in colloidal suspensions. *Journal of Physics-Condensed Matter*, 17(4):R187–R216, 2005.
- [223] L. T. Shereda, R. G. Larson, and M. J. Solomon. Local stress control of spatiotemporal ordering of colloidal crystals in complex flows. *Physical Review Letters*, 101(3):038301, 2008.
- [224] P. Jiang and M. J. McFarland. Large-scale fabrication of wafer-size colloidal crystals, macroporous polymers and nanocomposites by spin-coating. *Journal of the American Chemical Society*, 126(42):13778–13786, 2004.

- [225] S Venkatesh, P Jiang, and B Jiang. Generalized fabrication of two-dimensional non-close-packed colloidal crystals. *Langmuir*, 23:8231–8235, 2007.
- [226] W-L Min, P Jiang, and B Jiang. Large-scale assembly of colloidal nanoparticles and fabrication of periodic subwavelength structures. *Nanotechnology*, 19, 2008.
- [227] Y. Zhao and J. S. Marshall. Spin coating of a colloidal suspension. *Physics of Fluids*, 20(4):043302, 2008.
- [228] V. Sharma, Q. F. Yan, C. C. Wong, W. C. Cartera, and Y. M. Chiang. Controlled and rapid ordering of oppositely charged colloidal particles. *Journal of Colloid and Interface Science*, 333(1):230–236, 2009.
- [229] Y. K. Hong, H. Kim, G. Lee, W. Kim, J. I. Park, J. Cheon, and J. Y. Koo. Controlled two-dimensional distribution of nanoparticles by spin-coating method. *Applied Physics Letters*, 80(5):844–846, 2002.
- [230] C-W Kuo, J-Y Shiu, and P Chen. Size- and shape-controlled fabrication of large-area periodic nanopillar arrays. *Chemistry of Materials*, 15:2917–2920, 2003.
- [231] A Mihi, M Ocana, and H Miguez. Oriented colloidal-crystal thin films by spin-coating microspheres dispersed in volatile media. *Advanced Materials*, 16:2244–2249, 2006.
- [232] X. F. Peng and I. Kamiya. Two methods to prepare nanorings/nanoholes for the fabrication of vertical nanotransistors. *Nanotechnology*, 19(31):315303, 2008.
- [233] H. W. Deckman, J. H. Dunsmuir, and R. B. Stephens. Light-scattering from natural lithographically fabricated surfaces. *Journal of the Optical Society of America*, 72(12):1826–1826, 1982.
- [234] S. Fujii, P. D. Iddon, A. J. Ryan, and S. P. Armes. Aqueous particulate foams stabilized solely with polymer latex particles. *Langmuir*, 22:7512–7520, 2006.
- [235] W Lee, R Ji, U Goesele, and K Nielsch. Fast fabrication of long-range ordered porous alumina membranes by hard anodization. *Nature Materials*, 5, 2006.
- [236] P Hanarp, D S Sutherland, J Gold, and B Kasemo. Control of nanoparticle film structure for colloidal lithography. *Colloids and Surfaces A*, 214:23–36, 2003.
- [237] H-G Elias. *Makromolekuele, Ch 13.5*. Wiley-VCH, Weinheim, Germany, 2001.
- [238] H-N Lee, K Paeng, S F Swallen, and M D Ediger. Direct measurement of molecular mobility in actively deformed polymer glasses. *Science*, 323:231, 2009.
- [239] F D Egitto. Plasma etching and modification of organic polymers. *Pure & Appl. Chem.*, 62:1699–1708, 1990.
- [240] C J Zimmermann, N Ryde, N Kallay, R E Partch, and E Matijevic. Plasma modification of polyvinyltoluene and polystyrene latices. *J. Mater. Research*, 6:855, 1991.
- [241] M Lu, J Zhou, L Wang, W Zhao, Y Lu, L Zhang, and Y Liu. Design and preparation of cross-linked polystyrene nanoparticles for elastomer reinforcement. *Journal of Nanomaterials*, 2010:352914, 2010.

- [242] H. V. Jansen, M. J. de Boer, S. Unnikrishnan, M. C. Louwerse, and M. C. Elwenspoek. Black silicon method x: a review on high speed and selective plasma etching of silicon with profile control: an in-depth comparison between bosch and cryostat drie processes as a roadmap to next generation equipment. *Journal of Micromechanics and Microengineering*, 19(3):033001, 2009.
- [243] Solvents: Theory and application. Technical report, MicroChemicals GmbH, 2007.
- [244] M Ohring. *Materials Science of Thin Films*. Elsevier B.V., 2002. Chapter 12.7.3 pp. 767.
- [245] D R Lide. *CRC Handbook of Chemistry and Physics*. CRC Press: Boca Raton, Florida, 72 edition, 1992.
- [246] W Menz, J Mohr, and O Paul. *Microsystem technology*. Wiley-VCH, 2001.
- [247] Kirt R. Williams and Richard S. Muller. Etch rates for micromachining processing - part ii. *Journal of Microelectromechanical Systems*, 12(6):761–778, December 2003.
- [248] V Halte, A Benabbas, and J-Y Bigot. Surface plasmon dynamics in arrays of subwavelength holes: the role of optical interband transitions. *Optics Express*, 16:11611, 2008.
- [249] Thomas Kiefer. *Hydrogen sensors based on palladium micro- and nanostructures for fuel cell applications*. PhD thesis, EPFL, 2009.
- [250] The etch experiments were done in collaboration with Dr. Veronica Savu from LMIS1, EPFL. Similar experiments were done etching pores into bulk Si. The results are not shown. In Si dry-etch, the ER selectivity is higher and pores with an aspect-ratio much greater than two are realistic.
- [251] J M McMahon, J Henzie, T W Odom, G C Schatz, and S K Gray. Tailoring the sensing capabilities of nanohole arrays in gold films with rayleigh anomaly-surface plasmon polaritons. *Optics Express*, 15:18119, 2007.
- [252] Y Hirai, K Sugano, T Tsuchiya, and O Tabata. Criterion of process parameter sets for fabricating 3d long microchannel embedded in single-layer negative-photoresist. In *The 26th Symposium on Sensors, Micromachines & Applied Systems*,, 2009.
- [253] Brian O'Neill. Indium: Supply, demand & flat panel displays. Technical report, AIM Specialty Materials 25 Kenney Drive Cranston, Rhode Island 02920 USA, 2004. www.aimsolder.com.
- [254] Tft lcd makers drive indium shortage and evade it. *III-Vs Review - The advanced semiconductor magazine*, 18:2005, 2005.
- [255] T. H. Reilly, R. C. Tenent, T. M. Barnes, K. L. Rowlen, and J. van de Lagemaat. Controlling the optical properties of plasmonic disordered nanohole silver films. *ACS Nano*, 4(2):615–624, 2010.
- [256] S Kinoshita, S Yoshioka, and J Miyazaki. Physics of structural color. *Reports on Progress in Physics*, 71:076401, 2008.
- [257] X Zhang, J Zhang, Z Ren, X Li, X Zhang, D Zhu, T Wang, T Tian, and B Yang. Morphology and wettability control of silicon cone arrays using colloidal lithography. *Langmuir*, 25:7375 – 82, 2009.

- [258] D Meschede, editor. *Gerthsen Physik*. Springer, 23 edition, 2006.
- [259] M Guillaumee. *Optical Transmission Through Sub-Wavelength Slits in Metals : from Theory to Applications*. PhD thesis, EPFL, 2010.
- [260] <http://www.sspectra.com/sopra.html>.
- [261] C Hibert. *COMELEC C-30-S Parylene Coating Systems*. CMI - EPFL, 2007.
- [262] Brewer Science Inc. *ProTEK temporary protective coatings*, 2007.
- [263] The BSA measurements and analysis were done in collaboration with Dr. Bernard Wenger, CSEM S.A., Neuchatel, Switzerland.

A Appendix

A.1 Au dielectric properties

The dielectric properties of metals are complex and wavelength dependent: $\epsilon(\omega) = \epsilon'(\omega) + i\epsilon''(\omega)$. They are commonly described by the so-called Drude-model^{258,259}:

$$\epsilon(\omega) = \epsilon_{DC} \left(1 - \frac{\omega_p}{\omega^2 + i\gamma\omega} \right). \quad (\text{A.1})$$

(Note that equation A.1 only applies for metals where electrons in the valence band can be treated as an electron gas in which the electrons do not experience a restoring force²⁵⁹.) The plasma frequency $\omega_p = (\frac{ne^2}{\epsilon_0 m})^{0.5}$ is a function of the electron density n (on the order of 10^{23} cm^{-3}). $\epsilon_0 = 8.854 \times 10^{-12} \text{ As/Vm}$ is the vacuum permittivity, $e = 4.355 \times 10^{-19} \text{ As}$ is the elementary charge, and $m_e = 9.109 \times 10^{-31} \text{ kg}$ is the electron mass. Further, ϵ_{DC} is the metal dielectric constant at $\omega \Rightarrow \infty$. γ is the relaxation constant which is a measure of the damping or losses in the metal. If the damping γ is neglected, one immediately sees that $\epsilon(\omega) < 0$ for $\omega < \omega_p$ and $\epsilon(\omega) > 0$ for $\omega > \omega_p$. An example of this frequency dependent optical material properties, the data calculated using on the Drude-model²⁵⁹ and tabulated experimental data²⁶⁰ are shown in figure A.1 for plain Au.

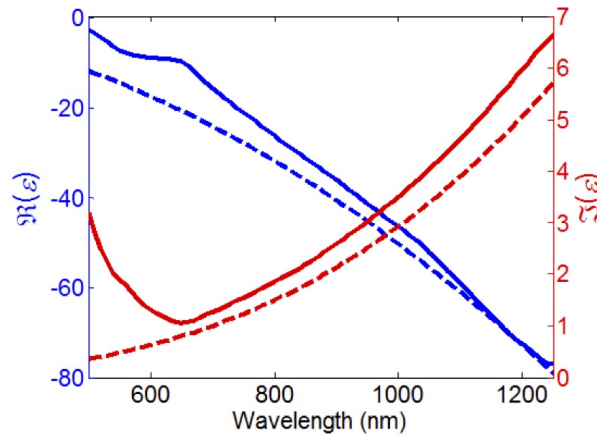
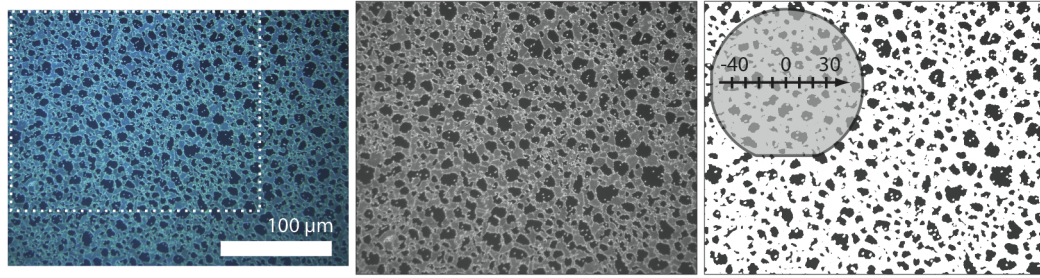


Figure A.1: Real (ϵ') and imaginary (ϵ'') dielectric constants of Au. The dashed line was calculated with the Drude-model (c.f. equation A.1). The solid line corresponds to experimental tabulated data²⁶⁰. Figure taken from Guillaume²⁵⁹.

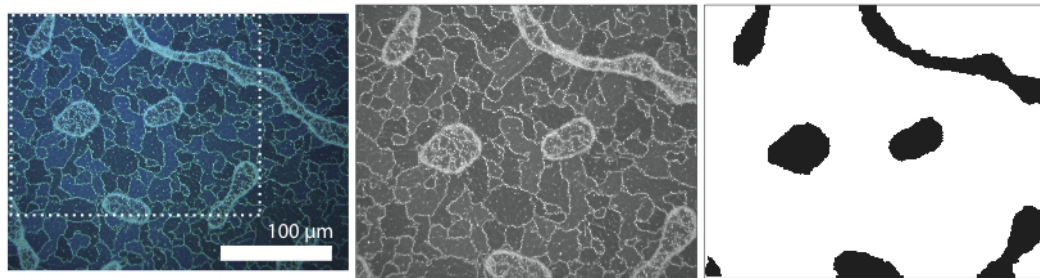
A.2 Analysis of spin-coated beads

Spin-coated bead layers were analyzed with an optical microscope with a differential interference contrast (DIC) and polarization filter. The filters allowed to maximize

the contrast between different bead layer types. The interest was to determine the area percentage of mono- and multilayers and empty areas, respectively referred to as *Monos*, *Multis* and *No-Beads*. Eight images were taken across each wafer with a pitch of 10 mm as shown in the inset in figure A.2a. A $50\times$ objective lens was used for the PSB836 and PSB535 coated wafers, a $100\times$ objective lens was used to analyze PSB284 coated wafers. Scanning electron microscope images were taken as a reference to correctly identify the different bead layer types as they appear in the optical microscope image.



(a) Selection of areas not covered with beads. (*No-beads*)



(b) Selection of bead multilayers. (*Multis*)

Figure A.2: Image treatment procedure to obtain the area percentage of *Multis* and *No-bead* areas. The images show PSB535 beads spun at 2000 rpm (figure A.2a) and at 800 rpm (figure A.2b).

First, the microscope images were cropped as indicated by the dashed rectangles in figure A.2. The cropped area had a size of $230\times 180\mu\text{m}^2$ and $45\mu\text{m}^2$ for $50\times$ and $100\times$ magnifications, respectively. The low contrast of the PSB284 bead layers made it necessary to reduce the analyzed area. After a grey-scale conversion, *Multis* or *No-beads* were selected by a thresholding procedure where possible, e.g. in figure A.2a. Areas were selected manually when a threshold could not be applied due to an insufficient contrast between the bead layers (figure A.2b).

Figure A.3 shows three images of each series with a scalebar of $50\mu\text{m}$ inserted; the respective spin-speed is indicated in the figure caption, all images were taken at $-20\mu\text{m}$ off the center of the wafer. The images were taken at a magnification of $100\times$ for PSB284 beads and $50\times$ for PSB535 and PSB836 beads.

The images that were analyzed are shown in figures A.4, A.5 and A.6. For the analysis

of the bead layers, the images were cropped and converted into greyscale images as described in chapter 2.3.3.

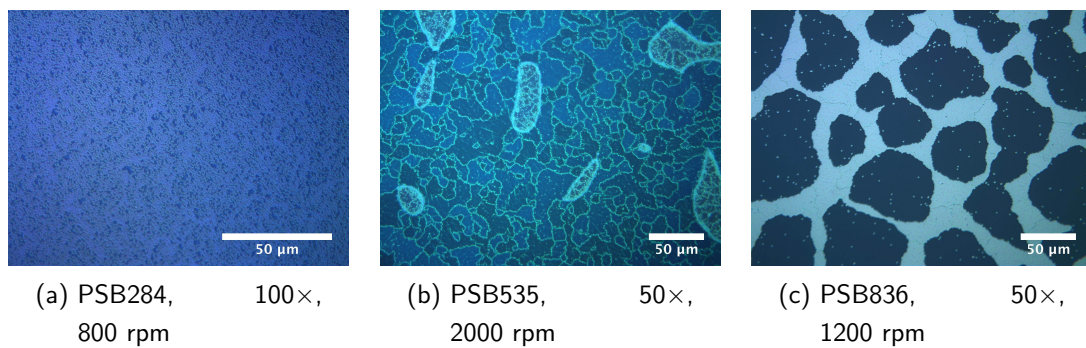


Figure A.3

PS284	Distance off center of wafer				
rpm	-40	-30	-20	-10	0
400					
800					
1200					
1600					
2000					

Figure A.4: PSB284 bead layers obtained at different spin-speeds.


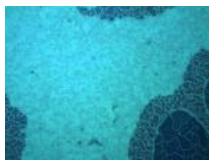

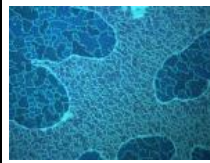
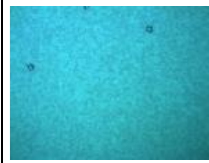
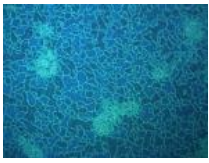
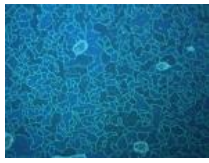


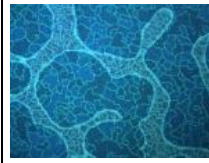




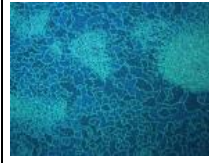

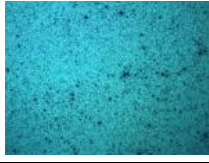
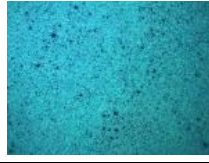







PS535	Distance off center of wafer				
rpm	-40	-30	-20	-10	0
400					
800					
1200					
1600					
2000					

Figure A.5: PSB535 bead layers obtained at different spin-speeds.






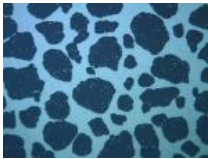






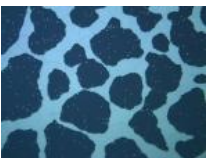










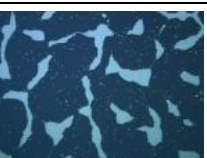

PS836	Distance off center of wafer				
rpm	-40	-30	-20	-10	0
400					
800					
1200					
1600					
2000					

Figure A.6: PSB836 bead layers obtained at different spin-speeds.

A.3 Dry-etch recipes

Machine	RIE [W]	Pressure [mTorr]	Pressure [mbar]	Gas flow [sccm]	DC Bias [V]	Radial PS bead ER [nm/min]	Remarks
O ₂ -RIE (B)	70	200	0.266	50	-250	90	
	80	200	0.266	50	-300	110 ~ 140	The radial etch rate was not always the same. It varied with the daily condition of the machine, e.g. due to contamination by previous processes.
	80	100	0.133	50	-350	N.A.	
	80	50	0.066	50	-400	90	
O ₂ -RIE (N)	30	400	0.533	50	-60	low	Size reduction of PSB517 beads can not be measured properly by SEM imaging after 4 min of etching.
	100	200	0.266	50	-250	(a) 60 (b) 100	(a) before machine maintenance (b) after machine maintenance
	100	200	0.266	50	-300	135	The DC bias could vary depending on previous machine usage. Consequently, the etch rate was also influenced.

Figure A.7: Oxford Plasmalab80plus O₂-RIE etch conditions. Standard conditions are listed in bold font.

Recipe name	Process type	Etch gases	Gas flow [sccm]	Cycle time [sec]	Pressure [mbar]	ICP (Source) [W]	RIE (Chuck) [W]	Chuck pulsation	DC Bias [V]	Etch rate [$\mu\text{m}/\text{min}$]	Remarks
MKL sharp	Si DRIE	SF ₆	300	2-3	$9 \times 10^{-3} \sim 2 \times 10^{-2}$	1500	90	pulsed	N.A.	0.5 ~ 1	ER depends on SF ₆ cycle duration, standard SF ₆ cycle time is 3 sec ; DC bias is low, only increases slightly during LF pulsation.
	Bosch-type	CH ₄	200	2		1500	0	LF			
		O ₂	100	1		1500	0	none			
SOI acc	Si DRIE	SF ₆	300	7	4×10^{-2}	1800	45	pulsed	N.A.	5	DC bias is low, only increases slightly during LF pulsation.
	Bosch-type	CH ₄	150	2	N.A.	1800	none	LF			
MK Si Opto	Si DRIE	SF ₆	20-45	cont.	3×10^{-3}	1500	15-30	RF	0 ~ 20	0.5	DC bias depends on wafer clamping, SF ₆ /C ₄ F ₈ ratio and RIE power; ER depends on SF ₆ /C ₄ F ₈ ratio and is mentions for SF ₆ /C ₄ F ₈ 40/55 sccm.
	continuous	C ₄ F ₈	45-55								
Si release	Si isotropic	SF ₆	300	cont.	1×10^{-1}	2000	0	none	0	4 (vert.) 2 (horiz.)	
SiO ₂ PR 5:1 (old)	SiO ₂ DRIE	C ₄ F ₈	17	cont.	8×10^{-3}	1500	180	RF	90 ~ 110	0.2	Etch rate may vary with SiO ₂ composition.
		CH ₄	13								
SiN LS 5:1	SiN DRIE	C ₄ F ₈	17	cont.	8×10^{-3}	1500	180	RF	90 ~ 110	0.25	Etch rate may vary with SiN type.
		CH ₄	13								

Figure A.8: Alcatel AMS200 DSE etch conditions.

A.4 Parylene-C

Parylene-C[®]²⁶¹ is a polymer which can be conformally deposited at room temperature. It is a biocompatible material, and also has interesting mechanical properties with a high Young's modulus of 3.2 GPa, a yield strength of 55 MPa and an elongation at break in the range of 10-30%. Its optical properties are less favorable as compared to rigid glass substrates, the refractive index is 1.639.

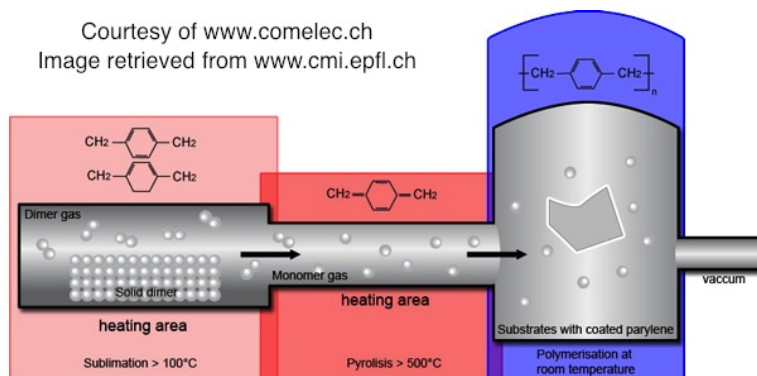


Figure A.9: Parylene-C deposition.

Parylene is deposited in vacuum chamber at a pressure of a few μ bar. Parylene is resistant to acids and bases such as HF and KOH; it swells in organic solvents but does not dissolve. It is etched in O_2 -plasma and can thus be patterned. Typical film thicknesses are a few 100 nm to tens of μ m. Figure A.9 shows the principle of the conformal room-temperature deposition process. For more information, c.f. www.comelec.ch. In a first heating stage, the solid dimer is sublimated. In the second heating stage, the dimer is decomposed into a monomer gas at high temperature. In the final stage, the monomer gas molecules polymerize into a pin-hole free continuous coating on the room temperature substrates. For more information, c.f. www.comelec.ch.

Parylene was used as the flexibly, transparent material for the transfer of thin porous gold films (c.f. section 5.3.4). In an initial experiment, the adhesion and mechanical stability of thin Au films to parylene was validated. For this purpose, a 200 nm thick Au film was evaporated onto a blank Si wafer, followed by the deposition of 5 μ m parylene. Neither the Si wafer nor the Au layer were pre-treated in a special way prior to the film depositions. The conformally deposited parylene film was cut with a scalpell at the wafer border. The Au/parylene double layer was then picked at one edge and could completely be peeled off. This is shown in the photographs in figure A.10. Thus, it was confirmed that the adhesion of parylene to Au is superior to the one of Au to Si. Although very thin, the parylene/Au was difficult to tear apart. This sufficed as a mechanical stability test.

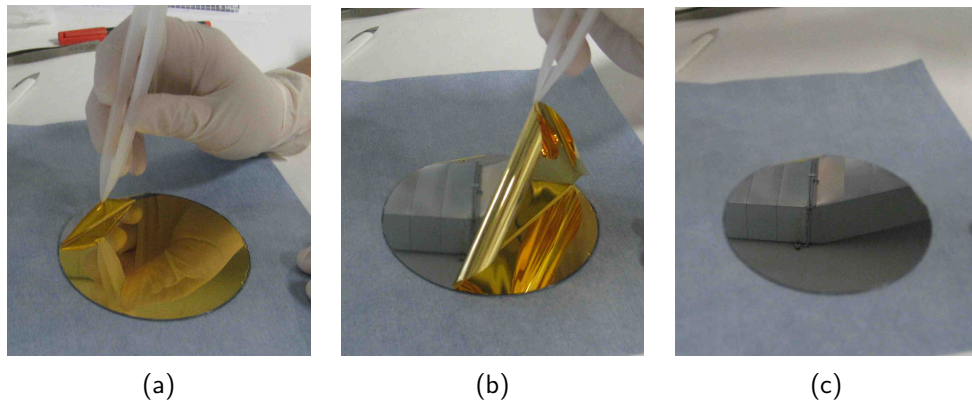


Figure A.10: 5 μm of parylene on 200 nm Au can be peeled off easily.

A.5 ProTEK

ProTEK® is a temporary protective coating developed and sold by Brewerscience Inc.²⁶². In this thesis, ProTEK B3-25 was used to avoid attack the frontside of Si wafers through pores in the frontside SiN layer. The coating is not etched in KOH, but can be easily removed in organic solvents such as Acetone or by dry-etch removal in an oxygen plasma. ProTEK was applied to the wafers by spin-coating as listed in table A.1. A primer is applied to the wafer surface prior to the spin-coating of ProTEK in order to enhance the adhesion of the ProTEK to the wafer. For the given parameters, the ProTEK film thickness was $\approx 9 \mu\text{m}$. Note that the hotplate bake times given in table A.1 30 sec longer as compared to the standard recipe to compensate for the reduced heat transfer from the hotplate to the almost-released membranes.

Process	Parameters	Comments
Primer		
O ₂ -RIE	100 W, 200 mbar O ₂ , 10 min	Ensures wafer surface free of polymeric and Cr residues
Dehydration	200°C for \geq 30 min convection oven	Promotes primer adhesion
Cooling	\approx 1 min	Wafer placed in laminar flow hood
B3 Primer spin-coating	30 sec 1000 rpm at 500 rpm/sec, V \approx 1 ml	Dynamic dispense onto rotating wafer
Primer bake	60 sec at 120°C on hotplate + 5 min at 200°C in convection oven	Handle wafer carefully, avoid touching wafer top surface with tweezers, place wafers horizontally in oven
ProTEK®		
B3-25 ProTEK spin-coating	30 sec 500 rpm at 500 rpm/sec + 60 sec 1000 rpm at 500 rpm/sec, V \approx 2 ml	Static dispense into middle of resting wafer until \approx 1/2 wafer is covered, then start spinning
ProTEK bake	90 sec at 120°C on hotplate + 30 min at 200°C in convection oven	Place wafers horizontally in oven

Table A.1: ProTEK® coating procedure.

A.6 SiO₂/SiN mask for Au membrane backside release

The backside release of porous Au films using Si pillars as lift-off template in KOH is described in chapter 5.3 using a 200 nm thick Al layer as dry-etch mask. Alternatively, a 650/200 nm thick SiO₂/SiN layer was used for this purpose as follows: Si wafers coated with 650/200 nm SiO₂/SiN were used as base substrates. This coating was selectively removed on the wafer frontside by (a) dry-etching of the SiN and (b) wet-etching of the SiO₂ layer. Thereafter, the wafers were re-oxidized by thermal oxidation for the fabrication of an intermediate SiO₂ oxide dot mask. Then, the process was performed as described in chapter 5.3. At process step Si5 in figure 5.15, instead of wet-etching an Al layer, the backside SiN was patterned by photolithography and dry etching. Then, the backside oxide was either wet- or dry-etched using the SiN as etch-mask.

A.7 Mask layouts

Masks for SiN membranes

Figure A.11 shows the first, figure A.12 shows the second mask design that were used for the fabrication of porous SiN membranes. In both cases, the chip size was $6 \times 6 \text{ mm}^2$ with 174 chips per wafer. The masks had flat alignment and frontside/backside alignment structures. Both designs contained chips with square membranes and membrane arrays with side-lengths ranging from 400 to 2400 μm .

From the designs, Cr masks were fabricated for use with positive tone photoresist. In the first design, the frontside mask was a bright-field mask (“what is green is Cr”), the backside mask was a darkfield mask (“what is empty is Cr”). In the second design, both front- and backside masks were dark-field masks. In both designs, one mask was mirrored.

The principal difference between both designs is that the first design foresaw “grill” structures within membranes larger than 800 μm . The bars had a width of 40 μm and were arranged to give an effective etch opening of approximately 400 μm also for membranes larger than that. The grill structures were integrated into the design in an attempt to compensate aspect-ratio dependent etching (ARDE) during Si-DRIE. Although this was to some extent successful, difficulties arose when the grill structures needed to be removed either by isotropic Si-DRIE or KOH wet-etching. Si etch loading also influences the etch rate, and therefore membranes of different sizes were homogeneously distributed across the wafer surface. A radial etch rate dependence was not taken into account.

In a second run, a mask design was made without grill structures in conjunction with a fabrication process that tolerates long KOH over-etch times. This alleviated the necessity to compensate for ARDE; radial etch rate variations and Si etch loading could also be ignored. Therefore, membranes of similar size or pattern (e.g. single or array) were grouped together. In the second design, the porous membrane area was limited to within the released region. A margin of at least 50 μm was foreseen, taking into account that the final KOH release step etches the Si under an angle of 54.7° which laterally reduces the membrane size. Backside manual cleavage trenches and frontside dicing marks were also integrated into the design.

Masks for Au membranes

Two sets of masks were designed for the fabrication of porous Au membranes. In the first design, the chips were arranged in line with initial e-beam writing tests where pattern stitching can be done with a pitch of 1.2 cm. Two types of chips were designed, one with square, the other with round membranes; each chip contained porous and non-porous membranes as well as areas with micro-patterned structures only. The membrane size

one each chip varied from 40 μm to 990 μm in diameter.

In the second design, chip size and arrangement was done in the same way as for the fabrication of the porous SiN membranes. The difference was that the margin between frontside and backside pattern were only 50 μm for all membranes because Au membranes were released by a final isotropic dry etch which enlarges the membrane size and does not shrink (as in case of KOH release).

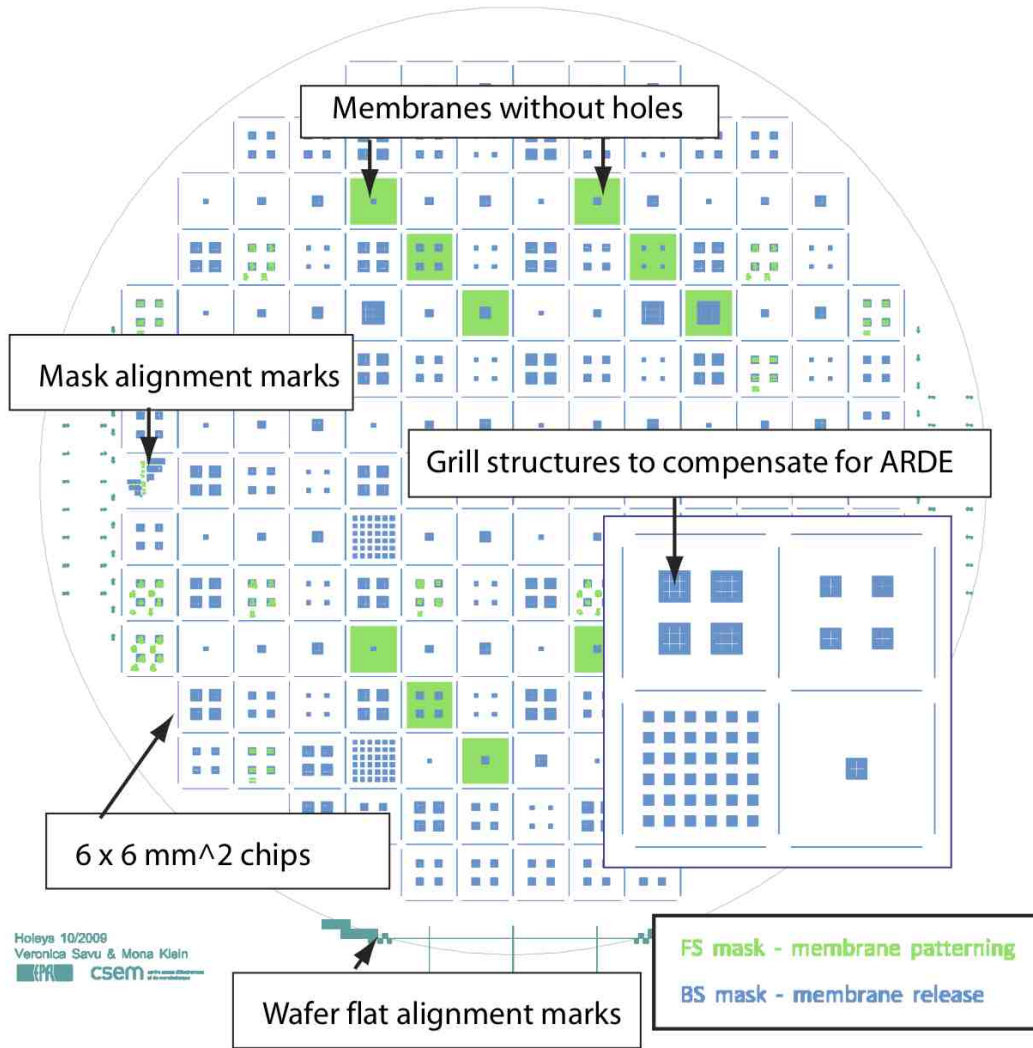


Figure A.11: First mask layout with ARDE compensation structures.

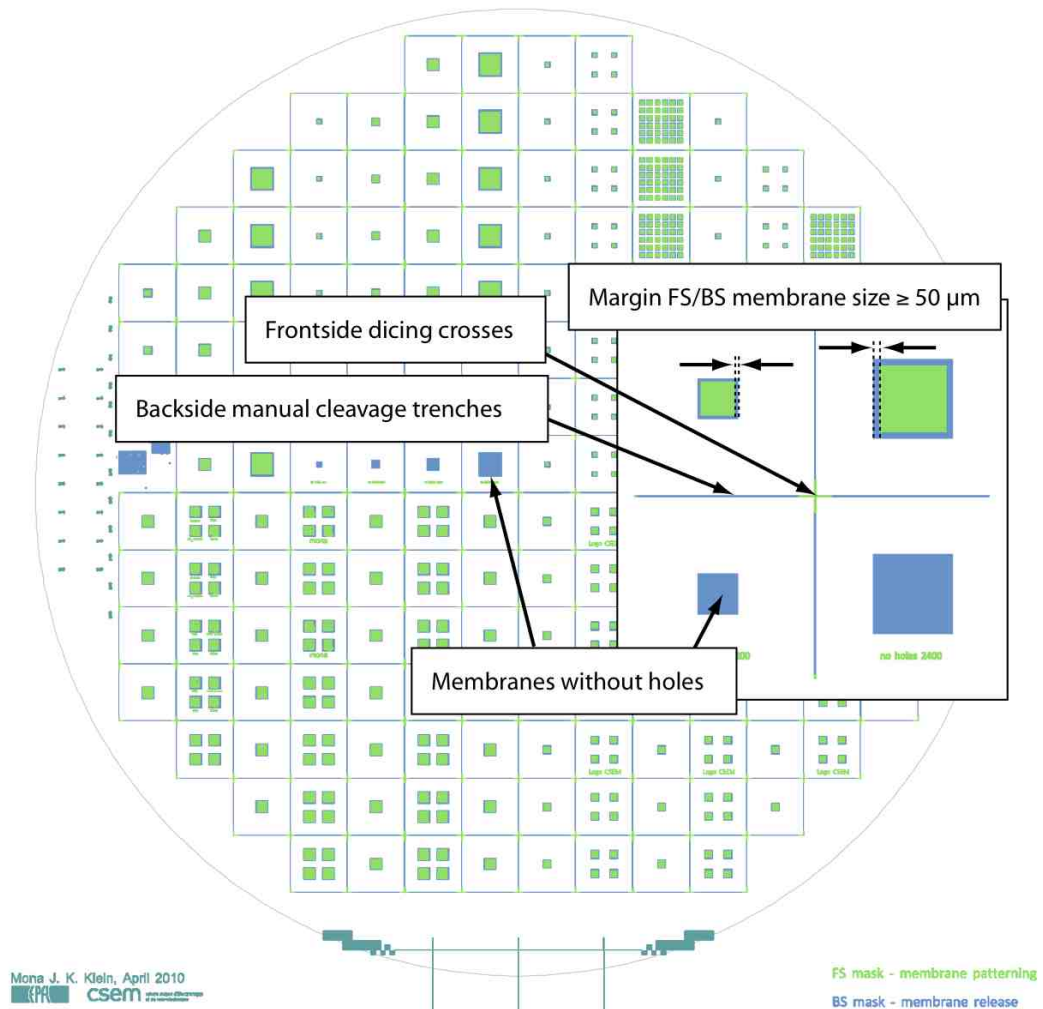


Figure A.12: Second mask layout for micro-patterned pores.

A.8 Transmission through sputter-etched hole arrays in Au films on glass substrates with increasing hole size

Light transmission through hole arrays in 200 nm thick Au films fabricated using the intermittent sputter-etch procedure was measured after 20 min, 30 min, 40 min and 50 min of cumulative etch time (c.f. section 5.2 and figure 5.13). The hole array parameters are $p \approx 419$ nm, $D_{hole,AuGlass}$ is increasing from 65 nm to 195 nm, and ff is increasing from 2% to 19%. Figure A.13 shows the corresponding spectra. Shown in the insets are SEM images of the respective holes. The lower left graph plots $D_{hole,AuGlass}$ as a function of cumulative etch time.

The light transmitted at 510 nm is due to the Au transparency window in this wavelength region. The long-wavelength transmission from 680 to 800 nm is mediated by SPs. The red-shift of the SP peak with increasing hole diameter is due to an interference with the WR anomaly around 620 nm.

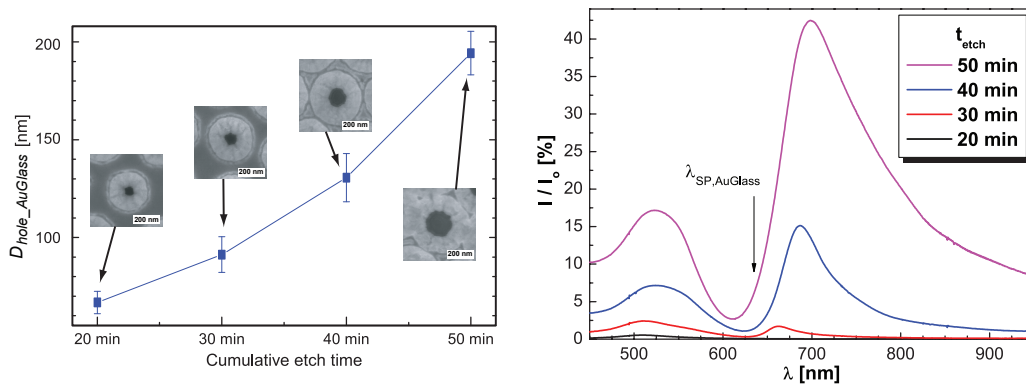


Figure A.13: Optical transmission through hole arrays of increasing $D_{hole,AuGlass}$ on a type A wafer fabricated by the intermittent sputter-etch procedure.

A.9 Transmission through free-standing and parylene supported Au membranes

As described in chapter 5.3, 200 nm thick Au films on a 10 μm thick flexible parylene layer (figure 5.16) as well as free-standing Au membranes with arrays of sub- μm holes (figure 5.24) were fabricated using SiO_2 pillars as a lift-off template. Here, no adhesion layer was used for the Au film. The hole array parameters were $p \approx 419$ nm, $D_{bs} = 180$ nm, corresponding to $ff = 16\%$ (figure A.14b). The optical spectra through free-standing and parylene supported membranes are shown in figure A.14.

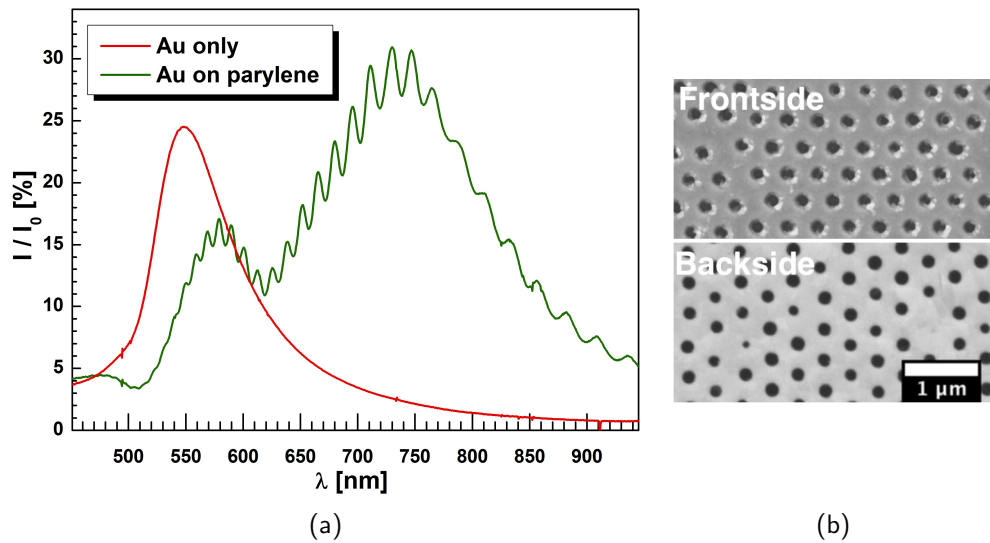


Figure A.14: (a) Optical transmission through hole arrays shown in (b) when supported by 10 μm parylene and in the free-standing case. (b) SEM images of the front- and backside of the characterized Au film on parylene and membrane with $p \approx 419$ nm, $D_{hole} = 180$ nm, $ff = 16\%$.

A.10 BSA adsorption measured by optical transmission through sputter-etched hole arrays

These measurements were done within an internal collaboration at CSEM S.A.²⁶³. Hole arrays on a type A wafer were used (c.f. section 5.2). First, the hole arrays were immersed in a PBS buffer solution (phosphate buffered saline, pH = 7.3). The corresponding transmission spectrum is shown in the inset in figure A.15. Then, the pure buffer solution was exchanged for PBS buffer containing a small amount of BSA (1 %w/w) and the transmission spectra were recorded continuously in time intervals of 10 sec.

BSA adsorption took place over a timescale of ≈ 15 min when no further changes in the transmission spectrum could be observed. This was measured by first performing a linear fit in the steep slope region from 715 to 725 nm, and then taking the measured intensity at 720 nm as a data point. The data points obtained in this way show a low-noise distribution. A plot of these data points over time is shown in figure A.15.

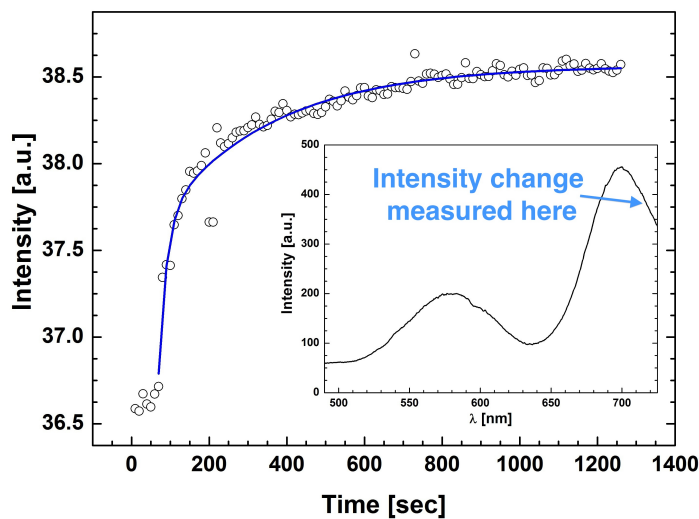


Figure A.15: Real-time monitoring of the adsorption of BSA at the hole array surface. Shown in the inset is the full transmission spectra of the hole arrays immersed in pure water. The change in intensity was recorded at a fixed wavelength as indicated by the arrow.

Acknowledgements

First of all, I would like to thank my jury, Prof. Osamu Tabata, Dr. Heiko Wolf, and Prof. Nico de Rooij, for going through this - not very short - manuscript, composing a report, taking the time to be there at the date of the exam. I very much appreciated their critical comments and suggestions that came up during the discussion.

Also, I would like to thank the jury president, Prof. Adrian Ionescu, who has hopefully enjoyed the oral exam as well.

Special thanks go to my thesis directors, Prof. Jürgen Brugger and Dr. Raphaël Pugin, who guided me through 3.5 years of Ph.D. work not only through regular discussions, but also by creating a stimulating work environment. At the same time, they gave me freedom to discover and try out un-conventional methods. They provided the means so that I could participate in educational seminars and conferences that contributed to my understanding of the nano-world and the underlying physics. Last but not least, I would like to thank them for critical suggestions and comments on the present manuscript that helped me a lot in the writing process.

This manuscript would not be here in this form without the help of colleagues and friends who minutely corrected various chapters. Nicolas, Rolf, and Mickaël, I want you to know that your help is very, very much appreciated, more than can be expressed by paying a couple of rounds of beer.

In a similar way, but on the personal side, my boy-friend Cédric contributed to this manuscript with his patience, love, care, and confidence in me, which will also make that I remember this summer not only as the summer-of-the-thesis. I thank him for being who he is, and fortunately he is with me.

No future without past. My academic life, but also my personality, has been greatly influenced through the work with three out-standing persons: Prof. Jan G. Korvink, Prof. Osamu Tabata, and Prof. Masayoshi Esashi. I would like to thank them for teaching me the reward of hard work, but also that work is not everything.

Keep on running - is one of my favorite citations of a former colleague, Yoshikazu Hirai, that, interpretation with care, has helped me to pass the downs between the ups. This shall now be supplemented with a word by Friedrich Nietzsche that I picked from JoSeP's webpage: *Ignore any idea that is **not** initiated during outdoor activity, while also the muscles are filled with blood.* How lovely is that ?

Beginning a new life in a new environment with a foreign language is never easy, and life in Neuchâtel was not so funny in the beginning. Now I don't want to move any more. And the reason is that I have friends and colleague-friends like Rolf, Andrea, Nicolas, Mickaël, Rob, Josep, Mimi, Edo, Ulrich, Susanne, Roberto and Antonio.

I don't know how things would have turned out if I had not had Ana as a colleague in the first 2 years. It's not only that "gemeinsam einsam" is easier to support. We also discussed science and she helped me understand things in the lab, encouraged me to try out new things, helped me to overcome setbacks, and was just fun in the office.

Many results in this thesis would not be there if it were not for colleagues like Nicolas, Bernard and, especially Veronica. For me, this is the ideal and efficient work collaboration that brought about the ever-so-often cited synergies.

What would I have done without Patricia and Ilona ? Thank you so much for reserving train tickets, planning travels, taking care of all those bureaucratic necessities, and always having a smile ready even if it rains.

Finally, I would like to thank my family. Especially my mother. Mothers are so forgiving. My mother always showed me that she loves me. And did all that was necessary, and much, much more, that I can live my life following my desires. Yes, she provided the conditions for self-fulfillment to me. And that is the greatest thing in life.

Mona J. K. Klein

Avenue des Alpes 70
CH-2000 Neuchâtel

Phone ++41 (0)32 725 2509
Mobile ++41 (0)76 207 2821
E-mail mjk.klein@gmail.com

Personal information: 30, single, German

Strengths

Micro- and nanofabrication expertise in different domains
Organised and pragmatic, goal-oriented working style
Dynamic, flexible, open-minded person

Education

- 2007-2010 **Docteur ès sciences (Ph.D.)**
Swiss Technical University Lausanne (EPFL), Switzerland.
Swiss Center for Electronics and Microtechnology (CSEM SA), Switzerland.
- 1999-2006 **Dipl.-Ing. in Microsystems Technology (M.Sc.)**
University of Freiburg, Germany.
- 1991-1999 **High-School**
Amos-Comenius-Gymnasium, Bonn-Bad Godesberg, Germany.

Grants

- 2007 **Bourse d'excellence de l'école doctorale** 1-year funding of doctoral studies at EPFL, Switzerland.
- 2005/06 **Baden-Württemberg Stipendium** 7-month research stay at Tohoku University, Japan.
- 2002/03 **DAAD fellowship for students** 10-month research stay at Ritsumeikan University, Japan.

Academic achievements**Ph.D. thesis Wafer-scale fabrication of arrays of sub- μm holes in thin SiN and Au membranes.**

- 2007-2010
- Combination of conventional, top-down with self-assembly based, bottom-up fabrication methods.
 - Nanosphere lithography.
 - Micro-patterned pillars and pores in Si, SiN, SiO₂.
- Applications: Plasmonics, filtration, stenciling, thin film photovoltaics, organic light emitting diodes.

Diploma thesis Design and fabrication of solenoidal microcoils for micro-MRI using RIE.

- 2005/06
- Reactive ion etching of borosilicate glass.
 - Anodic bonding of 3D hollow glass mold.
 - Galvanodeposition of Ni and autocatalytic Cu.
 - Metal-organic vapor deposition of Cu.
- Applications: Magnetic resonance imaging (MRI), microfluidics.

Professional Experience

- 1999-2006 **Student assistant** at different chairs, Freiburg University, Germany.
Installation of a contact angle measurement system; optimization of SU-8 photolithography process; acquisition of lab equipment for rheometry characterization.
- 2001 **Internship** at the Institute for Micro- and Informationstechnology HSG-IMIT, Germany.
Systematic testing of a micro-array printing system.

Skills

- Technical DRIE of Si, SiN, SiO₂. PVD. Wet-etching. Photolithography. Galvano-deposition. Nanosphere lithography. Polymer self-assembly. Parylene. SU-8. ProTEK. SEM, EDX, AFM, VIS spectrometry, ellipsometry, optical interference microscopy, profilometry.
- IT Image analysis (analySIS, ImageJ, Gimp), data treatment (Origin, Igor), simulation software (Matlab, Mathematica), documentation (Word, Powerpoint, Latex), graphics (Adobe Illustrator).

Extracurricular achievements

- 2010 Patrouilles des Glaciers (B Parcours, corresponds to 52 km of effort).
- 2008 Mountain-bike tour Neuchâtel – Porto in 3 weeks (1400 km).

Languages

- German mother tongue
English fluent
French spoken
Japanese basic knowledge

Hobbies and interests

Mountain-biking, alpine and cross-country skiing, badminton, climbing, creative design and artwork.

Appendix List of publications

Appendix to the CV of Mona J. K. Klein

List of publications

- 2010 *Wafer-scale fabrication of thin SiN membranes and Au films and membranes with arrays of sub- μm holes using nanosphere lithography.* Ph.D. thesis EPFL (submitted September 2010).
Nanoporous SiN membranes patterned by wafer-scale nanosphere lithography.
Oral presentation at the EIPBN conference, Anchorage, Alaska.
Nanoporous SiN membranes patterned by wafer-scale nanosphere lithography.
(submitted to JVST)
Inexpensive and fast wafer-scale fabrication of nanohole arrays in thin gold films for plasmonics.
Nanotechnology (21) 2010.
Co-author to: *Observation of enhanced transmission for s-polarized light through a subwavelength slit.*
Mickaël Guillaumée et al., Optics Express (18) 2010.
Co-author to: *Use of Force Spectroscopy to Investigate the Adhesion of Living Adherent Cells.* Gilles Weder et al., Langmuir (26) 2010.
Nanoporous Films for Sensing and Filtration. Scientific and technical report CSEM 2009.
- 2009 *Large area hole arrays fabricated by a templating method for refractive index sensing.*
Poster at SPP4 conference, Amsterdam, Netherlands.
Wafer-scale nanopatterning and fabrication of nanoporous membranes in SiN and Au.
Poster presented at the EDM research day EPFL 2009, Lausanne, Switzerland.
Subwavelength hole arrays in thin gold films fabricated by NSL and sputter etching for sensing applications.
Poster presented at the Summer School on Plasmonics 2009, Les Porquerolles, France.
- 2008 *Optical transmission of hole arrays fabricated by nanobead templating.*
Oral presentation at the MNE conference, Athens, Greece.
Mold metallization process for the batch fabrication of high-resolution MRI solenoidal micro-coils enabling low loss integration of electronic devices.
Poster at the ISMRM conference, Toronto, Canada.
Process for the fabrication of hollow core solenoidal microcoils in borosilicate glass.
J. Micromech. Microeng. (18) 2008.
- 2007 *RIE of Solenoidal Microcoil Glass Mould with Integrated Sample Container for Micro-MRI.*
Poster at the MEMS conference, Kobe, Japan.